Technical University of Delft

AE3200 Design Synthesis Exercise

Final Report

DELFFI Delta and Phi: Two nano-satellites for formation flying in Low-Earth Orbit (Phi group)

Version 1.0

Authors:

Koshear, Maryam	1511645
Liu, Yuejia	4091868
Murali, Sneha	4124197
Olsthoorn, Ronald M.	4037006
Pollier, Chabely M.	4114639
Srongprapa, Pattareeya	4125231
Wolff, Friederike	4110919

Supervisors:

Sundaramoorthy, Prem
Gransden, Derek
Doornbos, Eelco

July 2, 2013

TU Delft Delft University of Technology

Contents

List of Symbols

Greek symbol	Significance
α	Absorptivity
α	Energy accomodation coefficient
ϵ	Expansion ratio
ϵ	Specific orbital energy
η	Efficiency
η_{AR}	Array efficiency
η_{BCR}	Battery charging efficiency
η_{BDR}	Battery discharging efficiency
η_{cell}	Cell efficiency
η_{charge}	Charging efficiency
$\eta_{packing}$	Packing efficiency
γ	Specific heat ratio
Γ	Vandenkerckhove function
γ	Angle between velocity vector and inward surface normal
μ	Standard gravitational parameter
ω^b	Bus rot. speed relative to inertial ref.
ω_{rw}	Wheel speed
ϕ	Max. roll angle
ρ	Atmospheric density
τ	Shear stress
θ	Incidence angle
θ	Argument of latitude
θ	Max. pitch angle
ε	Emissivity

Latin symbol	Significance
A	Cross Sectional Area
A	Coil area
A^*	Area throat
A_{albedo}	Satellite's surface area facing albedo radiation
A_{array}	Array area
A_e	Exit area
A_p	solar average geomagnetic planetary index
$A_{planetary}$	Satellite's surface area facing planetary radiation
A_{ref}	reference area for drag coefficient
A_{solar}	Satellite's surface area facing the Sun
$A_{surface}$	Total spacecraft emitting surface area
a	Planetary albedo
a	Semi-major axis
$\hat{a}, \hat{b}, \hat{c}$	Rotational axes of reaction wheels (1,2,3)
B	Inverse ballistic coefficient
B	Magnetic flux
C_D	Drag coefficient
$c_{m,p}$	Thermal velocity of molecules
cp	center of pressure
D	Degradation factor
D	Residual dipole
d	Distance from the Sun to the planet
E	Young's Modulus
E_B	Battery stored energy
E_{loss}	Energy loss
F	Visibility factor
F	Thrust force
$F_{10.7}$	solar radio flux per unit frequency at a wavelength of 10.7 cm
F_b	Body reference frame
f_n	Natural frequency of nth mode
G_r	Receiver gain
G_t	Transmitter gain
H	Angular moment of s/c in frequency domain
He	Helium
H_{rw}	Angular momentum of reaction wheels
h	Altitude
h	Angular momentum of s/c
I	Moment of inertia
I_0	Standard solar flux
I_0	Wheel inertia (1,2,3)
i_c	Current in the magnetic torquer
I_d	Inertia due to displacement from Cg (1,2,3)
J	Mass moment of Inertia of the s/c
J_0	Body principle MOI without wheel
J_2	Dynamic oblateness of the Earth
J_a	Planetary albedo intensity
J_d	Inertia due to shift of COG
J_p	Planetary IR radiation intensity
J_s	Solar intensity
k	Stefan-Boltzmann constant
L	Length
L_a	Atmospheric loss
L_l	Line loss
L_{pr}	Polarisation mismatch loss
L_{pt}	Pointing loss
L_s	Space loss
M	Molar mass
M_{CGG}	CGG mass total
M_{rest}	Rest mass (remaining)

Latin symbol	Significance
M_{rw}	Reaction wheel moment
M_{tank}	Tank mass
M_{sys}	System mass
m	Mass
m_b	Body mass without wheel
m_b	Magnetic moment
m_{CGG}	CGG useable propellant mass
m_g	Wheel mass
$\dot{m}$	Mass flow
N	Number of turns in the coils
N_2	Nitrogen
n	Mode number
n	Mean motion
P	Load
P	Transmitting power
P_{array}	Amount of power required by the array
P_{charge}	Amount of power needed to charge the batteries
$P_{eclipse}$	Amount of power needed during eclipse
P_s	Total emitted power from the Sun
P_{sun}	Power needed during sunlight
p	Pressure
p_∞	Pressure free stream
p_c	Pressure chamber
p_e	Pressure exit
Q	Heat dissipation
q	surface reflectance
q	Distributed load
q	Unit quaternion
R	Data rate
R	Universal gas constant
R	Rotation matrix
R_e	Radius of earth
R_{rad}	Radius of the Earth's effective radiating surface
S	Speed ratio
T	Time interval
T_{aero}	Aerodynamic torque
T_c	Temperature
$T_{eclipse}$	Eclipse period
T_{gg}	Gravity gradient torque
T_m	Magnetic torque
T_s	Systems Temperature
T_{sr}	Solar radiation torque
T_{sun}	Sunlight period
T_t	Thrust misalignment
T_{tot}	Total disturbance
T_{WB}	Transfer from wheel ref. to body ref.
T_w	Spacecraft wall temperature
t	Time instant
t_0	Time at instant zero
V	Orbital velocity
V_e	Exit velocity
V_{eq}	Equivalent velocity
$Wh_{eclipse}$	Amount of Wh needed during eclipse
w	Displacement of cantilevered beam
w_n	Angular natural frequency of nth mode

List of Abbreviations

ADCS	Attitude Determination and Control System
AE	Acoustic Emission
AEOLDOS	Aerodynamic End-Of-Life De-orbit System
AO	Atomic Oxygen
BOL	Begin of Life
CGG	Cool Gas Generator
CID	Control Interface Document
MCU	Micro Controlling Unit
CHAMP	CHAllenging Minisatellite Payload
COMMS	Communications System
COTS	Commercial Off-The-Shelf
CPU	Computer Processing Unit
DET	Direct Energy Transfer
DH	Data Handling
DOD	Depth of Discharge
DoD	Department of Defence
ELV	Expendable Launch Vehicle
EoC	End of charge
EOL	End of Life
EPS	Electrical Power System
ESA	European Space Agency
FAST	Formation for Atmospheric Science and Technology demonstration
FIPEX	Flux-ϕ-Probe Experiment
FOV	Field Of View
GNC	Guidance, Navigation and Control
H/W	Hardware
ICT	Integrated Circuit Temperature
ISL	Inter-Satellite Link
LEOP	Launch and Early Orbit Phase
LEO	Low Earth Orbit
MEMS	Microelectromechanical systems
nrCGG	Number of cool gas generators
OBC	On-board Computer
OLFAR	Orbiting Low Frequency Array
PCB	Printed Circuit Board
PPT	Peak Power Tracking
PV	Photo-Voltaic
RTD	Resistance Temperature Detectors
SD	Secure Digital
SEU	Single Event Upset
SpaDe	Space Debris Elimination
SSWG	Sensor Selection Working Group
STK	Satellite Tool Kit
SWOT	Strengths, Weaknesses, Opportunities and Threats
TCS	Thermal Control System
TLE	Two-Line Elements
TMM	Thermal Mathematical Model
TT & C	Telemetry, Tracking & Command
TU	Technical University
UAV	Unmanned Aerial Vehicle
UHF	Ultra High Frequency
VHF	Very High Frequency
VKI	Von Karman Institiute
WBS	Work Breakdown Structure

Acknowledgements

The group wants to take the opportunity to gratefully acknowledge the people without whom it would have been impossible to write this report.

First of all, our major gratitude goes to Prem Sundaramoorthy, Derek Gransden and Eelco Doornbos, who have been amazing and very helpful coaches. They have supported us with a large amount of valuable information and honest criticism.

We would like to thank a few staff members and students of the Space and Control & Simulation departments of the faculty of Aerospace Engineering TU Delft for sharing their knowledge; Jasper Bouwmeester for letting us see the cleanroom and for sharing his experience in designing Delfi-C^3 and Delfi-n3Xt; Barry Zandbergen for supporting us and sharing information about propulsion and electrical power systems; Ron Noomen for providing us with the STK software; Carsten Macco for his insight on the thermal system and the thermal Excel tool; Bart Wiegant for letting us borrow equipment; Qiping Chu for helping out on the stability of the ADCS-system. To Chris Verhoeven and Steven Engelen from OLFAR, thank you so much for all the information you shared with us so willingly. The discussions we had were really helpful and truly contributed to the design. Special thanks to the Delta-team as they were more motivating than they realised. Thanks go out also to Wolter Willing, TNO for providing us with information about propulsion systems.

Finally, we would like to offer our gratitude to friends and family for the priceless and unconditional support.

Abstract

In the past 55 years, a lot of progress has been made in the field of spacecraft engineering, continuously making new technologies available and thereby enlarging the scope of possible missions. The trend which is at present most important is the miniaturisation of not only electronics, but also other devices such as MEMS. This has made space accessible for small institutions like universities by making use of piggy-back launch opportunities. The limits in budget and manpower call for the design of small spacecraft, which on their own cannot compete with any large space project. However, small spacecraft do offer significant advantages, one of which is the possibility for high coverage by using networks of multiple satellites. Even simple designs can provide valuable services or data. The latter is exploited by the mission QB50 which has been initiate by the Von Karman Insititute. 50 satellites will be deployed at the same altitude and perform *in-situ* measurements of atmospheric properties that will allow verification of climate models. This will allow short-term changes in the atmosphere to be monitored with a resolution that would not be possible with a conventional spacecraft design approach.
However, the dynamics of the QB50 network is uncontrolled. The satellites will drift apart in radial as well as in along-track direction, which is in this case beneficial to distribute the points of data-collection. For more sophisticated missions, however, constellations will have to be controlled. This is why in addition to contributing to the QB50 network, the first formation flight between two nano-satellites will be demonstrated. This will make it possible to sample locations in the atmosphere at a resolution of two minutes, thereby enhancing science return. Two types of formation flight will be carried out: a ΔV budget of 15 m/s has been decided upon together with the group designing the Delta satellite to perform a variety of maneouvers for acquisition, formation keeping, as well as reconfiguration. The second kind of formation flight is differential drag. The satellite design incorporates flaps to increase the drag coefficient by up to a factor three to adjust the relative decay rates. This technology is ideal to carry out moderately precise maneouvers of high negative ΔV and could be envisaged for the first part of the approach during debris removal missions. The demonstration of formation flight in general constitutes a stepping stone towards high-coverage missions with the potential for reconfiguration, such as telecommunication for remote areas.

Chapter 1
Introduction

Following the success of the Delfi-C^3 and the completion of the Delfi-n3Xt assembly, the Delft University of Technology started the development of its third nano-satellite project. This project, unlike it predecessors, consists of two satellites instead of one. They are known conjointly as DelFFi and separately as Delta and Phi. DelFFi is scheduled for flight in Low Earth Orbit (LEO) in 2015 as participants in the QB50 network, organized by the Von Karman Institute in Belgium.

A group of seven undergraduate aerospace engineering students were assigned the task of developing a conceptual design for the Phi satellite. This report documents what has been accomplished during the project. Prior to starting this report, a Project plan, a Baseline report and a Mid-term report have been submitted.

This report contains the final conceptual design. The description of the secondary mission objectives that have been chosen as well as the components for each subsystem. Detailed mass and power budgets have been created and the performance of the design to carry out all mission objectives has been evaluated.

In Chapter 2, the mission as a whole will be analysed and elaborated upon. The systems engineering part of the project is discussed in Chapter 3. Next, the primary payload from QB50 as well as the secondary payloads will be presented. The last part of the report deals with the detailed bus design. All subsystems are addressed and justifications for the choice of components will be given. Detailed performance analyses will be presented as well, together with sensitivity analyses and recommendations.

Chapter 2
Mission Design

This chapter deals with different aspects concerning the mission design of the project. First the mission description is presented, followed by the mission objectives, which are mainly divided into the primary and secondary payloads, and formation flying. Next, calculations of the satellite's lifetime are explained. The coordinate frames used and aerodynamics are discussed in the Section 2.4. The chapter is then rounded off with an explanation of the satellite configuration.

2.1 Mission Description

The DelFFi project is part of the QB50 network, initiated by the Von Karman Institute (VKI) in Belgium. This network involves fifty 2U and 3U CubeSats developed by educational and science institutes worldwide. The project's objective is to launch these satellites to orbit in the lower thermosphere to carry out *in-situ* atmospheric research using a set of predefined sensory payloads. Next to this primary payload, TU Delft is free to define its own mission objectives for the DelFFi project, which are the demonstration of formation flying between two 3U satellites a well as the secondary mission objectives that will be elaborated upon in Section 2.2.

2.2 Mission Objectives

In the following subsections, the three main mission objectives of the Phi satellite are explained. These are the demonstration of formation flying, the operation of FIPEX and thermistors (primary payload), and deployment, satellite health and impact monitoring (secondary payload).

2.2.1 Formation Flying

The primary mission objective of DelFFi the demonstration of formation flying. For this mission the nominal along-track distance is 1000 km. Successfully obtaining this objective would hold considerable technological and scientific significance, since formation flight between two CubeSats has never previously been executed in such a low orbit. The requirement of 1000 km separation is derived from the temporal resolution needed for the atmospheric data. Processes in the atmosphere are slow, and a temporal resolution of 2 min is the lowest spacing that would be of scientific interest. At an orbit of approximately 300 km altitude, this translates into an along-track separation of 1000 km. A successful demonstration would be a source of validation for tentative missions involving multiple nano-satellites flying in similar configurations collectively acquiring data. Realisation of such missions would consequently allow the scope of the current measurement capabilities to improve considerably.

2.2.2 Primary Payload

The main objective of the QB50 mission is the validation of current atmospheric models in the scarcely observed thermosphere. With 50 nano-satellites all taking *in-situ* measurements, this objective can be achieved with very high coverage. All participating satellites must carry one of two sets of sensors. Phi has been allocated the Flux-Φ-Probe (FIPEX) sensor developed by TU Dresden, which measures molecular and atomic oxygen concentrations. The satellite must also accommodate twelve thermocouples so that surface temperature measurements can be made to determine the flow field around the satellite.

2.2.3 Secondary Payload

Next to the primary payload (the FIPEX sensor and thermocouples) and the formation flying objective, a secondary mission objective can be chosen freely. With the available mass budget, two mission objectives of interest have been selected. These are cameras for monitoring the deployment of the satellite's antennas and solar panels, and acoustic sensors for analysing the vibrations of the satellite. More information can be found in Section 6.

2.3 Configuration

Satellite configuration is restrained by the DelFFi mission objective that Phi needs to be a 3U CubeSat and the QB50 requirements that the 0.1×0.1 m^2 face needs to points to the direction of the velocity. Since the satellite power generation and life time strongly depend on structure configuration choice, a comprehensive analysis should be made with respect to the relation between these two aspects. Besides, the configuration also has influence on the disturbance

Table 2.3.1: Performances depending on modules architecture

	3U	3U deployable 1	3U deployable 2	3U deployable 3
Power	1	4	5	3
Disturbance	3	1	2	5
Life time	5	1	3	4

on the spacecraft. However, due to the low altitude that Phi is orbiting, the aerodynamic torque will become very high. Considering a 3U CubeSat with only body mounted solar panels, the torque can be as high as 1.27×10^{-5} at 200 km altitude, as shown in Figure 2.3.1. For this level of disturbance, the power for the ADCS only is going to be around 2 W and around 9 W for the whole spacecraft. However, according to Clyde Space [60], the body mounted solar panel, providing 7.3 W on average, is not enough for the spacecraft to function normally.

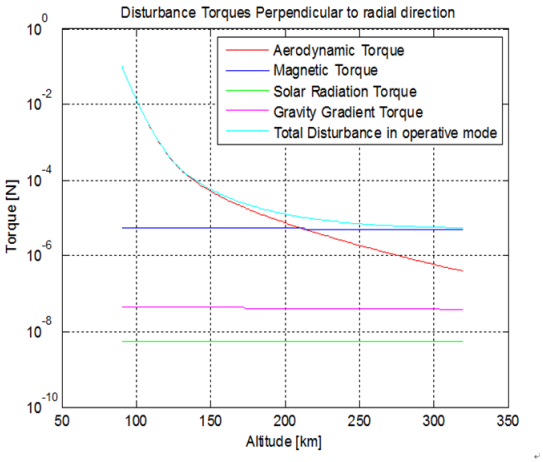

Figure 2.3.1: Disturbance on a 3U CubeSat

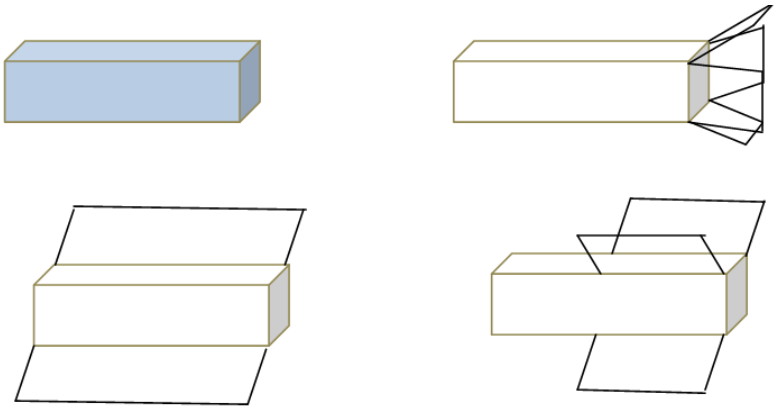

Figure 2.3.2: Configuration for four options

Deployable solar panel architecture, depicted in Figure 2.3.2, has been proposed and would result quite attractive because they would extend cross areas exposed to sunlight. However, that would means to constrain attitude towards sun direction, losing body mounted panels advantage and they would greatly increase the aerodynamic disturbance counteraction and sacrifice life time.
However, if taken the advantage of the aerodynamic torque as a way to stabilise the spacecraft, the deployable solar panels are of interest. The first deployable configuration on the top right has been demonstrated in Space Dart. However, due to the large frontal projected area, the spacecraft will decay rather fast in such a low altitude. However, for the second and third options, the projected area can be controlled by the pointing accuracy in the velocity vector direction.
The difference between the second and third choice is the area and location of wings. Wings of the second configuration have the same size as the side panel while those of the third one takes up only the back part of the side panel. The length of the wings in the third configuration is adjusted based on the power needed. The advantage of the third design is due to the shift of center of pressure on the spacecraft. The aerodynamic torque will counteract other disturbance and has stabilised effect. If four wings are taken on edges, pitch axis and yaw axis can be controlled by aerodynamic torque passively. However, the accuracy is limited and with four wings, the body mounted solar panel has a chance

to be in the shadow of the wing.

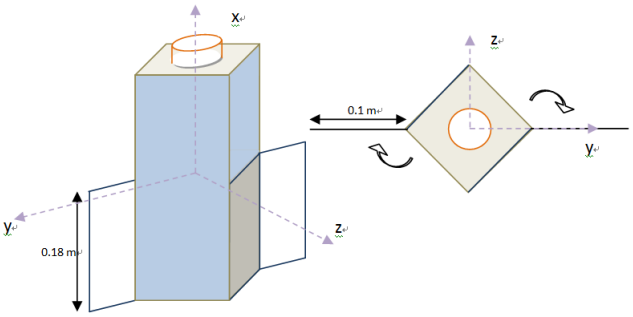

Figure 2.3.3: Configuration of the spacecraft above 200 [km]

With these in mind, the configuration of Phi is generated. It is the modified 3U deployable 3 configuration, 3U with 2 wings and 2 fins. Even though fins and wings have same dimensions, they are named differently based on their locations. According to Figure 2.3.3, Wings are on the edges on the y axis and fins are on the z axis. Looking from the top of the spacecraft, where the FIPEX is, before deploying, all deployables are folded counterclockwise. The whole life time of the spacecraft is divided into two phases, above 200 km and below 200 km. For the range above 200 km, missions, FIPEX, formation flying with propulsion and differential drag, that are most power consuming, will be demonstrated. Wings will deploy after detumbling mode while fins are deployed after 200 km as shown in Figure 2.3.4. In order to benefit the most from the Sun, the body surface exposed directly to the Sun will be covered with solar cells as shown in blue in the Figure 2.3.3. Both wings and one fin that on the upper side are solar panels. When the spacecraft decays to 200 km, fins deploy and passive aerodynamic torque control starts.

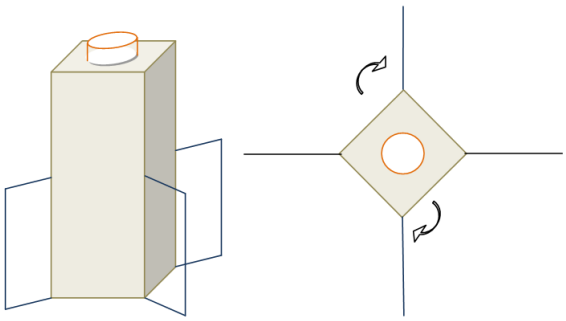

Figure 2.3.4: Configuration of the spacecraft below 200 [km]

2.4 Environment

2.4.1 Coordinate Frames

Attitude control deals with the orientation of the spacecraft axes with respect to an inertial reference frame. An instantaneous spacecraft attitude is commonly described by a pitch angle, a roll angle, and a yaw angle. They are defined for the orbital frame, F_0, where the spacecraft attitude is measured as an angular deviation of the spacecraft body axes from the axes of that frame. Besides orbital frame, one of the most frequently used inertial reference frame is Earth-centered inertial frame, F_I, shown in Figure 2.4.1.

The third reference frame is only used for illustration purposes. The origin lies in the center of the Sun, while the x-axis points toward the Earth which lies in the xOy plane. The z-axis is pointing to the ecliptic North pole. This frame is useful for calculations of the eclipse time because it can be used to easily express the relation of the orbit plane with respect to the sun, as shown in Figure 2.4.2.

The last reference frame is the body reference frame, which is a convenient frame for the analysis of spacecraft dynamics and control, because the control of angular velocity of the spacecraft is defined in the body frame F_b. The difference between body frame and orbital frame is the direction of the z- and the y-axis. As the spacecraft moves along the velocity vector, the x-axis should be tangent to the orbit plane, just like that of the orbit frame. However, as the spacecraft adjusts its orientation towards the Sun, the z-axis is not always aligned with the radial vector describing the position of the satellite in a circular orbit. The orbital frame and the body frame are described by $[\vec{o_x}, \vec{o_y}, \vec{o_z}]$ and $[\vec{b_x}, \vec{b_y}, \vec{b_z}]$, respectively.

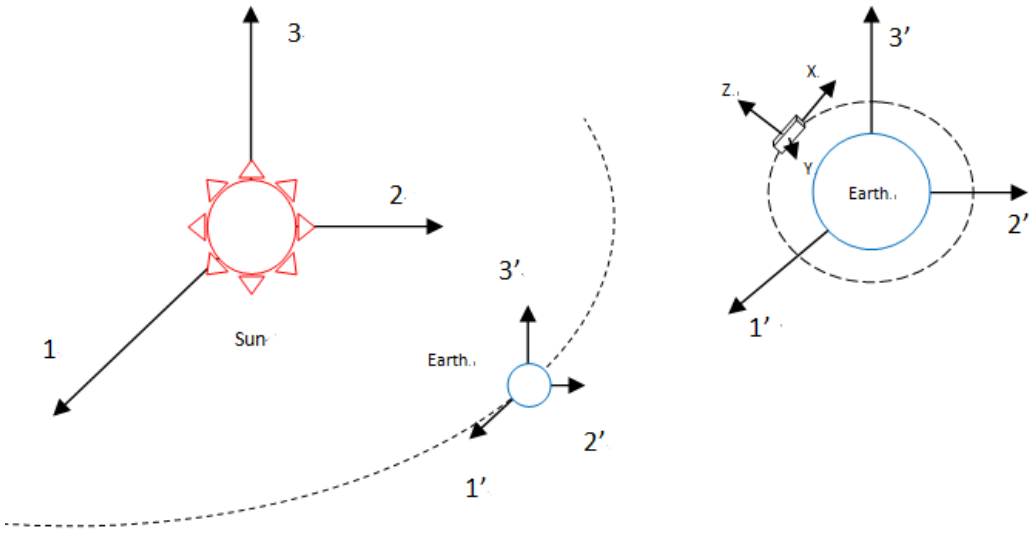

Figure 2.4.1: Reference frames, MS Word 2013

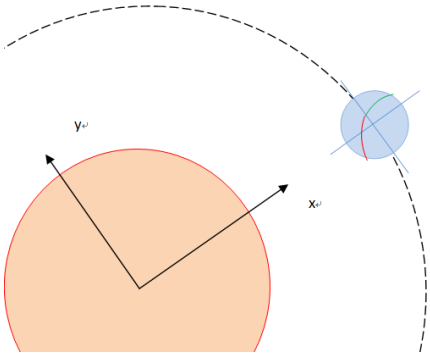

Figure 2.4.2: Sun-Earth reference frame

2.4.2 Aerodynamics

For the determination of the drag coefficient, the stability margin and aerodynamic torques, a program was written that uses an atmospheric model, the exact CubeSat geometry and Sentman's equations, see Equation2.4.2 [21]. All coefficients can be calculated for all altitudes as well as orientations.

The geometry is entered by entering the vertices of every panel. The four body panels are fixed and have the standard CubeSat dimensions (0.1 and 0.3 m), while the flap area can be varied by changing the lengths of the fins.

The entire geometry is rotated by multiplying the coordinate vectors of the vertices with the three Euler matrices for pitch, yaw and roll. The coordinate system used is the body frame. Density and temperature data are taken from the NRLMSISE-00 model for 2015, which gives the number densities of He, O, N_2, O_2, Ar, H and N. Subsequently, the thermal velocity of each of these particle species is calculated.

$$c_{mp,j} = \sqrt{2\frac{k}{m_j}T} \tag{2.4.1}$$

The drag coefficient for each panel can be determined from Sentman's Equations [21] which are based on the assumption of free molecular flow. This applies in those regions of the atmosphere where the density is so low that gas-gas interactions do not have to be accounted for. The drag force is calculated based on momentum and energy exchange between the incoming particles and the spacecraft. The assumption of free molecular flow holds until approximately 120 km, below which the flow regime is characterised as transitional flow.Here, interactions between gas particles become significant, but do not yet dominate particle-spacecraft interaction. This will occur below 90 km when the continuum flow begins. In this report, the drag coefficients have been calculated for altitudes down to 90 km using free molecular flow theory. Although this does not accurately represent the forces that will occur below 120 km, it is considered a good first order estimate since a simulation including transitional flow would be beyond the scope of this project. However, this is only a minor problem because the time the satellite spends at the lowest altitudes is very short, therefore the impact of using the calculated coefficients on the accuracy of the lifetime estimate is very low. Furthermore, QB50 only requires that the satellite has to provide attitude control until 200 km (PHI-QB50-SYS-1.2.2), so below this altitude the magnitude of the aerodynamic torques are of less importance.

It should be noted that a flat plate parallel to the flow also creates drag. This is due to the random thermal motion of the molecules surrounding the plate, which collide with it and exchange momentum. The magnitude of this effect will be discussed later.

The total drag coefficient is obtained by adding the contribution of each panel. In the following equations, the index j represents the different species of atoms, whereas i represents the different panels.

$$c_{d_{i,j}} = \left[\frac{P_{i,j}}{\sqrt{\pi}} + \gamma_j Q_j Z_{i,j} + \frac{\gamma_i}{2}\frac{v_{re}}{v_{inc}}\left(\gamma_i\sqrt{\pi}Z_{i,j} + P_{i,j}\right)\right]\frac{A_i}{A_{ref}} \tag{2.4.2}$$

$$S_j = \frac{v_{rel}}{c_{mp,j}} \tag{2.4.3}$$

$$G_j = \frac{1}{2S_j^2} \tag{2.4.4}$$

$$P_{i,j} = \frac{1}{S_j}e^{-{\gamma_i}^2 S_j} \tag{2.4.5}$$

$$Q_j = 1 + G_j \tag{2.4.6}$$

$$Z_{i,j} = 1 + \text{erf}\left(\gamma_i S_j\right) \tag{2.4.7}$$

$$\text{erf}\left(x\right) = \frac{2}{\sqrt{\pi}}\int_0^x e^{-y^2 dy} \tag{2.4.8}$$

$$\gamma_i = cos\left(\theta_i\right) \tag{2.4.9}$$

$$\frac{v_{rel}}{v_{inc}} = \sqrt{\frac{1}{2}\left[1 + \alpha\left(\frac{4RT_w}{v_{inc}^2} - 1\right)\right]} \tag{2.4.10}$$

Where v_{rel} is the velocity of the spacecraft with respect to the atmosphere, which is taken to be equivalent to the speed of the Earth, T_w is the wall temperature which has been estimated to be 300 K from [21], R is the universal gas constant, A_{ref} is a reference area that has been chosen to be 0.01 m^2, γ is the angle of the velocity vector with the inward normal vector, α and σ represent the energy accommodation coefficient and Maxwell coefficient which have been estimated with [21] to be 1 and 0.9, respectively. The energy accommodation coefficient represents the tendency of the impacting particles to acquire the wall temperature of the satellite, whereas the Maxwell coefficient shows the probability of the reflection of the particles to be diffuse or specular.

An extended version of the code has been created that includes shadowing of the wings and fins from the body. The algorithm works in the following manner:

1. Determine the surfaces that are exposed to the flow by taking the dot product of the surface normal vectors with the velocity vector and checking if it is greater than zero.

2. Determine the edges that make up the boundary of the frontal projected area by evaluating their distance to the panel centroid.

3. For each of the edges, create a plane that contains the edge as well as the velocity vector. Those planes will be called projection planes.

4. For each panel that does not project on other panels but is still exposed to the flow, create a plane that contains the panel. Those planes will be called intersection planes.

5. Determine the lines of intersection from each projection plane and each intesection plane.

6. Determine whether these lines lie within the panel. If this is the case, part of the panel lies in shadow.

7. Determine the intersection of the line of intersection with the edge of the polygon.

8. Create new vertices at these locations.

9. Split the polygon into two new polygons. One of those will be the shadowed part.

10. Determine which polygon is the shadowed part by taking the norm of each of the two polygons with the position vector from the geometric center of the entire satellite. The one with the smaller norm will be the part of the panel that is shadowed.

11. Delete the polygon that represents the shadowed part of the panel.

After that the drag coefficient is calculated as has been explained previously. When comparing the differences in torques obtained with and without the effect of shadowing, it has been found that for especially for large pitch and yaw angles (when a significant fraction of the deployables lie in shadow), the restoring torques are much higher. For a pitch and yaw angle of 10° as shown in Figure 2.4.4, the torques increase by 47 %. This is because due to high rotations away from the velocity vector and the shadowing of the backward moving wing, the forward wings also have a contribution to the restoring moment around the Z_B axis. The following analysis has been made for torques obtained without shadowing due to the tight schedule of the project. However, it has been shown that this is a conservative approach and that taking into account the effects of shadowing will make the design much more stable.

Center of pressure To determine if the spacecraft is stable, the center of pressure is calculated, the definition of which is:

$$cp = \frac{\int x \cdot p\,(x)\,dA}{\int p\,(x)\,dA} \tag{2.4.11}$$

where x is taken to be the distance from the geometric center, positive in the X_B direction. The pressure p is constant for each panel and can be obtained by dividing the drag force on each panel by its area. Contrary to the usual definition of the stability margin as the distance to the center of pressure to the center of gravity in the X_B direction, the distance in Z_B is of relevance here since the drag force acts parallel to the flow. A center of pressure above the center of gravity signifies an unstable spacecraft. Figure 2.4.10 shows that the presented configuration is stable.

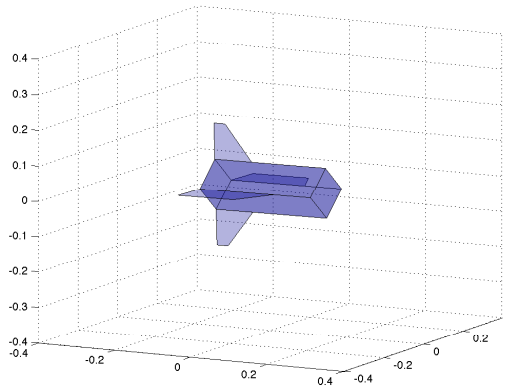

Figure 2.4.3: Visualisation of the aerodynamic model of the CubeSat

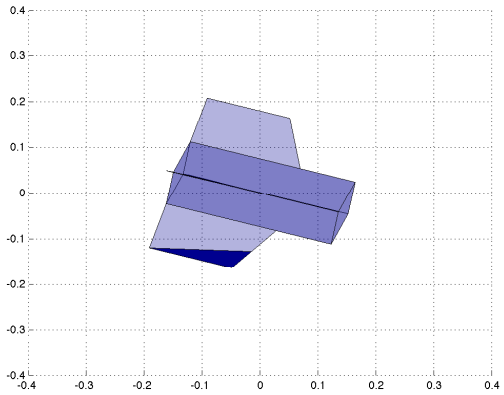

Figure 2.4.4: Visualisation of shadowing of one wing

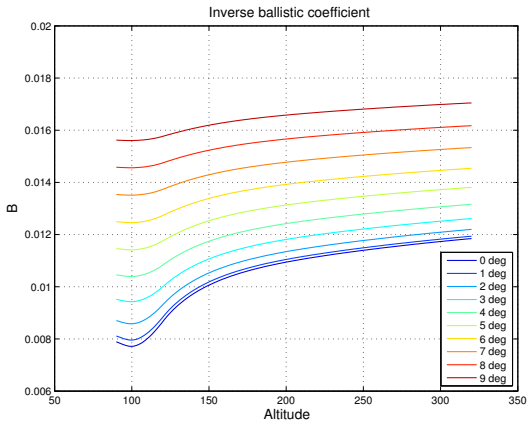

Figure 2.4.5: Ballistic coefficients for large pitch and yaw angles

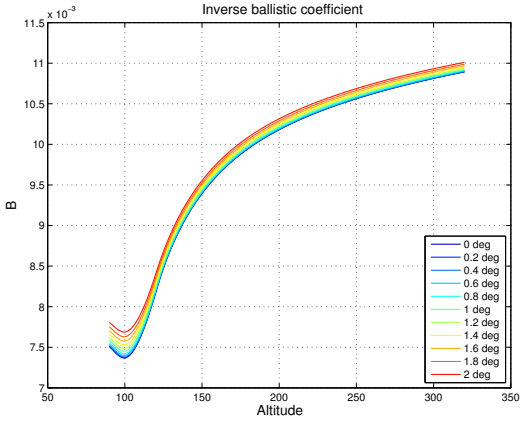

Figure 2.4.6: Ballistic coefficients for small pitch and yaw angles

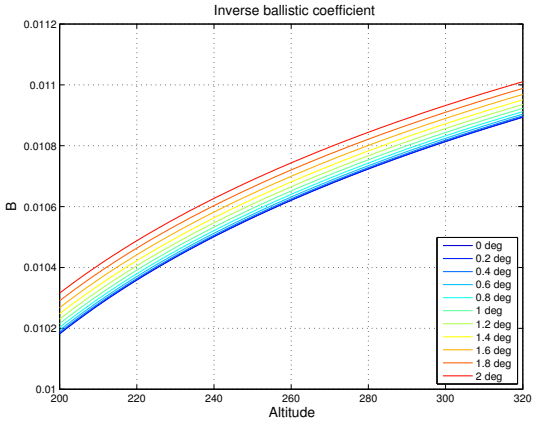

Figure 2.4.7: Inverse ballistic coefficients for small pitch and yaw angles

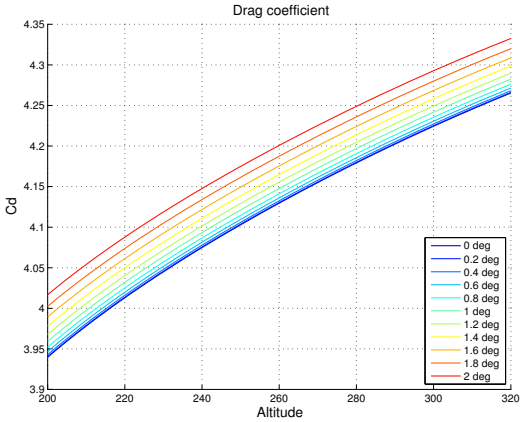

Figure 2.4.8: Drag coefficients for small pitch and yaw angles

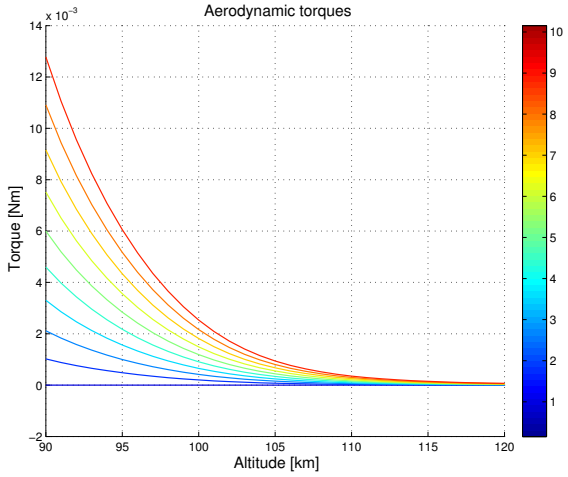

Figure 2.4.9: Aerodynamic Torques

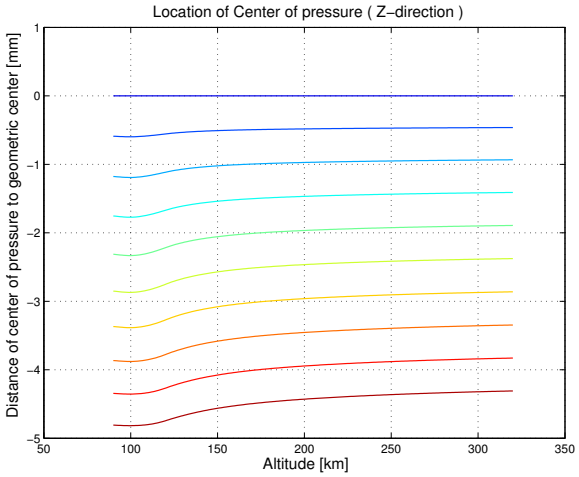

Figure 2.4.10: Aerodynamic torques for incidence angles from 0 to 10°

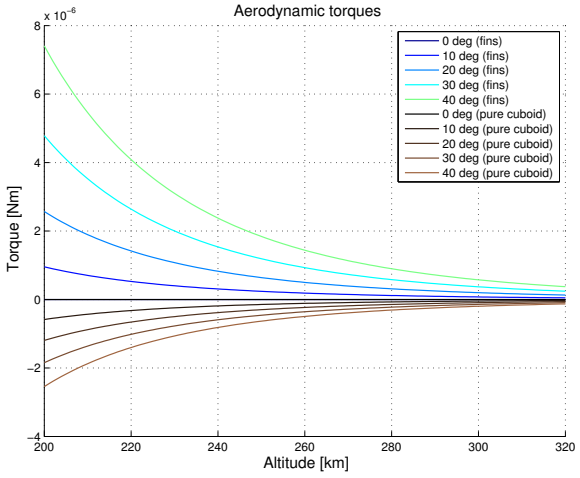

Figure 2.4.11: Aerodynamic torques for CubeSat with fins as opposed to standard configuration

2.5 Lifetime

The decay rates have been determined with a MATLAB script that calculates the energy loss due to drag, which is the drag force times the distance travelled during that timestep:

$$E_{loss} = \frac{1}{2}\rho \cdot V^2 \cdot A_{ref} \cdot C_D \cdot \theta \cdot a \tag{2.5.1}$$

where ρ is the density, V is the orbital speed, A_{ref} is an arbitrary reference area, C_D is the drag coefficient, θ is the argument of latitude and a the semi-major axis. From the difference in specific orbital energy before and after one time-step, the new semi-major axis can be calculated using:

$$\epsilon = -\frac{2}{\mu \cdot a} \tag{2.5.2}$$

where μ is the standard gravitational parameter of the Earth. The density is taken as an average for a specific altitude and taken from the NRLMSISE-00 model. The script takes into account an indirect effect by which J_2 influences the semi-major axis of the satellite. J_2 superimposes a sinusoidal fluctuation in semi-major axis onto the mean value, which using STK is found to have a half-amplitude of 10 km. The minimum occurs at the equator while the maximum altitude is reached over the poles. The atmospheric model is detailed enough to show density variations over radial distances of even 1 m. This induces different drag forces, and therefore a different energy loss history on each of the satellites. Depending on the initial location of the formation, one satellite will at any point in time experience a higher energy loss than the other. This effect will be investigated in **??**.

The F10.7 and the planetary geomagnetic index are taken from the recommended set of input parameters for QB50 [65]. Average expected values for 2015 are $F_{10.7} = 140$ and $A_p = 40$.

Chapter 3
Systems Engineering

System engineering focuses on managing complex engineering projects over their life cycle. As the project progresses, some deliverables in the Baseline and Mid-term reports need to be updated. In this chapter, system engineering items associated with the DelFFi project are presented and discussed.

3.1 Operations and Logistics

The operational flow diagram (see Figure 3.1.1) describes the operations and logistic concept associated with the ground station. From the ground, commands are given to the satellites to initialise the subsystems. Detumbling can then be performed while the satellite is tracked by the ground station. Then, the subsystems are checked. Subsequently, formation flying can be performed by determining the relative positions of the satellites and sending commands for the propulsive manoeuver. The position data received at the ground station can also be monitored for the semi-major axis decay. Formation flying can be performed in parallel with payload operation. In addition, the telemetry data is received at the ground station and checked for anomalies. This ensures that the payloads and subsystems are functioning as expected. Anomalies can include partial deployment failure of solar panels, failure of the ADCS, failure of the propulsion system, unexpected drift rates of orbital elements, etc. The first two operations (orbit injection and deployment of antennas and solar panels) are shown for completeness, although they are automatic. The operational flow diagram related to the last of the formation flying modes which will be elaborated upon in 7.1.1, meaning full autonomy and inter-satellite link.

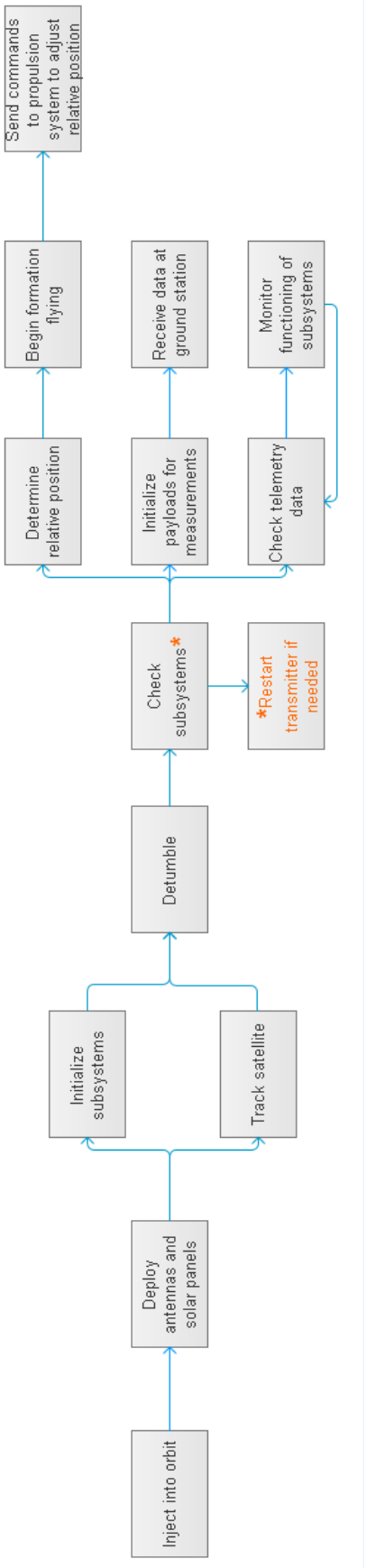

Figure 3.1.1: Operational flow diagram

3.2 Functional Flow Diagram

A functional flow diagram is constructed to clarify the sequence of events during the mission. The functional flow diagram is displayed in Figure 3.2.1. Each event will be discussed briefly.

3.2.1 Launch

The launch is planned to take place in the first half of 2015. Multiple nano-satellites will be launched in one launch vehicle and will be placed in 2U or 3U StackPacks.

3.2.2 Orbit Injection

After the launch, the satellite needs to be injected into orbit. The satellites in the launch vehicle will be injected one after the other, since this would increase the risk of satellite collisions. Therefore the satellite will have to wait a certain amount of time in the StackPack before it is injected.

3.2.3 Initialise Systems

Initialise Camera

The first system that has to be initialised is the deployment camera. During this phase of the mission the camera will use the energy stored in the battery before launch. Initialising the camera must be done before the solar panels and antenna's are deployed in order to record images of the deployment process. However, the rest of the sequence is not dependent on the success of this event. If the camera fails to respond within a fixed amount of time, the satellite will skip this event and move to the next step. This can be implemented by a safeguard.

Deploy Solar Panels

After the camera initialisation, the solar panels will be deployed, which will take a few seconds. The deployable solar panels will increase the available power and also the stabilise the satellite.

Initialise EPS

When the solar panels are deployed, the EPS can start charging the batteries and deliver power to the rest of the subsystems. The EPS regulator will start to operate.

Boot OBC

If the EPS is functioning properly, the OBC will boot. This subsystem is capable of controlling other subsystems and is responsible for collecting health log data.

Initialise ADCS, COMMS, GPS

When the EPS and the OBC are working, the satellite will initialise the remaining subsystems, the payloads excluded. The COMMS will turn the receiver on so that ground commands can be made. The GPS system will start to locate the satellite's position. Also, the ADCS will be started and the satellite will begin to detumble.

3.2.4 Perform Formation Flight

The formation flight will be performed after the subsystem initialisation. This event will run simultaneously with the payload initialisation and the measurement. A more elaborate description can be found in Chapter 7.

3.2.5 Initialise payloads

After that the subsystems have been initialised, the payloads will be started. Some calibration must be performed to verify that the measurements are valid. Then the payloads can start taking measurements.

3.2.6 Transmit data

A few times a day, the satellite will be within reach of the ground station. During that period, the satellite will turn on the transmitter and send payload and health log data to the ground station. When the transmitter has completed transmission, it will wait for a confirmation from the ground station, which will be issued if the transmission is completed without corruptions. Only after that, the transmitter can be shut down and the memory can be erased so that it can be re-used.

3.2.7 Satellite Disposal

The satellite will repeat the cycle of measuring and transmitting until end of life. When the altitude is approximately 90 km, the satellite will reach the end of its useful life due to either antenna bending of high Dopper shifts. The last batch of data will be sent to the ground station. After that, the satellite altitude will decay further until the atmospheric drag heats the satellite to the point where it burns up.

Figure 3.2.1: Functional flow block diagram

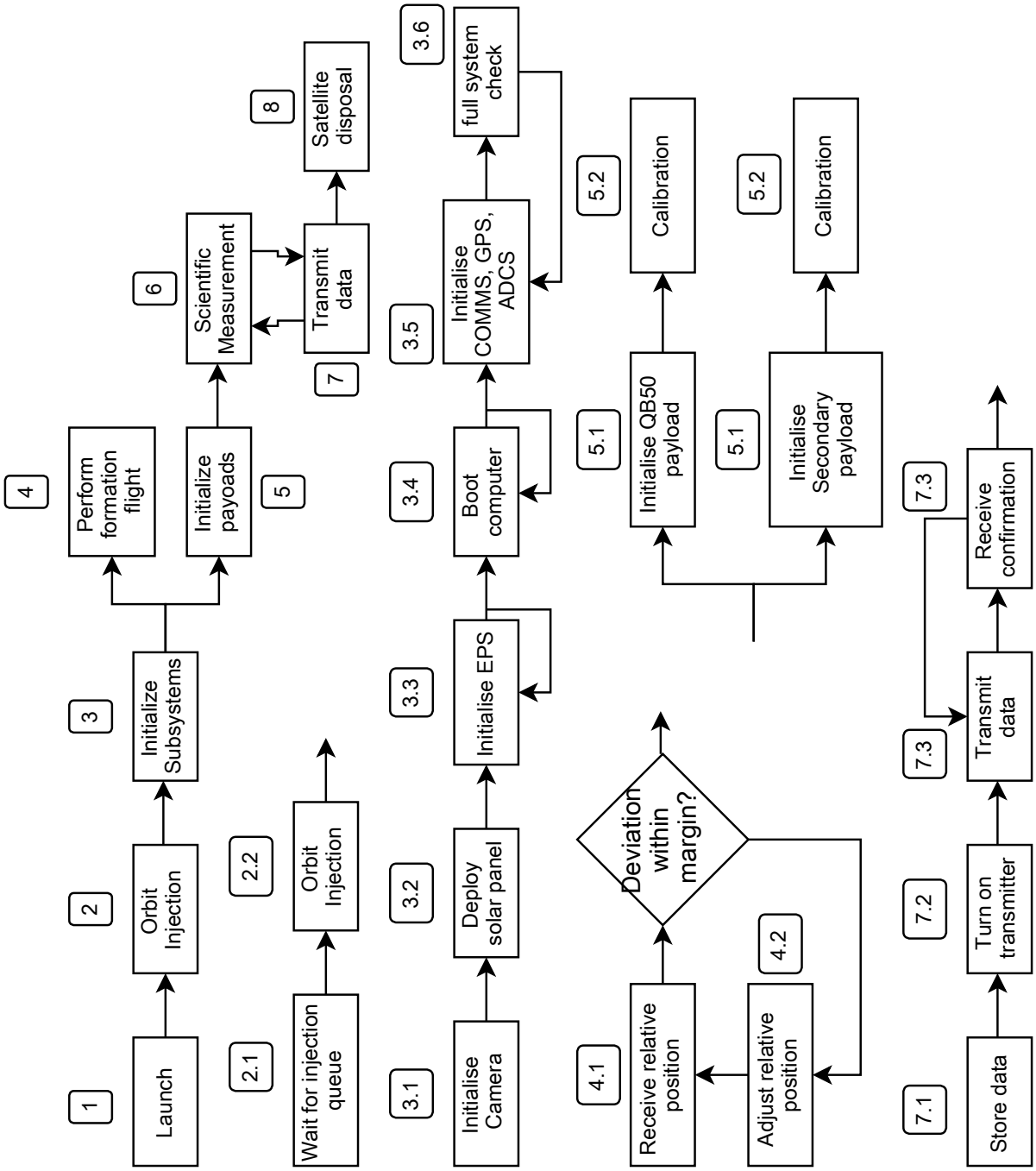

3.3 Functional Breakdown Structure

The functional breakdown structure is a tree in which all functions that the spacecraft has to perform are listed. It is an AND tree, which means that each item is the sum of the lower branches that lead to it. The functional breakdown structure will help the team to ensure every aspect is considered of the design. It is also an aid to seeing the big picture of how a team member's component fits into the complete design.

The breakdown structure starts out with 'Perform DelFFi mission'. As one can see in Figure 3.3.1, a space mission consists of a space segment and a ground segment. However, for the scope of the design synthesis exercise (DSE) the ground segment will only be addressed without going into detail. The space segment consists of the two nano-satellites Delta and Phi. Delta is only shown in the functional breakdown structure for completeness (for convenience, the block is coloured darker than the other blocks), as the team will only be designing Phi.

When designing a nano-satellite, various segments need to be addressed: the preparation and commissioning of the satellite, the use of the satellite and the disposal at the end-of-life of the satellite.

The tree has been split up; the elaboration on 'Operate subsystems' and 'Support subsystems' can be found on the successive pages (Figures 3.3.2 and 3.3.3.

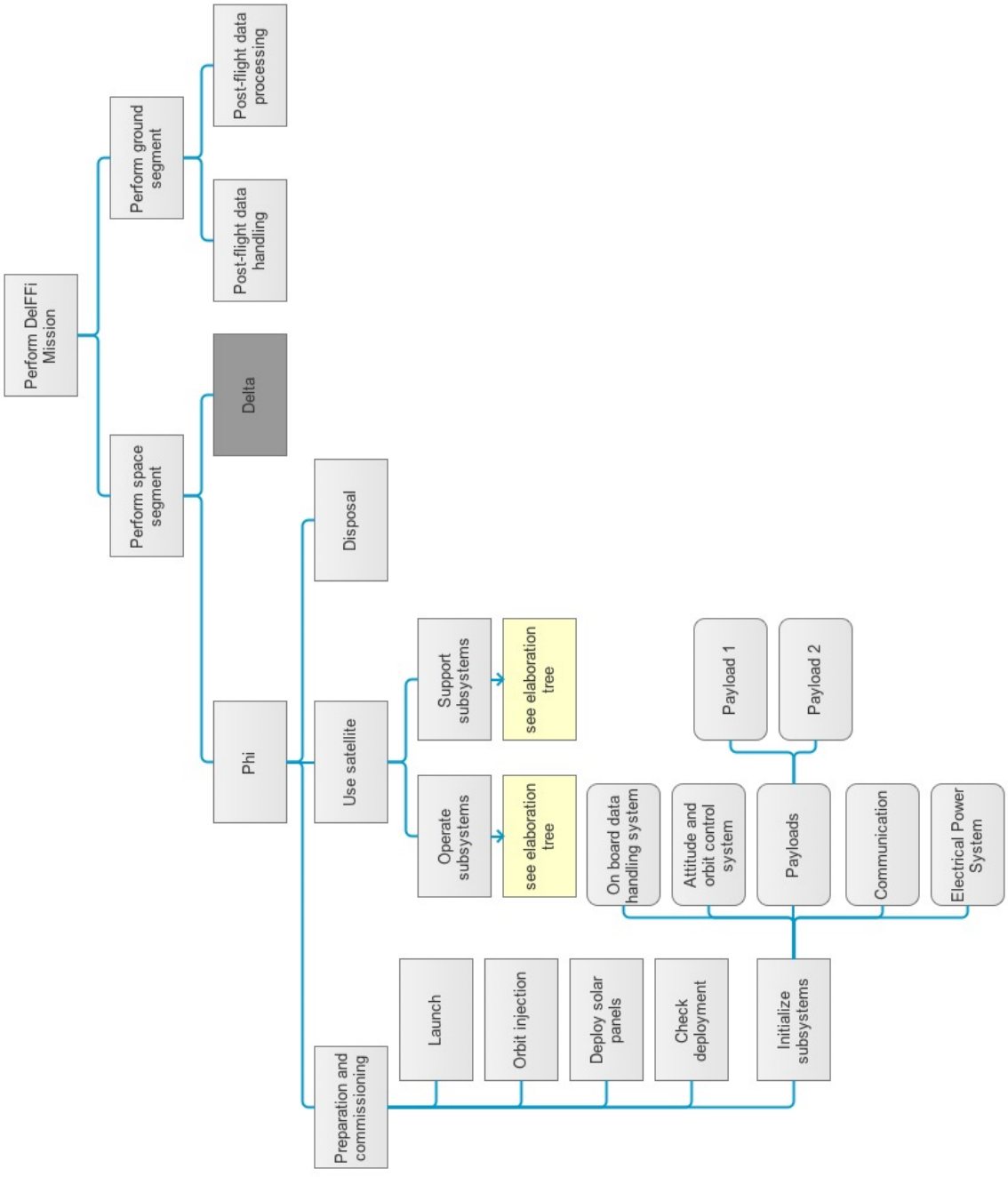

Figure 3.3.1: Functional breakdown structure, main tree

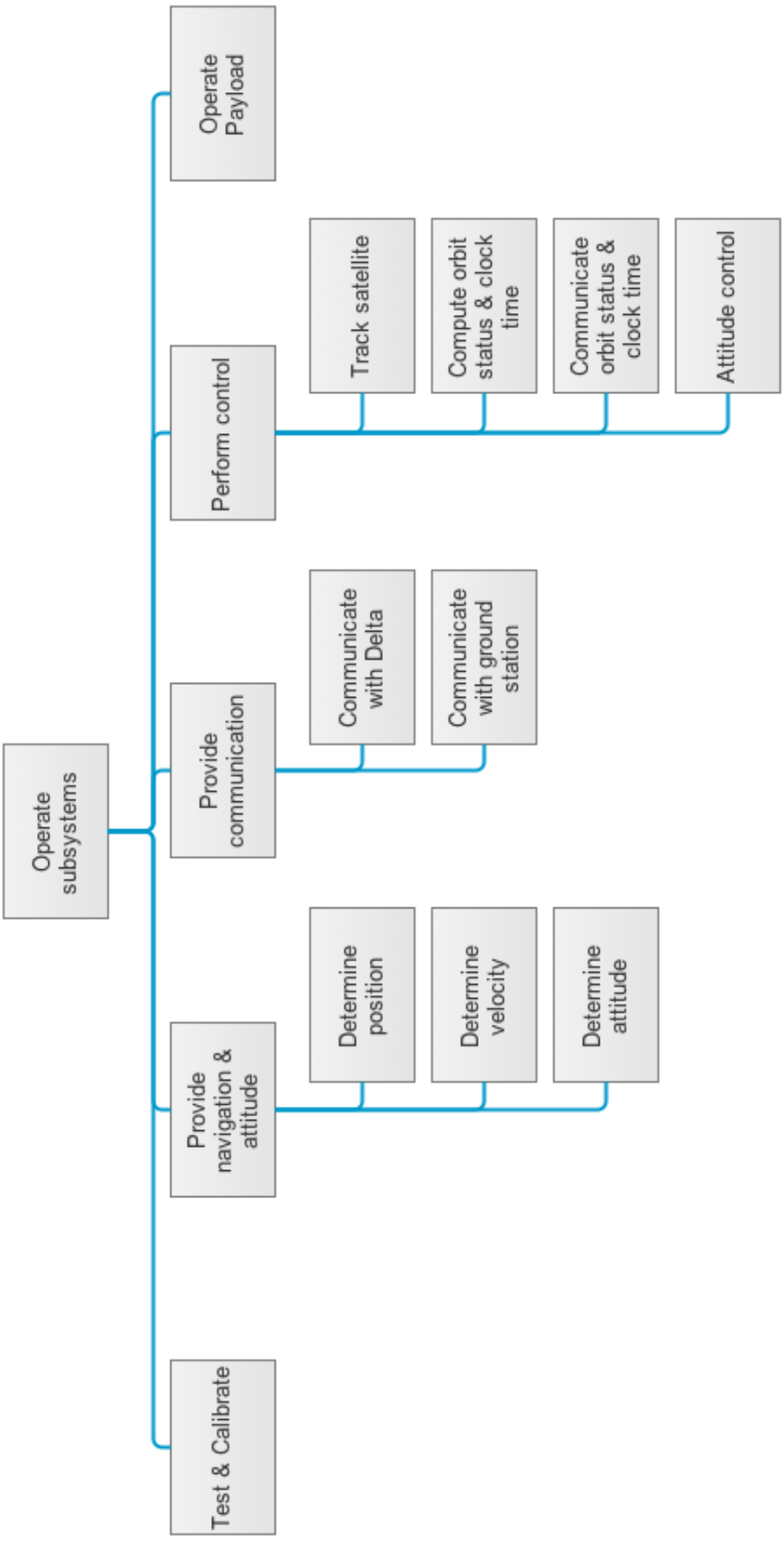

Figure 3.3.2: Functional breakdown structure, elaboration tree (operate subsystems)

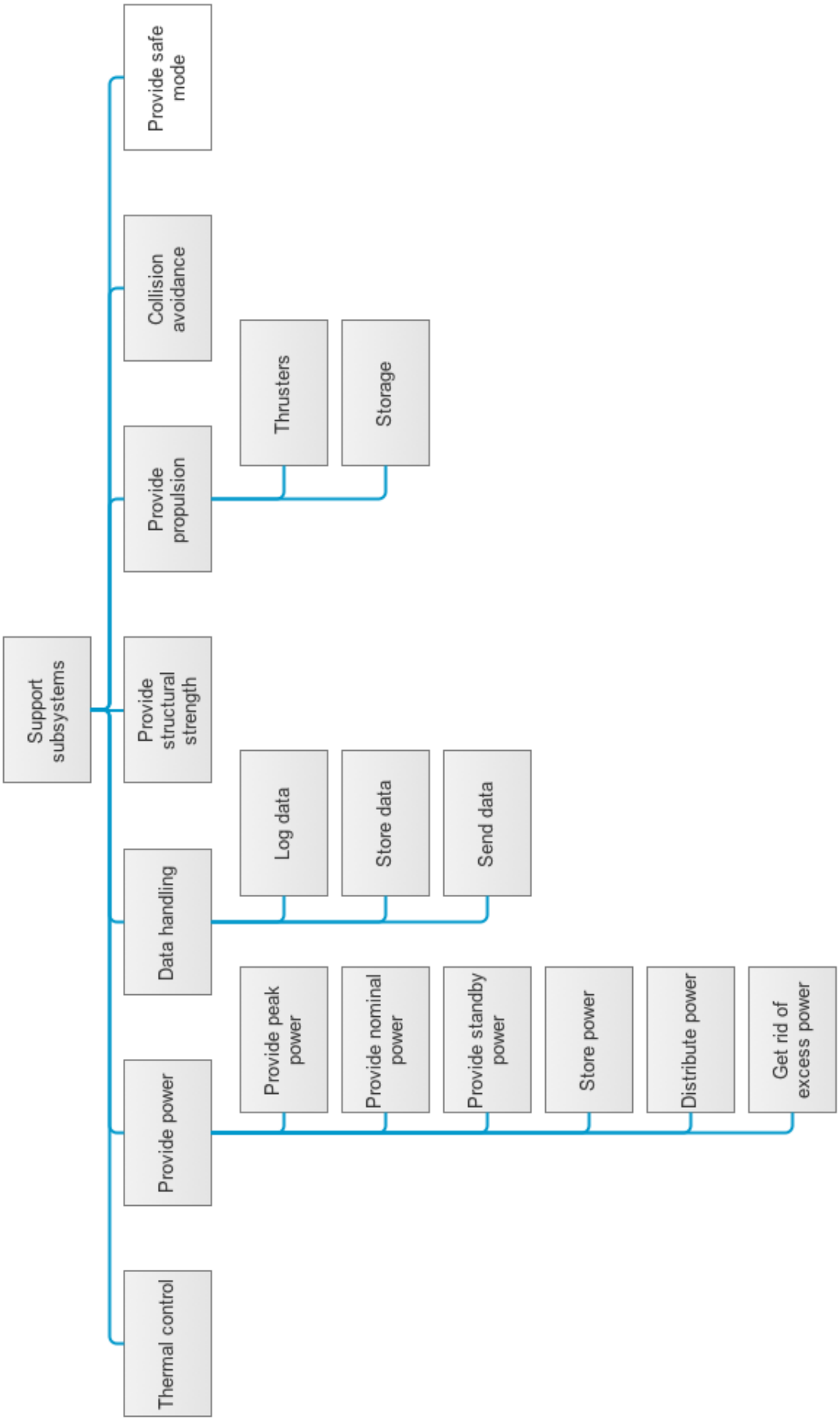

Figure 3.3.3: Functional breakdown structure elaboration tree (support subsystems)

3.4 Market Analysis

The progress in miniaturisation of electronic components enables the construction of smaller satellites, which can be built at lower cost and possess more flexibility, but generally have limited performance. However, as more units can fitted into a certain volume, CubeSats can take more tasks and become versatile. Back in the year 2000, CubeSats were still regarded as 'toys' because of their small size and meagre funding. However, their low expenses attract the attention of academic institutions and small companies for both scientific and educational purposes. From Figure 3.4.1, the number of pico-satellites launched per year is steadily increasing. Therefore, it can expected that more small satellites will be launched in the future.

While smallsat advocates have implicitly assumed that there is a substantial market for smallsats throughout the industry, it has been difficult to quantify the size of the market. A study conducted by Futron showed six markets that are most likely to be near-term users of a low-cost small satellite system [25]:

- Military science and technology
- Intelligence, surveillance, and reconnaissance
- Remote site communications
- Polling of unattended sensors
- High-resolution Earth observation
- Landsat-class data for environmental monitoring

The DelFFi mission is an autonomous formation flying demonstration between two 3U cubesats, the main objective of which is the education of students, but which also serves as a prototype for a possible future constellation. The reasons for using CubeSats for formation flying are their low complexity and low cost. Therefore, in this chapter, a market analysis specific for DelFFi is included, containing market segmentation and dimensions followed by a SWOT analysis. This section will be concluded with an estimated target cost made in comparison with similar CubeSats and a prediction of the upcoming development of this field.

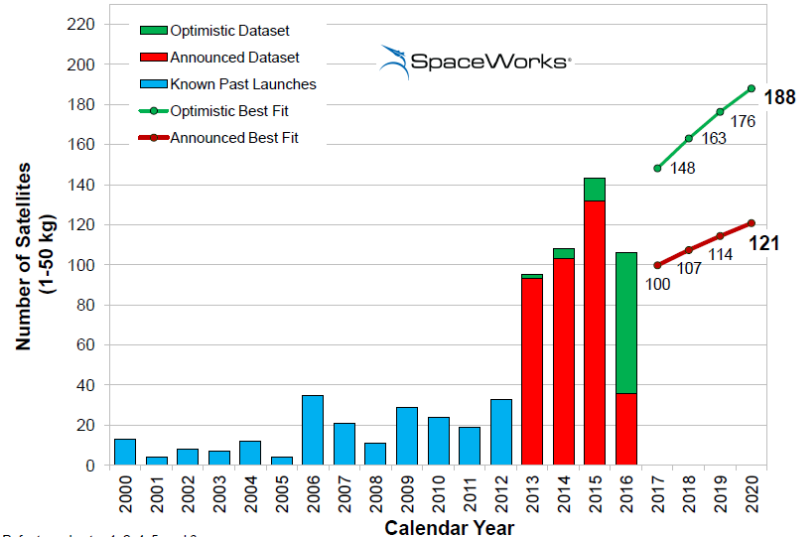

Figure 3.4.1: Number of launched pico-satellites per year

3.4.1 Market segmentation and dimension

Pico-satellites in low-earth orbit are notmally associated with one of four mission types: communications, science, remote sensing, and weather. The results of the market segmentation analysis are shown in Table 3.4.1 [51].

Table 3.4.1: Market segmentation

Segment Category	Market Size	Small Satellite Market Penetration
Communications	Large	some
Remote Sensing	Large	some
Science	Large	some
Weather	Small	some

LEO Communications has been one of the most successful markets for small spacecraft. Improvements in small satellite technology will permit more powerful small spacecraft to perform increasingly complex missions. However,

due to the limited transmitter output power of pico-satellites, larger satellites will continue to dominate this market segment.
Advances in instrument technology have enabled the construction of small spacecraft for Earth observation with a ground resolution of less than 10 m. Continued progress is largely dependent upon further miniaturisation of the remote sensing payloads. The most successful segment of the small satellite market are science missions. CubeSats are normally the cheapest method for conducting science missions in space. The lower cost of space access enabled by small spacecraft has dramatically increased the number and variety of space missions performed by the scientific community.

The QB50 sensor payload aims at gathering extensive environmental data in the lower thermosphere. Past missions have gathered data in this region with only one spacecraft and were therefore not able to capture short term processes in the atmosphere. Contrary to other atmospheric explorers, QB50 will provide multi-point measurement for up to 3 months. QB50 is unique in the market to study *in-situ* temporal and spatial variations of a number of key constituents and parameters in the lower thermosphere (90-320 km) with a network of about 50 CubeSats, separated by a few hundred kilometers and carrying identical sensors [54].

The secondary mission objective of the Phi satellite is the monitoring of the deployment process, the recording of the acoustic spectrum of the spacecraft and to perform formation flying using differential drag. The first two objectives are not new to the space industry. Cameras are a common payload in a spacecraft to observe the Earth or the spacecraft itself. The purpose of the Phi satellite is to monitor the deployment of solar panels and antennas. Even though a large amount of information on this can be found for big satellites, for CubeSats the data is rare due to the malfunctioning of COTS cameras in the space environment. The acoustic analysis has never been performed on a CubeSat. Therefore, from the scientific perspective, these two objectives are of high scientific interest. If they become a success, they can provide valuable information for future small satellite missions.

Formation flying with differential drag has also been proposed before, but has never been carried out in a real mission. The modelling of the behaviour of the spacecraft during differential drag manoeuvres is complex and highly dependent on data that is not easy to predict with high accuracy, like surface temperatures of the spacecraft. Therefore, not only the demonstration itself but also the data gathered from the demonstration will be of high scientific value. More detailed feasibility analysis is treated in Section 6.

3.4.2 SWOT Analysis

The SWOT analysis method is used to identify the current situation of the DelFFi program. It is a strategic planning tool used to evaluate the Strengths, Weaknesses, Opportunities, and Threats involved in pursuing the project as a business venture. It involves specifying the objective of the business venture or project and identifying the internal and external factors that are favourable and unfavourable to achieving that objective.

Strengths

- The project is designed by students from TU Delft, and is supported by TU Delft staff and experienced engineers from QB50, VKI, ISIS, OLFAR for provindin information and aiding in conceptual design.
- The chosen secondary mission objectives are of high scientific value.
- There are strong interests for cooperation in the space sector between different space companies and institutions.
- DelFFi provides a good platform for verification and validation of instruments and components.
- The manpower cost is lower than for CubeSats developed by profit organisations.
- The possibility of on-orbit reconfiguration within the formations offers multi-mission capability.
- Separating scientific payloads into two identical, simpler satellites can accomplish the same complex mission without the added design and operational overhead, while risking only one payload at a time.

Weaknesses

- The project is designed by students, who lack experience in the industry.
- Formation flying at low altitudes is not very common in space. This implies high technical risks for the project.

- Lack of information about deployment and definitive requirements from QB50. The designing process is going to be iterative due to possible modifications in the QB50 requirements and increases development budget.

- Previous missions have shown that images from COTS cameras often display poor quality. This could influence the scientific value of the pictures taken by the deployment cameras.

Opportunities

- There is increasing interest in demonstration of constellation maintenance in the future. DelFFi, a two-satellites model is a good start in demonstrating the feasibility of such missions.

- Similar projects can be designed for international cooperation, such as FAST (a Dutch-Chinese project). Therefore, many social benefits can be achieved after operation, the protection of the environment, etc.

- This project can also be used for commercial applications, such as selling data and pictures to other universities and organisations.

Threats

- Some potential competitors have the interest and capacities to develop CubeSats to demonstrate formation flying in the Dutch industry.

- The very short time-frame allocated to the design might necessitate a simpler design.

3.4.3 Cost Analysis

Target cost is critical when analysing the feasibility of the design. Even though CubeSats appear to be small and therefore cheap, the limit on the dimensions complicates many design issues, rather than simplifying them. Thus, the ratio of mass to volume can become extremely high compared to larger satellites.

In order to stay stay within budgets, most of the components are COTS products, reducing development and testing cost. Because the mission is mostly developed by students, labour cost for development is reduced. However, this university-developed project means the final budget is not available to the public. According to Pumpkin Inc., the costs for a 3U mission amount to approximately 1-2 million dollars, excluding launch.

3.5 Manufacturing, Integration and Assembly Plan

The Manufacturing, Integration and Assembly Plan is partitioned into four panels representing each stage of the production process. The activities in each column cannot commence until all the activities of the previous section have been completed. Actions is different columns can be done in parallel to one another, unless a specific order is indicated by the arrows.

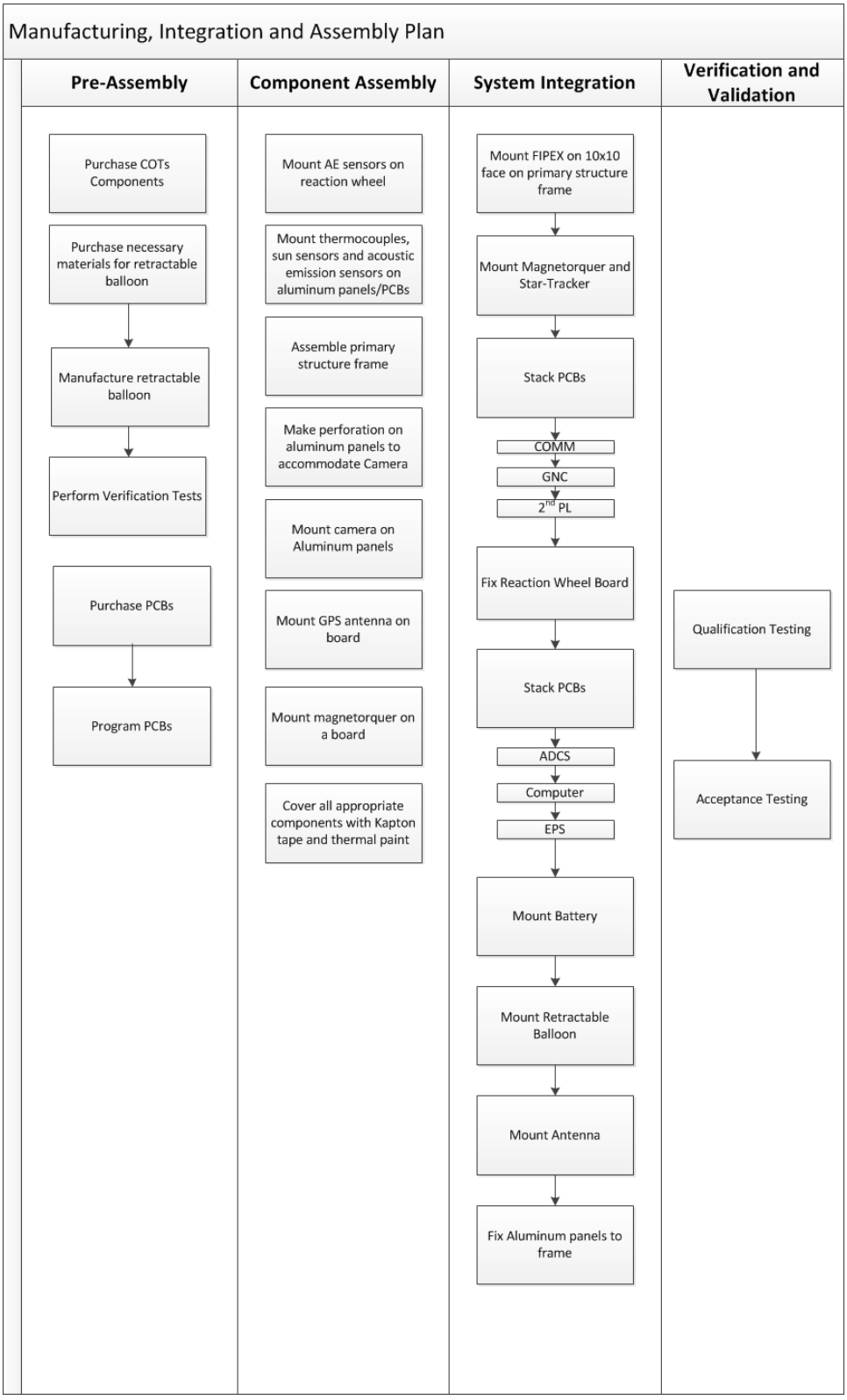

Figure 3.5.1: Manufacturing, integration and assembly plan

3.6 Project Design and Development Logic

This chapter treats the post-DSE phase of the project. The logical flow of the tasks for each subsystem is shown in a number of blocks.

Guidance, navigation and control (GNC) The figure below shows that before getting a satisfactory control strategy, many intermediate steps need to be implemented first. Of prime importance is the quantification of the accuracy of the thrust that is delivered by the cold gas propulsion system. This should be done for a variety of thrust levels. The result will be used to validate the control strategy and the nominal mission scenario, since heavy dependency on the provided impulse accuracy has been found. The result could be validated by running it on a

high-precision orbit propagator. Therefore, in the post-DSE phase, more investigations will be done about thrust accuracy and on-board algorithm. Together with a more precise propagator, the control strategy can be validated and modified.

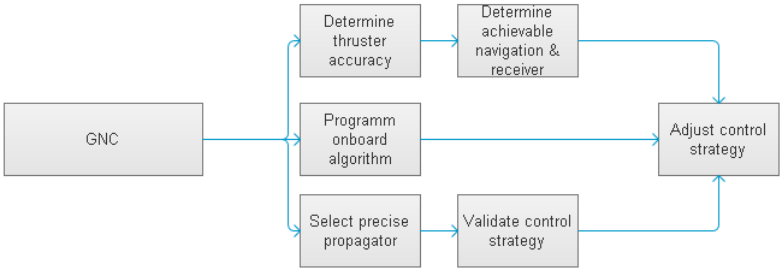

Figure 3.6.1: Project design and development logic of subsystem GNC.

Propulsion The propulsion system has many components that can be changed (in size), replaced or improved. For example, the cold gas generator (CGG) is improving continuously and becomes more efficient for the overall system. Also the size and material choice for example the CGG and the plenum is changeable. Hence, there is room for improvements in the system. The next logical step is to investigate these options on how to improve the existing propulsion system, $T^3\mu PS$.

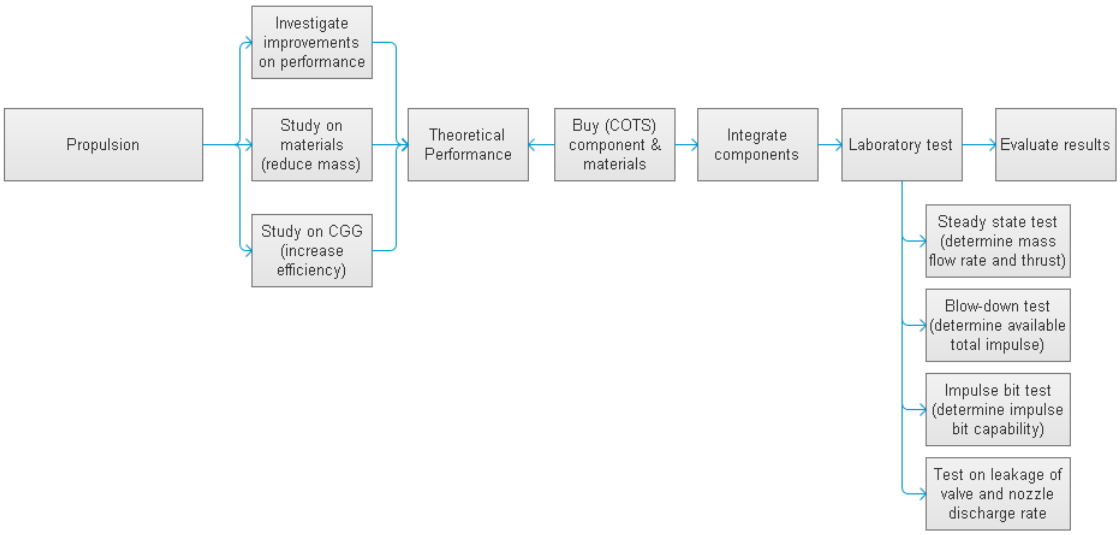

Figure 3.6.2: Project design and development logic of subsystem Propulsion.

Attitude Determination & Control System (ADCS) This subsystem is responsible for controlling the spacecraft to its desired attitude within a certain range of time and a certain accuracy. Therefore, the focus after in the post-DSE phase lies on the attitude determination and control modeling and testing. The only thing remaining for configuration design is the usage of a MEMS gyroscope. If a light, power inexpensive product can be found, without exceeding the mass and power constrain, MEMS gyroscope will be considered to take onboard for attitude rate estimation. Improvement in the stability algorithm leads to a better master controller of the attitude determination system. The block of activities from this subsystem is repesented in Figure 3.6.3.

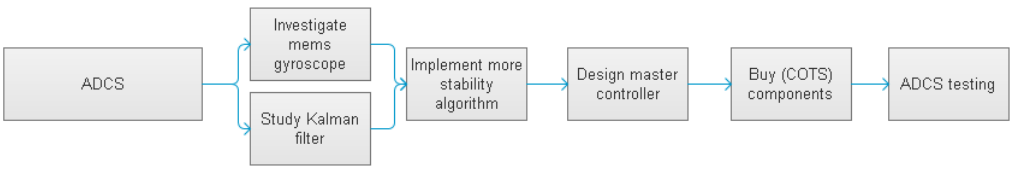

Figure 3.6.3: Project design and development logic of subsystem ADCS

Communications (COMMS) This subsystem has to provide communication with the ground station and the Delta satellite. So far, the design is frozen and the next step is to purchase the COTS components. In addition, tests are conducted, such as the radio for intersatellite link, frequency, and on power consumption. The block activities are presented in Figure 3.6.4:

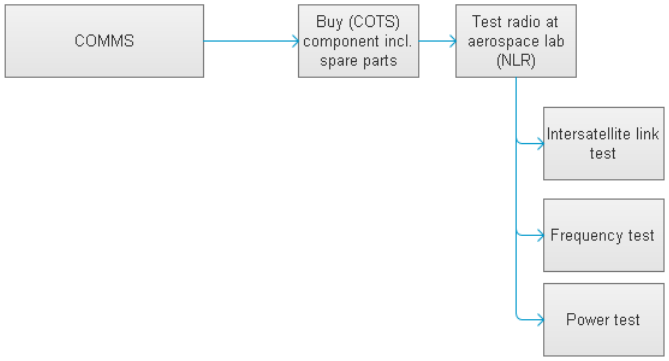

Figure 3.6.4: Project design and development logic of subsystem COMMS

On-board Computer (OBC & DH) This subsystem handles all the data and communicate within the spacecraft. The next step in the post-DSE phase is to develop a custom MCU for the secondary payload. The hardware of this component will be tested for performance, the software of this component should be tested for bugs, see Figure 3.6.5. After the MCU has been developed, the verification and validation procedure will performed on the complete data handling system.

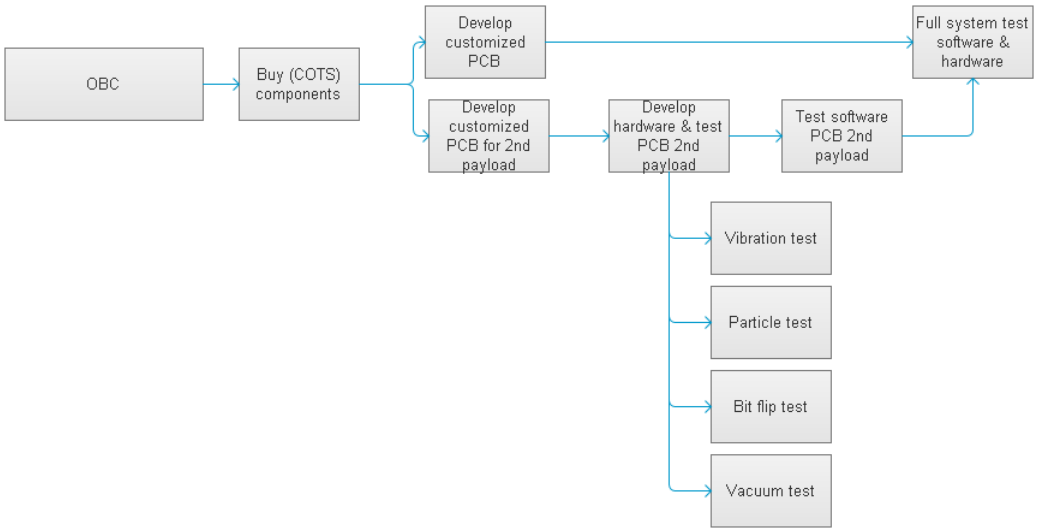

Figure 3.6.5: Project design and development logic of subsystem OBC & DH

Electrical Power System (EPS) The EPS provides power to all power consuming systems to guarantee the spacecraft operating normally during life time. After DSE, EPS launched into post-design stage. Products are purchased and tested according to user manual of QB50 to validate the design. The activity for EPS in post-DSE phase can be found in Figure 3.6.6.

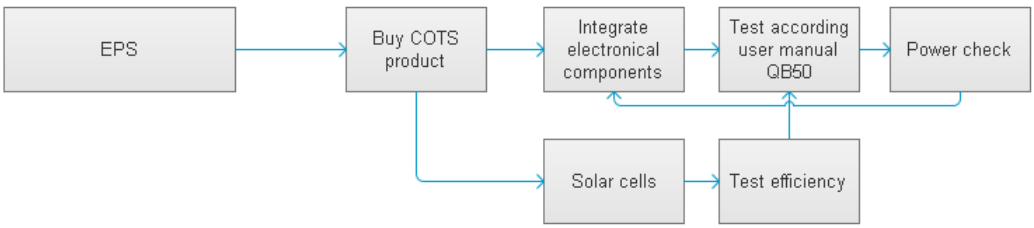

Figure 3.6.6: Project design and development logic of subsystem EPS

Thermal System Thermal System guarantee all components works within the operation temperature range. Some components like cameras for secondary objective, will be exposed to the surrounding environment. Therefore, thermal

test on the whole system is necessary, shown in Figure 3.6.7:

Figure 3.6.7: Project design and development logic of subsystem Thermal

Structures In the post-DSE phase the structure of the satellite is going to be tested for vibrations and any failure inside the satellite, see Figure 3.6.8. If the results turns out to be undesired also another investigation is done on different chassis of the satellite.

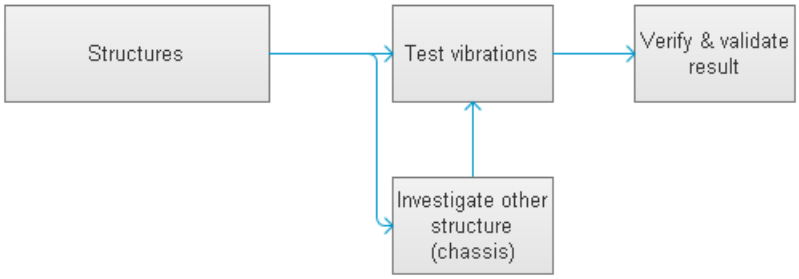

Figure 3.6.8: Project design and development logic of subsystem Structures

Secondary Payload The secondary payloads, camera and acoustic sensor will be exposed to the surrounding environment. After the DSE phase the first step to undertake is the testing. Both payloads are sensitive and affected by vibrations. See the block diagram in Figure 3.6.9.

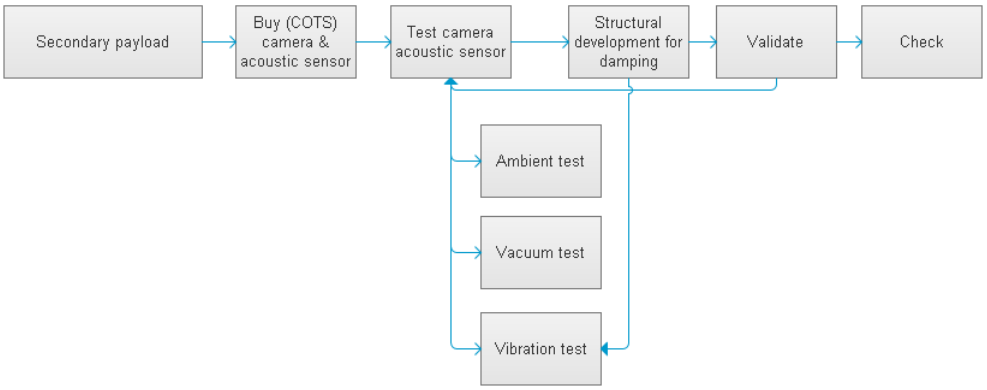

Figure 3.6.9: Project design and development logic of secondary payloads

3.7 Cost Breakdown

The cost breakdown provides an estimate of all the costs incurred during the design and development phase of the Phi satellite. The main phases that are to follow are the production of the satellite, verification testing and operation. The DelFFi project is offered a budget of 2 million Euro by TU Delft. Neglecting any indirect costs arising from the involvement of paid faculty members throughout the design phase headed by the DSE group, the upcoming phases listed are entitled to the entire initial budget.

Table 3.7.1: Cost Breakdown

Phase		Cost (Euros)
Production	Components	270000
	Assembly	5000
	Infrastructure	10000
	Duplication	540000
	Labour	0
Testing	Component-level	300000
	System-level	100000
	Flight model	20000
Operation	Ground station	5000
	Labor	0
Total		1250000

Production Most of the components used in the CubeSat will be purchased from commercial outlets. The figure cited in the table is simply a sum of the costs of all the components, outlined in detail in the Budget Breakdown Chapter of this report. The production of the "flaps", as well as the spacecraft assembly, may result in extra costs since facilities and equipment may not be available for use in the university. Duplications of the final configuration are expected to be produced, both for testing purposes and for storage purposes as was the case for the Delfi-C3 and the Delfi-N3xt. In the cost budget, it is assumed that there will be at least two duplications. A majority of the time spent on the production of the satellite will be by students, who are not paid for their input. Nevertheless, indirect labour costs arise when faculty members like professors or PhD students work on the project since they are paid by the university, which is the primary source of funding for the project. In some cases, experts may have to be outsourced.

Testing All individual components must be tested in order to verify that they function and meet their purpose independently. Then tests are performed on the entire spacecraft system after the separate components have been integrated. These component-level and system-level tests are known as qualification tests. Large cost ranges have been allocated to these two activities in case either a component or the final configuration does not pass the verification tests. If this were to happen, changes have to be made in the design, which may result in added resource expenditure. The component-level tests include the sum of costs of all the different components. After the entire system has been verified, an acceptance test must be performed on the flight model for validation. Assuming the qualification tests were conducted properly, the acceptance test is more likely to be successful. Therefore, a smaller portion of the cost budget has been allocated to this.

Operation The ground station operations, which is situated in the Electrical Engineering, Mathematics and Computer Science faculty at TU Delft, will most probably be looked after by students, eliminating any labour costs. Nevertheless, costs arise in the maintenance of the ground station, which will consume electricity. Also, new software may need to be purchased for updating the tracking devices available at the station.

3.8 Risk Assessment

"Risk is the potential for performance shortfalls, which may be realised in the future with respect to achieving explicitly established and stated mission to the areas of safety, technical, cost and schedule of the project itself," stated by NASA Risk Management Procedural Requirements [48]. Therefore, risk analysis plays an important role for identifying potential failures and planning methods to circumvent any issues. This chapter contains risk assessment of DelFFi Phi CubeSat, on the technical side and the mission side, respectively. Technical risk assessment is used to identify the risk items in subsystems, while the mission risk management plan analyses risks from the perspective of missions and operations. For both of them, the potential technical risks that could occur in the development of the CubeSat are identified and listed. The probability of occurrence and the severity of the performance consequence on the mission for each event is assessed and illustrated in a risk map . Afterwards, measures and suggestions are given to reduce risks for the events that are estimated to have the highest risks.

3.8.1 Technical Risk Assessment

The risk map, Figure 3.8.1, gives a clear overview of risks that subsystems and important hardware bring along. For each individual subsystem, the failure modes are identified and listed as risk items below the figure.
The performance consequence for a risk event is estimated by considering the impact on the mission objectives of the DelFFi CubeSat in case of failure of the subsystem. The probability of an event is estimated on statistical data obtained from [22]. The performance consequences are divided up into four categories: catastrophic (failure to accomplish the two primary mission objectives), critical (failure to accomplish one of the primary mission objectives),

marginal (major performance reduction or failure to accomplish secondary mission objectives) and negligible (minor performance reduction). The upper right portion of the grid is usually coloured red to signify that risks that are placed in this area should cause serious concern and redistribution of resources. The lower left portion of the plot is commonly coloured green, meaning small risk with small consequence, as the group desires to minimise the risk.

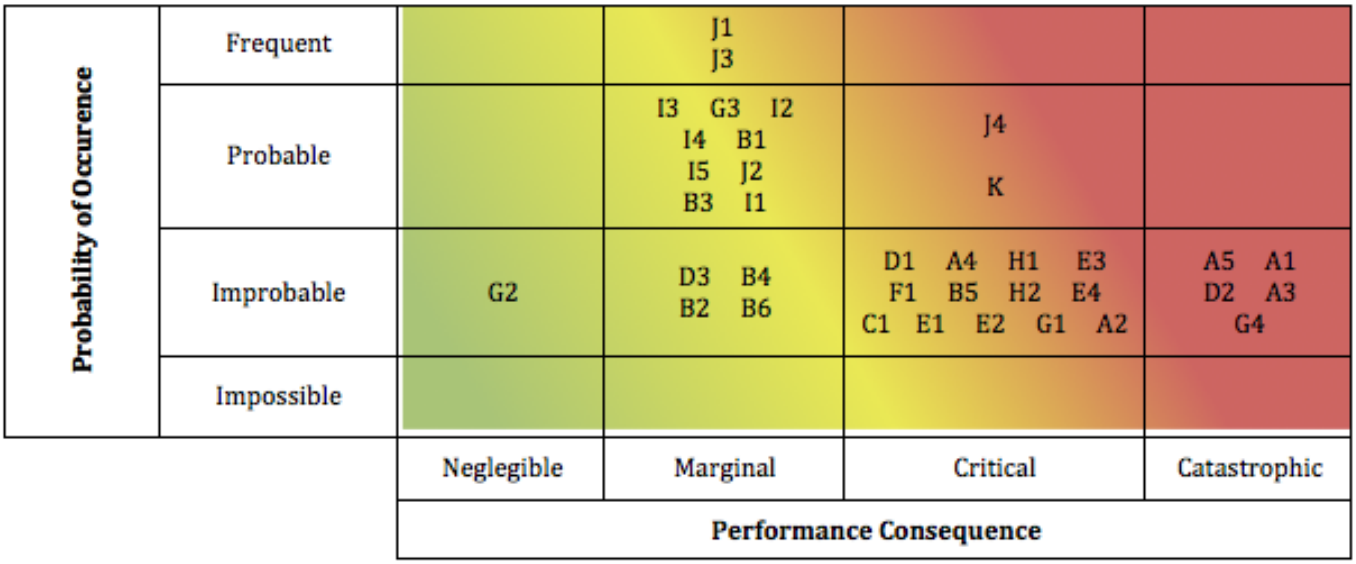

Figure 3.8.1: Technical risk assessment

A. Electrical Power System

1. Short-circuit failure
2. Single-point failure
3. Open-circuit failure
4. Battery overcharging
5. Battery leakage

B. Attitude Determination and Control System

1. Star tracker failure
2. Magnetometers failure
3. Sun sensors failure
4. Reaction wheels for roll-axis control failure
5. Reaction wheels for yaw- and pitch-axis failure
6. Magnetorquers failure

C. Guidance

1. GPS receiver failure

D. Communications

1. Receiver failure
2. Transmitter failure
3. Inter-satellite link failure

E. QB50 Payloads

1. Thermistor component failure
2. Thermistor electronic failure
3. Sensory payload component failure
4. Sensory payload electronic failure

F. Thermal Control System

1. Releasing tape

G. On-board Computer

1. Processor failure
2. Memory failure
3. Software failure
4. Connector failure

H. Structure

1. Failure due to static loads
2. Failure due to resonance

I. Secondary Mission Objective

1. Camera damage due to shock loads
2. Camera damage due to radiation
3. Pictures are blurry
4. Electronic failure
5. Component failure

J. Propulsion

Table 3.8.1: Sources of mission risk

Hardware/Software	Systematic
Requirements	Logistics
Technical baselines	Concurrency
Test and Evaluation	Cost
Modelling and simulation	Management
Technology	Schedule
Production/ Facilities	External factors
Industrial capabilities	Budget

Table 3.8.2: DelFFi-Phi mission risks

	Risk Category	Mission Risk	Responsible Party
a	Schedule	Failure to deliver DelFFi to QB50 deadline (DSE phase).	System engineer
b	Payload	Failure to operate primary and secondary payload	Payload group
c	Bus	Unable to communicate with or gather information from Delta	COMMS, ADCS
d	Bus	Unable to perform formation flying	GNC, Propulsion
e	Bus	Unable to maintain the orbit	GNC, propulsion
f	Personnel	Loss of human knowledge and experience	System engineer
g	Cost	Mission cost overwhelming	System engineer
h	Support	Ground station non-operate	

1. Leaking pipes
2. Calibration of nozzle fails
3. Leakage of valves
4. Opening of the valves fails

K. Failure of Delta satellite

The risk that a failure in opening of the valves adds to the spacecraft risk depends on when the failure takes place. If the failure happens before performing the first demonstration of formation flying, the risk is critical as one of the first mission objectives can not be established in the primary way (but it can still be performed by use of differential drag). If it happens afterwards, the risk is marginal as the propulsion system is not really needed anymore.

3.8.2 Mission Risk Assessment

It is difficult to identify the risks for subsystems before determining all the specifications of the design. However, it is useful to start with the mission concepts and operations and to identify the potential risks during the life cycle. To identify risks and their root causes, work breakdown structure (WBS) is particularly useful in identifying product and some process oriented risks. For each fundamental element of WBS, their potential to fail can be estimated based on common sourses of risk. Two main categories of risks issues are hardware and systematic. Table 3.8.1 lists typical sources of mission risk according to the DoD Risk Management guide [42]. The mission and logistics of DelFFi has been described in Chapter 4 that the main goal of the mission is dependent upon the ability of the spacedraft to gather scientific and spacecraft health data, and communicate with ground station and Delta. Therefore, the mission risks are identified based on the success of mission objectives. These risks are combined the seven identified risks for the DelFFi mission and listed in Table 3.8.2.

Similar to Figure 3.8.1, each of the mission risks from Table 3.8.2 is plotted on a risk map. After identifying the risks, it is important to include a mitigation strategy in the assessment. According to DoD, risk mitigation is the selection of the option that best provides the balance between performance and cost [42]. There are four options to perform the mitigation: avoid, control, transfer, or assume. One or more ways can be applied to risk items.

- Avoiding risk by eliminating the root cause and/or the consequence,
- Controlling the cause or consequence,
- Transferring the risk,
- Assuming the level of risk and continuing on the current program plan.

For each of the risks, at least one mitigation strategy should be documented. Having multiple methods of mitigation decreases the likelihood and consequence that the risk would have upon mission success. Since the technical

Table 3.8.3: Mitigation plan

Mission Risk	Root Causes	Mitigation Plan
a	One or more subsystem(s) unable to finish design before deadline Integration between all subsystems unable to finish before deadline	Develop a backup plan for each subsystem design that meets all non-killer requirements Systems engineer should make sure that no conflicting requirements exist between subsystems
b	Malfunction of payload Mistakes during integration	Testing components before integration Testing payload after integration
c	Transmitter or receiver failure	Redundancy
d, e	GPS failure Propulsion system failure Position determination system failure	Testing components before use Redundancy Redundancy
f	One or more member unable to continue their work	Multiple responsible person for one subsystem
g	Components are too expensive Other costs	Back-up plan with compromised performance System engineer responsible to control the budget

specifications are not known yet for the subsystems, it is hard to give a detailed risk mitigation plan for each risk. As the design status matures, these mitigation strategies also mature. Therefore, for subsystems, several general rules that can be taken to minimise the technical risks are given. First of all, redundancy will be integrated in the design such that failure of a single component does not lead to complete failure of a subsystem and potentially mission failure. Secondly, strict verification and validation methods should be performed to prove that all requirements are met by the subsystems and that the complete design will successfully perform its intended task. Also, the complete space segment as a whole must be verified and validated. Thirdly, commercial-off-the-shelf components (COTS) can be used to reduce the time consuming and costly verification process. Qualification and acceptance tests have already been performed on most COTS parts; however, attention should be paid to operating COTS components in the space environment.

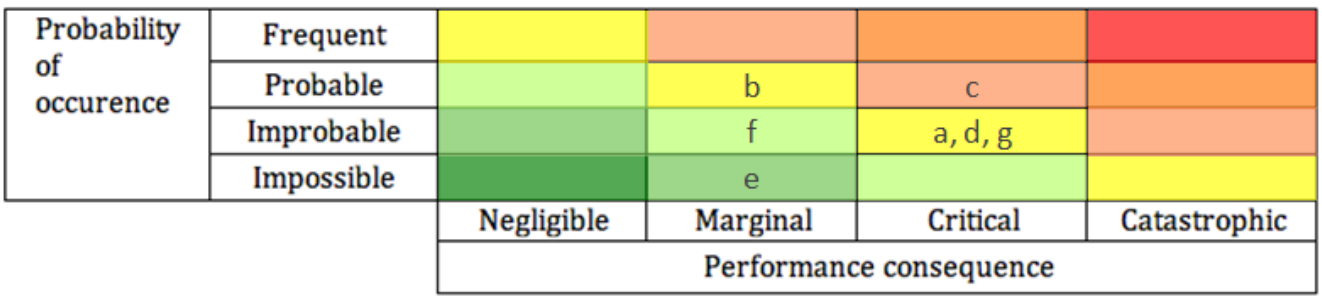

Figure 3.8.2: Mission risk assessment

A tentative mitigation strategy for each risk item is listed in Table 3.8.3 based on the root causes.

3.9 Sustainable Development Strategy

As there is growing interest for small satellite development not only among universities, but also other establishments for both commercial and military purposes, it is important not to ignore their potential impact on the environment. Throughout the development, production, and launch of the satellites, all kinds of technology processes are carried out, including the manufacturing, testing, and disposal of raw materials. These resources are finite and effort should be exerted to prohibit environmental degradation.

3.9.1 Green Manufacturing

Also, after the end-of-life, these satellites should either be destroyed during re-entry or returned back to Earth, instead remaining in orbit or disposed of in the ocean. Since the number of small satellites to be launched is projected to grow, one has to consider greener manufacturing, meaning that environmentally friendly technology should be used as much as possible. The intended benefits would include a reduction in waste, less frequent use of toxic materials and greater employment of green technology.

When considering missions comparable to that of DelFFi's, requirements are relatively less complex considering objectives are not as ambitious as faraway space explorations. Also, the short lifetime of the CubeSat makes it easier to bring the cost down at LEO. Meaning in its LEO the CubeSat will be below the Earth's radiation belts, which is very important because CubeSat uses low cost Commercial-Off-The-Shelf (COTS) components.

This low initial altitude of the Phi mission has the advantage of a milder radiation environment, which provides new opportunities to use low cost Commercial-Off-The-Shelf products. From the previous CubeSat projects it turned out that these COTS products work well enough at LEO's during the short mission life. An example of one of the spin-off products that can be considered is the (micro) SD card for memory storage. This is small and light enough for a nano-satellite. By using the technology that is already available, less time, money, and material resources are wasted, since no new research, expensive laboratory tests and machinery have to be done. If some research is needed it will be carried out in less extensive method because these tests are subjected for validation. Hence no money is spent for example on new manufacturing process or material property tests (which is already available from terrestrial industries experience).

In turn, this saves a considerable amount of resources for the CubeSat design, and is hence beneficial for the sustainability of the environment.

3.9.2 Space Debris

Not only should the Earth be considered for sustainability but also the space environment. Over the last 20 years the amount of debris in LEO in particular has increased rapidly. For this reason NASA, ESA, several country governments and independent organisations have been starting to invest more in the removal and prevention of future debris. This is a slow process and there is no definite solution at present. Research, however, is continuously being carried out. For example, Raytheon BBN Technologies and University of Michigan are developing the Space Debris Elimination (SpaDE) system to remove debris from orbit by firing focused pulses of atmospheric gases into the path of targeted debris[26].

Figure 3.9.1: ESA space debris model [7]

The 6th European Conference was held at the European Space Operations Centre on space debris in Germany from April 22 to 25 this year. The representatives from all fields were invited to attend this four-day event, according to officials at the European Space Agency. At this conference they discussed the build-up of potentially harmful debris in orbit, and addressed possible ways to remove defunct satellites and other pieces of errant space hardware. A list of discussed topics include:

- debris environment modelling
- on-orbit & re-entry risk assessments
- orbit prediction & determination
- debris mitigation & remediation
- hypervelocity impacts & shielding

The publication of the proceedings will be held in July 2013[8].

Regarding this mission, no debris will be left in space after the disposal of the satellite. At the low orbit of 320 km, the satellite will just burn up during re-entry. However, the CubeSat can still have a valuable contribution towards the solution of the debris problem. NASA invites students to submit a response to this inquiry to assist in the planning and development of potential launch opportunities for CubeSat missions on-board NASA-sponsored Expendable Launch Vehicle (ELV) launch services. The industry could also submit information that will allow NASA to assess various design alternatives for orbital debris mitigation options applicable to CubeSat missions in LEO. As a result, NASA's knowledge of the industry's capability and viability will be improved, as well as the overall understanding of CubeSat mission designs.

3.9.3 Debris Proposal For Phi

One of the ideas for the Phi's secondary mission objective was the 'Space Debris Removal' using aerogel foam and electrodynamic tether.

Even though the idea did not score well in the trade-off table on the criteria cost, weight, volume, risk and originality; it is still worth mentioning as a strategy for sustainability. Even though at present the feasibility of such a concept is questionable, further developments in technology will certainly aid in making this feat more achievable.

Implementing aerogel foam or electrodynamic tether on Phi are at the moment quite risky. The project schedule cannot accommodate detailed research for these problems. As the students' knowledge concerning satellite design is limited and the formation flying mission carries higher precedence (which exerts more pressure on the Phi's satellite design envelope) no risk is taken to implement a technology that is not thoroughly proven to work. It might be possible in the future when the idea is reshaped with newer findings.

In the secondary mission objective section it was mentioned that the research done on the aerogel foam and electrodynamic had medium complexity on space debris removal and therefore feasible. Even with this relatively positive result the constraints that the present CubeSats are given make this option challenging. In turn this demands for more creative ideas as the CubeSat's capabilities are not developed much for the debris purposes. The operational capability of other application purposes of the CubeSats has just started to develop and it is uncertain what the possibility will be over 10 years.

3.9.4 Satellite Measurement Data

Another subject for the secondary mission objective was monitoring climate by measuring carbon dioxide level (CO_2) at 320 km altitude. This option, monitoring climate, was not considered, knowing that there is no originality in this.

However, the data received from existing satellites has contributed significantly in the move towards a more sustainable economy, establishing a healthy environment and enhancing human life. At first it seems as if this topic has been overdone, considering how in the past 30 years[34] satellites have already done about the same observations and is still continuing to do so. Nevertheless, the evolution of nature and the human race is not characterized by static behaviour, but in fact changes over time. Therefore, the carbon levels change over time as well. In turn, a continued data is still desired by the scientists. This carries insights regarding the rate of global changes and the contraction at the lower thermospheric altitudes.

With the changing climate and the extreme magnitude that natural disasters are getting due to increasing Earth temperatures, the demand for more climate research is imperative. One of the main factors that contributes to the global temperature changing is CO_2, which acts as a greenhouse gas by capturing the (short wave) radiated heat from the sun and re-emit it back to the earth. The Earth gets warmer and warmer which results more in evaporated water. This water vapour absorbs even more (long wave) radiation from the Sun and quickens the global warming even faster than CO_2 [41].

At lower atmosphere CO_2 functions as a heater, but at the higher atmosphere it works as a coolant. This cooling property makes the upper atmosphere contract, resulting in less drag on satellites and space junk [39]. In turn, the debris in higher orbital altitudes decelerates slower to the earth. Hence, more collisions will occur between the space debris, and another worrisome scenario arises: a triggered Kessler Syndrome. Fragments of junk can smash with other working satellites, which in turn creates more pieces of junk in space. The new pieces then collide with other debris and create even smaller fragments that go on colliding with everything in their paths.

Therefore, it becomes more important to gain knowledge about the carbon cycle in the thermosphere as the carbon level changes quicker in this layer. Even though the Phi satellite does not carry out climate monitoring, the next CubeSat can take this into account, especially considering how important the data on carbon level is for life on Earth and also for the debris problem.

Nevertheless, Phi is going to aid in validating atmospheric models by using FIPEX. This measures the time resolved behaviour of atomic and molecular oxygen (AO). This gives information on the AO level during the mission at the LEO[49]. Atomic oxygen causes erosion of the material when it comes in contact. The thermal-optical properties degrade together with the solar cells. Another worrisome effect the AO has is that it damages the visibility of the optical measurement devices. The measurement are used to validate the models made on Earth. This aids sustainability since the data can be used as a reference for predicting material degradation.

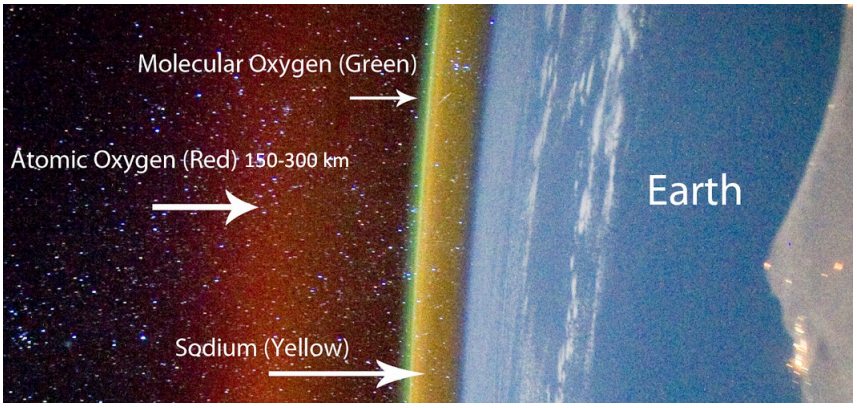

Figure 3.9.2: Atomic oxygen layer [49]

3.9.5 Formation Flying

For the formation flying use is made of the differential drag method to adjust Delta's and Phi's altitude with each other. Formation flying with this method consumes less energy. To create drag two designs were proposed in the Formation Flying chapter. The materials and devices that are used for manufacturing are COTS products. For example, for the chord, Dyneema material is proposed. This is used in fishing and other (offshore) industries. The device that is used for retraction is a small motor that is normally used for small moving objects (e.g. toys).

3.9.6 End of Life

Another way to approach sustainability is to reflect on which purposes one can give the satellite when the it reaches its end of life. This is exactly what the engineers at the University of Glasgow and Clyde Space Ltd did. After investigating this issue, they came up with the Aerodynamic End-Of-Life De-orbit System (AEOLDOS) [57]. The functionality is almost the same as a normal parachute, only it is attached to the CubeSat (before launch). It works as follows: The moment the satellite reaches the end of its operational life, the parachute opens in order to generate aerodynamic drag. This gives an "aerobrake" to the velocity of the CubeSat, which causes the satellite to de-orbits. This lightweight parachute is made from a thin membrane supported by tape measure-like struts, see Figure 3.9.3. As soon as the springs pop open, aerodynamic drag is generated against the extremely thin upper atmosphere that still exists in near-Earth space. While the satellite falls out of orbit the drag increases, causing the CubeSat to burn up more controllably during its descent. This means that the satellite does not contribute to space debris.

Figure 3.9.3: AEOLDOS, developed by University of Glasgow and Clyde Space Ltd [58]

Chapter 4
Budget Breakdown

Presented in this section are the mass, cost and power budgets for the final design. Table 4.0.1 lists the mass and cost of all of the components that comprise the final design. The mass of the satellite is constrained by CubeSat requirements to a maximum of 3.6 kg. The total mass for this exercise's final design is , which leaves a relatively small margin for implementing more components in the detailed design phases. The portion of the Phi budget allocated to purchasing the components alone was 500000 euros. It can be seen from the sum of the costs of each of the components that this figure was significantly overestimated, since only half of this amount is actually required.

Table 4.0.1: Mass and cost budget

Subsystem	Component	Units	Unit Mass(g)	Unit Cost (Euros)	Retailer
EPS	FleXible Board	1	139	6712	ClydeSpace
	Battery	1	137	123	ClydeSpace
	Solar Panels	2	135	35000	ClydeSpace
	Deployables	2	79	20000	ClydeSpace
OBC	Computer	1	65	4750	CubeSat Shop
ADCS	Sun Sensors	2	5	2500	Sinclair
	Star Tracker	1	90	50000	SSBV
	Magnetometer	1	5	38	SparkFun
	Reaction Wheels	3	83	6000	TU Delft
	Magnetorquer	3	30	1200	CubeSat Shop
	PCB	1	83	50	
GNC	GPS Reciever	1	30	12000	CubeSatShop
	GPS Antenna	1	9	3	Laipac
Propulsion		1	438	30000	TU Delft
COMM	VHF Antenna	1	100	4000	CubeSat Shop
	VHF Transiever	1	85	6750	CubeSat Shop
Sensory Payload	FIPEX	1	400	0	provided by TU Dresden
	PCB	1	40	50	
	Thermocouples	13	12	5	Omega
	Flaps	1	50	2000	
Secondary Payload	Camera	2	2.5	32	
	Acoustic Sensor	19	15	70	
Thermal	Kapton Tape	10	1	7	Kapton Source
	Thermistors	5	3	5	HoneyWell
Structures	Primary+Secondary Structure	1	580	3800	CubeSat Shop
	Hinge	1	75	660	Pumpkin
	Harness	1	75	750	ClydeSpace
Total			3550	265603	

Unlike the mass and cost budgets, the development of the power budget was not driven by any direct constraints, but rather the energy requirements of the different subsystems. Nevertheless, limitations imposed by the spacecraft's mass, volume, sunlight exposure level, etc, were taken into account. Table 12.1.1 lists the power allocated to each component.

Chapter 5
Sensory Payload

The Phi satellite will take 2 sets of sensory payloads onboard, primary and secondary. All sensors are described and chosen in this chapter.

5.1 Primary Payloads

To take part in the QB50 project, all participating satellites must carry and operate one of two sets of selected sensory payloads for atmospheric research and meet the QB50-SYS-1.5.2 requirement, which states that "each Cubesat carrying a set of standard QB50 science sensors shall communicate a volume of at least 2 Megabits of science data per day to the ground station that is operated by the university providing the CubeSat". This Phi satellite will be carrying the Flux Φ Probe experiment (FIPEX) developed by TU Dresden and twelve thermocouples. In this section, specifications pertaining to both payloads are elaborated upon. Payload specifications are taken from the QB50 Control Interface Document (CID) [54] and the QB50 Sensor Selection Working Group (SSWG) report [56].

5.1.1 FIPEX

The purpose of the FIPEX payload is to measure the time-resolved behaviour of atomic oxygen (AO) and molecular oxygen (O_2) in the lower thermosphere. The data gathered will primarily be used to validate current atmospheric models. Since AO is a dominant species above 200 [km] altitude and varies with geographic location, time, and solar activity, the data will also provide valuable insight on the effects that its concentration may have on corrosion rates of spacecraft operating in the thermosphere, especially those composed of vulnerable materials such as aluminium. The payload is composed of an electrochemical cell containing a solid oxide electrolyte micro sensor. An Au cathode is used to detect atmospheric oxygen and a Pt cathode is used to detect O_2 The payload has a very high sensitivity, possessing the capability to distinguish between the two species at pressures down to 10^{-10} mbar.

The payload specifications derived from the CID are listed in Table 5.1.1, next to the corresponding subsystem. Refer to Figure 5.1.1 for an illustration of the payload-spacecraft interface.

Table 5.1.1: FIPEX payload specifications

Subsystem	Aspect	
Structures	Mass	< 400 g
	Volume	$10 \times 10 \times 47$ cm
	Surface Area	258.3 cm^2
ADCS	Orientation	Payload must face direction of the velocity vector
	Pointing Accuracy	$\pm 10°$
	Pointing Knowledge	$\pm 2°$
Data Handling	Data Rate	16 kB/hour
EPS	Power Line	12 V
	Average Power	77 mW
	Maximum Power	200 mW
Thermal	Operational Temp. Range	-20 to 40 $°C$
	Non-Operational Temp Range	-35 to 60 $°C$
	Standby	-25 $°C$

The CID does not specify the sensor data rate. However, the SSWG report states an estimation of approximately 16 kByte/hr.[56] This is equivalent to 128 kilobits per hour(1 byte=8 bits). A detailed duty cycle is not presented either. Rather, it is simply stated that it is not required for the FIPEX to be taking measurements at all times. Nevertheless, it can be calculated how long this payload has to be active per day to meet the minimum data communication requirement of 2 Megabits.[54]

5.1.2 Thermocouples

Thermocouples measure the surface temperature of the spacecraft's outer structure. This data is valuable for flow field modeling since the temperature directly effects the behaviour of surrounding molecules. When these molecules make contact with the satellite's surface, they are reflected away. The characteristics of this beam then determines factors such as the momentary drag coefficient. In the QB50 CID, it is recommended that one thermocouple is placed

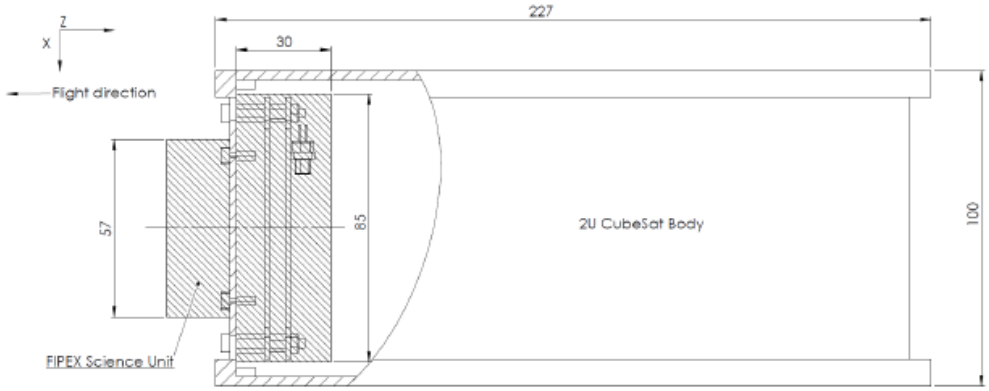

Figure 5.1.1: FIPEX payload interface

on the inner surface and outer surface of each side of the spacecraft, meaning that twelve thermocouples in total are mounted to the spacecraft. Most existent thermocouple sensing elements possess flight heritage and can be purchased as a COTS component.

Though no information regarding the thermocouples is available in the CID, the SSWG report does present an optimal number of thermocouples, their placement and recommended sampling rates.

1. **Amount and Placement** According to the SSWG report, "for surface temperature measurements, at least one temperature sensor per side recommended. Altogether 12 sensors provide cross-check on each side and good coverage".

2. **Sampling Rate** : The SSWG also offers guidance on setting the sampling rate. It states the time interval between measurements is dependent on the angular velocity of the satellite attitude. Table 5.1.2 the table provided in this document, listing the recommended sampling rate with respect to the satellite's angular velocity. The data acquired in a hundred second time interval is also given for each sampling rate.

Sampling interval [s]	Resolvable angular rate [°/s]	Data rate [byte/s]	Data collected in 100 minutes [kB]
0.1	1800	180	1080
0.2	900	90	540
0.4	450	45	270
0.8	225	22.5	135
1.6	113	11.3	67.5
3.2	56	5.63	33.8
6.4	28	2.81	16.9
12.8	14	1.41	8.4
25.6	7	0.70	4.2
51.2	4	0.35	2.1
102.4	2	0.18	1.1

Figure 5.1.2: Thermocouple sampling rates [56]

The expected angular velocity encountered during detumbling mode is less than $10° \cdot s^{-1}$, and during nominal mode is $0.132° \cdot s^{-1}$. According to the table, during detumbling, measurements must be taken every 12.8 seconds resulting in 1.41 $B \cdot s^{-1}$. During nominal operation, a sampling interval of 102.4 seconds is taken, resulting in a data rate of $0.18B \cdot s^{-1}$.

Thermocouple Choice The choice of thermocouple type taken on board is open to the the designer. Three of the available options are thermistors, resistance temperature detectors(RTD) and integrated circuit temperature (ICT) sensors. Thermistors and RTDs use semiconductors and metallic materials respectively by measuring their resistance which is dependent on the temperature. ICT sensors use transistors, which will provide voltage outputs that vary with temperature provided the input is fixed. These three sensors have varying capabilities in terms of measurable temperature range, measurement uncertainty and power required. Table 5.1.2 contains information about these capabilities for each sensor. The requirements that drive the trade-off between these options is mainly the accuracy. The requirements driving the trade-off, which are equally important, between the options are:

1. The thermocouples should be have a suitable temperature measurement range that comply with the mission environment, which ranges from approximatley 10-30 degrees.

Table 5.1.2: Thermocouple characteristics

	Range [$°C$]	Accuracy[°]	Power [mW]
Thermistors	-55 to +150	±0.05-±0.2	2 to 40
RTDs	-50 to +500	±0.15	3 to 10
IC Temp. Sensors	-50 to +150	$\pm 0.5 - 2$	0.5

2. A maximum of +/- 1 $°C$ uncertainty is required for the application of temperature data in analyzing drag measurements.[56]

ICT sensors require significantly less power, though their measurements can deviate up to +/- 2$°C$. RTDs can measure across a considerably wider temperature range, although it is highly unlikely that temperatures at any point in the mission will exceed the range of the other two sensors. When calibrated well, thermistors are capable of accuracies of down to +/- 0.05$°C$. Its accuracy range, nevertheless, is similar to that of the RTD. With these aspects all taken into consideration, it seems that RTDs are the optimal choice.

5.1.3 Duty Cycle Calculation

According to the paper published by the QB50 sensor selection working group (SSWG) on March 2012, the assumed data rate for a single FIPEX payload sensor is estimated to be around 16 kBytes per hour. This is equivalent to 128 kbits per hour(1 byte=8 bits). A duty cycle for these payloads must established in order to ensure that the 2 Mbit per day requirement is met. Aside from FIPEX, the sensory payload also consists of twelve thermocouples. The data rate for the thermocouples are determined by the angular rotation rate of the satellite. As stated earlier, the satellite is expected to have a sampling interval of 12.8 s when detumbling and 102.4 s when operating nominally. This corresponds to a data rate of approximately 967.68 $kb \cdot day^{-}1$ and 126.72 $kb \cdot day^{-}1$ respectively. Assuming that the satellite is operating nominally, (meaning a lower data volume gathered from the thermal sensors is communicated) the FIPEX payload will have to carry out measurements for a minimum of 14.625 hours per day to fulfill requirement QB50-SYS-1.5.2. In other words, the payload will have to be active for at least 60.93%(=14.625/24*100) of the satellite's lifetime.

Chapter 6
Secondary Mission Objectives

For the secondary mission objectives, two were chosen for the Phi satellite: cameras for taking pictures of the CubeSat's deployables, and acoustic emission sensors for analyzing the vibrations of the satellite. The following sections discuss the trade-off and selection of the secondary mission objectives, as well as the final design of each of these payloads and their mission concepts.

6.1 Trade-off

Before making a trade-off between the different options for the secondary mission objective, trade-off criteria need to be defined. Afterwards, this trade-off criteria will be assigned with weights to include their relative importance in the trade-off. Next, the criteria will be assessed for the options that are left after imposing the constraints and feasibility upon the secondary mission objective design option tree. Weights are assigned to all criteria. The weights of criteria are listed below in the Table 6.1.1 and shown in the table as the width of the column.

For secondary payloads, there are more constraints imposed on them than other objectives. Due to the schedule, mass and cost limits, the secondary mission can not be too ambitious and should fit in the existing design and budgets. The most important concerns about secondary missions are their originality and scientific value. Here, the originality means completely new concepts and the existing ones with other methods or having implementing effects on the research results. Cost and volume are given the lowest weights because of the ample cost and space budget available now. Complexity is given a high weight factor as well, because the secondary mission objective needs to be able to be designed within the schedule of the DSE project, so if the design becomes more complex, meeting the requirement on the schedule becomes less possible. Mass and schedule are less important for the possibility to simplify the design based on the needs and restraints.

The assessment of the options will be done by grading every criteria with a +, 0 or -. To have a good overview at first sight, the colours green (+), red (-) and grey (0) are used. A plus means the option scores good on the criterion, a minus means it is not viable with the criterion and a 0 means a neutral score. The trade-off table can be found in Figure 6.1.1. In the end, two missions yield the highest score, compared with other options, acoustic spectral analysis and monitor deployment. And because of their similar mission objective and complementary results, both of them are taken in the Phi satellite.

Table 6.1.1: Trade-off Criteria

Criteria	Weight	Criteria	Weight
Originality	5	Mass	3
Scientific value	5	Schedule	2
Complexity	4	Cost	1
Risk	4	Volume	1

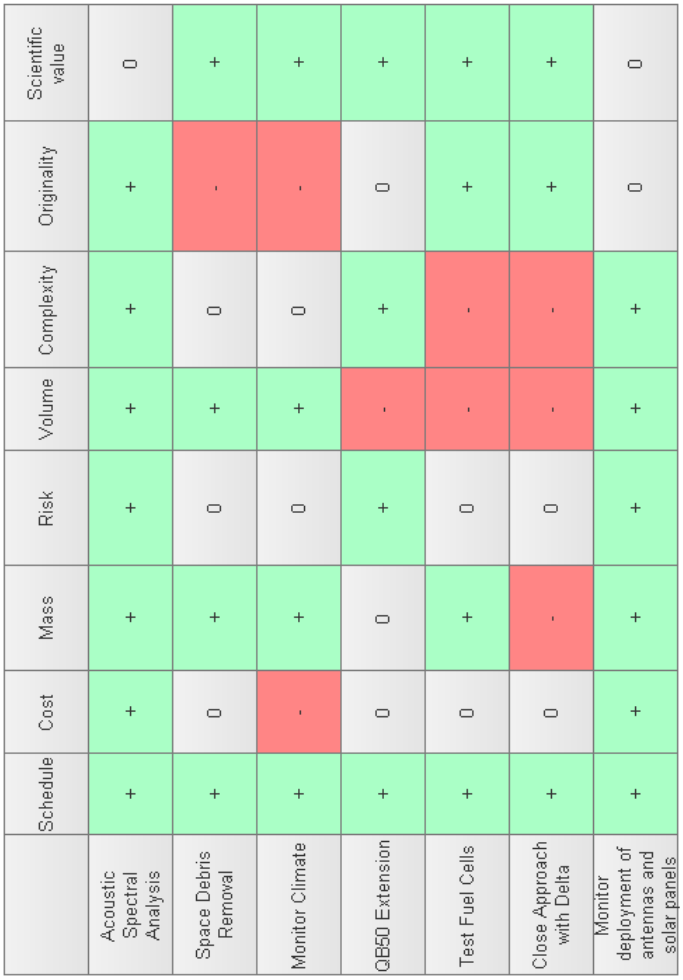

	Schedule	Cost	Mass	Risk	Volume	Complexity	Originality	Scientific value
Acoustic Spectral Analysis	+	+	+	+	+	+	+	0
Space Debris Removal	+	0	+	0	+	0	-	+
Monitor Climate	+	-	+	0	+	0	-	+
QB50 Extension	+	0	0	+	-	+	0	+
Test Fuel Cells	+	0	+	0	-	-	+	+
Close Approach with Delta	+	0	-	0	-	-	+	+
Monitor deployment of antennas and solar panels	+	+	+	+	+	+	0	0

Figure 6.1.1: Secondary mission objective trade-off table

6.2 Camera payload

The camera payload is constrained by the available volume and mass budget. With this in mind, the payload has to be sized accordingly. This subsection explains the chosen COTS components and justifications, payload sizing, and failure modes.

Chosen COTS components

Due to the mass and volume constraints, a nano camera was chosen (see Figure 6.2.1) for the secondary mission objective. It weighs only 1 gram and is a COTS product designed for use on UAV's. Because of its small size, the camera resolution is only satisfactory (since a long focal length and large aperture diameter are both needed for a high resolution image). Another problem with a COTS camera is that it must be tested to see if it can withstand the shock loads of the satellite during launch and the vibrations during operation (see 6.2.2). Therefore, two cameras will be mounted on the satellite to increase the chance of mission success. In order to see the deployables (solar panels and antennas), the camera must be able to cover a wide enough angle. For this reason, a wide angle lens for the nano camera dimensions was also selected as an add-on (see Figure 6.2.2).

In Table 6.2.1, the specifications and budgets for the chosen COTS camera and wide angle lens are listed (per unit of camera and lens).

6.2.1 Operation and coverage

Each of the two cameras will be mounted on the long side where there is no body-mounted solar panel. The location of this will be just above the deployable solar panel (so that the panel will not make contact with the camera lens during launch), as shown in Figure 6.2.3. The camera will jut out of the cut-out in the satellite approximately 4 mm, which still leaves space between the lens and the StackPack (9 mm of free space between the wall of CubeSat and the StackPack [55]). For the contribution to the center of gravity (although not significant for such a small mass), each camera is positioned, widthwise, in the middle of the wall.

Figure 6.2.4 depicts the deployables which are partly covered by the Field of View (FOV) angles of the camera. Each camera will be tilted approximately 10° towards the deployable solar panel (ones that will be deployed at initial

Figure 6.2.1: 1g nano camera [3]

Figure 6.2.2: Wide angle lens for nano camera [6]

Table 6.2.1: Camera + wide angle lens specifications

Mass [g]	1 (camera) + 1.5 (wide angle lens)
Cost [€]	40.8 (camera) + 14.9 (wide angle lens)
Retailer	FPV Hobby
Power consumption [W]	0.335
Dimensions [mm]	11.5 x 11.5 x 13
Resolution	782 x 572
Horizontal FOV [deg]	110
Vertical FOV [deg]	82

orbit) and 10° downwards to be able to see the antenna.

In the case that both cameras can survive in space, only one camera will operate at a time, in order to lower the power consumption. The first camera (on the side of the longer antenna), will take a video of the deployment process. This process lasts for only a few seconds. Thus to be able to see the before and after pictures, the camera will be set to record for 10 seconds, at 48 frames per second (slow-motion, since it takes twice as long to play back in a 24 fps projector [4]). When this is done, the first camera will be turned off and the second one switched on. It will take a few snapshots of the deployed solar panel and the antenna in range of the FOV. In the case that one of the camera fails, the other one will be responsible for recording the video and take pictures. The footage will be stored on the secondary payload's customized PCB until it can be downlinked to the ground station. The video should not exceed 2 Mbytes.

6.2.2 Failure modes

Since it is unknown whether or not the selected COTS camera will function in the severe conditions in space without proper testing, a redundancy was made by having two cameras instead of one in order to decrease the chance of failure. Different failure modes exist for this rather vulnerable payload. The first is the shock loads during launch that could damage the camera if it is not properly protected by a structure that absorbs the shock. Since the time constraint is limiting for designing a new system around the camera, a quick solution is to leave a gap between the cut-out in the wall of the satellite and the camera lens so that the vibrations will damp out.

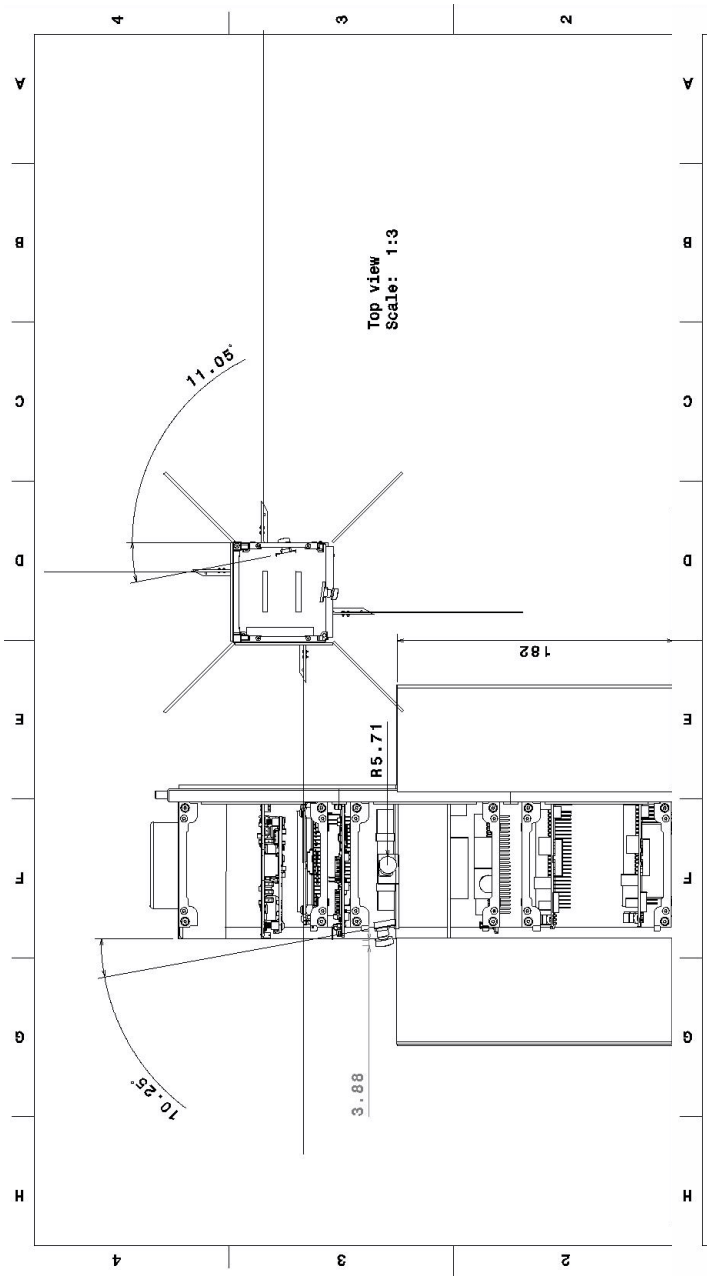

Figure 6.2.3: Camera mounting on satellite

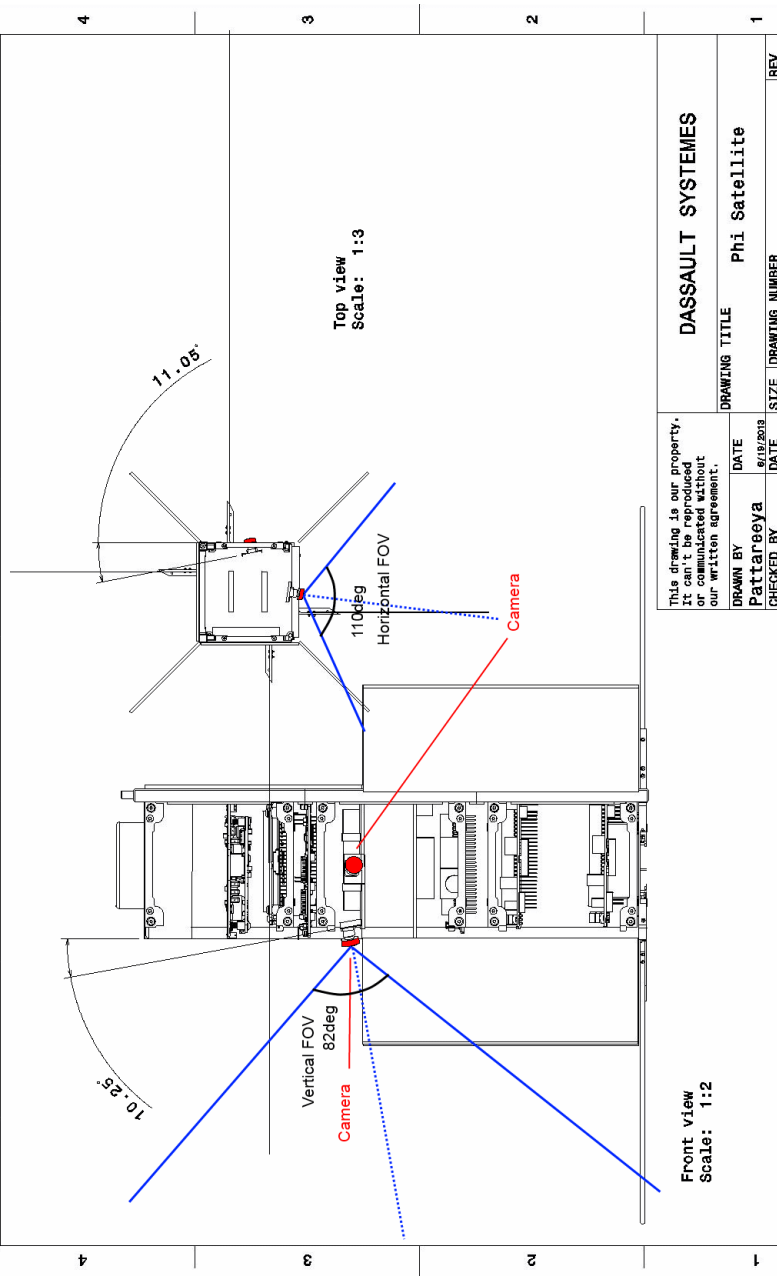

Figure 6.2.4: Field of view of camera and coverage

If the cameras survive the launch loads, in orbit there is also the danger of residual frequency which may prevent the camera from taking quality or useful images. This can be prevented by radiometric calibration and having two cameras that downlink different pictures to the ground station for image filtering and post-processing.

Other concerns include thermal variations in space, which for this mission should not be detrimental for the cameras due to the achieved temperature ranges (see Chapter 13), and radiation in space. Further recommendations would be to look into a damping system with the possible use of springs or a silicone-based structure around the secondary payload PCB (where the cameras are connected to). Vibration tests should be performed to ensure their feasibility.

6.3 Acoustic Emission Testing

Acoustic emission refers to the generation of elastic sound waves following a redistribution of stress in a material after a force is applied on it. Acoustic emission sensors, which are available commercially off-the-shelf, are used to perform non-destructive tests to evaluate the structural integrity of the body by detecting defects such as cracks. [19]

Many of the AE sensors available today rely on the piezoelectric effect. The piezoelectric effect describes a phenomenon observed in dielectric crystals where electricity or electric polarity is generated in response to being acted on by a mechanical force. This effect is reversible, meaning the inverse event (a mechanical force arises in response to an applied voltage) is also true. Examples of materials that exhibit piezoelectric properties include berlinite, top and quartz. These sensors can be purchased as a COTS component.

Two applications for the AE sensors were considered. One is impact detection, where the sensors are placed on the aluminium panels that comprise the primary structure to identify cracks and other defects that arise due to collision with space debris. The other is condition monitoring, where vibrations emitted from moving components are measured to verify that it is working properly. In the following two sections, each application is elaborated upon further. This will be followed by an experimental set-up proposal designed to verify that the application would be reproducible on the spacecraft.

6.3.1 Condition Monitoring

It is estimated that approximately half of all CubeSats launched are unable to even partially fulfill their mission objective due to critical component failure. Of the remaining, 25% have partial mission success due to minor component failure. This means that only one in eight of all CubeSats launched enjoy full mission success. Nevertheless, even when a mission objective is achieved fully, the successful CubeSat is not necessarily devoid of defects. For instance, the Delfi-C3, having obtained its objective, carried a non-functioning radio transponder that causes complications. It can thus be concluded that the risks of a component either malfunctioning or becoming inoperative are extremely viable.

With this in mind, it is clear that inspection during the spacecraft's operation would be useful. Acoustic emission(AE) testing is a form of non-destructive testing, meaning that the structural component or system under observation is inspected for damages and imperfections without undergoing any impairment. During AE testing, the frequencies of the elastic vibrations that propagate through a body when it is subjected to stress are measured. These vibrations are in the ultrasonic range ($>$ 16 kHz). AE testing as a secondary mission objective will provide the ground station team with valuable information regarding the operation status of the instruments on board and/or the structural integrity of the satellite.

These sensors are designed specifically to discover structural defects early on, meaning that they have been used extensively in impact tests. On the other hand, their application in condition monitoring, which refers to the process of evaluating the health of a machine while it is in operation, is limited. For this reason, an experimental set-up has been proposed to deliver more insight on if and how AE sensors can be used to monitor reaction wheels. This particular component is chosen because it carries considerable importance since the primary mission objective of formation flying heavily relies upon this component.

Experimental Setup The experimental set up consists of two items: the acoustic emission (AE) sensor and a functioning miniature reaction wheel. Ideally, the reaction wheel should be mounted onto a flat board, as this is a reasonable representation of how the reaction wheels will be situated with respect to Phi's final configuration. The AE sensor will be placed on the board next to the reaction wheel. The experimental set-up is designed with the anticipation that the output of the acoustic emission sensor will vary with the reaction wheel's spinning velocity. It is also hypothesized that the data gathered will allow for insight on the health of critical components such as reaction wheels. The primary objective of this experiment, therefore, is to identify characteristic frequencies of the instrument when it is operating nominally at the intended rotational velocity range. It would then become possible to identify instrument error when measurements taken on board during operation differ significantly from these frequencies.

It is important to choose the appropriate sensor for this application. Van Allen, a company that produces and distributes AE sensors, recommend that sensors used for testing small components have a frequency range above 400 kHz [2]. Micro100 Sensor, produced by Mistras, was chosen because it has a measurable frequency range of 200-900 kHz and a mass of only 5 g.

Figure 6.3.1: Mistras Micro100 sensor /citeMistras

6.3.2 Impact Detection

Throughout the design of Phi, the threat posed by space debris was only acknowledged as a residual risk. Precautionary and\or protective measures specifically against space debris impacts were not implemented, considering its relatively small size and short mission duration. Therefore it is necessary that the risk of space debris collision throughout the mission is analyzed before considering the implementation of AE sensors for impact detection.

Table 6.3.1: Space debris flux

Height (km)	320	260	210
Diameter(m)	Flux (particles/m^2/year) at a specified altitude (km)		
10^{-5}	22.1	594	438
10^{-4}	22.1	18.1	9.57
10^{-3}	0.0373	0.0251	0.0217

A risk assessment was carried out with ORDEM2000, a space debris environment modeling software. This software distinguishes space debris from meteoroids, defining the former as man-made fragments deriving from defunct spacecraft, launch vehicles, etc. and the latter as naturally occurring particles. Because at altitudes below 2000 km the concentration of space debris significantly exceeds that of meteoroids, only space debris is considered. The desired output from this software is the flux rate, which is the number of particles of a specified size that will impact a spacecraft surface area of 1 m^2 over one year. To generate this output, the software requires the user to input the orbital characteristics of the mission (semi-major axis, eccentricity and inclination) and the mission year.

One limitation of this software is that its model only includes altitudes above 200 km, even though Phi is expected to be in operation as its orbit decays below this altitude. However, the general trend is that the concentration of space debris reduces along with altitude, implicating that the chances of collisions below 200 km altitude will be less than at higher altitudes. Thus, the satellite is less vulnerable to space debris at lower altitudes.

Table 6.3.1 displays the flux computations for circular obits at altitudes of 320, 260 and 210 km. Particles larger than 10^{-2} m were discarded, seeing as their flux rates were in the order of 10^{-6}, indicating that a collision with such particles will occur once every million years.

Particles with a diameter of 10 μm (10^{-5}m) produce resolvable craters on the satellite surface, and also disturb the satellite altitude and position. This would have a detrimental effect on achieving Phi's primary missionary objective of formation flying. Those with diameters of 100 μm can produce considerable damage on sensitive sensors and/or solar cells. Particles in these two size ranges will probably reduce the quality of the mission, but will not cause any critical failure to take place. Particles over a millimeter long will penetrate 3-5 mm wall thickness and form holes. A collision of this sort would significantly threaten the continuation of the mission. From these computations, it can be concluded that although the probability of catastrophic collision with an object having dimensions exceeding 1 mm is highly improbable, the spacecraft will still likely come into contact with smaller particles that will cause minor disruptions and/or damages.

Experimental Setup This section will first briefly summarize experiments carried out relevant to this application. Following this, the theory behind impact localization techniques is described. The section concludes with a detailed description of the experimental set-up.

Several tests have already been carried out to see if data from AE sensors can be used detect and locate an impact. Schafer and Janovsky investigated measurements made by AE sensors that were mounted on a 700 x 500 mm aluminium sheet with Fba 2 mm thickness. By using 6 sensors with frequency ranges between 100-450 kHz situated on the four corners and at both ends of the central axis, they were able to predict all impacts within an accuracy of 6 mm. Following these results, they were able to conclude that "ultrasonic transducers are suitable to perform the task of detecting hypervelocity impacts on the structure". In another experiment conducted by Prosser et al., low velocity (1.2 km s^{-1}) impacts were distinguished from high velocity(7 km·s) impacts using AE sensor data. They concluded that "AE signals for low and high velocity impacts were easily differentiated from their frequency content and modal analysis. Low-velocity impacts produced signal with little extensional mode and large flexural mode components".

To localize a source on a flat aluminium sheet, a minimum of three sensors are required. The positions of the i^{th} sensors are denoted by x_i and y_i, which are known. t_i describes the time at which the impact is detected by the sensor, which usually corresponds to when a peak amplitude is recorded or measurements cross the threshold frequency. The spatial coordinates x and y of the impact, as well as the time of its occurrence, t are the three values that must be calculated. To proceed with solving for these variables, it is neccessary to know the speed of wave propogation in the given material. In the previously mentioned experiment conducted by Schafer and Janovsky, the wave propagation speed through an Aluminum 7075 sheet (the material used to construct the external envelope of the satellite) was calculated to be 5360 m·s^{-1}. The product of the time lapse $(t_i - t)$ and the wave propagation speed is the perpendicular distance between the impact and the ith sensor. Using the Pythagorean theorem, three equations can be formed:

$(x - x_i)^2 + (y - y_i)^2 = c^2(t_i - t)^2$

Where c is the velocity of the sound wave. These three equations can be used to solve for the three unknowns corresponding to the position and time of the impact.

To test this application, three sensors can be mounted on the 4 longer panels that comprise the CubeSat structure. According to Vallen Systems, the frequency range of sensors used for structural integrity inspection should be 100-400 Hz. Therefore, Micro30F, a different AE Sensor from Mistras is used that has a bandwidth of 100-700 Hz. After these sensors are mounted, impacts can be simulated using either an impact tower or an automated hammer. The data gathered from this experiment will provide insight on the trend and deviations in data that would follow an impact.

Chapter 7
Guidance, Navigation and Control

This chapter will discuss both the powered formation flight as well as the secondary mission objective of formation flight using differential drag. Because the formation maintenance will be carried out in a very different manner, this chapter is divided into two parts so that each strategy can be discussed separately.

7.1 Powered Formation Flight

The primary mission objective of DelFFi is the demonstration of in-track formation flight. The easiest way of achieving maintenance of a specified along-track distance is by implementing propulsion. Relative motion can be achieved by placing satellites at different altitudes through thrusting. However, due to the low orbit and the resulting high densities (high compared to vacuum), use can be made of the differences in the decay rates to manoeuvre the two satellites to the same altitude.
This chapter will show different modes displaying different levels of autonomous formation flight in which the formation will be operated. Subsequently, the calculation for the ΔV budget will be shown. The next section will give insight into the behaviour of the formation and present the dependency on a variety of factors that tend to disperse the formations. After that, the main failure modes of the satellite and their impact on the mission objective of demonstrating formation flying will be discussed, together with alternative mission scenarios. To conclude, the simulation of a complete nominal mission scenario will be presented.

7.1.1 Modes of formation flying

There are different ways of communication to coordinate and control the two satellites. The following choices have to be made:

- Inter-satellite link vs use of ground station
- Distributed vs central control
- Location of command generation

The modes are visualized in Figures 7.1.1 to 7.1.4. The segment in bold generates the commands, red and blue arrows represent the flow of position information and commands, respectively. The four combinations have been chosen that can be performed one after the other in order of increasing complexity:

1. **Ground station control** The ground stations receives position information from the satellites at every overpass and propagates the position to calculate an estimate of when the next manoeuvre is necessary. This control scheme is the simplest one. The behaviour of the formation can be directly observed, anomalies can easily be corrected and commands computed by the software can be checked by an operator before the uplink. First manoeuvres can even be performed during an overpass. However, care has to be taken of the fact that there can be periods of no contact lasting up to 12 hours (as has been determined with STK). Therefore, the condition for sending a thrusting command is not that one satellite has reached the edge of the control box, but that it is expected to do so within the next interval of no contact.

2. **Centralised satellite control, ground station in the loop** One satellite collects position information from the other, propagates the position of both and issues commands. The data is relayed by the ground station. This is a step towards more autonomy by changing the center of control to the computer of the satellite while keeping the communication channel the same. It is a milestone towards the inter-satellite link because the formation does not rely on computations on the ground station any more.

3. **Centralised satellite control, inter-satellite link** This mode will make use of the same hardware as for the link to the ground station, but the signal will be very weak due to the limited power generation on the other satellite. Data will now be transmitted and received at a very low data-rate, while all other aspects stay the same. Navigation accuracy and reaction time of the formation can be traded for power. In terms of visibility, it is always possible to communicate with the other satellite, but updating the positions continuously is power-consuming. Decreasing the navigation accuracy theoretically decreases the data-rate, but the impact on the power budget is assumed to be low. A capable propagator would be beneficial to limit the amount of inter-satellite data-transfer.

4. **Distributed satellite control, inter-satellite link** Showing distributed control does not add at all to performing the science objective. However, this control scheme becomes convenient for formations with more than two satellites or swarms. This mode is more power consuming because both satellites have to transmit their positions while with centralised control one satellite is receiving most of the time, and only issues a commands from time to time. This does not influence the power budget since the EPS is sized for worst case. However, if the power during one stage of the mission becomes less than what the system has been designed for, the system might be able to use this excess power in another useful way (taking more pictures or making more acoustic data measurements and performing some processing to not influence the downlink data volume). The control strategy for distributed control can be kept to a large extent. The difference is that in this mode the processing has to be carried out by both satellites and that rather than detecting which satellite is at the lower altitude and depending on that issuing a command, the algorithm will first check it the satellite on which it is running is at the lower altitude than the other. If this is the case, it will calculate a possible manoeuvre, if not, it will not do anything and keep checking the condition in regular intervals.

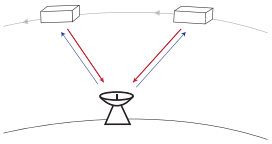

Figure 7.1.1: Ground station control, centralised command generation

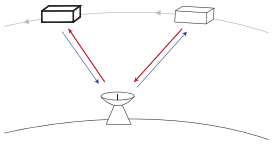

Figure 7.1.2: Centralised satellite control, ground station in the loop

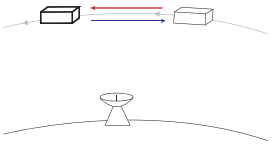

Figure 7.1.3: Centralised satellite control, inter-satellite link

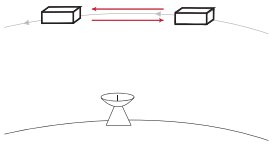

Figure 7.1.4: Distributed satellite control, inter-satellite link

The design options for GNC concern mostly the determination of position as well as the control actuation. The latter is so extensive that it is considered a separate subsystem and will not be treated here. Details can be found in Chapter 8.

7.1.2 Analysis of formation dynamics

Multiple aspects need to be taken into account when developing the control strategy. The following effects on the formation will be evaluated in this chapter:

1. Mass difference due to thrust history
2. Thrust accuracy
3. Initial altitude difference
4. Formation flying starting altitude
5. Spacecraft attitude errors
6. Control box size
7. Effect of osculation of semi-major axis due to J_2
8. Short term density fluctuations

The formation will be analysed mainly with respect to the following parameters:

1. Δ V
2. Number of manoeuvres
3. Total altitude loss
4. Average altitude difference

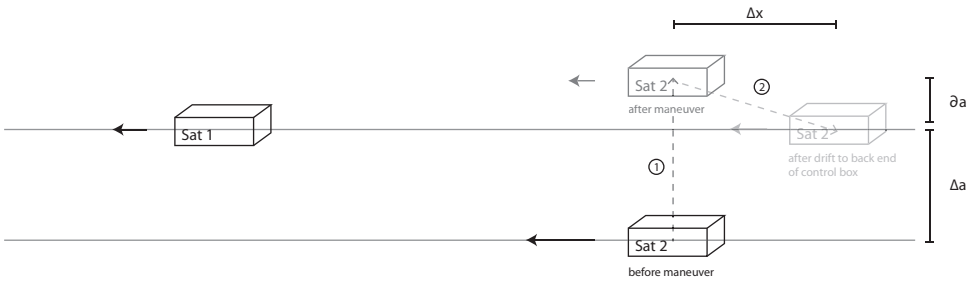

Figure 7.1.5: Formation maintenance manoeuvre using thrusters

Thrust history The thrust history influences the relative mass of the satellite and therefore the inverse ballistic coefficients. As the satellite expels propellant it becomes lighter and experiences higher deceleration due to drag which results in a higher decay rate. This effect is small as can be shown in the following example: the maximum possible difference in mass is the mass of the expelled propellant which is 88 g as will be shown in Chapter 8. An extreme scenario would be if one of the satellites made a manoeuvre using all of the propellant immediately after deployment. In this case, the inverse ballistic coefficient changes by 0.000297 which translates to a difference in lifetime of 1.5 days. This scenario is unlikely to occur and under nominal conditions, both satellites will perform manoeuvres during the formation flying period, therefore this effect can be neglected, especially for time intervals much shorter than the mission lifetime.

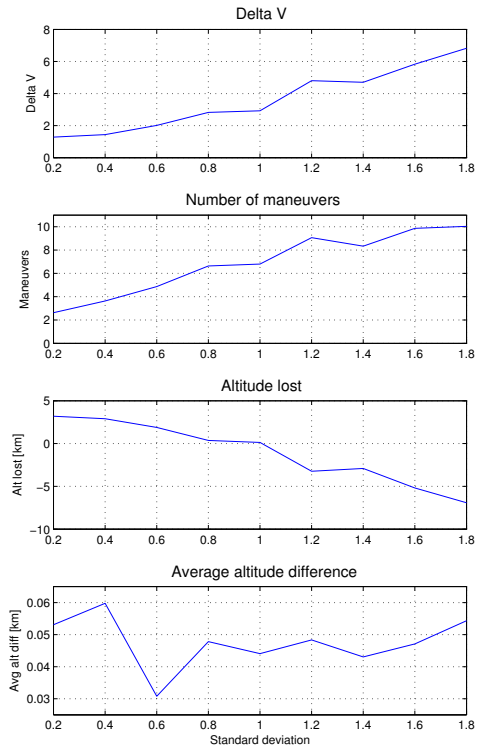

Figure 7.1.6: Effect of thrust accuracy on the behaviour formation

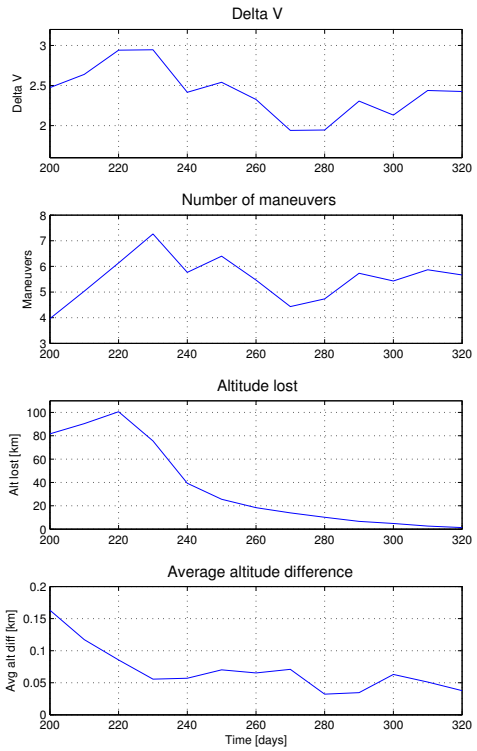

Figure 7.1.7: Effect of the different initial altitudes on the formation

Thrusting accuracy In this context, the thrusting accuracy relates to the actual ΔV delivered by the propulsion system as opposed to the commanded ΔV. This is related to the accuracy of the thrust, the pointing error during thrusting and the duration of the manoeuvre. The latter varies significantly depending on the thrust level chosen, and is shown in Figure 7.1.13 for both feasible thrust levels. The effect of thruster inaccuracies is shown in Figure 7.1.8 for 5 % and 10 % deviation in thrust level from nominal. Figure 7.1.9 shows the needed ΔV for a given altitude difference as a function of mean altitude of the formation. For small altitude corrections, this can be considered independent of formation altitude.

The effect of thrusting accuracy was incorporated in the formation flying simulation in the following manner: when

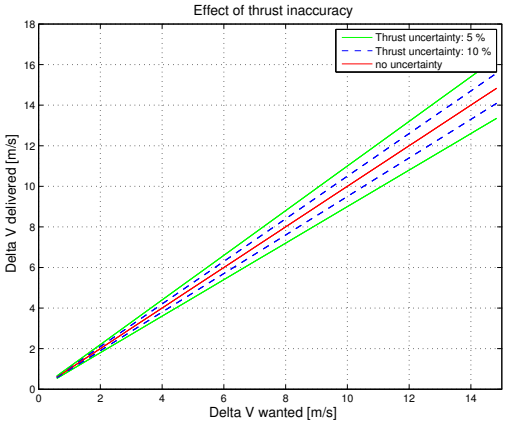

Figure 7.1.8: Effect of thrust uncertainty on the delivered ΔV as opposed to the commanded ΔV

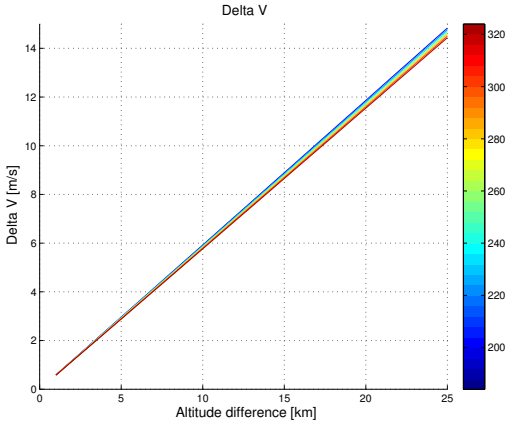

Figure 7.1.9: ΔV needed to achieve a certain altitude change as a function of initial altitude

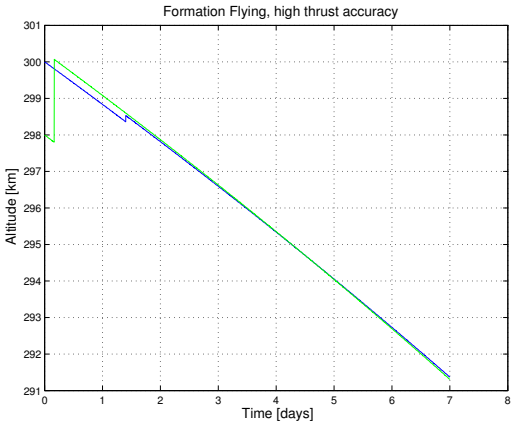

Figure 7.1.10: Satellite altitudes in formation with high thrust accuracy (Standard deviation: 0.1)

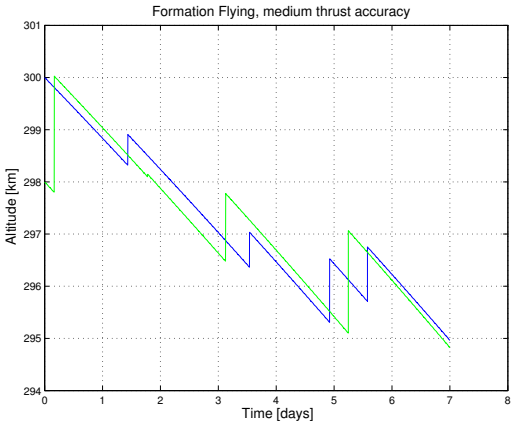

Figure 7.1.11: Satellite altitudes in formation with medium thrust accuracy (Standard deviation: 0.8)

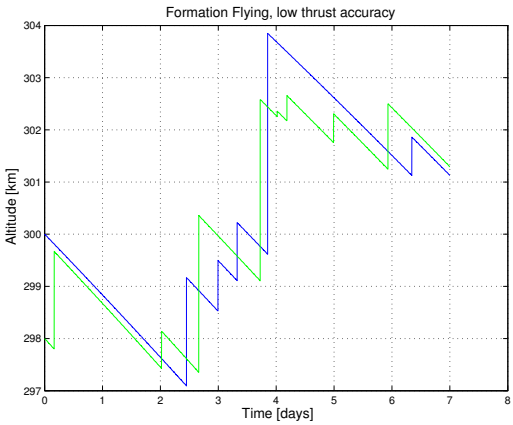

Figure 7.1.12: Satellite altitudes in formation with low thrust accuracy (Standard deviation: 1.5)

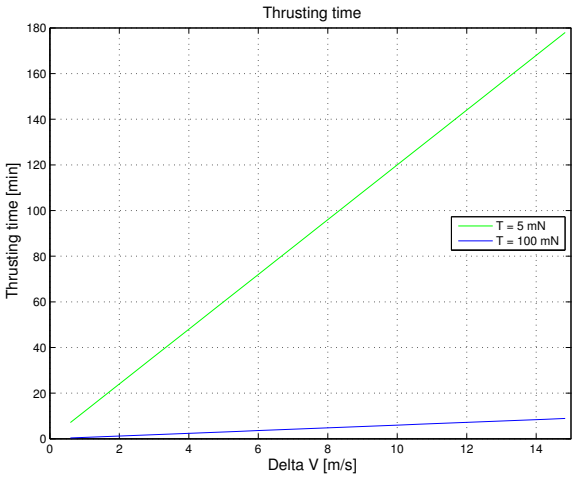

Figure 7.1.13: Thrusting time as function of required ΔV

one satellite reaches the front end of the control box, it will be set to the altitude of the other satellite plus an offset that is governed by a Gaussian distribution. However, after the calculation of the offset a check has been implemented to verify that the new altitude is actually above the initial altitude. If this is not the case, a new offset is calculated. It is not claimed that this probability distribution accurately represents the behaviour of the thruster, but aims at identifying general trends due to the uncertainty in this parameter. This is due to the fact that information on the thrust accuracy of the T3-cold gas thruster is not available.

Figures 7.1.10, 7.1.11 and 7.1.12 show the behaviour of the formation for standard deviations of 0.1, 0.8 and 1.5. It can be seen that this translates into altitude deviations of 0.2 to 1.5 km from nominal conditions, which can be translated into an error in delivered ΔV with Figure 7.1.8. It can be seen that at high thrust inaccuracies the difference

in altitude between the two satellites after the manoeuvre leads to relative drift rates that are so high that frequent manoeuvring is necessary. At some point, the entire formation will have the tendency to increase the altitude. This is shown more clearly in Figure 7.1.6, which shows different parameters characterising the behaviour of the formation. Subfigure 3 shows the altitude lost, which relates to the average altitude at the end of the specified timespan as opposed to the initial altitude. It can be seen that above a standard deviation of 1 the altitude lost becomes negative, meaning that the height of the formation has increased. This undesirable effect is reflected even more clearly in the ΔV budget, which almost doubles when going from a standard deviation of 0.2 to 1.
In conclusion, the standard deviation describing the uncertainty in the thrust level should definitely be less than 1, but ideally below 0.6 to limit the ΔV that is needed purely due to this uncertainty. It is recommended that tests should be conducted to fully understand the behaviour of the thruster, or to investigate the possibility of making guidance system closed-loop. The thruster could be set to a low thrust level and during thrusting the increase in semi-major axis could be monitored with the GPS receiver and compared to the expected one.

Initial altitude difference The initial altitude difference relates to the difference in initial conditions of the satellites after a manoeuvre. This uncertainty originates from thrust errors and navigation accuracy. This paragraph is strongly related to the previous one, because thrust uncertainty induces an undesirable altitude difference, and can be seen as a more detailed view on the dynamics of formation maintenance and give insight into the exact manoeuvres that will be conducted. Figures 7.1.14 to 7.1.17 show the times in between two manoeuvres as well as the relative altitude at the time when one satellite reaches the edge of the control box as well as the dependency of these parameters on altitude.
It can be seen that the inter-maneuever time as well as the relative altitude at thrusting increases with decreasing initial altitude difference. This is expected because the closer the radial distance of the satellites in the beginning, the smaller the relative mean motion and the more time it will take to accumulate differences in argument of latitude. The longer the inter-manoeuvre time, the more altitude is lost. From Figure 7.1.16 it can be seen that the satellite will never reach the top or bottom side of the control box because the relative altitude remains below 100 km at all times, even at extremely low altitude and high control accuracies. This simplifies the control strategy in the sense that every manoeuvre will have to correct the same along track separation, which is half of the side of the control window.

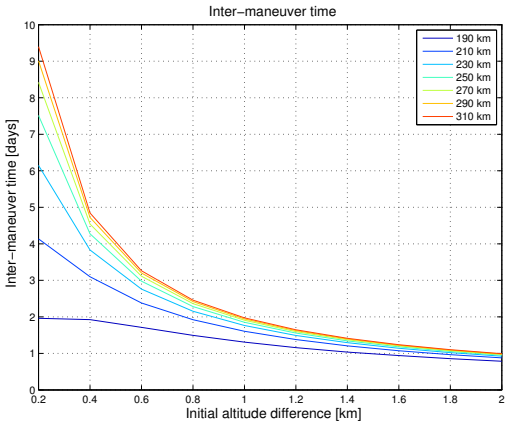

Figure 7.1.14: Inter-manoeuvre times for initial altitude differences from 0 to 2 km

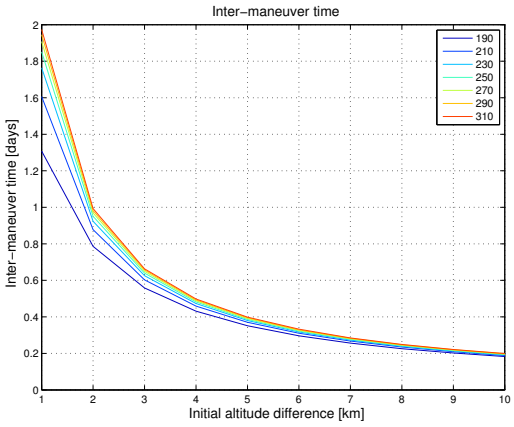

Figure 7.1.15: Inter-manoeuvre times for initial altitude differences from 0 to 10 km

From Figure 7.1.14 it can be concluded that the formation flying period should definitely be extended to more than 7 days when the control accuracy in radial direction decreases below 800 m. In that case, the inter-manoeuvre time for the high altitudes becomes comparable to that of the entire formation flying period. It is not possible to give a definite minimum of manoeuvres that should be carried out in order to "demonstrate formation flying", but three manoeuvres are considered to be an absolute minimum. However, if the modes of different complexity are all to be carried out, then the minimum amount of manoeuvres has to be multiplied by the number of modes to be performed.

The extension of the formation flying period is mandatory for control accuracies below 800 m, but such an extension is the only sensible way of carrying out the mission since the ΔV budget is 15 m/s irrespective of the control accuracy, and it is recommended to use all of it over the course of the mission, not only to investigate the behaviour of the formation, but also to increase the lifetime of the satellites. There are two counteracting effects when performing manoeuvres: the increase in decay rate due to the lower mass after propellant expulsion and the increase in altitude and therefore longer lifetime of the manoeuvre. As has been shown previously, the maximum decrease in lifetime due to the first effect is 1.5 days for a velocity change of 15 m/s at beginning of life, while a velocity change of 2 m/s at 300 km altitude will increase the lifetime by three days. Therefore, it can safely be concluded that it is always beneficial to perform formation flying as long as possible.

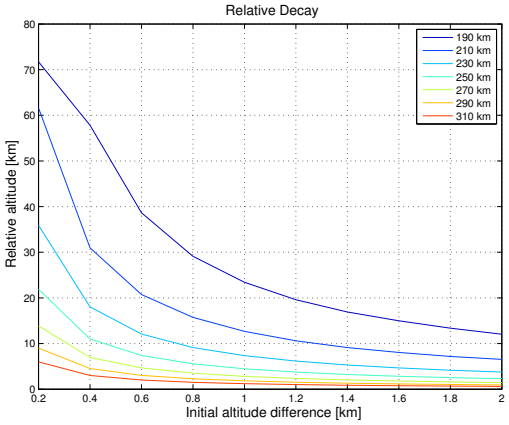

Figure 7.1.16: Relative altitudes at manoeuvre for initial altitude differences from 0 to 2 km

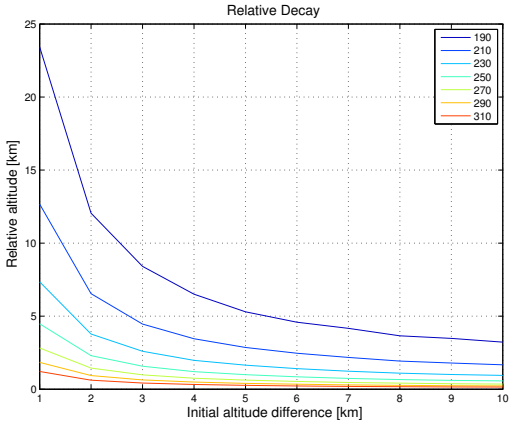

Figure 7.1.17: Relative altitudes at manoeuvre for initial altitude differences from 0 to 10 km

Another effect that should be noted is that the inter-manoeuvre times for very low control accuracies converge to the same value of 0.2 days for all altitudes. At short inter-manoeuvre times, the control strategy should take into account the eccentricity induced by thrusting. Care should be taken that manoeuvres are carried out at opposite points in the orbit because increasing the velocity at only certain arguments of latitude will make the orbit eccentric. This will decrease the lifetime because for the same semi-major axis, a satellite in an eccentric orbit will experience a higher energy loss than a circular orbit due to the lower altitude at perigee. This effect can be neglected for long inter-maneuever times because the atmosphere will has a circularising effect on the orbit. It could also be considered to first perform half of the change in ΔV, waiting until the argument of latitude increases by π and then performing the second half of the manoeuvre.

These graphs have been generated for infinite control accuracy in along-track direction. The effect of errors in this direction are equivalent to a difference in control window size and do not impact the magnitude of drift in along-track direction. The impact of this parameter is more intuitive and of less importance and is not investigated in this report.

Formation flying starting altitude In the initial phase of the project it has been agreed with the Delta group that formation flying should be carried out immediately after LEOP. The justification was based on the assumption that the lower drag forces at that altitude would make more manoeuvres per time interval necessary. Also, the ΔV needed to achieve a certain altitude change increases with decreasing altitude as shown in Figure 7.1.9. However, both effects are quite small as can be seen in Figure 7.1.7: both the needed ΔV and the amount of manoeuvres display small variations, but no clear trend is observed. The difference in starting altitude is reflected in the altitude lost over the entire formation flying period (which in this case has been set to 7 days), which was expected because of the exponential encrease in experienced drag forces, but also in the average altitude difference between the satellites. The latter shows that the relative decay rates increase at lower altitudes, but the effect is not pronounced enough to display a significant effect in the ΔV budget. However, it might still be desirable to keep the relative semi-major axis low: making the tracks of the satellites as close as possible would enhance the science return from the atomic oxygen data. The more the tracks are identical, the more do the differences in the atomic oxygen data reflect the processes in the atmosphere and the less is the bias due to the difference in location at which the measurements are taken. The measurements are of relevance not only to the science community, but also to similar missions because short-term atmospheric processes also influence the relative decay rates, as will be explained below.
Another justification for the scheduling of the formation flight at the beginning of the mission to increase the formation flying time in case of the ADCS failure of one satellite. In that case, high relative decay rates will occur, which will be lower at higher altitudes.

Spacecraft attitude errors As has been shown in Section 2.4.2, the drag coefficient changes with the attitude, see Figure 2.4.8. To evaluate the long term effects of the spacecraft attitude motion, the assumption has been made that the spacecraft oscillates around the velocity vector in such a way that pitch and yaw angle can be described as by sine curve with an amplitude of the pointing accuracy. By comparing Figures 7.1.18 and 7.1.19, it can be seen that the average inverse ballistic coefficient for 2° pointing accuracy does not differ much from that during nominal pointing. For 10°, the difference is to nominal pointing 0.00106. The worst case relative decay due to this effect can be calculated by assuming one satellite remains in nominal pointing attitude at all times, while the other one remains at the worst case deviation from the velocity vector. At 300 km altitude, this translates to an inter-manoeuvre time of 3.5 days. However, this is a worst case that is unlikely to occur because the attitudes of both satellite will oscillate. The effect becomes more clear when looking at Figure 7.1.20: increasing the difference in inverse ballistic coefficient will increase the ΔV needed and as a result the altitude lost will decrease. This could be important for future similar missions for *in-situ* atmospheric measurements with requirements on how the data-points should be distributed over

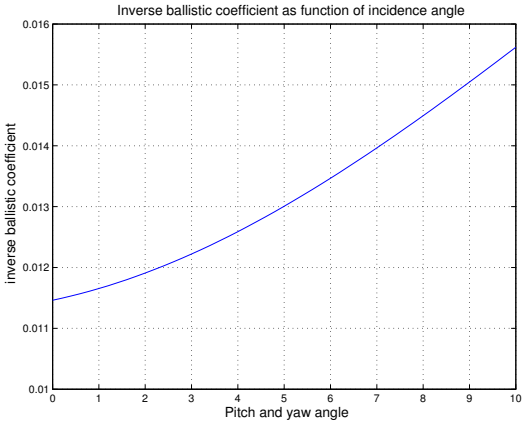

Figure 7.1.18: Dependency of ballistic coefficient on pitch and yaw angle

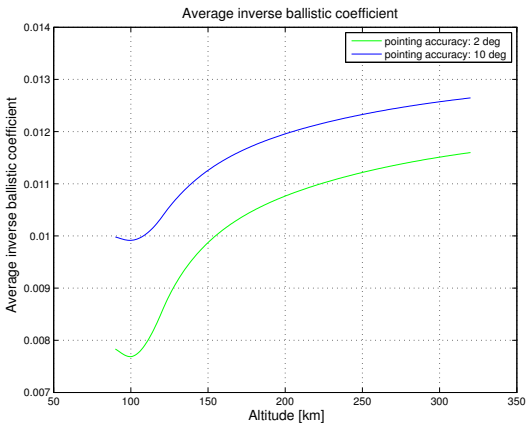

Figure 7.1.19: Effect of starting latitude on the relative altitude

the altitude range to maximise science return. To obtain more valuable data on temporal resolution of atomic oxygen as well as its dependency on altitude, the relative ballistic coefficient should be minimised as much as possible. The average altitude difference will be low but the altitude lost during two manoeuvres will be high, leading to an even distribution of thrusting times over the entire altitude range. This is scientifically more interesting than performing all manoeuvres at high altitude and after that ceasing thrusting activity an letting both satellite decrease very fast. However, this is a requirements that is in conflict with the lifetime extension. A manoeuvre is more effective the higher the altitude (see Figure 7.1.9 in terms of increasing the altitude and therefore the lifetime. However, the lifetime requirements will probably be derived form the expected science return, so reduced lifetime can be traded to some extent against a better radial data-point distribution.

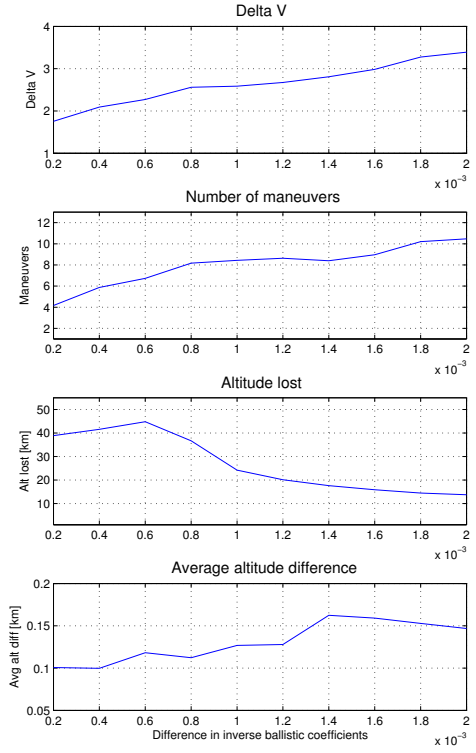

Figure 7.1.20: Effect of the difference in ballistic coefficients on the formation

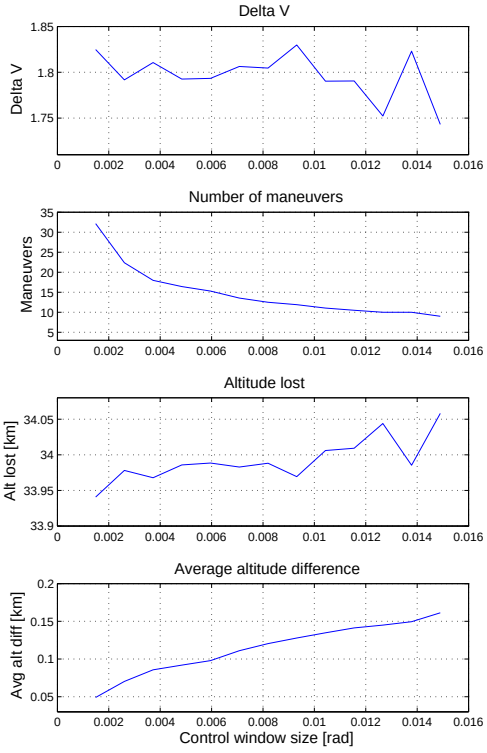

Figure 7.1.21: Effect of control window size on the behaviour of the formation

Control box size In this paragraph, the control box denotes a region, the boundary of which will determine when a manoeuvre takes place. Of course, it is possible to have a large control window and a control strategy that keeps it in a region that is smaller and inside of the control box, but for simplicity of terminology the control box edge will determine the manoeuvre. The effect of choosing a size of the control box is twofold: a smaller control window

necessitates fewer manoeuvres, but this comes at the price of a loss in lifetime. The longer a satellite decays before thrusting, the higher the drag force it will encounter, as opposed to if a smaller manoeuvre was performed earlier. Designing a control strategy for minimum atmospheric loss is opposite to the aim of keeping the amount of manoeuvres at a minimum, because often scientific data is considered corrupted when measurements are taken during thrusting. Also, the propulsion system is expected to be less efficient and less accurate at low thrust levels and short thrusting times, because of the uncertainties of the mass flow rates through the valve. As has been explained previously, no information is available on this and testing is necessary to quantify this effect.
Figure 7.1.21 shows the effect of the control window size on various parameters showing the behaviour of the formation. The control window has been varied from 100 to 10 km, but no effect can be seen in the ΔV budget. The amount of manoeuvres performed increases drastically, and a small trend in the altitude loss reflects the lower effectiveness of the same amount of ΔV when the control window is increased.

Effect of osculation of semi-major axis due to J_2 Gravity is a conservative force and does not directly change the energy of the orbit. However, the oblateness of the Earth causes the semi-major axis to vary sinusoidally around its mean value over the course of the orbit with a period of half that of the orbital period. Over the equator, the osculating semi-major axis will reach a minimum, while the maximum occurs over the poles. The half-amplitude of this motion is approximately 10 km, as has been determined with STK, and remains almost constant over a large part of the altitude range. To be able to account for this effect, a second fictitious altitude is calculated at each time-step: the mean semi-major axis is used to determine energy and velocity, but the density to calculate the drag force will take as an input altitude the mean osculating element with a superimposed sine function:

$$a_{osc} = a_{mean} + 10 \sin\left(2\theta + \frac{\pi}{2}\right) \tag{7.1.1}$$

The effects of this can be seen in Figures 7.1.22 to 7.1.25 which show the relative altitudes of the two satellites for a period of 10 days at a starting altitude of 10 km. It results in a relative altitude difference that is purely due to the initial conditions: at the start, one satellite will be travelling in a region of higher density, and will decrease in altitude more than the other. In the next timestep, the satellite that decreased more will encounter an even higher density and the radial distance increases further. The effect reverses every quarter of an orbit since it is always the satellite that is closer to the equator that experiences higher drag. It has been found that the effect depends on the initial argument of latitude of the formation as well as on the the inter-satellite spacing. Figures 7.1.22 to 7.1.25 show this dependencies for two datasets where both parameters have been varied from 0 to 160° 8 to 160°, respectively. The plots only show every 200th timestep to make the visualisation more clear. Figures 7.1.24 and 7.1.25 do not reflect the actual behaviour accurately since the low frequency periodic motion after day two is actually fully covered by noise of equal amplitude. The graphs only serve to show the variations in steady-state value for different initial conditions. The effects are quite complex, and a full analysis is out of the scope of this project. This is because the effect of varying altitude is coupled with the even stronger effect of the density varying over the latitude. At 300 km the variation in density due to a 10 km change in altitude is $0.375510^{-11} kg \cdot m^{-3}$ whereas the density over the north pole is $0.846510^{-11} kg \cdot m^{-3}$ higher than over the south pole. However, it can be concluded that the relative semi-major axis varies in a sinusoidal manner with a period close to the orbital period, but also experiences a periodic variation on the scale of a day and a secular drift such that the mean value approaches a steady value after two days. The sign and magnitude of this steady-state value is strongly dependent on the initial condition and has an absolute value of below 40 cm. It can It can therefore safely be neglected.

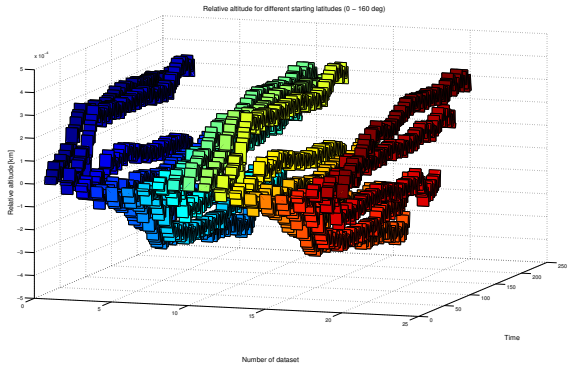

Figure 7.1.22: Effect of starting latitude on the relative altitude

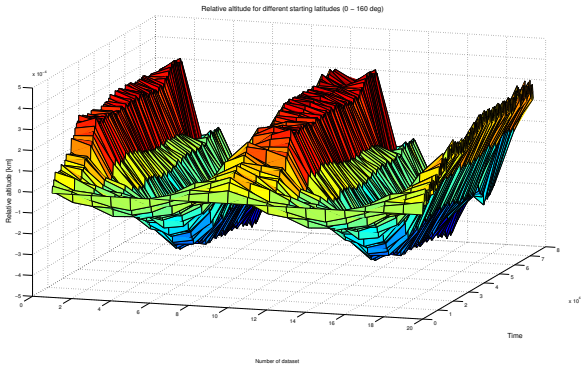

Figure 7.1.23: Effect of starting latitude on the relative altitude

Short term density variations The problem encountered when trying to evaluate this effect is that the data needed to predict it is not available at present and its acquisition is the primary mission objective of QB50. There have not been previous formation flying missions at similarly low altitudes. Therefore, an upper bound on the variability can be set by using data from CHAMP which represents time-scales of approximately 40 s, [52]. This is a little shorter than

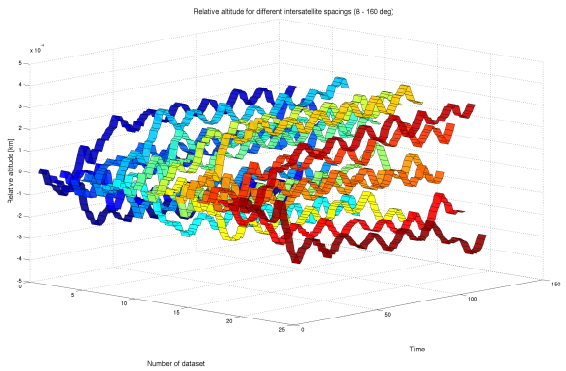

Figure 7.1.24: Effect of satellite spacing on the relative altitude

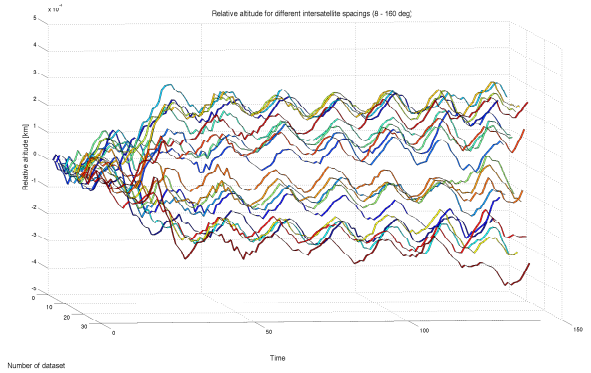

Figure 7.1.25: Effect of starting latitude on the relative altitude

the relevant timespan, but the satellites are likely to undergo the same variation and the observed effect is expected to be much lower. Data from the CHAMP satellite suggests that on average the variability on the density is 5 % and 15 % during a geomagnetic storm and should be treated as a theoretical upper bound. From Figure 7.1.26 it can be seen that the relative density difference can have a large effect on the inter-manoeuvre time; a decrease in 50 % is possible. However, as has been explained above it is impossible to know how much this effect as predicted from CHAMP data has to be scaled down. This uncertainty will have implications on how long the formation flight will in the end be conducted, but has not direct implications on the design. It should also be noted that this disturbance is expected to average out.

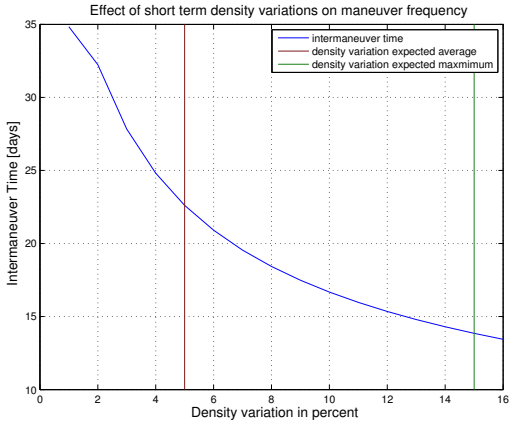

Figure 7.1.26: Dependency of inter-manoeuvre time on short term density variations

7.1.3 Failure modes

The following paragraph lists failure modes of the GNC as well as those of other subsystems that are not catastrophic and can be mitigated by reconsidering the orbit control strategy:

- **GPS receiver hardware failure** This will necessitate position determination from the ground. The ground station can track the satellite and/or uplink TLE to allow the OBC to propagate the position. Formation flight can still be carried out at reduced position accuracy.
- **Propulsion system failure of one satellite** As long as the ADCS of that satellite is still working, the drag experienced by this satellite is not greater than nominal. Formation flying can still be demonstrated for more than a week. It is recommended to reduce the pointing accuracy of the satellite that has not failed to 10°. This will lead to higher descent rates on the satellite with the operational propulsion system, which can increase its altitude and at the same time adjust the along-track separation without having to rotate the satellite to reduce the velocity by thrusting. The process of frequent rotation, stabilisation and return to nominal orientation adds complexity and is time consuming. The latter will lead to gaps in coverage of the data gathered by FIPEX. A note shall be made on the aerodynamic torques: although the orientation of 180° from nominal is unstable due to aerodynamic torques, these have been shown to be negligible at the altitudes at which formation flight will be performed (see Section 2.4.2).
- **Failure of the ADCS to point the GPS antenna to zenith** GPS data cannot be received regularly. The ground operator may choose to uplink TLE instead or carry out manoeuvres whenever the position data allows this, and not when the edge of the control box is reached.

- **Complete ADCS failure of one satellite** The ΔV budget is sized to account for this. The manoeuvres will be carried out by the satellite with the operational ADCS. Due to the increased drag coefficient, the failed satellite will experience a significantly higher decay rate and the operational satellite will have to follow this is feasible from the point of view of the ΔV budget, but would result in an unsatisfactory reduction in lifetime. It should be considered to shorten the time during which formation flying with the failed satellite is demonstrated and consider an alternative mission scenario, such as overtaking the satellite and acquiring a new position relative to it or even to perform formation flying with another (uncooperative) satellite form the QB50 mission.

Prior to this, the results of a simulation of the behaviour of the formation at 300 km altitude will be presented. The simulation includes aerodynamic drag as well as J_2.

7.1.4 Delta V budget

The ΔV budget is composed out of two parts, the acquisition of the first formation as well as the formation maintenance.

Formation acquisition manoeuvre The best as well as the worst case are considered in the following. The CubeSats will be deployed into orbit at the same altitude with a temporal spacing of 10 - 20 seconds with a velocity of 1 - 2 m/s. In the best case, Phi and Delta will be the first and last ones to be injected. This gives the satellites an initial along-track separation of 2 km. If they are injected immediately after their relative distance is so small that it can be assumed to be zero. To acquire the desired formation, either the trailing satellite has to move to a lower orbit by decreasing its kinetic energy or the leading satellite has to increase its kinetic energy to move to a higher orbit. Both options will lead to a relative motion of the two satellites that will decrease the angular distance between them. For the actual manoeuvre, it is recommended to keep remaining propellant mass in the two satellites equal to ease an extension of the formation flight period. Both satellites shall raise their orbits to increase their lifetime at the same time. However, the calculations will be made assuming only one satellite is able to perform a manoeuvre to account for the thruster failure of one of the satellites.

The velocity change needed is dependent on the time available for the acquisition manoeuvre because the higher the relative semi-major axis, the faster the relative motion. The needed altitude difference can be found as a function of the time available for the drift phase.

$$\Delta\theta = (n_2 - n_1) \cdot T_{drift} \tag{7.1.2}$$

where $\Delta\theta$ is the change in angular separation that is achieved with the manoeuvre, n is the mean motion and T_{drift} is the time between the two thruster firings. Inserting expressions for the mean motion

$$n = \sqrt{\frac{\mu}{a^3}} \tag{7.1.3}$$

the following equation is obtained:

$$\Delta\theta = \left(\sqrt{\frac{\mu}{(a_i - \Delta a)^3}} - \sqrt{\frac{\mu}{a_i^3}} \cdot T_{drift} \right) \tag{7.1.4}$$

Because the manoeuvre is a low-thrust manoeuvre, the change in velocity is the difference in the orbital velocities of the initial and final orbit:

$$\Delta V = 2 \cdot \left(\sqrt{\frac{\mu}{R_e + h_i - \Delta a}} - \sqrt{\frac{\mu}{R_e + h_i}} \right) \tag{7.1.5}$$

Solving for the best and worst case scenario the needed ΔV as a function of time available for acquisition is shown in Figure 7.1.27. As expected, it can be seen that the difference between the best and the worst case scenario is negligible since it amounts to a difference of only 0.005 m/s.

The longer the time, the smaller the altitude change and therefore also the velocity change needed to obtain the spacing of 1000 km. The time available for the manoeuvre is not known, but the time for the LEOP is set to 9 days. The satellite is required to detumble within 2 days. The first manoeuvre can be carried out immediately after the satellite is stabilised, seven days are left for the formation acquisition manoeuvre. The requirement for the velocity change is then 1.2 m/s.
Note that the duration of the LEOP was set after an initial estimation of the detumbling time which was 5 days. Only after this the requirement on the detumbling time was taken into account. This should translate into a shorter LEOP, but the requirement was fixed in conjunction with the Delta group and is now considered final.

Formation maintenance manoeuvre In the following, the mathematical formulation of a manoeuvre for arbitrary initial conditions will be explained. It will be shown for the case in which the trailing CubeSat has a lower altitude, but the opposite case can be derived in a similar manner.

It has been found that for long time spans the along-track drift is significantly higher than the drift in semi-major axis. The inverse is true for a single orbit, but small differences in mean motion due to different altitudes cause the along-track distance to vary rapidly when time spans of a few orbits or more are considered. In the next section it will be shown that every manoeuvre will be triggered by the CubeSat reaching either the back or the front end of the

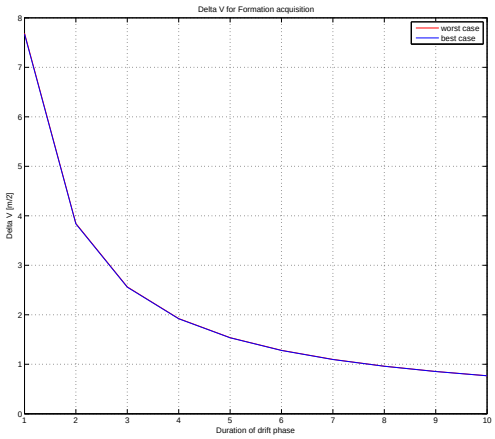

Figure 7.1.27: ΔV for formation acquisition

control box. The latter will be considered here. For most science missions it is necessary to maximise the time between two thrusting periods because only then is the payload data meaningful. Although there is no such requirement for the QB50 payload, it is considered of scientific value to demonstrate such a guidance algorithm for implementation on future science missions.

The control strategy is shown in Figure 7.1.5 follows. Initially, the trailing CubeSat (2) is at an altitude Δa lower than the leading CubeSat (1). Therefore, it approaches CubeSat (1) until it reaches the front end of the control window. The thruster is fired to raise the orbit to by an altitude $\Delta a + \partial a$. This causes CubeSat (2) to drift away from CubeSat (1). ∂a is chosen in such a way that the CubeSat will just touch the back face of the control box during descent at the moment when it is at the same altitude as CubeSat (1). It is assumed that the expulsion of propellant during the manoeuvre is not enough to change the sign of the relative inverse ballistic coefficient, meaning the CubeSat that had a tendency to loose altitude more quickly before the manoeuvre will retain that tendency after the manoeuvre. This can be described by the following equations:

$$T_{drift} \cdot n_{rel} = \Delta\theta \tag{7.1.6}$$

where T_{drift} is the timespan from the end of thrusting to the time where CubeSat (2) touches the back end of the control box, n_{rel} is the relative mean motion and Δx is the along-track distance track distance travelled during T_{drift}, which is 100 km.

$$T_{drift} \cdot \left(\frac{da}{dt}\right)_{rel} = \partial a \tag{7.1.7}$$

where $(\frac{\partial a}{\partial r})_{rel}$ is the relative decay rate.

$$\frac{da}{dt} = -\frac{a^2}{\mu} \cdot B \cdot \rho \cdot F \cdot v^3 \tag{7.1.8}$$

Combinig those equations and inserting 7.1.8 for the decay rate yields

$$\partial a = \frac{\Delta\theta(\sqrt{(a_1 - \int_0^t((\frac{da}{dt})_1\, dt)\cdot\mu)\cdot\rho_1\cdot F\cdot B_1} - \sqrt{(a_2 - \int_0^t((\frac{da}{dt})_2\, dt)\mu)\cdot\rho_2\cdot F\cdot B_2})}{\int_0^{T_drift} \sqrt{\frac{\mu}{a_1 - \int_0^t(\frac{da}{dt})_1 dt)^3)}} - \sqrt{\frac{\mu}{a_1+\Delta a+\partial a} - \int_0^t(\frac{da}{dt})_2\, dt)^3}} \tag{7.1.9}$$

This equation has been solved by running the simulation for successfully increasing ∂a and checking the angular distance between the satellites at the time they are at the same altitude. The ∂a that yields an angular distance closest to the width of the control window is considered optimal. For nominal conditions (difference in inverse ballistic coefficients of 0.001 and at an altitude of 300 km), the value for this parameter has been determined to be 0.37 km. The corresponding time until the two satellites reach the same altitude is 80 hours.

ΔV Budget The duration of the powered formation flight which is to be performed directly after the LEOP has been set to 7 days. The satellite will be designed such that even if the attitude control of one satellite fails, formation flight can still be demonstrated for one week. This results in a ΔV requirement of 7.4 $m \cdot s^{-1}$. The acquisition of the formation has been shown to add 1.2 $m \cdot s^{-1}$. This results in a total ΔV requirement of 8.6 $m \cdot s^{-1}$.

The agreed upon requirement for the total velocity change is 15 $m \cdot s^{-1}$.

7.1.5 Nominal mission scenario

Figure 7.1.28 and illustrates the proposed nominal mission scenario. It includes a variety of different manoeuvres, configurations and communication architectures in order to perform as much technology demonstration as possible within the 15 $m \cdot s^{-1}$ budget. Detailed information can be found in Table 12.1.2.

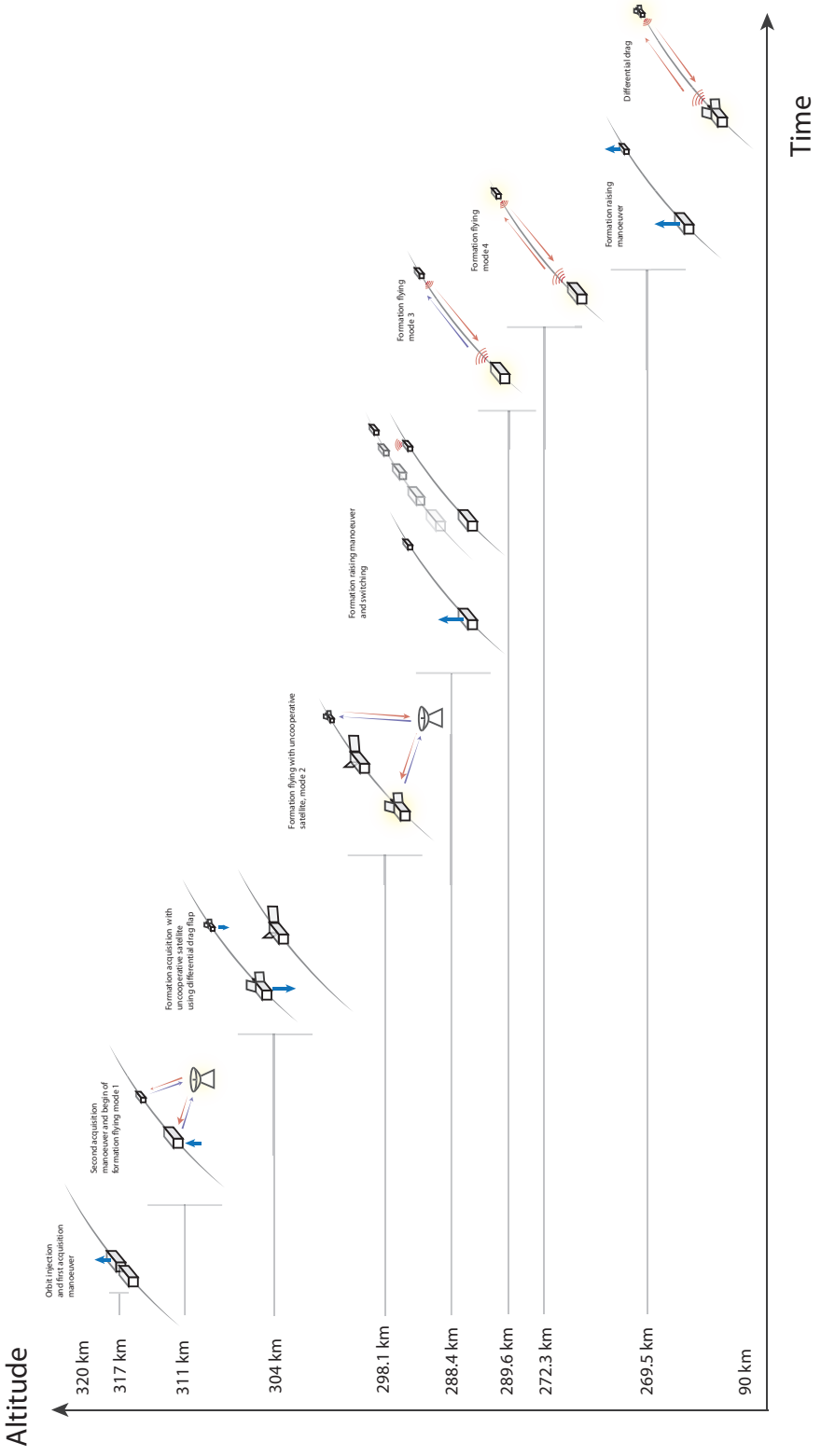

Figure 7.1.28: Illustration of nominal mission scenario

Table 7.1.1: Nominal mission scenario

Description	Initial altitude [km]	Duration [days]	ΔV $[m \cdot s^{-1}]$
Tumbling (LEOP I)	320	2	0
Acquisition (LEOP II)	317	7	0.6
Formation Flying mode 1	311.5	7	0.25
Formation acquisition with uncooperative satellite	304.3	7	0
Formation flying with uncooperative satellite, mode 2	298.1	7	0.8
Formation raising manoeuvre and position interchange (ISL testing)	288.4	1.3	6
Formation flying mode 3	289.6	7	0.9
Formation flying mode 4	272.3	7	1.1
Formation raising II and differential drag	269.5	9	5

- **Detumbling (LEOP I):** After orbit injection, the satellite will be tumbling and will have to recover from the specified tip-off rates within two days. Due to its rotation rates, the satellite will have an inverse ballistic coefficient that is almost twice its nominal value.
- **Acquisition (LEOP II):** As soon as the satellite is stabilised and the propulsion system check-out is performed, the first formation manoeuvre is performed. This is followed by a 7-day drift phase after which the second manoeuvre is performed.
- **Formation Flying mode 1:** The first mode is performed. Commands are generated at the ground station.
- **Formation acquisition with uncooperative satellite:** Both satellites descend to form a formation with three satellites, one of which is an arbitrary uncooperative CubeSat from QB50. Such a formation will be of high scientific value, since three measurements will be taken with a temporal spacing of 2 min between successive passes. The altitude of the uncooperative satellite has been obtained assuming it detumbles within two days and after that operates at a pointing accuracy of 10°. The altitude change is negative and quite significant and is achieved by making use of the flaps for differential drag. Although this is not yet differential drag formation flight, the achieved decay rates with the flaps can be compared to the expectations.
- **Formation flying with uncooperative satellite, mode 2:** The second mode is performed in the three-satellite formation. Since the command generation is still centralised, adding another satellite does not change the control strategy except for the fact that the Phi and Delta have to change position with respect to the third one.
- **Formation raising manoeuvre and position interchange (ISL testing):** The formation is raised to increase the lifetime and at the same time the positions between leading and trailing satellite are interchanged. This will demonstrate that the formation is able to reconfigure itself, but is also beneficial for the testing of the inter-satellite link.
- **Formation flying mode 3:** Formation mode 3 will begin when the satellites are at the closest distance. The performance of the inter-satellite link will then be monitored as the satellites drift apart to their nominal positions. This mode will be flown for 7 days.
- **Formation flying mode 4:** Another 7 days are allocated to formation flight using an inter-satellite link, this time using distributed control.
- **Formation raising and differential drag:** A last second formation raising manoeuvre will be carried out to maximise the residual lifetime. After that differential drag formation flight will be carried out until communication to the ground station ceases due to the bending of the antennas due to aerodynamic forces. The estimated amounts of possible differential drag manoeuvres possible its 4.

In this scenario, the total lifetime is 50 days. This means that the requirement on the lifetime as given by QB50 is not satisfied. However, is should be noted that the main reduction in lifetime is due to the formation acquisition with an arbitrary QB50 satellite with no propulsion and low pointing accuracy, which will already in the first part of the mission be at a significantly lower altitude than the DelFFi formation. Due to the low pointing errors of Phi and the use of propulsion which will be primarily used to increase the orbital velocity, there is a high probability that it will

have a longer lifetime than most of the QB50 satellites. The only source of high drag on Phi is the addition of wings and fins. However, this will make it possible to provide stability below 200 km, making if possible to take and transmit measurements until 95 km altitude. This has been considered more valuable than a satellite with a longer lifetime that only operates up to an altitude of 200 km. Also, the value of demonstrating differential drag, a formation with three satellites and a formation with uncooperative satellite is considered more valuable than an extended mission lifetime.

7.2 Differential Drag

7.2.1 Theory

Differential drag makes use of the possibility of controlling the differences in ballistic coefficients of the spacecraft and therefore the relative decay rate. This is possible by controlling drag coefficient as well as frontal projected area by rotating the satellite or the use of deployables such as solar cells if the angle they make with the spacecraft can be controlled. Although this eliminates the need for a propulsion system, it should be noted that the velocity of a satellite can only be decreased. Relative distance can be maintained, but at the expense of altitude lifetime. Also, variable-angle solar panels make the design more complicated and vulnerable to failures. Using the attitude control system might result in high power requirements.

Radial distances can be corrected by increasing the ballistic coefficient of the satellite at the higher altitude and letting its semi-major axis decay until it reaches the same altitude as the second satellite. To control the along-track direction, both satellites have to descend to an altitude that is lower than their initial altitude. They do so after each other and the manoeuvres are timed in such a way that the desired change in along-track direction can be achieved. The sequence of manoeuvres is shown in Figure 7.2.1.

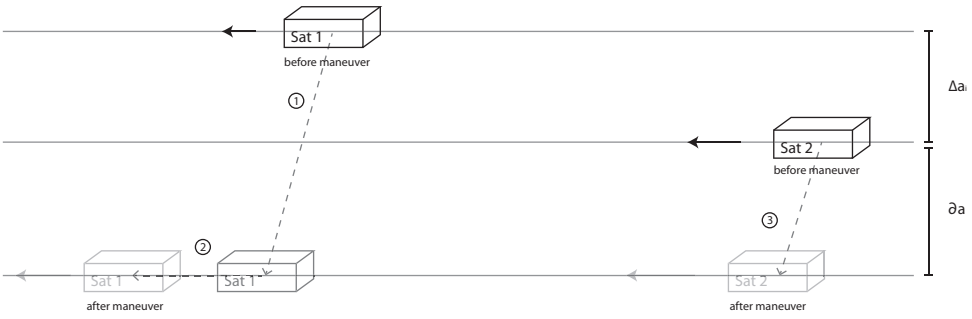

Figure 7.2.1: Formation maintenance manoeuvre using differential drag

7.2.2 Failure modes

The failure to demonstrate formation flight using differential drag can result from failure to adjust the ballistic coefficient accurately. Also, since the decay rate shows heavy dependence on the density which is not predictable with high accuracy, those rates could be highly over or underestimated. Moreover, assumptions on the wall temperature and the absorption coefficient have been made during the determination of the drag coefficient. The latter is completely unknown since the only data available is for metals. Since a large amount of the surface of the satellite is covered by solar panels, this introduces further uncertainty. Due to all these assumptions and the comparatively long timescale of the differential drag manoeuvres, it is advised to make the system closed-loop by comparing the expected decay rate by the one observed in the data from the GPS sensor. As will be explained later, dedicated hardware will be used to achieve the higher descent rates, because using the attitude of the spacecraft would generate descent rates that are too small and would interrupt science measurements. Only options have been chosen that are able to provide a continuous range of drag coefficients. The decay rate can be accurately adjusted during manoeuvre (3) when timing is critical to achieve the desired along-track separation. It is recommended to use only a fraction of half of the maximum achievable decay rate during the manoeuvre (3) to be able to also increase the decay rate, in case deviations to the expected one are observed. This fraction shall be determined by observing the behaviour of the satellite during the first week of the mission to see how well the model and reality correspond. Higher correspondence will allow for the fraction to increase.

Equations are presented for the case in which the trailing satellite has a lower altitude. During T_1, CubeSat (1) descends to an altitude that is ∂a lower than that of CubeSat (2). It continues to fly at its nominal ballistic coefficient. This manoeuvre is followed by a drift period of T_2 where neither of the CubeSats performs their manoeuvres. Finally, CubeSat (2) descends to the same altitude as CubeSat (1). It should be noted that this is not the same as the altitude at which CubeSat (1) was after T_1, its semi-major axis has decayed in the mean time.

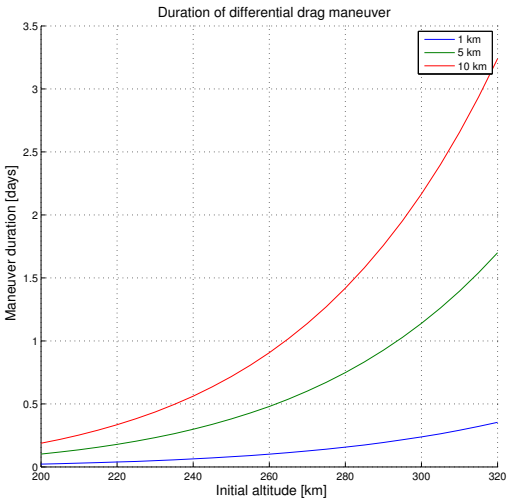

Figure 7.2.2: Manoeuvre time for differential drag manoeuvres of 1, 5 and 10 km altitude change

The equations describing this process are the following:

$$\int_0^{T_1} \left(\frac{da}{dt}\right)_{\beta_1} dt + \int_0^{T2+T3} \left(\frac{da}{dt}\right)_{\beta_2} dt = \Delta a + \partial a \tag{7.2.1}$$

$$\int_0^{T_1+T_2} \left(\frac{da}{dt}\right)_{\beta_3} dt + \int_0^{0+T3} \left(\frac{da}{dt}\right)_{\beta_4} dt = \partial a \tag{7.2.2}$$

$$\int_0^{T_1+T_2+T_3} (n_2 - n_1) dt = \Delta\theta \tag{7.2.3}$$

The use of differential drag is very beneficial for large negative velocity changes that are not time-critical. It has been decided that in order for differential drag to be useful, the satellite should be able to fulfil the same type of manoeuvres using differential drag as will be carried out with the propulsion system. However, all manoeuvres will be of velocity decreasing kind. This is not necessary a drawback, but can be complementary to the propulsion system: due to the occupation of the front phase by FIPEX, the only available place for the nozzle is the back panel. This necessitates rotation of the satellite if a velocity decreasing manoeuvre is needed, which will interrupt the scientific measurements. It has been decided that any differential drag manoeuvre should therefore be able to comply with to the same requirements as the powered formation flight. One free variable remains, which can be eliminated by setting a time constraint to the manoeuvres. This has been decided upon by setting a requirement that a differential drag formation acquisition manoeuvre should not take longer than any other activity that will be performed by the spacecraft. The longest preparatory activity that will be performed during the mission is the process of detumbling which will take two days. The maximum duration of a differential drag manoeuvre is therefore also set to two days. Figure 7.2.2 shows the duration needed for manoeuvres of 1, 5 and 10 km altitude change as well as the dependency as function of altitude for a drag coefficient of 12.5 corresponding to four flaps perpendicular to the flow, each of 0.01 m^2 area. It can be seen that altitude changes of 5 km can be achieved within two days at all altitudes. This corresponds to a ΔV saving of 8.3 $m \cdot s^{-1}$ of 48.7 g. In this respect, differential drag even outperforms propulsive formation flight: This kind of manoeuvre will be suggested later in this section to perform formation acquisition with an uncooperative satellite at a much lower altitude. This would have consumed almost 50 % of the available propellant and would not have been justifiable. Figure 7.2.2 also shows that even larger manoeuvres are possible for time spans that are only slightly larger. A 10 km manoeuvre corresponds to 16.7 $m \cdot s^{-1}$ ΔV and 98 g of propellant, which is more than the entire budget.

The drawback of differential drag is the altitude loss associated with every manoeuvre that aims at adjusting the along-track separation the requirement for a maximum manoeuvre time translates into the need for a ∂a of 3.5 km to achieve sufficient relative motion.

7.2.3 Differential drag mechanism

The options for controlling the relative ballistic coefficient are the rotation of the satellite or the control the angle of a deployable that increases the frontal projected area. The introduction of such a mechanism is complex and increases the risk of failure. Not only failure to deploy could lead to significant reduction in capability to perform the mission, but partial deployment failure results in a non-diagonal inertia matrix and an offset of the center of gravity from the geometric center. This increases the disturbance torques on the spacecraft due to thrusting and aerodynamic drag. The consequences of partial deployment will be investigated if the EPS necessitates the use of deployable solar

panels. Due to the complexity of the candidates discussed, other separate mechanisms are devised to perform the formation flying between two satellites, balloon and flaps. The first design control the surface area by inflating and contracting the balloon. The other one is to change the frontal area by deploying flaps. In this section the balloon design will be discussed first, followed by flaps. Before discuss about the requirements imposed on each design, a general consideration about the mechanism is introduced.
From the QB50 requirements the following conditions have to be taken into account before proceeding:

Top level requirements

- PHI-QB50-2.5.1. The payload shall withstand a maximum pressure drop rate of 3.92 $kPa \cdot s^{-1}$.
- PHI-QB50-2.6.1. Inflatable structure shall not cause debris.

The first requirement is established so that during the folding of the balloon the residual air that is trapped inside does not cause the balloon to explode. This must taken into account when packing the balloon material in the stowage.

7.2.4 Design 1: Balloon

Second level requirements

- PHI-MO-DD-6.1. Design shall not protrude outside the envelope (after deployment no clash with satellite components).
- PHI-MO-DD-6.2. Design shall not exceed 50 g. (reserved from total mass budget allowance).
- PHI-MO-DD-6.3 Design shall be easy integrable into the standard CubeSat configurations.
- PHI-MO-DD-6.4 The flap system shall withstand 0.8 N.
- PHI-MO-DD-6.5 The balloon shall remain operational for 5 days.

- Furthermore the environmental conditions in the thermosphere layer imposes a third level of requirements that need to be satisfied to meet requirement PHI-MO-DD-6.6. The material selection that is discussed later has to take the following factors into account:

- Atmomic oxygen, which will cause rapid erosion of materials.
- radiation (ultra-violet), can heat the inflatable structure.
- large temperature ranges, from 375 K to 2770 K[20]
- high vacuum
- cosmic rays
- aerodynamic drag
- microgravity
- gravity-gradient effects: mechanically interconnection experience small forces.

Inflatable balloon design Several designs were sketched and not all of them were candidates to meet the second level requirements and the mass constraint. The mass budget for the design is only 50 g.

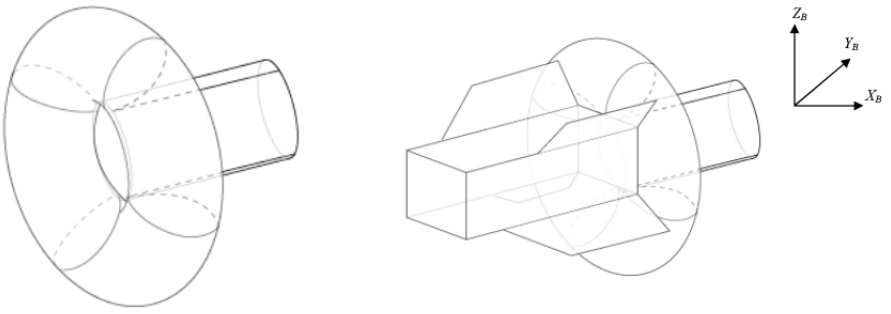

Figure 7.2.3: Inflatable balloon design 1.1

Design 1.1

As can be seen in Figure 7.2.3 the envelope consists of two inflatable systems. To inflate the system several times (without wasting gas) the air should be stored somewhere else when the system is contracted. To inflate the balloon a certain amount of gas needs to be delivered by the cool gas generator (CGG). The inflation pressure is constant and equal to 0.2 bar, which is found to be common in literature [33]. Cold gas from the propulsion system is used to inflate the back part first while the front part is still contracted. Several cords are attached to the cylinder and the torus in a loop in such a way that when the back part is contracted this cord length is available for the front part to inflate. When the front part of the balloon is contracted, the chord length is available for the back part to inflate. So the gas can go from the cylinder to the torus and vice versa, depending on which chord is retracted. When no drag is desired, the cylinder is inflated, because this area has very small effect on drag. The higher the frontal area perpendicular to the velocity vector the more drag is induced. The torus therefore plays the key role in terms of drag generation, whereas the cylinder has less effect on drag. Though the flow passing across the cylinder does increase drag too, due to the thermal motion of the molecules, it has a small contribution to the differential drag.

Foil The balloon skin (cylinder and torus) is made from a polyimide film called Upilex-S. An advantage of this material is that it can undergo high temperatures without experiencing degradation of its properties. The layer can be coated with vapour deposited aluminium to improve thermo-optical properties. The thickness of Upilex-S is 25 μm, and the mechanical property are shown in Figure 7.2.4.

Chord The chord is made from Dyneema, which has a strength-to-weight ratio higher than that of the nylon or polyester. This material has a wide range of applications, including sailing and sport fishing. In addition, Dyneema has a low density when compared to Kevlar or Zylon, but the material is not very heat resistant, see Figure 7.2.5. Since the wire is inside the balloon, heat does not pose a problem.

Properties	Unit	Typical Values						Test Method
		UPILEX-25S(25μm)				UPILEX-75S(75μm)		
		-269°C	-196°C	25°C	300°C	25°C	200°C	
Tensile Strength (MD)	MPa	735	647	520	290	360	270	ASTM D882
Stress at 5% Elongation (MD)	MPa	---	---	260	90	210	110	ASTM D882
Elongation (MD)	%	10	15	42	67	50	80	ASTM D882
Tensile Modulus (MD)	MPa	---	---	9100	3700	6900	3800	ASTM D882
Tear Strength-Initiation [Graves] (MD)	N	---	---	230	---	290	---	ASTM D1004
Tear Strength-Ipropagation [Elmendorf] (MD)	N	---	---	3.2	---	4.2	---	ASTM D1922
Folding endurance [MIT]	Cycles	---	---	>100,000	---	>25,000	---	ASTM D2176
Density	$\times 10^3$kg/m^3	---	---	1.47	---	1.47	---	ASTM D1505
Coefficient of Kinetic Friction (film-to-film)	---	---	---	0.4	---	0.4	---	ASTM D1894
*MD: Machine Direction								

Figure 7.2.4: Mechanical properties of Upilex-S [37]

	Density (gcm^{-3})	Longitudinal Tensile Modulus E_1 (GPa)	Transverse Tensile Modulus E_2 (GPa)	Poisson's ratio ν_{12}	Shear Modulus G_{12} (GPa)	Longitudinal Tensile Strength σ (MPa)	Longitudinal Thermal Expansion α_1 (10^{-6} K^{-1})	Transverse Thermal Expansion α_2 (10^{-6} K^{-1})	Heat Resistance °C	Cost $/kg
Kevlar (49) Kevlar (29)	1.47	154 61	4.2	0.35	2.9	2800	-4	54	550 450	4.50
PE (Spectra) PE (Dyneema)	0.97 0.975	66-124[1] 115				2300-3250[2] 3500	- -12		150	12.00
PBO Zylon AS PBO Zylon HM	1.54 1.56	180 270				5800	-6		650	15.00
Al_2O_3	3.9	385	385	0.3	154	1400	8.5	8.5		25.00

[1]Spectra 900 E=66-73GPa; Spectra 1000 E=98-113GPa; Spectra 2000 E=113-124GPa
[2]Spectra 900 σ=2.1-2.6GPa; Spectra 1000 σ=2.9-3.25GPa; Spectra 2000 σ=2.9-3.5GPa
PBT = Poly(p-phenylene-2,6-benzobisthiazole)
PE = Gel Spun ultra high molecular weight polyEthylene (Spectra®,Dyneema®)
PEN = polyEthylene Napthalate (Pentex®
PBO = Poly(p-phenylene-2,6-benzobisoxazole)

Figure 7.2.5: Off-the-shelf industrial fibers and their main properties. [37]

Tube The tube was fabricated by the Phi group, so that the model can comply with the strict requirements that it needs to be flexible and can withstand harsh environment in space. The material Mylar was used. The best way to make it airtight was to light it with a candle. . The method was not precise enough, because the flame is influenced by the behaviour of air in its proximity, which in turn is affected by activities like breathing. The diameter of the tube should be 1 cm but this value was not constant through the length of the tube. Another method to make the tube airtight was ironing it. This approach was not suitable as Mylar is heat resistant to high temperatures, and therefore would not melt. Glueing Mylar with Bison is also not recommended for precision work. On Figure 7.2.6 one can see the result of the 'home made' tube:

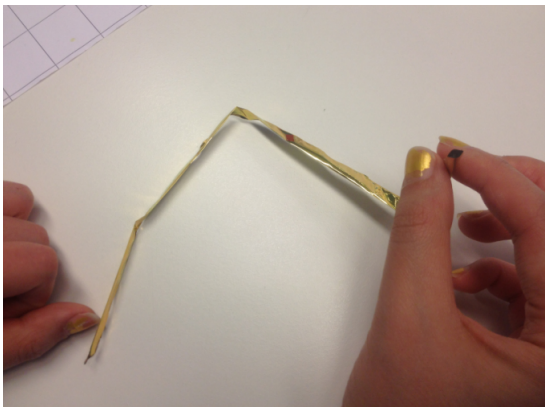

Figure 7.2.6: Home made tube from Mylar using a candle as the merger tool.

Figure 7.2.7: Step Motor with ULN2003 driver board DC 5V

In practice the tube material selected is Technora®, an aramid fibre. Reasons for its selection are its good folding properties, its large temperature range, and its small available thickness, 70 μm [37].

Retraction mechanism The motor that is suitable for the pulling and retracting the chord given the low cost and mass is €4 and 32 gram respectively. The step motor needs 5 V and has a diameter of 2.8 cm, see Figure 7.2.7.

Schematic representation of the balloon with the satellite shows the components that is used to inflate the balloon system. A cool gas generator is used to produce nitrogen gas into the balloon from a valve. The battery and the valve regulates the inflation and the transmitter gives the signal to inflate.

Design 1.2 The next design is made from Mylar. To save gas two sheets are glued in a special way. The outer edges are free of glue to enable strength. On one of the edges two (red) wires are attached, see Figure 7.2.9. When no drag is desired the red wires are rolled in. By retracting these two red wires the flaps closes the pyramid tail. The tail has the same height and width as the satellite hence the flow will not encounter any protrusion of the balloon design, see Figure 7.2.10 for closed configuration.

For this design three pattern are made for the flaps to give it some strength when it is opened. As can be seen from Figure 7.2.12 the one on the right has more sharp corners than the other two. This is interesting to test because the sharp edges could give some problems when the balloon is inflated. Note the red arrows on the right figure. At the edge where the flaps will be folded when the wire is pulled in there should be as less as possible air. This makes the

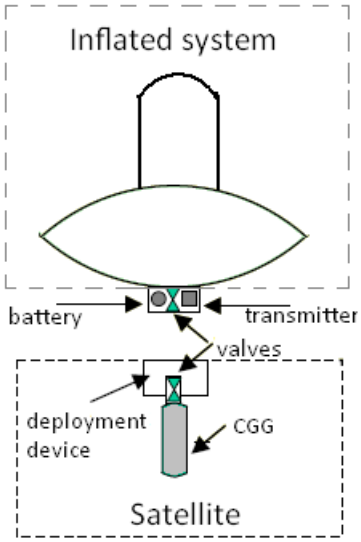

Figure 7.2.8: Schematic of the balloon's deployment port, MS Paint 2013

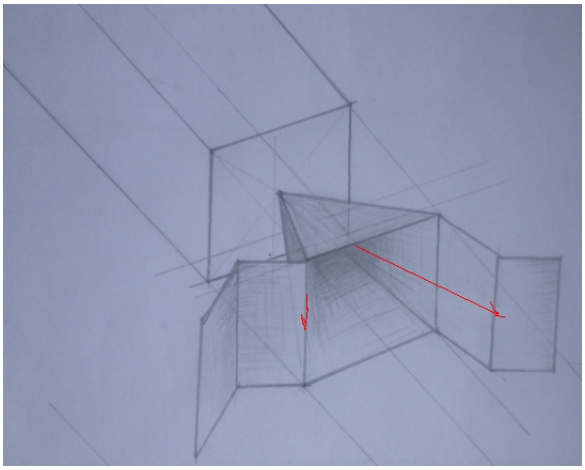

Figure 7.2.9: Inflatable balloon design 1.2 showing glue pattern.

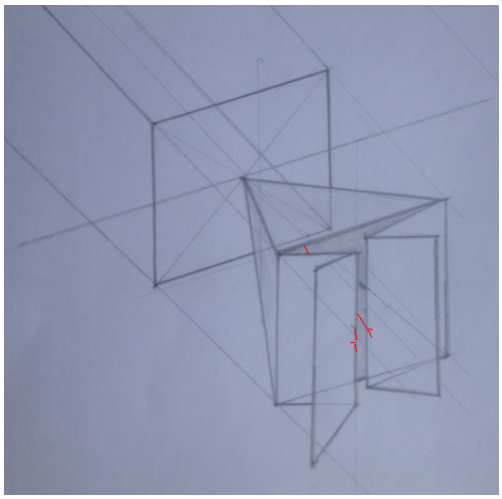

Figure 7.2.10: Inflatable balloon design 1.2, focussed on closed flaps. [64]

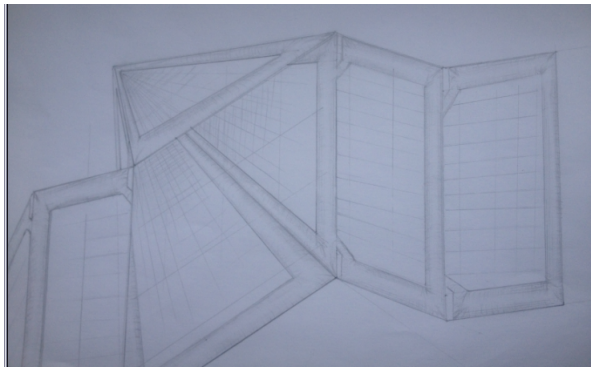

Figure 7.2.11: Inflatable balloon design 1.2, where only the edges are inflated. [64]

closing of the flaps easier. Four prototypes were made to test the pattern and the stress concentration that corresponds with the pattern. One prototype is made to test the side of Design 1.2 in vacuum chamber. How nitrogen gas and this material will act together in space condition. Another three hexagon was used to investigate the different pattern : a circular patter in the middle, a rounded plus sign and a cornered plus sign, see Figure 7.2.13.

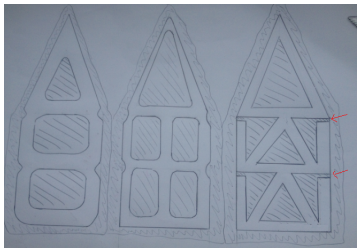

Figure 7.2.12: Inflatable balloon design 1.2, pattern flaps [64]

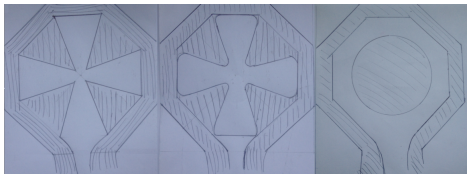

Figure 7.2.13: Inflatable hexagon with a circular, round and sharp edged pattern. [64]

For the nozzle a regular balloon is used. The upper piece was cut and glued to the prototypes, see Figure 7.2.14.

The tests of the prototypes were not successful. The inflatable designs were not airtight and the Mylar and glue were not compatible. The glue worked even more contrarily: the glue was so hard that it worked more as a razor. From Figure 7.2.12 one can see the triangular shape where just above the top of the triangular the nozzle was placed. During the inflation the air flow filled the Mylar material. The air pushed the material against the this top piece of the triangular. The contact between the edge of the glue and the the Mylar material worked as a razor. This is shown in Figure 7.2.15 where clearly at the top point of the triangular glue shape Mylar is torn. In the right side of the figure the circular shaped hexagon is also torn next to the glue. Apparently the glue is too hard for this particular material.

Figure 7.2.14: A rubber balloon piece to function as a nozzle for the prototypes. [64]

Figure 7.2.15: Tear start at the "neck" of a prototype. [64]

The lessons learned from the tests are that the process of inventing and testing a design requires precision and detail. Time is spent in research for the right material, then to test the designs the manufacturing process should be suitable for the design. The glue was also tested for different kind. From Figure 7.2.16 one can see that to tight the edges of the glass fiber the spray glue was the most promising candidate. The distribution of the sticky material is more even than the liquid glue and it dries also quicker.

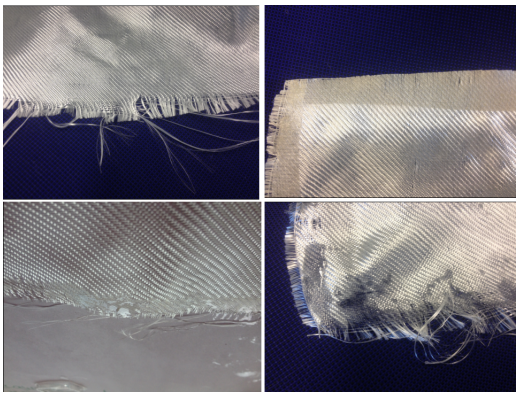

Figure 7.2.16: Performance of Bison liquid glue and spray glue. [64]

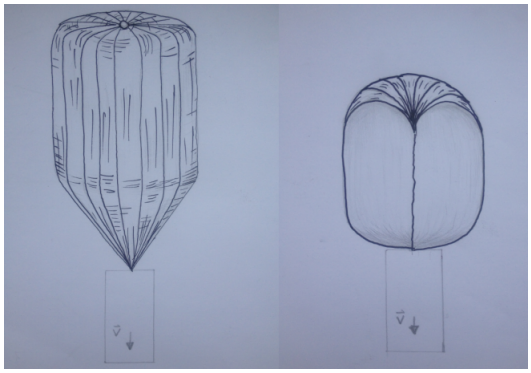

Figure 7.2.17: Inflatable balloon. [64]

The glass fibre material is glued on the edges with two different types of glue. The liquid glue seemed to be less efficient. The distribution of the compound was not evenly spread out as can be seen in the left below on Figure 7.2.16. When dried out, this liquid glue was more curtailed, see right below on the figure. The spray however worked perfect. The sticky particles were evenly distributed, as seen in the upper right picture. The disadvantage if this method was the resulting gas emission.

Design 1.3 This design works in the same principle as the previous design, only it differs in shape and more use is made of tubes. There is also a chord that can be contracted to increase frontal area.

Stowage and deployment The maximum dimensions of the standard CubeSat are 100 x 100 x 340.5 mm. The flanges of the ribs are maximum 8.5 mm. This leaves a storage of around 90 x 90 mm. The balloon is folded and stored in a storage device which looks like as in Figure 7.2.18.

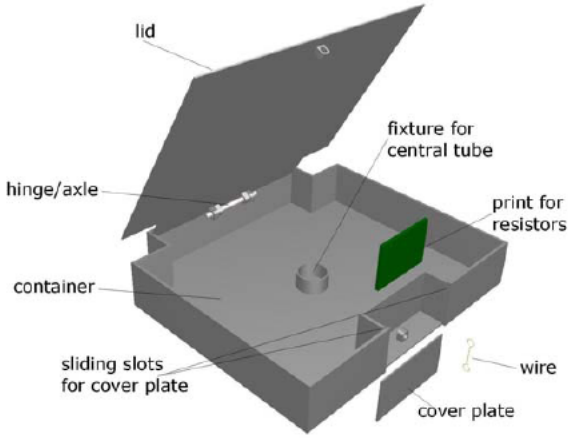

Figure 7.2.18: Stowage device[37]

The height is taken roughly 10 mm for the stowage device before it reaches the height of Printed Circuit Board (PCB). The lid of the stowage device is held down by a Dyneema wire which is melted by a resistor to open the lid. The balloon materials, foil and tubes and chord are folded inside this devices. Since the volume of the storage is very small attention is paid to the folding. The foil must be folded in small packages, a high packing efficiency is needed. Also according the requirement *PHI-QB50-2.5.1* the folding should be sucked out of air.

The deployment of the balloon is assist by pressurizing the tubes or the channels inside the foil (depending on the balloon foil design). This gas is produced by a cool gas generator (CGG). One unit of CGG cartridges delivers around 0.12 litres of volume. This happens in roughly one second and depending on the temperature 0-225° C the resulting internal pressure of the inflatable tubes are 0.97-1.76 bar [37]. In the tests of the prototypes no internal pressure could be measured, hence this number is taken for a rough estimation.

7.2.5 Design 2: Flaps

The second design that can assist the differential drag method is obtained from the rotational flaps.

Requirements There is only one requirements for the flaps, 400 cm^2 is needed for the desired drag. For the symmetry, four flaps are implemented, each with minimal 100 cm^2 of area. Since this flap covers almost a third of the satellites surface the solar cells are attached on top of the four flaps. The flaps functions then also as a solar array.

Design 2.1 Four flaps are made, each with a width of 8 cm and a length of 14 cm. The 2 cm from the width are reserved for the resistors. The 1.5 cm space is used for the hole. In the figure below one can see the first design, where use is made of hinges and springs. When the wire is burned the springs pushes the flaps up. A chord that goes through the hole in the middle changes the angle of flap to the satellite surface. With the movement in angles the amount of drag can be changed. A strong material is selected to withstand deformation (bending) and still be able flexible enough not to break when the chord pulls on the materials. A new kind of material is in development, the new nano-architecture aluminium alloy with strength of steel and very low density.

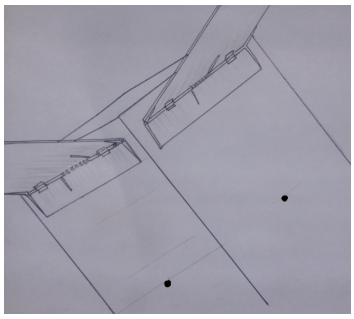

Figure 7.2.19: Movable flaps with hinges and springs. [64]

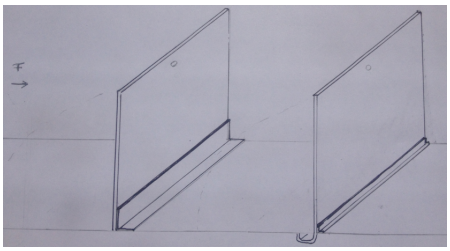

Figure 7.2.20: Movable flap with another attachment concept at the surface. [64]

Design 2.2 The second design is the same as the first design only the attachment to the satellite skin is changed. A cut is made on the skin where the flap goes through. The rounded lower part keeps the flap perpendicular to the skin. The force that pushes against the flap can change the flap angle only to 90° maximum, see Figure 7.2.20.

In the next figure different small designs is presented for the backside of the flip. It's function is to keep the flap on the skin so it does not fall inside the satellite. This extra attachment at the backside is only attached to the flap and has free contact with the satellite surface, see Figure 7.2.21.

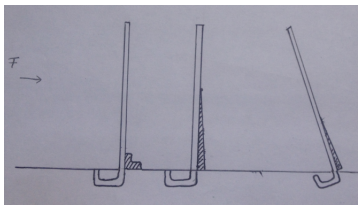

Figure 7.2.21: Different backside of the flaps. [64]

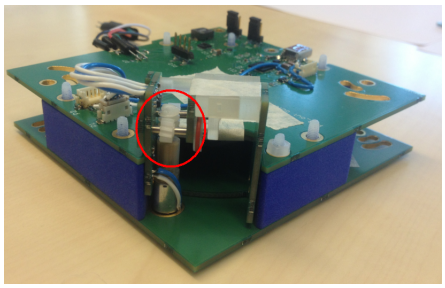

Figure 7.2.22: Deplyoment mechanism flap. [23]

Deployment The flaps are pulled in and out by the same motor as the one used for inflatable balloon. A chord goes through the flaps, through the satellite's skin and finally to the deployment mechanism. From there this chord is pulled. This is illustrated in Figure 7.2.22 in the red marked circle where the chord goes through it. Inside the two plates a disk rotates and rolls the chord.

The flaps are attached to the satellite with Dyneema. A resistor heats this wire till it burns. Since there are flaps on each side of the satellite four resistors are built on the sides of the satellite, see Figure 7.2.23. The small hook shape holds the wire and is rotated to the right. When the wire is burned the hook shoots to the left.

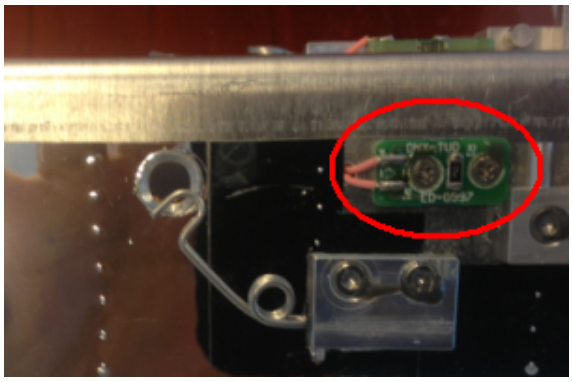

Figure 7.2.23: Resistor, indicated in red circle.[12]

Figure 7.2.24: Inflatable structure pyramid [37]

7.2.6 Discussion

The production and testing with pressure provided insight on how difficult it is to make a inflatable design of any kind. The selection of material, glue type and air-tightening methods became very important during the 'manufacturing' of the prototypes. The small burst and misalignments of the sheets of the foil required special techniques since the foil requires precision work. The pattern that was chosen could not be realised with the present glue type. It became important to think of other air-tightening methods or materials because non of the prototypes was airtight. Although the outer edges got 10 mm width of glue this could not prevent an leakage. The tubes were the most difficult part of the inflatable deployment components to make. The diameter is very small and no guarantee is given that this home made tube works when pressurized. The diameter changes over the length as this was hard to control it due to the unstable flame of the candle light. In practice when qualified engineers make inflatable balloon should use more high-techniques tools as this is a fine needlework.

7.2.7 Design Trade-off

A trade off is made between Design 1.2 and Design 2.1. The other designs needs to be investigated further to make it more feasible. In terms of mass, balloon designs uses very light materials. However the deployment system and storage in total adds more weight and volume. To get a rough idea about the mass and volume a reference study was conducted. The total mass and volume was estimated 100 g and 103 cm^3 for an inflatable system [37], see Figure 7.2.24.

The flaps on the other hand do not need storage volume as this is placed on the outer layer of the satellite. The same motor is used as for the balloon designs for the deployment. The power consumption of the flaps depends on how often the flaps needs to change angle, but it is expected to be less than the balloon. Although the CGG for the balloon needs 13 W for only a second every time when gas is produced, the chord that is pulled and rolled out needs

power over longer time. This same motor will pull or roll out the flaps with less power as the “chord” for the flaps are much shorter. The downside of the flap design is the mass. The flap is made from aluminium and has higher density than the foil from the balloon design. Manufacturing the balloon is more difficult than manufacturing the flaps. Also the storage of the inflatable structure is less simple than the flaps. The inflatable structure needs to be folded in a particular way to have a higher packaging efficiency. This is more complex than the flap design. Feasibility scores good with the flap design. Also the risk is less, the attachment and mechanism are reliable while the inflatable balloon has more uncertainties in for example material, inflation system, tubes, stress concentrations, adhesive attachment and rigidity development (exposure to wide temperatures).

Table 7.2.1: Trade-off between inflatable design and rigid flap.

Criteria	**Balloon**	**Flap**
Mass (incl. deployment devices)	-	-
Volume	-	+
Power	-	+
Manufacturing	-	+
Feasibility	-	+

Chapter 8

Propulsion System

The first nano-satellite mission with propulsion system was the Canadian Advanced Nanospace eXperiment, CanX-2[43], and no other CubeSat has been flying with a propulsion system. Miniaturization technology enables future CubeSats to perform more missions, like orbit change and raising, formation flying, fine attitude control, or drag-make-up and de-orbit. In this section, the propulsion system required for performing formation flying is designed. The final decision on the propulsion system flows down from the design requirement that comes from QB50 and PHI mission design. This is discussed in the section Requirements. Then more theory is given on the chosen propulsion technology in order to understand how the technology works. The theoretical performance of this system follows right afterwards. The corresponding failure modes and sensitivity analysis gives insight in the propulsion system. Finally, recommendations are given to conclude this chapter.

8.0.8 Requirements

There are not any clear-cut requirements for the miniaturized propulsion system in the QB50 System Interface Control Documents[71]. Nevertheless, using the 'CubeSat Design Specification Rev. 12', the following must be taking into consideration:

- PHI-GQR-1: No toxic materials shall be used.
- PHI-GQR-2: No pressurized containers shall be used.
- PHI-GQR-3: Pyrotechnics shall not be permitted.
- PHI-GQR-4: No pressure vessels over 1.2 standard atmosphere shall be permitted.
- PHI-GQR-5: Total stored chemical energy shall not exceed 100 Watt-hours (= 369 kJ).
- PHI-MO-FF-7.1: Both satellites shall have a ΔV budget of 15 ms^{-1} for formation maintenance.

The first concerns is about dumping the choice of the pyrotechnic igniter and valves because of heat generated by the exothermic chemical reaction. The requirements from QB50 and the size of the spacecraft eliminate many candidates, which are more suitable for a big satellite, from our design list. The propulsion technology that is compatible for the nano-satellite is elaborated in the Theory section.

8.1 Cold Gas Propulsion Technology

There are many propulsion systems with different capabilities available on the market or still under development. A more elaborate explanation of the different propulsion technologies that exist for micro- or nano-satellites can be found in Midterm Report[36]. Two technologies were selected for the trade-off, a cold gas system ($T^3\mu PS$) and an electrothermal system (MEMS Resistojet).

During the first formation flight, the propulsion system will assist the spacecraft to change its orbit. To demonstrate differential drag two designs are developed, a balloon and one flap design. First the balloon design was chosen, but it was decided not to go for it as it was less feasible and more risky than the flaps Hence the propulsion system has no extra implementation for the balloon design.

8.1.1 Theory

Cold gas propulsion is simple, reliable, and cheap when compared to other propulsion technologies. Nitrogen (N_2) and Helium (He) are always used as the propellant gas for their characteristics: inert and low molecular mass. During operation, the gas is released by the valve from a tank through the thruster. The gas composition can be an almost pure gas, for example 99% nitrogen (N_2) and 1% other chemical compounds.

Gas is delivered by cool gas generator (CGG). Propellant storage is in solid phase. The advantage of this phase compared to the liquid phase is the absence of sloshing. Sloshing disturbs attitude control and pointing of the satellite if high accuracy is needed.

When ignited from CGG, the gas is released and the remainder stays in the CGG as a slack material. The gas leaves the generator at ambient temperature without additional thermal impacts on external components. The low storage pressure is typically between 1 and 4.5 bar and makes a pressure regulator redundant.

In Figure 8.1.1 a diagram is presented for the Phi satellite's propulsion system:

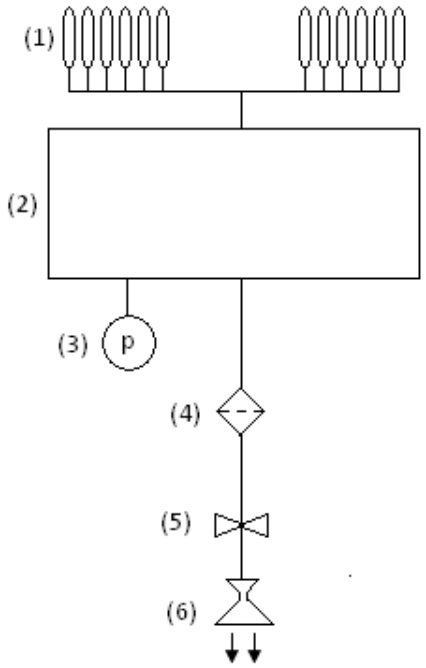

Figure 8.1.1: Schematic of Phi satellite cold gas system, MS Paint, 2013

The cold gas blow-down rocket engine typically consists of a:

1. cool gas generators
2. plenum
3. pressure sensor
4. filter
5. valve
6. nozzle (one thruster)

When the system is initialized, the first CGG is activated and fills the plenum with N_2. Since the thruster operates in a blow-down mode the pressure decreases in the plenum. When the pressure reaches a certain low set-point, the next CGG is activated. Hence a pressure sensor is placed in the plenum. The gas that leaves the plenum contains some small solid particles. This can clog the tube, therefore a filter is introduced for preventing this. The thrust generation is regulated by an on/off switch called a valve regulator. This valve has a full open and a full closed configuration. At the final stage a nozzle assembly is used to accelerate the exhaust velocity.

8.1.2 H/W and S/W diagrams

The hardware (H/W) and software (S/W) block diagram of the propulsion system is illustrated in Figure 8.1.2.The micro-controller collects data to ignite, pressurize and open the valve.

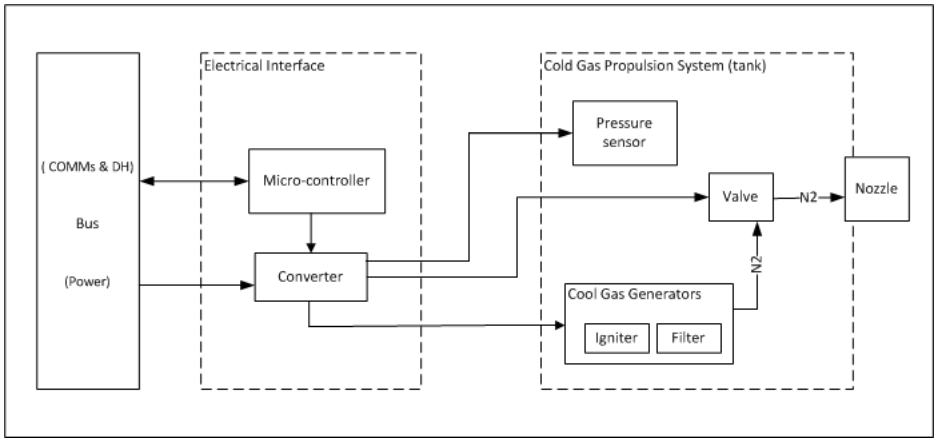

Figure 8.1.2: Cold gas propulsion system block diagram, made with MS Visio, 2013

The electrical interface is connected with all other components. The filter is the same box as the CGG and is placed inside the tube. The electrical interface connects the propulsion system with the bus of the nano-satellite. The power bus is connected to micro-controller that carries out four functions: converts the right voltages from the power bus to individual components, handles the pressure data, monitors CGG ignitions and actuates the valve. The data from pressure sensor is then sent back to the bus of Communications and Data Handling (COMMs & DH).

8.1.3 Theoretical Performance

Two aspects must be considered with respect to formation flying with Delta: maintaining the initial relative position and velocity. Due to atmospheric drag and Earth's gravitational field, the orbital altitude will decay. The Delta and Phi satellites drift apart due to differences in area, position and mass. It is the task of the propulsion system to correct this.

Before starting with the calculation, some assumptions were made:

Assumptions

1. Thermal condition neglected : As the system T$^2\mu$PS is a cold gas with blow down system the chamber pressure varies along the orbit and is not actively controlled. As a result, the chamber pressure is dependent on the overall thermal profile of the CubeSat (knowing that the temperature is as function of pressure). In this first assumption this thermal factor is not considered during the calculation for both of the propulsion types.

2. Ambient conditions: The temperature of cold gas is usually taken at ambient conditions, hence the gas leaves the tank at chamber temperature T_c of 297 K. This is the internal temperature of the plenum, the temperature outside the titanium case is kept at -40° and 75° degree Celcius [14].

3. Supersonic isentropic flow

4. Ideal gas

Furthermore, the following parameters are known about the T$^3\mu$PS [15]

- Expansion ratio (area ratio) $\varepsilon = 9.45$
- Area throat $A^* = 7979$ μm^2
- Chamber pressure $p_c = 3.5$ bar
- Propellant gas = N_2
- Satellite mass $M_{S/C} = 3.6$ kg
- CGG mass $m_{CGG} = 16.3$ g
- CGG useable mass for propellant $m_{CGGp} = 4.21$ g
- Specific impulse I_{sp}= 68 s

The impulse bit determines the duration of the thruster calculated in Equation 8.1.1

$$I_b = M_{S/C} \cdot \Delta V = F \cdot t_{min} \tag{8.1.1}$$

Where I_b is the impulse bit in [s], Δ V change in velocity in $m \cdot s^{-1}$, F the thrust in [N] and t_{min} the smallest time in [s] that the thrust is delivered. With $M_{S/C} = 3.6$ kg and Δ V of 15 $m \cdot s^{-1}$ gives I_b.

$$\Delta V = V_{eq} \cdot ln\left(\frac{M_i}{M_f}\right) \tag{8.1.2}$$

Where V_{eq} is the velocity of the reaction mass when it leaves the satellite, called equivalent velocity in $m \cdot s^{-1}$, M_i the initial mass in kg and M_f the final mass kg. The final mass is the initial mass minus the propellant mass, where M_i=$M_{S/C}$. Rewriting Equation 8.1.2 for propellant mass M_p gives:

$$M_p = M_{S/C}\left(1 - e^{\frac{-\Delta V}{V_{eq}}}\right) \tag{8.1.3}$$

The unknown is the V_{eq}, which is calculated from the thrust equation divided by the mass flow:

$$V_{eq} = \frac{F}{\dot{m}} = V_e + \frac{(p_e - p_\infty)}{\dot{m}} A_e \tag{8.1.4}$$

Where $\dot{m}$ is the mass flow rate $kg \cdot s^{-1}$, V_e is the exit velocity, p_e the exit pressure [Pa], p_∞ the free stream pressure Pa and A_e is the nozzle exit area [m^2]. Note that the p_∞ is zero at high altitude in space. All of the variables in equation 8.1.4 depend on the dimension of the nozzle. The mass flow is determined from:

$$\dot{m} = \sqrt{\gamma}\left(\frac{2}{\gamma+1}\right)^{\frac{\gamma+1}{2(\gamma+1)}} \frac{p_c}{\sqrt{\frac{RT_c}{M}}} A^* \tag{8.1.5}$$

Where γ is specific heat ratio of gas, which is 1.4 for N_2, R is the gas constant 8314 $J \cdot K^{-1} \cdot mol^{-1}$, M the molar mass of M_2, 28 [g]. The throat area A^* was already given above, 7979 μm^2. Together with chamber temperature of 298 K the relation of $\dot{m}$ and p is determined:

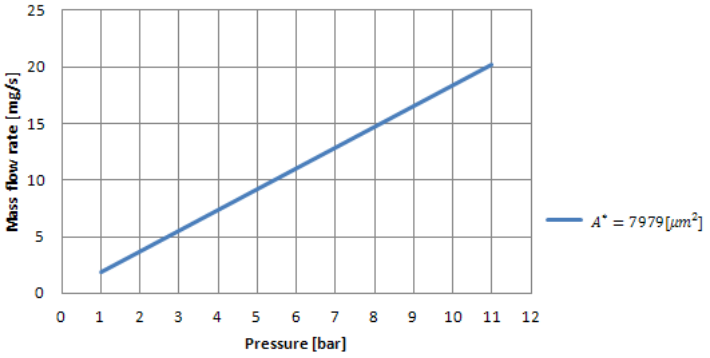

Figure 8.1.3: Propellant mass versus specific impulse for different ΔV's

From Figure 8.1.3 for chamber pressure of 3.5 bar the mass flow is 6.44 $mg \cdot s^{-1}$.
For a given expansion ratio the tank pressure p_e can be determined using the following relation:

$$\frac{A_e}{A^*} = \varepsilon = \frac{\Gamma(\gamma)}{\sqrt{\frac{2\gamma}{\gamma-1}\left(\frac{p_e}{p_e}\right)^{\frac{2}{\gamma}}\left[1-\left(\frac{p_e}{p_c}\right)\right]^{\frac{\gamma-1}{\gamma}}}} \tag{8.1.6}$$

Where $\Gamma(\gamma)$ is:

$$\Gamma(\gamma = 1.4) = \sqrt{\gamma}\left[\frac{2}{\gamma+1}\right]^{\left(\frac{\gamma+1}{2(\gamma-1}\right)} \approx 0.6847[-] \tag{8.1.7}$$

Substituting this back in Equation 8.1.6 and equate this with $\varepsilon = 9.45$ gives $\frac{p_e}{p_c} = 0.06264$, see Figure 8.1.4

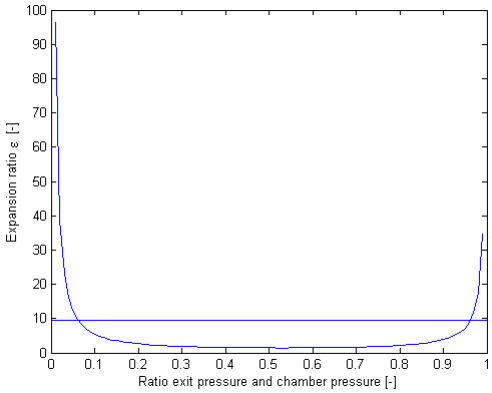

Figure 8.1.4: Expansion ratio ε=9,45 versus $\frac{p_e}{p_c}$, Matlab 2013

Finally the exit velocity can be determined to be substituted in Equation8.1.4:

$$V_e = \sqrt{\frac{2\gamma}{\gamma-1}\frac{RT_c}{M}\left[1-\left(\frac{p_e}{p_c}\right)^{\frac{\gamma-1}{\gamma}}\right]} \tag{8.1.8}$$

All of the parameters in Equation 8.1.8 are known, substituting them all gives an exit velocity of 581 ms^{-1} Substituting this back in Equation 8.1.4 together with Equation 8.1.5 gives for V_{eq}=852.52 ms^{-1}. From Equation8.1.6 the exit Area A_e is obtained knowing that A^*= 7979·10^{-6} m^2.

Finally, the required propellant mass is obtained, this is from Equation8.1.3:

$$M_p = 3.6\left(1 - e^{\frac{-15}{852.52}}\right) \approx 0.0628kg \tag{8.1.9}$$

The total system mass is the mass of the propulsion system inclusive the CGG's, plenum, sensor, nozzle, valves, printed circuit board and electrical interface. The system mass is the sum of CGG's mass M_{CGG}, empty tank M_{tank} and the remaining mass M_{rest}. Each CGG is 16.3 g where only 4.21 g out of it is useable for propellant. Hence, for a required propellant mass of 62.8 g one needs:

$$\text{number CGG} = \frac{M_p}{m_{CGG}} = \frac{62.8}{4.21} = 15units \tag{8.1.10}$$

The features of the tank mass are determined by the designer: how it should look like and what volume must be reserved for it. The most optimal shape is a spherical one in terms of structural integrity, but it less space efficient. A cylindrical tank is then a better option, see Figure 8.1.5

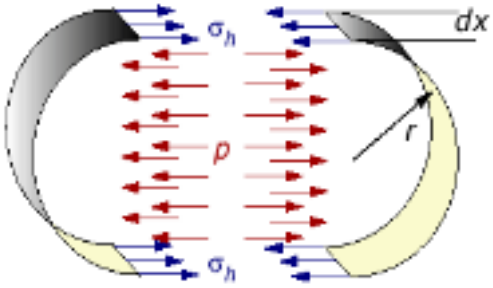

Figure 8.1.5: Cylindrical tank with indicated pressure vessel stresses [10]

The force that is pressing on the sides are pressure times area. The stress is:

$$\sigma = \frac{force}{area} = \frac{p(\pi r^2)}{2\pi rt} = \frac{pr}{2t} \tag{8.1.11}$$

Where σ is the tensile stress in Pa, r is the radius of cylinder in m and t is the thickness of the plenum. The force that is pressing on the sides are pressure times area, hence:

$$\sigma = \frac{force}{area} = \frac{P\pi r^2}{2\pi rt} = \frac{Pr}{2t} \tag{8.1.12}$$

The pressure that acts on the area can be described as force:

$$F = p(\pi r^2) = \sigma(2\pi rt) \longrightarrow t_{min} = \frac{p \cdot r}{2\sigma} \tag{8.1.13}$$

For a cylindrical tank shape t = $2t_{min}$, hence the mass of the tank is then:

$$M_{tank} = \rho \cdot 4\pi r^2 pt = \rho \cdot 4\pi r^2 p \cdot 2\left(\frac{p \cdot r}{2\sigma}\right) \tag{8.1.14}$$

The material of the tank is titanium, this has a density of 4430 kg m^{-}3 and the tensile stress is 950 MPa[30], the radius of the tank is 16 mm[28]. Substituting these parameters gives around 42.7 g. The total mass of CGG is the mass that one CGG unit has, which was given earlier (16.3 gram)

$$M_{CGG} = \text{nrCGG} \cdot M_{CGG} = 15units \cdot 16.3 = 244.5g \tag{8.1.15}$$

The mass of the other components, like valve, nozzle etc are around 68 gram [16].
Finally the total system mass M_{sys} can be determined. This is:

$$M_{sys} = M_{CGG} + M_{tank} + M_{rest} = 244.5g + 42.7g + 68g = 355.2g \tag{8.1.16}$$

8.2 Sensitivity Analysis

In this section a change in major system parameter is investigated. Sensitivity analysis is made for variation on the requirements following directly from the mission objective, namely ΔV. The propellant mass needed for a specific ΔV can be determined through Tsiolkovsky equation:

$$\Delta V = V_{eq} ln\left(\frac{M_{S/C}}{M_e}\right)$$

A change in ΔV results in a change in required propellant mass. To indicate how sensitive the change is, take for ΔV 10 ms^{-1} where all of the rest of the parameters stay fixed (e.g. V_{eq} is 98.1 ms^{-1}, M_0 is 10 ms^{-1}). The required propellant this ΔV gives is 0.969 kg. For a ΔV of 11 ms^{-1} the propellant mass is 1.06 kg, this is $\sim$ 10% increase. Taking 12 ms^{-1} this is $\sim$ 19%. Hence an increase in required total ΔV of 20 % will result in an increase in required propellant budget of $\sim$ 19%. The propellant mass increases almost linearly with the total required velocity change capability.

8.3 Failure Mode

It is not difficult to imagine what will happen when propulsion system fails. The failure of the propulsion system on one of the spacecraft is not catastrophic, because the propellant mass is sized such that formation flying can still be demonstrated in that case. However, if the failure occurs due to a design flaw it is likely that the failure occurs on the second spacecraft as well.

There are failure modules (externally & internally) on several levels that impact propulsion system. First the externally factors are treated which affects the desired performance. Next the internal factors are presented, these are the individual components inside the design of the propulsion system.

- *Environment* - Failure to model the space environment correctly when conducting tests of propulsion system on ground.
- *Software error* - Computer errors can cause the thruster to fire undesirable. If this happens at the beginning of the launch for some time then the required ΔV cannot be met.
- *Manufacturing* - Some manufacturing errors such as improper welding or shell damage during handling can cause tank shell rupture.
- *Calibration error* - Inaccuracy in calibration can decrease thrust and propulsion efficiency. The nozzle is very small and high precision tools are needed. Even with the sophisticated equipment one can expect a lower quality in the nozzle.
- *Individual components* - The most critical components are the valves and the piping. The ignition process is not guaranteed to run as expected. The relieve valve can fail to open. The plenum tank is then over pressurized. In some cases this results in a rupture of the tank. Valves can leak which will results loss of pressurisation and lifetime. The failure rate of individual components are listed in Table8.3.1.

.

Table 8.3.1: Failure rate data for cold gas propulsion system[69]

Components	Failure rate (in 10^{-9} hours or 10^{-9} operations.)
Tank	1.5
Valve (fully open)	23.3
Valve (fully closed)	44.4
Pressure sensors	196
Filters	1

8.4 Verification and Validation

Verification - Verification is done on the propulsion system from DelFFi N3xt. Comparing the theoretical results with the papers that are available on DelFFi performance shows whether the calculations are done properly. The ΔV of DelFFi is 6.3 $m \cdot s^{-1}$ and given that the specific impulse is 68 s this requires a propellant mass of 37.22 g with a 10% contingency margin[15]. As can be seen in Figure 8.4.1 this is true for specific impulse of 68 s, where the same propellant mass is obtained. Hence the method of calculations are hereby verified from paper [15].

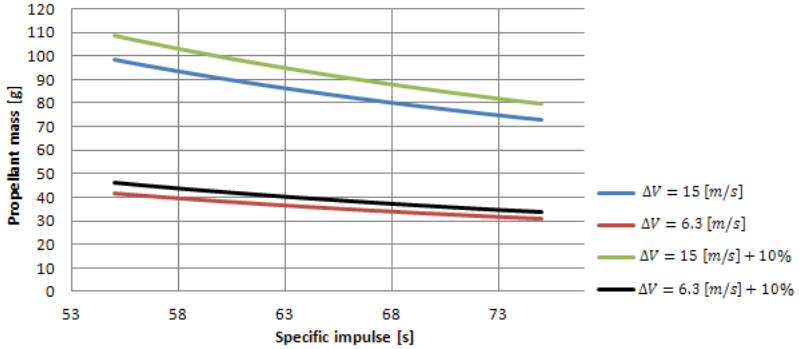

Figure 8.4.1: Diagram of propellant mass versus specific impulse for different ΔV's, MS Excel 2013

Also, the components can be verified by testing them in vacuum as well as at ambient conditions. As said before, the nozzle quality can be of a lower quality due to manufacturing. The ratio of the actual nozzle discharge to the theoretical discharge is often different. This discharge coefficient can be calculated and by testing the propulsion system (for nozzle) the theoretical performance is then verified. This can also be done for the valves. However, the detailed testing procedure of the components (e.g. valve leakage, volume tank strength etc.) is costly and is not cut out for this project.

Validation It is not easy to validate the design by comparing with other missions, because most CubeSats do not have an implemented propulsion system. One useful reference is Delfi-N3xt, which after launch will be able to provide data on the $T^3\mu PS$. Also, data derived from bigger satellites can still be applied to micro-satellites.

8.5 Recommendation

Given the short time span not much time was left to go in depth on several aspects. For instance, the leak rate of the valve on the blow down performance where one will encounter the Knudsen number which is at the moment an unclear term. A more detailed examination of the failure modes will help in improving the system's performance. However, time should be made available to do that considering that there are entire thesis reports on even the tiny nozzle (see MEMS Resistojet nozzle, unbelievable small scaled nozzle). By increasing the exit area of the nozzle the exit velocity can be increased, this decreases the propellant mass on its turn.

Also some benefits can be gained when searching for alternative propellant type and comparing that back with the N_2. There are CubeSats with propulsion system consisting of a liquid-fuelled cold-gas thruster system (e.g. using sulphur hexafluoride with high storage density).

Although $T^3\mu PS$ is ready for launch there are still some issues with this system, e.g. the ignition device which now and then fails. Furthermore, considering the failure rates of individual components from section *Failure Modes* there is much to investigate and to change.

It is definitely worth to look into all the mentioned areas as well. Then there is good chance to improve the current propulsion technology.

Chapter 9

Attitude Determination and Control Subsystem

This subsystem determines the attitude of the spacecraft and controls its orientation and stabilisation in space, despite the external disturbing forces acting on it. The Attitude Determination and Control System (ADCS) defines directly the rotational motion of the satellite about its center of mass. The attitude control task can be divided into three subtasks: 1) measuring attitude, which is done by attitude sensors; 2) correcting attitude, which is done by torquers and actuators; 3) a control law, which is software that determines the magnitude and direction of torque in response to a given disturbance. The ADCS, is a classic feedback control system, which is illustrated in the block diagram of the Phi satellite in Figure 9.0.1 [67].
As depicted in the diagram, the sensors used for the ADCS system are:

- three-axis magnetometer (1x)
- sun sensor (2x)
- star tracker(1x)

The actuators are:

- magnetic torquers (5x)
- reaction wheels (3x)
- aerodynamically stabilising fins

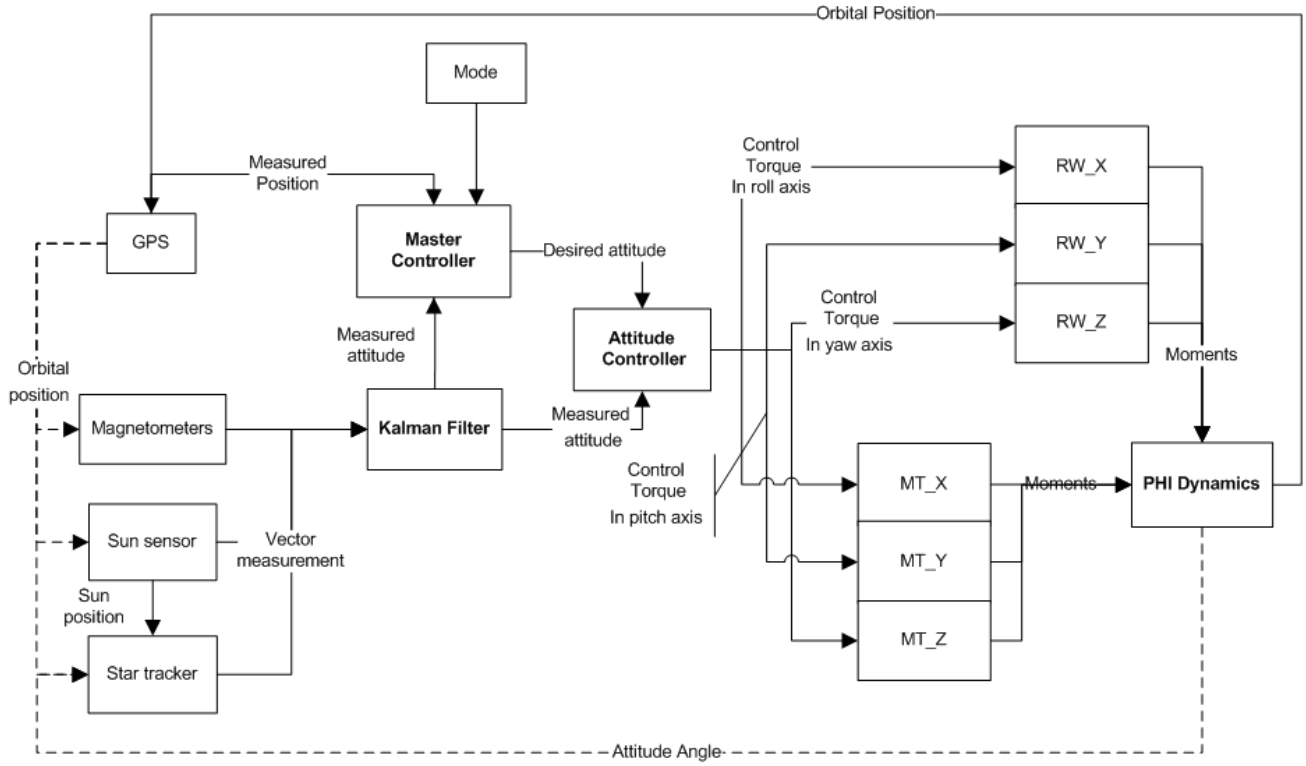

Figure 9.0.1: Attitude determination and control block diagram

9.1 CubeSat Model and Requirements

9.1.1 CubeSat model

In order to conduct a simulation of the CubeSat motion, the inertia matrix has to be found. Table 9.1.1 shows the center of mass of the whole satellite without reaction wheels C_0, and the center of mass of the whole spacecraft C.

Table 9.1.1: Symbols used for CubeSat model

J_0	Body principle MOI without wheel	I_0	Wheel inertia (1,2,3)
J_d	Inertia due to shift of COG	I_d	Inertia due to displacement from C_g (1,2,3)
m_b	Body mass without wheel	m_g	wheel mass
T_{WB}	transf. from wheel ref. to body ref.	$\hat{a}\ \hat{b}\ \hat{c}$	rotational axes of reaction wheels (1,2,3)
ω^B	Bus rot. speed relative to inertial ref.	ω_{rw}	wheel speed

The distance from C_0 to C is $\vec{d_b}$ and the distance from reaction wheels to C is $\vec{d_{rw_{1,2,3}}}$. The following table gives the symbols used and together with their meaning:

To simplify the calculation, wheel rotation axes are aligned with the body axes. Therefore, the entries of T_{WB} are constants.

The moment of inertia after transforming the C_g of each element to the body frame C_g can be calculated by using the parallel axes theorem:

$$J_B = J_0 + J_d = J_0 + m_b[(\vec{d_b} \cdot \vec{d_b})\vec{E_3} - \vec{d_b}\vec{d_b}^T] \tag{9.1.1}$$

$$I_{1,2,3} = I_{0_{1,2,3}} + I_{d_{1,2,3}} = I_{0_{1,2,3}} + m_g[(\vec{d_{rw_{1,2,3}}} \cdot \vec{d_{rw_{1,2,3}}})\vec{E_3} - \vec{d_{rw_{1,2,3}}}\vec{d_{rw_{1,2,3}}}^T] \tag{9.1.2}$$

The entries of the inertia matrix have been found using MATLAB and have been verified with CATIA.

9.1.2 ADCS Requirements

The ADCS design is derived from pointing requirements from subsystems, payloads, and QB50 mission requirements [55]. As the final configuration and mission objectives of the satellite has been determined in Section 2.3, all requirements imposed on ADCS system are derived and listed in Table 9.1.2.

Table 9.1.2: ADCS requirements

Related to	Type of requirement	Accuracy
Subsystems		
EPS	Orientation of solar array to sun	rough
Communication	Pointing to the ground station (nadir)	omni-directional (VHF)
Payloads and components		
FIPEX	Aligned with velocity vector	$\pm 10°$
Modes and Operations		
Lifetime extension	decrease of drag coefficient	$\pm 2°$
Detumbling	detumbling within 2 days	from $10° s^{-1}$ to $0.132° s^{-1}$
Safe mode	Attitude stabilisation	rough
Formation flying	Orientation of antenna to Delta	none (omni-directional (VHF))

According to the table, the driving requirement is mission design. Due to the high aerodynamic drag in lower orbit, it is more desirable to have a higher pointing accuracy that is necessary for the payloads to increase the lifetime of the satellite.

Detumbling mode According to the QB50 requirements, the satellite shall be able to recover from a tip-off rate of $10° s^{-1}$ within 2 days. During this phase, due to high rates, sun direction drifts rapidly over from sun sensors field of view. However, given the tip-off rate, an open-loop control can fulfill the task. The control system will perform spin stabilisation first and after slowing the spin rate to a certain level $\omega_{Detumble}$, 3-axis stabilization will take over to provide more precise attitude control.

The orbital period of Phi at 320 km is 90.93 min or 5455.6 s. This yields the angular velocity of satellite with respect to the ECI reference frame, given by

$$\omega_{Detumble} = 2 \cdot \frac{\pi}{5455.6} = 0.0023\ [rad \cdot s^{-1}] = 0.132[° s^{-1}] \tag{9.1.3}$$

Partial sun pointing The spacecraft is orbiting around the Earth. While pointing into the velocity vector, the satellite will rotate around the roll axis in a way that is most beneficial to the solar power. According to Figure 9.1.1, partial sun pointing is achieved when the projection of the surface normal vector of the wing onto the eclipic plane is parallel to the sun vector. And in Figure 9.1.2, it shows that the sun vector lies on the X-Z-plane of the body frame. The angular velocity around roll axis with respect to the ECI reference frame is $\omega_{sp} = 1.171° \cdot day^{-1}$, which has been determined using STK.

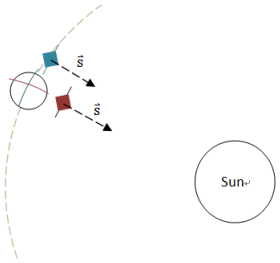

Figure 9.1.1: Illustration of partial sun pointing
(a) 2D view

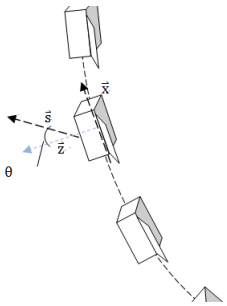

Figure 9.1.2: Illustration of partial sun pointing
(b) 3D view

9.2 Mathematical Attitude Representation

It is critical to represent the attitude in mathematical terms such that the computer can process the attitude information. There are many mathematical constructs used to represent the attitude of a rigid body in three-dimensional space. As mentioned in the Mid-term report [36], Euler angles and quaternions are used for calculation and simulation. Euler angles are used to ease the visualisation of the rotation of the spacecraft, and during nominal mode with small rotating angles. Quaternions are useful during detumbling mode, because the spacecraft will rotate for more than 90 degree, which is not possible with Euler angles due to singularities.

Euler angles Euler angles are defined by sequential rotations of the original and intermediate reference frames. For space applications, a 3-2-1 rotation sequence is favoured. Three rotation matrices for each angle can be found in [67]. Combined together, the rotation matrix is:

$$R = R_\phi R_\theta R_\psi \tag{9.2.1}$$

Unit quaternion A quaternion is represented as a vector,

$$q = \begin{bmatrix} q_0 & q_1 & q_2 & q_3 \end{bmatrix}^T = \begin{bmatrix} q_0 \\ \mathbf{q_{1:3}} \end{bmatrix} \tag{9.2.2}$$

where

$$\mathbf{q} = \begin{bmatrix} q_1 \\ q_2 \\ q_3 \end{bmatrix} = sin(\Phi/2)\hat{e} \tag{9.2.3}$$

$$q_0 = cos(\Phi/2) \tag{9.2.4}$$

the unit-column vector $\hat{e}$ is the representation of the rotation axis, and Φ is the rotation angle. The orthogonal matrix corresponding to a clockwise/left-handed rotation by the unit quaternion $q = q_0 + iq_1 + jq_2 + kq_3$ is given by the homogeneous expression in Equation 9.2.5, which transform the orthogonal system into the desired one.

$$R = \begin{bmatrix} q_0^2 + q_1^2 - q_2^2 - q_3^2 & 2(q_1q_2 - q_0q_3) & 2(q_0q_2 + q_1q_3) \\ 2(q_1q_2 + q_0q_3) & q_0^2 - q_1^2 + q_2^2 - q_3^2 & 2(q_3q_2 - q_1q_0) \\ 2(q_1q_3 - q_0q_2) & 2(q_1q_0 - q_2q_3) & q_0^2 - q_1^2 - q_2^2 + q_3^2 \end{bmatrix} \tag{9.2.5}$$

As to the value of $\mathbf{q}$ can be calculated by using Euler angles.

9.3 Disturbance Torques in Space

The ADCS design budget was calculated to ensure that the actuators would be capable of overcoming the largest disturbances that the satellite will experience. The disturbances that the budget takes into account are gravity gradient, solar pressure, magnetic, thrust misalignment, which are treated in this section, and aerodynamic disturbance, which have been discussed in Section **??**. During deputy mode, thruster is used to adjust the distance between two satellites. Therefore, thrust misalignment is considered only during formation flying, while others exist during the whole operation time. Due to the high value of of the torques orginating from the thruster misalignment, the torque during formation flying will be the driving requirement of the whole spacecraft.

9.3.1 Magnetic Torque

- Type of disturbance: Cyclic
- Influenced by: orbit altitude, residual spacecraft magnetic dipole, and orbit inclination

Table 9.3.1: Summary of all external torques during formation flying

Torques	T_x [N]	T_y [N]	T_z [N]
T_{aero}	$3.482 \cdot 10^{-10}$	$-2.570 \cdot 10^{-6}$	$5.844 \cdot 10^{-7}$
T_m	$5.371 \cdot 10^{-7}$	$4.765 \cdot 10^{-7}$	$1.255 \cdot 10^{-7}$
T_{sr}	$1.466 \cdot 10^{-8}$	$1.466 \cdot 10^{-8}$	$1.466 \cdot 10^{-8}$
T_{gg}	$1.096 \cdot 10^{-10}$	$4.103 \cdot 10^{-8}$	$4.087 \cdot 10^{-8}$
T_t	-	$\pm 2.400 \cdot 10^{-5}$	$\pm 2.400 \cdot 10^{-5}$
T_{tot}	$5.518 \cdot 10^{-7}$	$2.143 \cdot 10^{-5}$	$2.477 \cdot 10^{-5}$

- Formula:

$$T_m = D \times B \tag{9.3.1}$$

D is the residual dipole of the vehicle and B is the magnetic flux. The magnetic flux is estimated from the World Magnetic Model from Aerospace Toolbox in MATLAB.Figure 9.3.1 plots the magnetic torque about each axis for one orbit at 200 km.

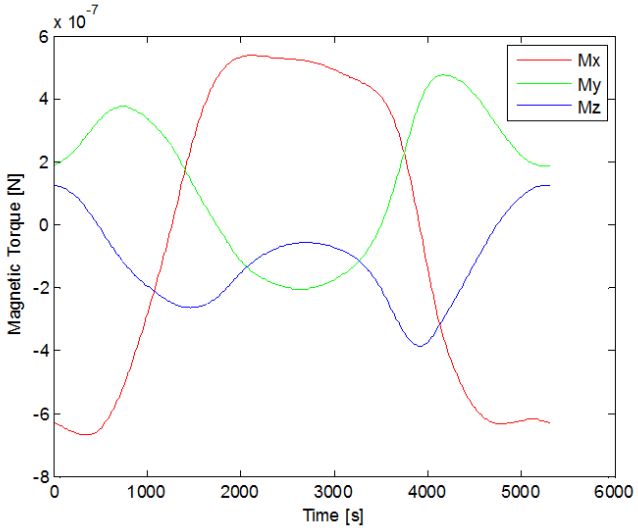

Figure 9.3.1: Magnetic torque acting on the spacecraft sbout each axis

9.3.2 Gravity Gradient Torque

- Type of disturbance: Cyclic
- Influenced by: spacecraft orientation and orbital altitude
- Formula:

$$\overrightarrow{T_{gg}} = \frac{3\mu}{\left|\overrightarrow{R_{cm}}\right|} \hat{\overrightarrow{R}} \times J \hat{\overrightarrow{R}} = \begin{bmatrix} (J_z - J_y) R_z R_y \\ (J_x - J_z) R_x R_z \\ (J_y - J_x) R_x R_y \end{bmatrix} \cdot \frac{3\mu}{\left|\overrightarrow{R_{cm}}\right|} = \begin{bmatrix} (J_z - J_y) \sin(2\phi) cos^2(\theta) \\ (J_x - I_z) \sin(2\theta) cos(\phi) \\ (I_y - I_x) \sin(2\phi) sin(\phi) \end{bmatrix} \cdot \frac{3\mu}{\left|\overrightarrow{R_{cm}}\right|} \tag{9.3.2}$$

where,

- $\overrightarrow{T_{gg}}$ = maximum gravity torque about each axis,
- R_{cm} = orbit radius,
- μ = gravitational constant of Earth,
- θ = maximum pitch angle deviation of the z axis from local vertical
- ϕ = maximum roll angle deviation of the z axis from local vertical

Shown in Figure 9.3.2, gravity gradient torque depends on the altitude and attitude of the spacecraft. For a more precise attitude control, torques in all three axis decrease at least 90% compared the highest torque can expected. However, during conceptual design phase, the maximum torque can expected in each axis is considered.

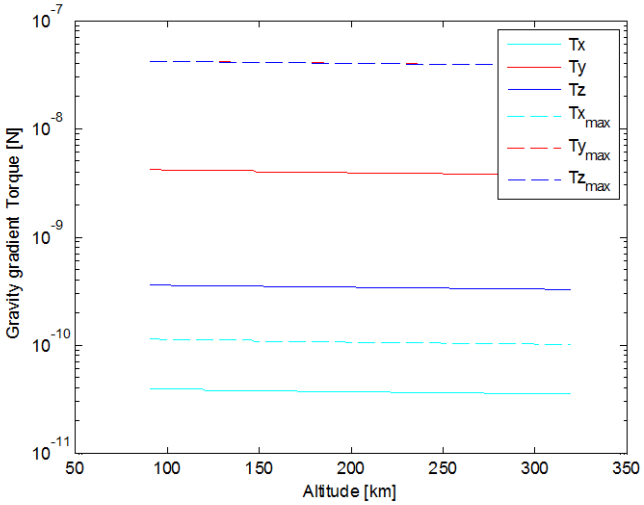

Figure 9.3.2: Gravity gradient torque on the spacecraft in each axis

9.3.3 Solar Radiation Torque

- Type of disturbance: Cyclic
- Influenced by: spacecraft geometry, spacecraft surface reflectivity, and center of gravity location
- Formula:

$$T_{sr} = \frac{F_s}{c} A_s (1+q) \cos\theta_i (C_{ps} - C_g) \tag{9.3.3}$$

where,

- T_{sr} = solar radiation torque,
- $F_s = 1367 W m^{-2}$ solar constant,
- $c = 3 \cdot 10^8 m s^{-1}$ speed of light,
- $C_{ps} - C_g = 10\%$ of the maximum edge,
- q= surface reflectance,
- θ_i = angle of incidence to the sun.

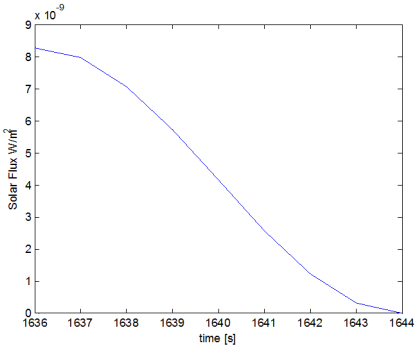

Figure 9.3.3: Solar flux when the vehicle enters penumbra

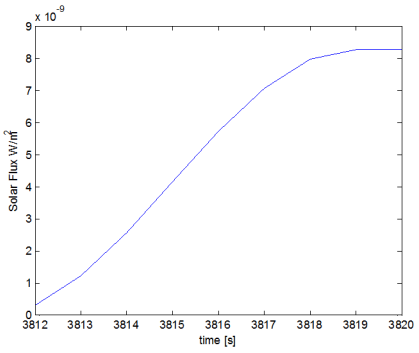

Figure 9.3.4: Solar flux when the vehicle exits penumbra

Because the spacecraft is always aligned with the velocity vector, the projection of the spacecraft on the plane perpendicular to the sun vector varies over the course of the orbit. This will lead to variations in the solar radiation pressure. When a spacecraft experiences solar eclipse by the Earth, a solar torque is generated by the nonuniform solar radiation pressure within penumbra. For the Phi satellite, the spacecraft passes through the penumbra region within 8 s, and the strength of the solar radiation pressure is depicted in Figure 9.3.3 when entering eclipse and Figure 9.3.4 when exiting eclipse. And the full variation of solar radiation torque during one full orbit is shown in Figure 9.3.5.

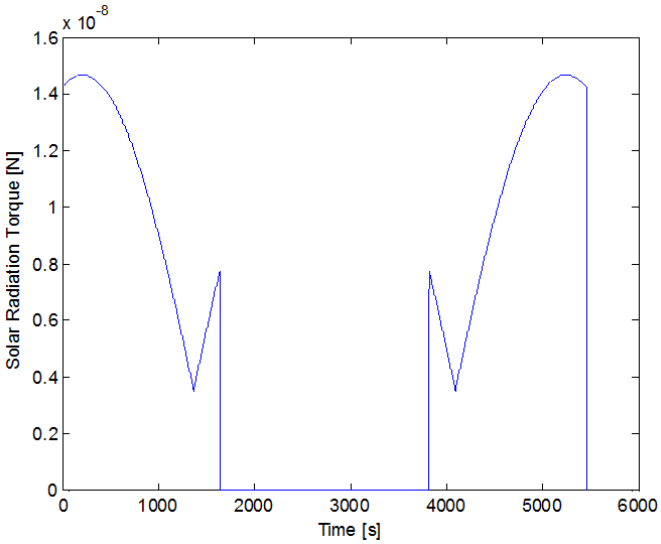

Figure 9.3.5: Solar radiation torque experienced by the spacecraft around each axis

9.3.4 Thrust Misalignment

- Type of disturbance: Secular
- Influenced by: thrust level, uncertainty of center of mass, uncertainty of thrust work line
- Formula:

$$T_m = F \cdot s \tag{9.3.4}$$

Because the propulsion system used in Phi is the same as Delfi-n3Xt, and is also assembled in TU Delft laboratory, similar assumptions can be made[68]:

- inaccuracy in determining satellite C_m: $\pm 2.5mm$
- inaccuracy in thruster position due to installation in the spacecraft: $\pm 1mm$
- thrust off-set: $\pm 0.3mm$

9.4 Sensors

There are three common measurements performed in LEO: radial direction, via horizon sensors, sun direction and magnetic field directions. For high inclination orbits such as the one in the mission considered here, there is a particular concern about the singularity in the area aroung the pole. In addition, for CubeSats, requirements on the miniaturisation of the sensors is particularly stringent. Therefore, horizon sensors are not a good option due to its high mass and power consumption. A combination of the magnetic field and sun vector measurement provide good performance during the time when the satellite is in sunlight. As can be seen in Figures 9.4.1 and 9.4.2, those vectors never align along the orbit path and no singularities can occur.

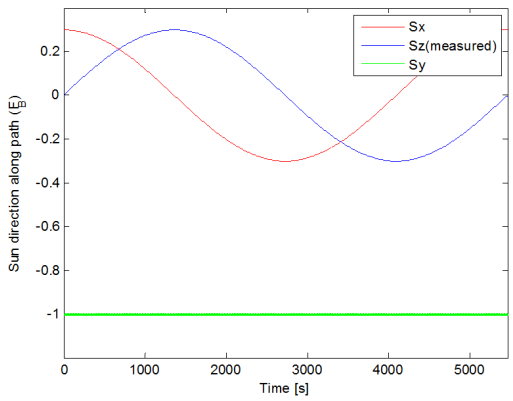

Figure 9.4.1: Sun direction along orbit path

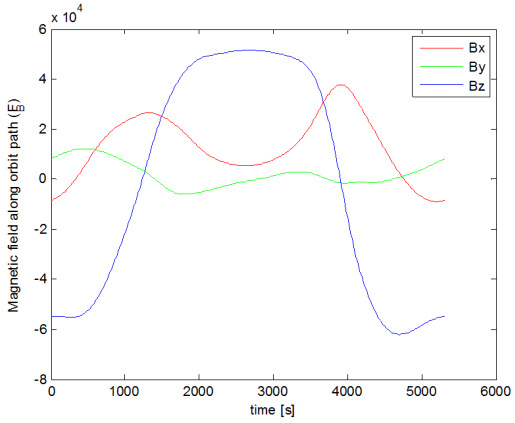

Figure 9.4.2: Magnetic field along orbit path

However, the sun sensor's functionality is limited to the time when the satellite is not in eclipse . And due to the variation and inaccuracy of the magnetic field, the performance of magnetometer can not fulfill the requirement

Table 9.4.1: Attitude determination solutions and performances summary

	Sun sensor	Star Tracker	Magnetometer
Company	SSBV	ST-200	PNI Corp
Field measurement range	114°	-	$\pm 1100 \mu T$
Accuracy	$< 0.5°$	$30''$	-
Mass [g]	< 5	50	5
Power supply voltage [V]	5	3.3-5	3.3
Power consumption [mW]	< 50	220 (Nom.) 650(Peak)	1.5
Size $[mm^3]$	$33 \times 11 \times 6$	$30 \times 30 \times 38.1$	$25.4 \times 15.4 \times 19$
Operating temperature	$[-25°C - +50°C]$	$[-25°C - +50°C]$	$[-25°C - +90°C]$
Comment		internal gyroscope	

during formation flying. Therefore, a possible alternative solution is represented by recent improvement in low-cost miniaturised star tracker technology. The final combination of attitude control system is summarised in Table 9.4.1.

9.5 Actuators

The choice of the actuators is a combination of three reaction wheels and five 3-axis magnetic torquers. The initial analysis of the different actuators eliminated other potential choices as shown in [36].

9.5.1 Reaction wheels

Reaction wheels must be able to withstand the disturbance torques around its axis. Assuming that all the disturbances are given around the axis of the wheel, the torque output for the reaction wheel is equal to the sum of disturbance torques and includes a margin factor of 100%. According to Table 9.3.1, the maximum torque during the mission is $2.447 \cdot 10^{-5} Nm$ abouth the Y axis. And the minimum torque produced by reaction wheel is the twice as much as the disturbance $2.447 \cdot 10^{-5}$ Nm.
One of the main problems encoundered when using reaction wheels in space is saturation. The wheel must change its own angular momentum in order to impart a torque on the Cubesat. In a worst case scenario the wheel must continually provide a torque in one direction, this will cause the wheel to continuously accelerate in one direction. Eventually the motor reaches the maximum angular velocity and cannot continue to accelerate the wheel. In this condition the wheel is referred to as being saturated, and therefore cannot provide further torque to the satellite.
In order to guarantee that the wheel is never completely saturated it is necessary to quantify the momentum storage that the wheel must provide each orbit. To do so we consider all forces as secular, in this way assuming that all forces act all the time on the axis, and get the following approximation for the momentum that needs to be stored during one orbit. For the Phi satellite, the thruster will operated 5 to 6 times during deputy mode, and thrusting lasts for 10 s. In this way, the momentum storage of reaction wheel should be $4.894 mNms$.

9.5.2 Magnetic torquers and momentum dumping

Magnetic torquers are induction coils which are used to create a magnetic field. This field interacts with the Earth's magnetic field and creates a torque which is then used to change the attitude of the spacecraft. Because the produced torque is proportional to the Earth's magnetic field, the magnetic torquers are more effective at the low orbits, making them suitable for the DelFFi mission.

The major drawback of this method of attitude stabilisation is its dependency on the cross-product between the normal vector of the coil area and the magnetic field vector. This implies that if both vectors are parallel the produced torque is zero, meaning that there will be one direction about which no torque can be produced, namely the one parallel to the magnetic field. For the sizing of the torquer, momentum dumping should be considered first.

As the perturbing forces are acting on the satellite's body, the reaction wheels will accelerate constantly to counteract these forces. This acceleration will continue until the reaction wheels are saturated, meaning that attitude manoeuvring is not possible anymore. The excess momentum must be unloaded, which can be done by making use of a momentum dumping scheme which is in general done in CubeSats by using magnetic torquers. As the magnetic torquers produce torque in one direction, a reaction wheel can be decelerated while producing a net torque of zero.

In order for the magnetic torquers to be able to perform momentum dumping of the reaction wheels, they must produce a torque than is higher than the current perturbing torques that are present in that orbit.

The relevant equations for the sizing of the torquers are

$$i_c = \frac{P}{U} \tag{9.5.1}$$

and

$$m_b = i_c NA \tag{9.5.2}$$

where A is the coil area, N is the number of turns for the coils, and m_b is the total magnetic moment which is used to find the torque produced by magnetic torquer given by

$$\tau_b = m_b \times B_b = m_b \cdot B_b sin(\alpha) \tag{9.5.3}$$

where α is the angle between Earth's magnetic field and the magnetic moment produced by the magnetic torquer. The final selection of the components is given in Table 9.5.1

Table 9.5.1: Attitude control solutions and performances summary

	Reaction Wheel (3×)	Magnetic Torquer (5×)
Torque $[mNm]$	1	
Momentum $[mNm \cdot s]$	7	-
Mass [grams]	90	30
Power [W]	0.2(Nom) 0.7(Peak)	0.2
Voltage [V]	3.3 -6	5
Size [mm]	$50 \times 40 \times 27$	$70 \times 9 \times 9$
Operating temp.	$[-40°C - 70°C]$	$[-35°C - 75°C]$

9.6 ADCS Stability

9.6.1 Rigid body dynamics

In order to build a simulation to represent the satellite's altitude control system and do verify that it meets the mission requirements, the equations of motion had to be developed, which can then be built into Simulink. These models were tested and subsequently used to validate the controller design. The equation of motion were established based on Euler's rotational equations of motion:

$$\dot{\mathbf{h}}^B = \mathbf{J}\dot{\omega}|^B = \sum \mathbf{M^B} \tag{9.6.1}$$

$$\mathbf{J}\dot{\omega}|^B + \omega^I \times \mathbf{J}\omega^I = \mathbf{M_{rw}} + \mathbf{T_{dist}} \tag{9.6.2}$$

In Eqn.9.6.1, ω^B is defined with respect to the body reference frame. However, the angular velocity derived from ADCS modes are represented in the inertia reference frame. Therefore, ω^I has to be converted into the body frame as shown in Eqn.9.6.2. **J** is the moment of inertia in the body reference frame, which is a full matrix, of the whole system including the reaction wheels. Because the reaction wheel is a momentum exchanging device, different from e.g. thrusters whose generated momentum depend on their mounting locations, the locations of reaction wheels do not influence the moment inertia. Therefore, the mass moment of inertia of reaction wheels does not need to be considered separately. For the external moments shown on the right side of Equation 9.6.3, torques generated by magnetic torquers are absent. This is because reaction wheels and magnetic torquers should not be operated at the same time. Magnetic torquers should only be turned on for detumbling and momentum dumping in order to avoid influencing the operation of other components due to their high magnetic flux.
For a three dimensional system, it is more clear to convert Euler's dynamic equation in matrix form:

$$\begin{bmatrix} J_{xx} & -J_{xy} & -J_{xz} \\ -J_{xy} & J_{yy} & -J_{yz} \\ -J_{xz} & -J_{zy} & J_{zz} \end{bmatrix} \begin{bmatrix} \dot{\omega_x} \\ \dot{\omega_y} \\ \dot{\omega_z} \end{bmatrix} + \begin{bmatrix} 0 & -\omega_z & \omega_y \\ \omega_z & 0 & \omega_x \\ -\omega_y & \omega_x & 0 \end{bmatrix} \begin{bmatrix} J_{xx} & -J_{xy} & -J_{xz} \\ -J_{xy} & J_{yy} & -J_{yz} \\ -J_{xz} & -J_{zy} & J_{zz} \end{bmatrix} \begin{bmatrix} \omega_x \\ \omega_y \\ \omega_z \end{bmatrix} = \begin{bmatrix} M_{rw_x} \\ M_{rw_y} \\ M_{rw_z} \end{bmatrix} + \begin{bmatrix} T_{dist_x} \\ T_{dist_y} \\ T_{dist_z} \end{bmatrix} \tag{9.6.3}$$

9.6.2 Rigid body kinematics

The spacecraft is orbiting in a circular orbit with an angular velocity of $n = \sqrt{\frac{\mu}{R_{cm}}^3}$ around Y axis, that $\omega^O = -|\omega^O|\bar{\mathbf{Y}}$. And ω^B can therefore represented in the orbital frame.

$$\omega^B = \omega^{B/O} + \omega^O = \omega^{B/O} - |\omega^O|\hat{o_y} \tag{9.6.4}$$

The transformation between orbital frame and the body frame is the rotation around x axis (X-axis), taking clockwise as positive.

$$\begin{bmatrix} \hat{b_x} \\ \hat{b_y} \\ \hat{b_z} \end{bmatrix} = \begin{bmatrix} cos\phi & sin\phi & 0 \\ -sin\phi & cos\phi & 0 \\ 0 & 0 & 1 \end{bmatrix} \begin{bmatrix} \hat{o_x} \\ \hat{o_y} \\ \hat{o_z} \end{bmatrix} \tag{9.6.5}$$

The angular velocity of B relative to O is represented in the body frame as

$$\omega^B = \omega_x \hat{b_x} + \omega_y \hat{b_y} + \omega_z \hat{b_z} \tag{9.6.6}$$

From Eqn. 9.6.5, $\hat{o_y}$ can be easily represented in the body frame.

$$\hat{o_y} = sin\phi \hat{b_x} + cos\phi \hat{b_y} \tag{9.6.7}$$

Inserting both Eqn. 9.6.6 and 9.6.7 into Eqn. 9.6.4 and arranging the result in matrix form yields Equation 9.6.8

$$\begin{bmatrix} \omega_x \\ \omega_y \\ \omega_Z \end{bmatrix} = \begin{bmatrix} \dot{\phi} \\ \dot{\theta} \\ \dot{\psi} \end{bmatrix} - n \begin{bmatrix} sin\phi \\ cos\phi \\ 0 \end{bmatrix} \tag{9.6.8}$$

Finally the kinematic differential equations of the spacecraft in the circular orbit are derived:

$$\begin{bmatrix} \dot{\phi} \\ \dot{\theta} \\ \dot{\psi} \end{bmatrix} = \begin{bmatrix} \omega_x \\ \omega_y \\ \omega_Z \end{bmatrix} + n \begin{bmatrix} sin\phi \\ cos\phi \\ 0 \end{bmatrix} \tag{9.6.9}$$

Equation 9.6.9 together with three dynamic equations in the previous section (Equation 9.6.3),a set of six linearised equations is derived for linear stability analysis. Combining the linearised dynamic and kinematic equations by differenciating Eqn.9.6.9 and inserting it into Eqn. 9.6.3 yields

$$\begin{bmatrix} \ddot{\phi} \\ \ddot{\theta} \\ \ddot{\psi} \end{bmatrix} - n \begin{bmatrix} \dot{\phi} sin\phi + cos\phi \\ \dot{\phi} cos\phi - sin\phi \\ 0 \end{bmatrix} = \mathbf{J}^{-1}(\mathbf{M_{rw}} + \mathbf{T_{dist}} - \begin{bmatrix} \dot{\phi} - nsin\phi \\ \dot{\theta} - nsin\phi \\ \dot{\psi} \end{bmatrix} \times \mathbf{J} \begin{bmatrix} \dot{\phi} - nsin\phi \\ \dot{\theta} - nsin\phi \\ \dot{\psi} \end{bmatrix}) \tag{9.6.10}$$

However, the resulting equation is not linear due to the trigonometric coefficient in the equation. In order to linearise the equation, all Euler angles can be assumed to be small such that $sin\phi \approx \phi$, $cos\phi \approx 1$, and $\omega_y \approx -n$. In addition, the moment of inertia in the body frame is converted into principle moment of inertia, which can be calculated in CATIA. To conclude, the final equation is listed below as Equation 9.6.11.

$$\begin{bmatrix} \ddot{\phi} - n\dot{\phi} \\ \ddot{\theta} \\ \ddot{\psi} \end{bmatrix} = \mathbf{J_P}^{-1}(\mathbf{M_{rw}} + \mathbf{T_{dist}}) \tag{9.6.11}$$

9.6.3 Attitude Stability

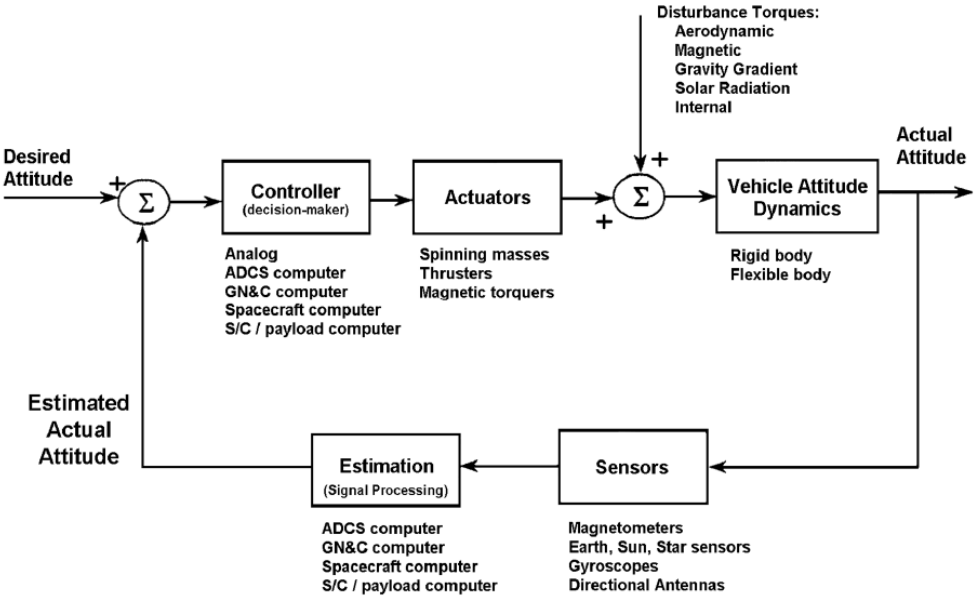

Figure 9.6.1: Close loop of ADCS system

The ADCS system is a close-loop system as shown in Figure 9.6.1. To design a three-axis control scheme (controller), the following steps have to be carried out: the time derivative of the angular momentum of the reaction wheel

constitutes a control torque which can be implemented using proportional and differentiation control laws.

$$\dot{\mathbf{H}_{\mathbf{rw}}} = {\mathbf{k_p}}^T \begin{bmatrix} \phi \\ \theta \\ \psi \end{bmatrix} + {\mathbf{k_d}}^T \begin{bmatrix} \dot{\phi} \\ \dot{\theta} \\ \dot{\psi} \end{bmatrix} \tag{9.6.12}$$

The three-axes closed-loop system can be written as

$$J_{xx}\ddot{\phi} + (k_{d_x} - J_{xx}n)\dot{\phi} + k_{p_x}\phi = T_{dist_x} \tag{9.6.13}$$

$$J_{yy}\ddot{\theta} + k_{d_y}\dot{\theta} + k_{p_y}\theta = T_{dist_y} \tag{9.6.14}$$

$$J_{zz}\ddot{\psi} + k_{d_z}\dot{\psi} + k_{p_z}\psi = T_{dist_z} \tag{9.6.15}$$

Laplace In these closed-loop control systems, in total six control gains need to be determined. This task is called the controller synthesis. There are many ways to design the gains. Here the so-called disturbance rejection method to design the control gains is used.

Laplace transforms of above equations are

$$(J_{xx}s^2 + (k_{d_x} - J_{xx}n)s + k_{p_x})\phi(s) = \frac{T_{dist_x}}{s} \tag{9.6.16}$$

$$(J_{yy}s^2 + k_{d_y}s + k_{p_y})\theta(s) = \frac{T_{dist_y}}{s} \tag{9.6.17}$$

$$(J_{zz}s^2 + k_{d_z}s + k_{p_z})\psi(s) = \frac{T_{dist_z}}{s} \tag{9.6.18}$$

The steady state rotation of the spacecraft can be obtained by using the final value theorem

$$\begin{bmatrix} \phi_{ss} \\ \theta_{ss} \\ \psi_{ss} \end{bmatrix} = \lim_{t\to\infty} \begin{bmatrix} \phi(t) \\ \theta(t) \\ \psi(t) \end{bmatrix} = \begin{bmatrix} \frac{T_{dist_x}}{k_{px}} \\ \frac{T_{disty}}{k_{py}} \\ \frac{T_{dist_z}}{k_{pz}} \end{bmatrix} \tag{9.6.19}$$

The steady state angle is determined by the requirement of the space mission. In this case, steady state rotation angle is set to 2°. The closed-loop transfer function is compared with a standard second order system:

$$H(s) = \frac{\phi}{T_{dist_x}} = \frac{1}{J_{xx}s^2 + (k_{d_x} - J_{xx}n)s + k_{p_x}} = \frac{\frac{1}{J_{xx}}}{s^2 + 2\zeta_x\omega_{n_x}s + \omega_{n_x}^2} \tag{9.6.20}$$

$$H(s) = \frac{\theta}{T_{dist_y}} = \frac{1}{J_{yy}s^2 + k_{d_y}s + k_{p_y}} \tag{9.6.21}$$

$$H(s) = \frac{\psi}{T_{dist_z}} = \frac{1}{J_{zz}s^2 + k_{d_z}s + k_{p_z}} \tag{9.6.22}$$

Comparing the coefficient, the value of k_p and k_d can be easily achieved. For this stage, setting up model for stability is done, and the simulation can be done with stability.

9.7 Sensitivity Analysis

The size and configuration of the ADCS is highly dependent on other subsystems, especially on the GNC system. The ADCS is particularly sensitive to driving requirements and maximum torques. However, so far all the components have been sized for the worst case scenario with a precise estimation for all disturbances that can be expected. However, the shifting of center of gravity has not been considered yet. According to Table 9.3.1, thrust misalignment is most influencing disturbance in space. Therefore, the constraint on the propulsion system with respect to the accuracy and estimation of the c.g. should be precise enough to decrease the influence imposed on ADCS system. Otherwise, the final design will not change dramatically in the future.

9.8 Verification and Validation

The verification and validation plan is intended to assure the nominal operation of all components. The attitude determination and control system is simulated with MATLAB, to the model should be verified before proceeding to the next step in the design process. For certain altitudes, some parameters have been calculated by using an Excel sheet, and compared with values from the simulation. Validation encompasses a wide variety of highly interrelated activities, and all of them need to be validated:

- **Requirement validation** : ensuring the right requirements are used for design.
- **Model validation** : ensuring the models that support design decisions are correct.
- **Component validation** : testing of sensors and actuators before assembly.
- **System validation** : validation of entire system.

9.9 Recommendation

MEMS gyroscope can be considered to be taken onboard which is lightweight and displays good performance characteristics. A more detailed stability analysis can be made with Simulink or equivalent programs.

Chapter 10
Communication System

This chapter will elaborate on the communications subsystem of the Phi satellite. First, the communications flow diagram of the satellite mission will be presented. Subsequently, a downlink and uplink scheme will be shown, which will clarify the amount of time that is available to the satellite for downlink and uplink. The chapter will continue with the final component trade-off. After the trade-off the chapter will continue with the link budget for the uplink, downlink and inter-satellite link. Then, a sensitivity analysis of the communication system will be shown. The chapter will finish with the verification and validation procedures.

10.1 Communication flow diagram

The satellite will communicate with different segments during the mission. An overview of the whole communication system of the mission is shown in Figure 10.1.1. Four segments are present in this mission:

- Phi Satellite
- Delta Satellite
- Ground Station
- GPS Satellite

In order to send payload data to the ground station as well as to send commands to the satellite, a link between the satellite and the ground station is necessary. Besides the link with the ground station, the satellite will also communicate with the Delta satellite. In modes 3 and 4 of formation flying, the communication between the two satellites will be achieved using an inter-satellite link (ISL). Another link exists between the satellite and the GPS constellation. This link is used to determine the position of the satellite, which is of prime importance to the GNC system.

Figure 10.1.1: Communication flow diagram

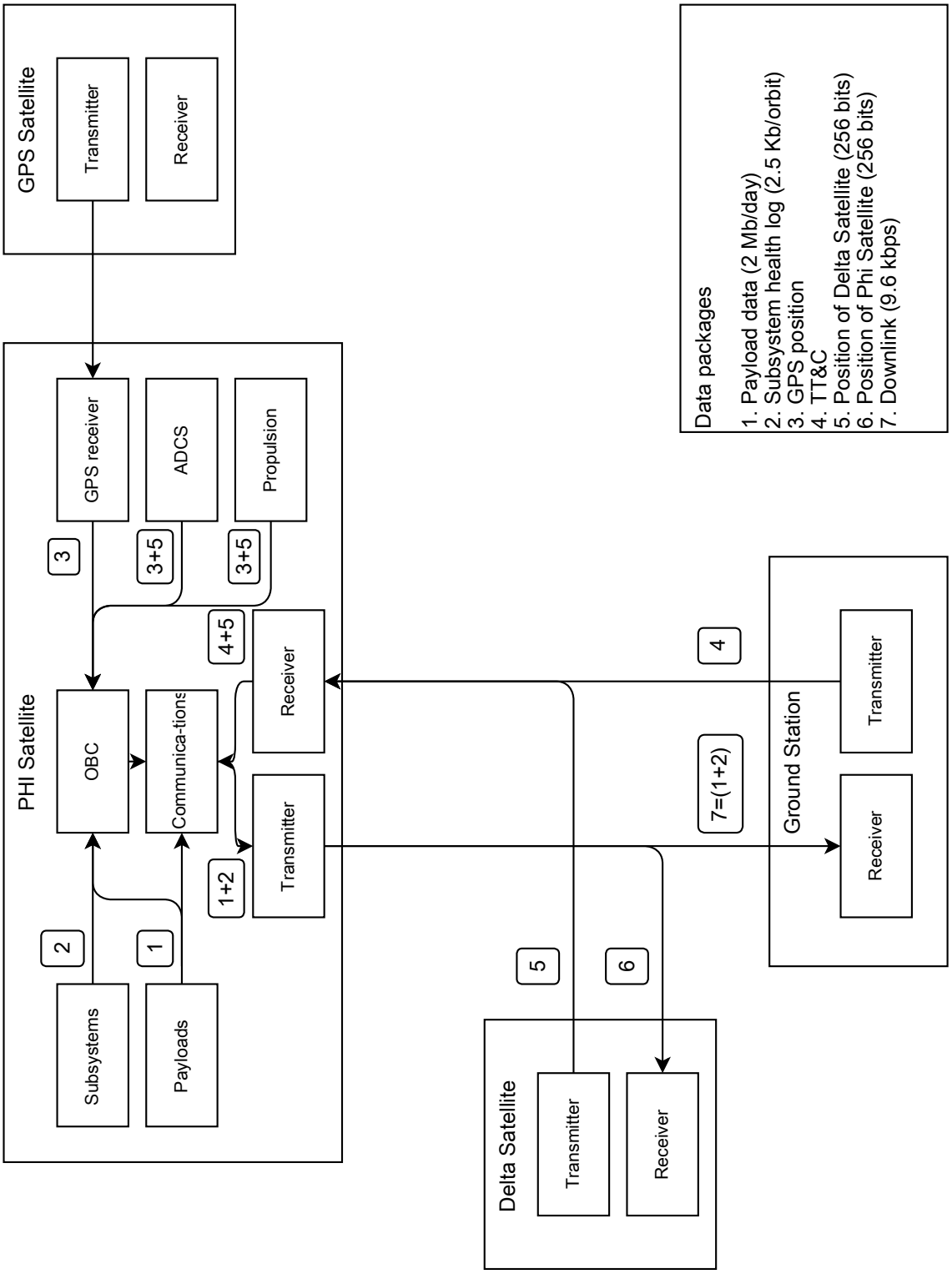

10.2 Uplink and Downlink Scheme

Prior to starting the design of the communication system, an estimation of the downlink and uplink time has to be made. Therefore, the STK software was used to determine the amount of overpasses over the ground station as well as the duration of those overpasses. A summary of the simulation results is displayed in Table 10.2.1. The number of overpasses as well as the duration of the overpasses changes with the altitude.

Table 10.2.1: Uplink & Downlink time

Height	Average number of overpasses per day	Average time of overpass in [s]	Total link time in [s]
350	6	443	2663
300	5.5	409	2244
250	5	373	1860
200	4.57	334	1524
150	4	249	996
100	334	241	810
90	3	230	690

10.3 Data Volume

Three types of data will be transmitted to the ground station:

- QB50 payload data
- Secondary payload data
- System health log data
- Position data

The data volume of each type of data was determined to make a proper data rate requirement on the downlink. Each type will be discussed briefly.

10.3.1 QB50 payload data

The primary payload consists of a FIPEX instrument and thermal sensors. Atmospheric properties will be measured with these sensors and the measurement data will be stored in the mass memory of the satellite before it is sent to the ground station. The amount of data from the primary payload that the communication system has to be able to downlink has been postulated by QB50 to be 2 Mbytes per day [55].

10.3.2 Secondary mission data

Besides the QB50 payload, two other payloads will be present in the satellite: An acoustic experiment and camera payload. Both devices are producing data that needs to be transferred to the ground station as well.

Deployment monitoring camera

The video data is used for monitoring the deployables of the satellite. The most interesting part of the mission is at the very beginning, when the solar panels and antennas are being deployed, the duration of which will be less than a few seconds [5]. Compression techniques will be used to decrease the amount of data that is being sent to the Gound Station. The use of compression techniques is allowed because objects can still be recognised if the pixel data is compressed. Using data compression techniques the video data can be reduced to 100 $KB \cdot s^{-1}$. A video image will be made at the very beginning of the mission, which will be sent to the ground station in multiple pieces. This video will be 10 seconds long. The camera will take more pictures of the deployables during the mission. These pictures will not be bigger than 100 kbytes each, depending on the compression ratio.

Acoustic Sensor

The other secondary payload is an acoustic sensor. Detailed measurements of the acoustic spectrum of the satellite will be taken every orbit. Besides that, the acoustic sensors will be on stand-by. If there is a peak in the frequency spectrum due to, for example an impact, the acoustic sensor will measure this and the data from that period of time will also be sent to the ground station. In contrast to the video camera, the exact values of the vibrations are important for the data analysis. Therefore, data compression cannot be used. Data rates of uncompressed acoustic measurements can go up to 100 $KB \cdot s^{-1}$ as well. A total volume of 10 seconds of acoustic measurements can be sent to the ground station every day.

10.3.3 Health log data

The health log will produce 2.5 kbytes every orbit. This estimation is based on the health log needs of each of the subsystems.

Table 10.3.1: Data volume per day

Data source	Data volume $[KB \cdot day^{-1}]$
Primary payload	2 000
Camera	10 000
Microphone	10 000
Health Log	18
Total	22 018

10.4 Inter-satellite link

The communications system of the satellite is not only used for providing the downlink and uplink. Since one of the objectives is to perform the formation flying without the use of a ground station, an inter-satellite link has to be established during the mission. The data that will be sent through the inter-satellite link will contain information about the position of the satellite. One package of ISL data will be 256 bits, containing the position of the satellite and a time flag. The ISL will not operate during ground station contact. Due to the small size of the ISL data package, the data rate of the ISL can be decreased in order to satisfy the link budget.

10.5 Final design

Several options were considered during the trade-off of the communications system.

- VHF link
- UHF link
- S-Band link
- Multiple links

The VHF link was the final choice of the trade off. A key factor which made the VHF link the best choice was its omni-directionality. Turning the satellite to point an antenna to a receiving target (ground station or satellite) is a costly operation in terms of power and drag coefficient. Also, communication to the ground station should also be possible before the satellite has been detumbled as well as in safe-mode. Another factor was the power consumption that is lower for VHF compared to UHF.

10.5.1 Component trade-off

Different VHF link components are available on the market. There are separate transmitter and receiver components available but also half duplex transceivers that are able to transmit and receive simultaneously. The considered candidates and the important design criteria are summarised in Table 10.5.1.

Table 10.5.1: VHF Link Considered Candidates

Retailer	Component	Data rate [kbps]	Power (transmitter on) [W]	Mass [g]	Price [€]
ISIS	TRXUV	9600	1.5	85	6 750
Clyde-Space	CMCi CubeSat UVTRX	9600	4	90	8 600
Astrodev	Li-1 Radio	> 9.6	10	70	5 000
Astrodev	Helium-100 Radio	34.5	6	77	4 900

A trade-off of all the considered candidates has been made, based on the criteria in Table 10.5.2. Due to the fact that all components are not very costly, a relatively low weight has been assigned to the first criterion. However, the mass is an important criterion because the the requirement is more difficult to meet. This is also true for the power criterion in the trade-off. Radio systems use a substantial amount of energy when transmitting, so this criterion will be given the highest weight. The last criterion is the achievable data rate, which has been given a medium weight because this is not a high data-volume mission and data rate is important but not the main driver. The Astrodev Li-1 does not implement the PC104 bus in its design. This means that this part needs to be adjusted in order to be compatible with the satellite. Therefore, the PC104 will receive a penalty of 5 points. Based on the weights of each criterion, a trade-off has been performed. The results of the trade-off are displayed in Table 10.5.2.

Table 10.5.2: Trade-off criteria for COMMS component

Criterion	Weight
Cost	2
Mass	4
Power	5
Data Rate	3

Table 10.5.3: Considered COTS OBC's

Component	Cost	Mass	Power	Data Rate	Penalties	Total weighted
ISIS TRXUV	3	3	5	3	0	52
Clyde-Space CMCi Cube-Sat UVTRX	4	3	2	3	0	36
Astrodev Lithium-1	5	4	2	5	-5	46
Astrodev Helium-100	5	4	2	4	0	51

The result of the trade-off is that the final choice is the ISIS TRXUV.

10.5.2 Antenna system

The TRXUV is compatible with the ISIS antenna board that consists of four deployable antennas along with a deployment mechanism. No other COTS boards are suitable for the VHF frequencies. The other option would be developing a new antenna board.

10.6 Link budgets

The link budget of the spacecraft's communication system is displayed in Tables 10.6.1 to 10.6.3. Equation 10.6.1 was used to construct the link budgets.

$$\frac{E_b}{N_0} = P + L_l + G_t + L_{pt} + L_{pr} + L_s + L_a + G_r + 228.6 - 10log(T_s) - 10log(R) \tag{10.6.1}$$

The different elements of the link budget can be divided up into four groups: Transmitter, path, receiver and remaining. In the transmitter group, the power and gain as well as line losses and pointing losses are included. The path group includes all losses the signal encounters on the way from satellite to the ground station. The receiver group consists of the receiver gain and the receiver line losses. In the remaining group the data rate is accounted for as well as the system temperature, the margin and the Boltzmann constant. The values of the transmitter group are based on the characteristics of the chosen transmitter [32]. Values in the path group are determined based on the main characteristics of the link. Using [35] [44], the atmospheric loss, space loss, pointing loss and polarisation loss can be determined. For calculating of the space loss, Equation 10.6.2 is used.

$$L_s = \left(\frac{4\pi d}{\lambda}\right)^2 \tag{10.6.2}$$

Using a turnstile antenna configuration, a circular polaristion can be generated. When the circular signal is received by a circular ground station, the polarisation loss will be zero. The receiver group is based on the current ground station that is used for the mission [31].

Table 10.6.1: Link budget for downlink

Item	Symbol	Units	Value
Transmitter			
Power	P	dBW	-8
Antenna Gain (minimum)	G_t	dB	-4
Line loss	L_{lt}	dB	-2
Path			
Polarisation loss	L_p	dB	0
Space Loss	L_s	dB	-139.25
Atmosphere Loss	L_{at}	dB	-2
Receiver			
Antenna Gain	G_r	dB	12
Line Loss	L_{lr}	dB	-2
Pointing Loss	L_{pr}	dB	-0.5
Remaining			
Data Rate	R	dB	-39.8
Noise Temperature	T_s	dB	-24.3
Boltzmann addition	k	dB	228.6
Margin	$\frac{E_0}{N_0}$	dB	-8.7
Energy-per-Bit to Noise-Density Ratio	$\frac{E_0}{N_0}$	dB	10
Bit Error Rate	$\frac{C}{N_0}$	-	10^{-6}

Table 10.6.2: Link budget for uplink

Item	Symbol	Units	Value
Transmitter			
Power	P	dBW	24
Antenna Gain	G_t	dBiC	16.4
Line loss	L_{lt}	dB	-2
Path			
Antenna Pointing Loss	L_{pt}	dB	-1
Space Loss	L_s	dB	-148.95
Atmosphere Loss	L_{at}	dB	-2
Polarisation loss	L_p	dB	0
Receiver			
Antenna Gain	G_r	dB	-10
Line Loss	L_{lr}	dB	-4
Remaining			
Data Rate	R	dB	-30.8
System Noise Temperature	T_s	dB	-27.87
Boltzmann addition	k	dB	228.6
Margin	$\frac{E_0}{N_0}$	dB	-32.4
Energy-per-Bit to Noise-Density Ratio	$\frac{E_0}{N_0}$	dB	10
Bit Error Rate	$\frac{C}{N_0}$	-	10^{-6}

The link budget for the inter-satellite link is displayed in Table 10.6.3.

Table 10.6.3: Link budget for the inter satellite link

Item	Symbol	Units	Value
Transmitter			
Power	P	dBW	-5
Antenna Gain	G_t	dBiC	-4
Line loss	L_{lt}	dB	-2
Path			
Space Loss	L_s	dB	-135.7
Atmosphere Loss	L_{at}	dB	0
Polarisation loss	L_p	dB	0
Receiver			
Antenna Gain	G_r	dB	-10
Line Loss	L_{lr}	dB	-4
Pointing	L_{pt}	dB	-0.5
Data Rate	R	dB	-24.08
Remaining			
System Noise Temperature	T_s	dB	-27.87
Boltzmann addition	k	dB	228.6
Margin	$\frac{E_0}{N_0}$	dB	-5.5
Energy-per-Bit to Noise-Density Ratio	$\frac{E_0}{N_0}$	dB	10
Bit Error Rate	$\frac{C}{N_0}$	-	10^{-6}

10.7 Antenna bending

The end of the operational life of the satellite is determined by the last point in time where data transmission to the ground station is possible. This could be due to the reduced efficiency of the antenna due to the aerodynamic loads that cause bending. Since the chosen antennas have been designed for use at altitudes that are much higher, their behavior at low altitudes has to be investigated.

The same code as for the determination of the drag coefficient of the satellite has been used. A panel with the dimensions of the antenna is aligned parallel to the flow, and then rotated around the Z_B axis by 2°. This will give the worst case loads because the two degrees in yaw represent the worst case orientation of the CubeSat with respect to the velocity vector for a pointing accuracy of 2°. The deflection has been calculated by using the following equations from beam theory:

$$EI\frac{d^4w}{dx^2} = q\,(x) \tag{10.7.1}$$

$$I = \frac{1}{12}dt^3 \tag{10.7.2}$$

where E is the Young's modulus which is 180 GPa for steel, which is the material of the antenna, I is the moment of inertia of the cross-section as given in Equation 10.7.2, w is the deflection of the antenna, q is the line load applied to it, t, d and l are the thickness, the width and the length which are 0.5 mm, 60 mm and 0.5 m, respectively. The length of the antenna is determined by the wavelength used for downlink, which is 146 MHz. Since the uplink frequency is higher (446 MHz), the antenna will be shorter, and lower loads and deflections will occur. Therefore only the downlink antenna will be investigated. Its length is a quarter of the wavelength. The load is given by dividing the drag force by the area of the panel and then by the length.

$$q\,(x) = \frac{\frac{1}{2}\rho V^2 A_{ref} C_D}{dl^2} \tag{10.7.3}$$

Figure 10.7.1 shows the worst case antenna deflections for different altitudes. From [24], the maximum tip deflection for which the antenna is still usable is 5°. It can be concluded that the last contact time will be at an altitude of 95 km.

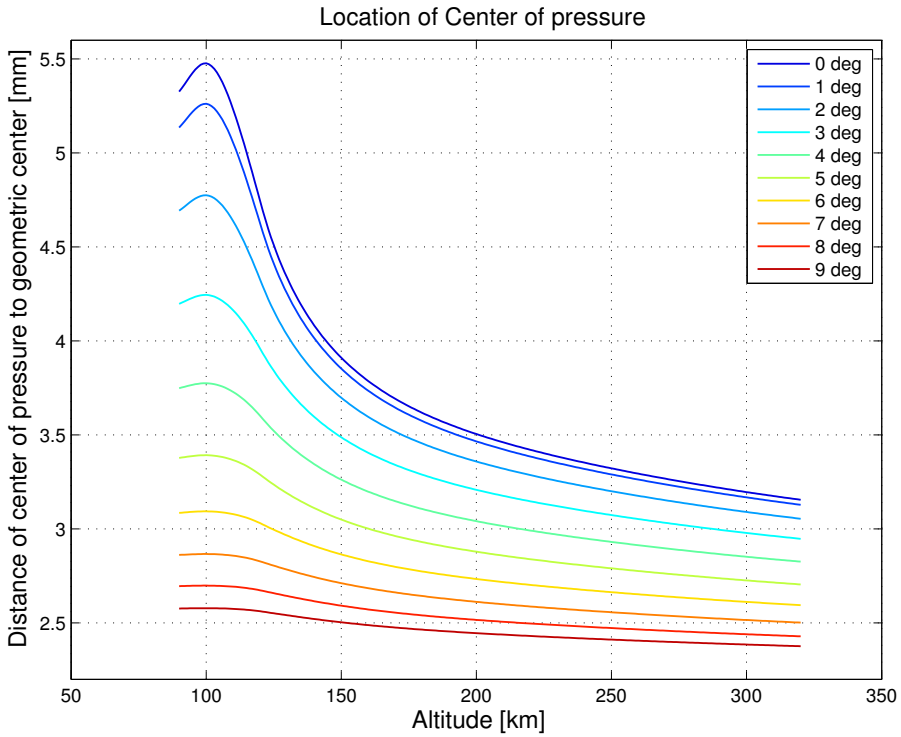

Figure 10.7.1: Worst case antenna deflection for different altitudes

10.8 Sensitivity Analysis

The performance of the communications system is dependent on other subsystems. The most sensitive dependency is the link between the communication system and the EPS. If the EPS is malfunctioning and not capable of delivering the energy needed to power all subsystems, the satellite will limit the amount of data that the satellite is able to downlink. Also, the satellite is designed to shut down unnecessary subsystems when tumbling occurs and use all available power to recover from the anomaly. A priority list has been made that shows which data packets have priority in case an anomaly occurs and power is scarce:

1. Receive data
2. Transmit health log data and position
3. Transmit primary payload data
4. Transmit secondary payload data
5. Transmit ISL data

The most important function of the communication system is the receiver. It is designed to be on continuously, so that the satellite can receive commands at all times. Secondly, it is critically important that the satellite is able to send health log data to the ground station, especially when there is an anomaly. This data can give more information about what is causing the satellite to malfunction, so that appropriate measures can be taken. Thirdly, the ISL needs to be able to transmit the satellites position when it is performing formation flight without the ground station. This is more important than the primary payload data, because the data from the primary sensors can also be stored on the systems memory and be sent to the ground station later on. This is not true for the ISL, because the functioning of the guidance system is dependent on the information from the other satellite. The last priority is transmitting payload data from the secondary payload.

10.9 Verification and Validation

The communications system will be tested thoroughly before it receives qualification for use in space. As the components have to survive the vibrations during launch, a vibration test has to be performed. Besides the launch, the components need to function in the space environment as well. This means that the components need to be able to

function in the temperature range that the spacecraft will experience, be able to function in vacuum and be resilient to plasma interaction as well. The advantage of using COTS components is that most of these tests have already been performed on the hardware.Since duplicating these tests is not necessary, this will save both time and money.

10.9.1 Functional Tests

Besides launch tests and space environment tests the components must be tested for performance. It has to be shown that the radiated power that is produced by the radio is as high as expected. This kind of tests can be performed at a test range, such as the NLR test range, where the Delfi-C3 was tested. Besides the transmitter, the receiver sensitivity must also be tested.

10.9.2 ISL Tests

Due to the importance of formation flying in the Phi mission, the ISL has to be tested thoroughly. Similar to the general link test, the transmitter has to be tested for the ISL data rate as well. But instead of using a normal ground station receiver, a satellite receiver has to be used. Using this method, proper functioning of the ISL can be ensured.

Chapter 11
On-Board Computer and Data Handling

The OBC & DH system handles all the data that is produced by the subsystems of the satellite. First, the data handling architecture of the satellite will be explained. After that the hardware and software configuration of the satellite will be addressed using the H\W & S\W diagram.

11.1 Data Handling Diagram

The data handling diagram of the satellite is presented in Figure 11.1.1. As can be seen in the diagram, the design is based on the federated bus model that has been chosen over other data handling architectures. The standard bus that is used by most COTS retailers is PC104. The use of this bus allows easy integration of most components. Multiple MCU's are connected to the bus, each of which will control the subsystem that is connected to and acts as an interface for the central OBC. The systems that will be controlled by an MCU are:

- EPS
- ADCS
- GPS
- COMMS
- Propulsion
- Sensory Payload
- Secondary Payload

Figure 11.1.1: Data handling block diagram

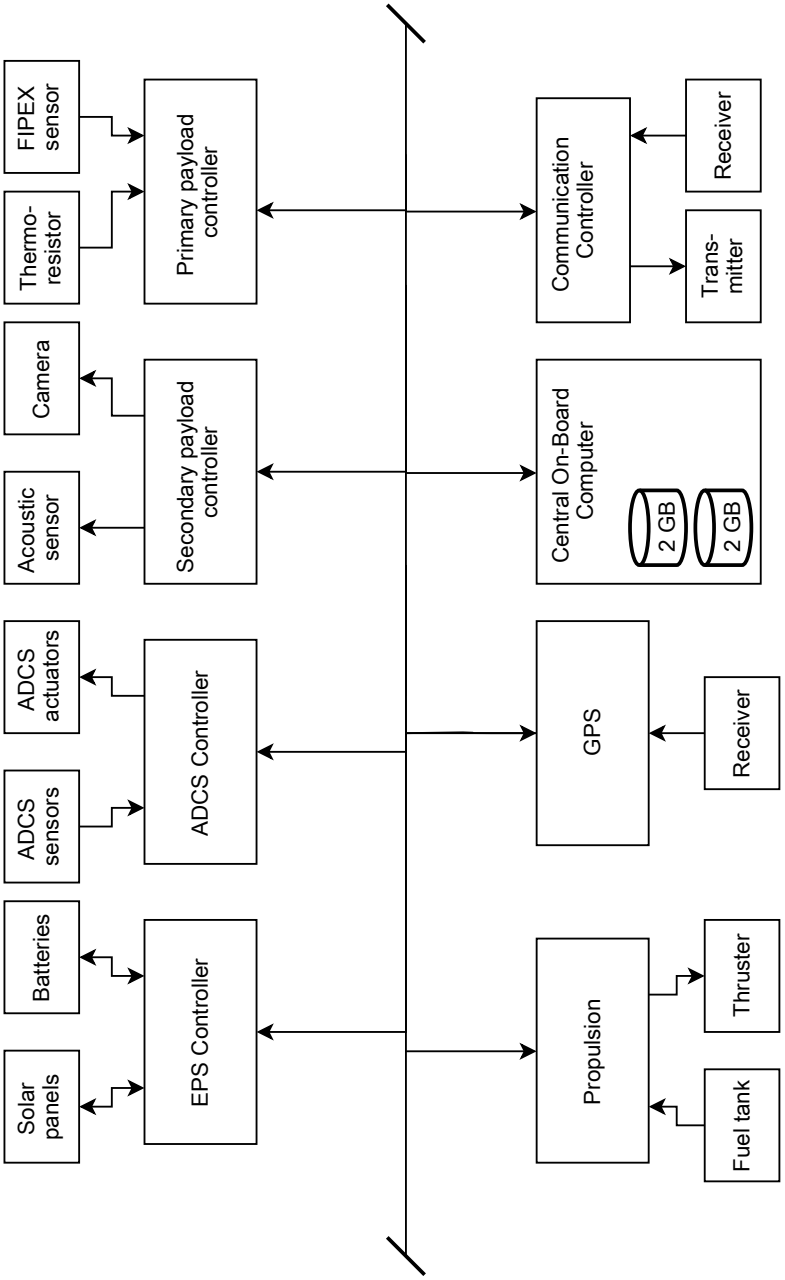

11.2 H\W & S\W diagram

In order to provide a clear overview of the data handling system a H\W & S\W diagram is constructed. The H\W & S\W diagram is presented in Figure 11.2.1. For clearness, the H\W & S\W of the ground station is included. Most of the tasks are performed by the central OBC, but some of the tasks are assigned to different components of the satellite. The reason that some components have their own control software is that it is important for those systems to be able to function autonomously.

11.2.1 Central OBC

The central OBC controls the other nodes of the satellites data handling system. Operating systems are available for nano-satellites, such as FreeRTOS or eCos. Besides the satellite control module, the central OBC also has a module for health logging. This module will check the functionality of all the subsystems and store this information in the OBC's health log. Another function that the central OBC has to perform is mass storage. Both the primary and the secondary payload will send data to the OBC for mass storage. Another module that will make use of this is the health logging module. Finally, the formation flying module will determine the relative distance of the two satellites by comparing the GPS positions of the Phi and the Delta satellites. The Delta's position is either obtained over the ground station or the ISL. Based on the relative distance of two satellites the formation flying module will decide whether the satellite's orbit needs to be adjusted.

11.2.2 GPS

A GPS receiver has been integrated in the satellite design. It includes a software package called the Satellite Tracking module and its basic function is to determine the satellite's position using the GPS antenna. When the position of the satellite is determined, the position will be sent to the central OBC on which the formation flying algorith is run.

11.2.3 ADCS

The ADCS has its own MCU to control the ADCS sensors as well as actuators. An attitude control module will be installed on this MCU to determine the attitude of the satellite, based on which it will issue commands to the actuators.

11.2.4 EPS

The EPS controller will regulate the energy distribution in the satellite. It will control the voltage of the different PCB's but will also regulate the power consumption of each component.

11.2.5 Primary payload

An MCU is included in the primary payload, that will create an interface for payload control. The software installed on this MCU will produce science packages based on the measured data and will handle commands from the central OBC. This software package will be included in the payload package from QB50 and therefore does not need to be custom developed.

11.2.6 Secondary payload

Besides the primary payload, the secondary payload is also equipped with a dedicated MCU and a software module. An important task that this MCU will perform is data processing since video and acoustic measurements are very data intensive and a large amount of the measured data is not interesting for the mission. Video data of 48 fps will be taken and compressed for downlink. The acoustic sensor will make a detailed measurement for a few seconds every orbit. Additionally, the acoustic sensors will record the vibrations of impacts on the satellite. A software package needs to be developed that filters out these measurements. The module will also provide an interface to the OBC that will control when the camera needs to be activated or deactivated. Both the video data and the acoustic measurements needs to be sent to the OBC for storage, before it is sent to the ground station. Data packages are constructed, similar to the sensory payload data packages. The only difference is that these packages will carry another identifier so that they are not confused with the sensory payload data packages or the health log packages.

Figure 11.2.1: H\W & S\W diagram

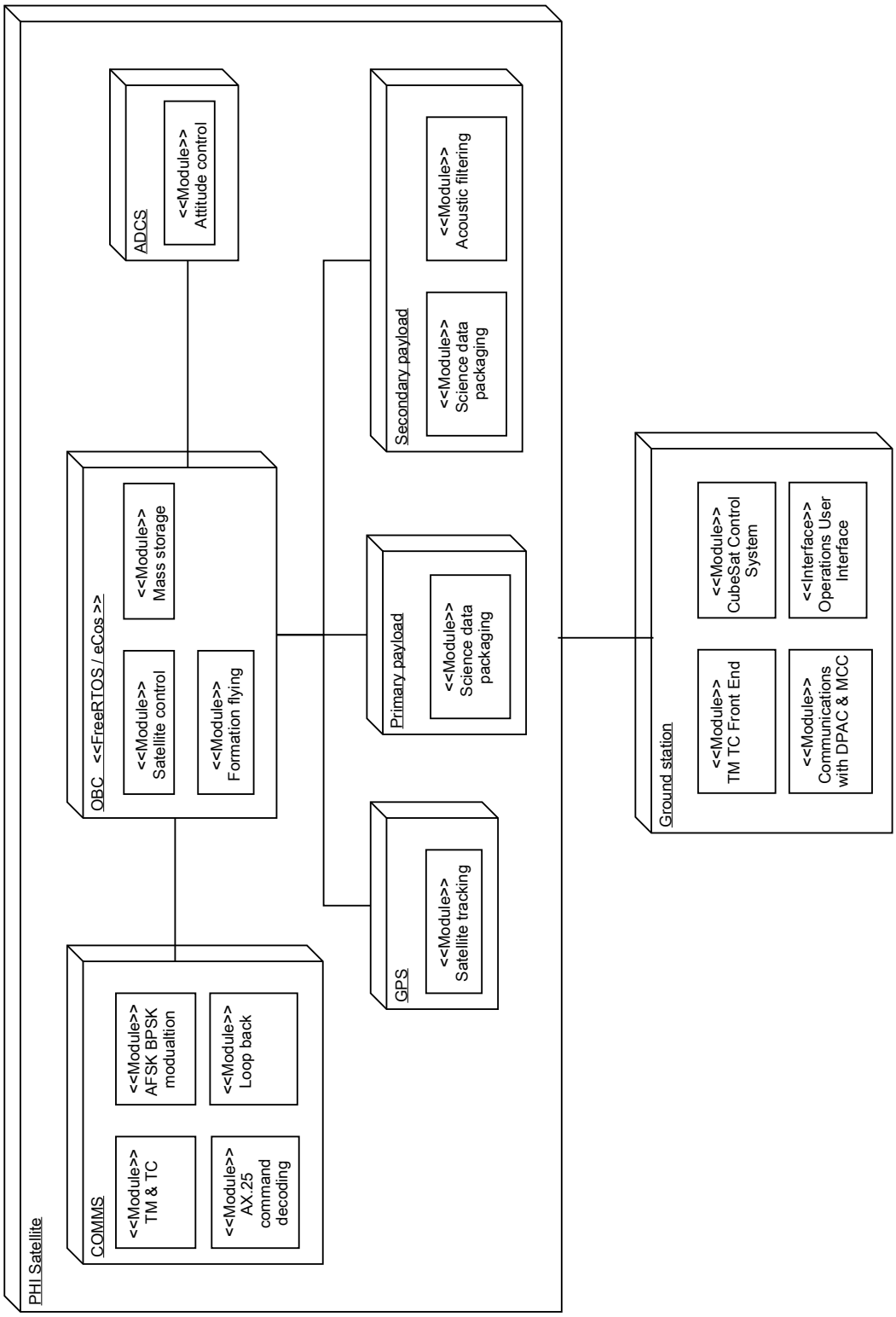

11.3 Components Trade-off

Different OBC's are available on the market. Some s/c components retailers also offer to build customized versions of the COTS components to meet special requirements of the customer. Also, there is the option of developing and building the computer. This is a time and money consuming method but the advantage is that can perform tasks that are very specific to our mission. Developing a customised computer is considered necessary if the satellite has special requirements on the OBC which are not met by COTS components. Several candidates are considered for choosing the OBC. All the considered candidates and the most important characteristics in terms of trade-off are listed in Table 11.3.1.

Some of the candidates only have one memory slot available for mass storage, other candidates can have multiple slots of memory. The QB50 requirements clearly states that the satellite has to have at least two slots of 2 GB of

Table 11.3.1: Considered COTS OBC's

Retailer	Component	Memory	Power [mW]	Mass [g]	Price
ISIS	NanoMind A712D	1x2GB	120	50-55	4 750,00
ISIS	Cube Computer	2X2GB	130	65.84	4 500,00
ISIS	Q6 Processor Board	2x4GB	1 000	23	13 886,24
ISIS	Andrews Model 160 High Performance Flight Computer	1x2GB	5 000	70	35 706,23
Pumpkin	CubeSat Kit Flight Motherboard Rev. D	1x2GB	1500	77	1 200,00

memory available. This means that if the NanoMind A712 or the Andrews Flight Computer is used, at least two of these OBC's have to be implemented in the design. The trade-off criteria that were used for the component trade-off are listed in Table 11.3.2.

Table 11.3.2: Trade-off criteria for OBC component

Criterion	Weight
Cost	2
Mass	4
Power	4
Memory	3

Table 11.3.3: Trade-off COTS OBC's

Component	Cost	Mass	Power	Memory	Total weighted
NanoMind A712D	4	4	4	2	46
Cube Computer	4	4	4	4	52
Q6 Processor Board	2	2	2	5	45
Andrews Model 160 High Performance Flight Computer	1	1	1	4	22
CubeSat Kit Flight Motherboard Rev. D	3	2	2	1	25

11.4 Sensitivity Analysis

The OBC&DH subsystem has a very flexible design. Due to the modularity of the bus architecture, extra components can be added or eliminated without major consequences. The chosen architecture also allows for individual components to operate independently which reduces the potential of the occurrence of single point of failures, making the design more robust. This does not mean that the design is not sensitive to changes. The design is sensitive for an increase in two design parameters:

- Memory size
- Computational capacity

The current design has a total memory of 4 GB, which is plenty for the current amount of data that will be stored. However, if there is a design change that demands a storage capacity that exceeds the current amount of memory, an increase in mass storage will be necessary. An example could be an increase in the duty-cycle of the deployment camera. This would increase the amount of memory needed. The same is true for the computational capacity. The chosen central OBC has a 32-bit ARM processor with a maximum frequency of 48 GHz. It is a powerful processor and the OBC has few tasks which demand continuous computation. The result is that the processor will be in sleep mode the majority of the mission. Though, if intensive computer tasks are added to the OBC, this processor might prove too slow.

11.5 Verification and Validation

The data handling system needs to be verified and validated before the system can be operated. This is done on a variety of different levels.

11.5.1 Component Tests

Every component of the data handling system must be able to survive the launch. Therefore a vibration test must be performed on all components of the data handling system. After the launch, the components will be subjected to the space environment. The components need to function in the temperature range which the satellite will experience but they also need to be able to function in vacuum and withstand SEU from particles.

11.5.2 Hardware Tests

Specific tests for the hardware need to be performed in order to verify that data handling system works as anticipated. Individual hardware components should first be tested individually: the speed of the processors should be measured as well as clock drifts. The processors need to be tested for worst case scenarios to verify that the processors are able to perform all the required calculations within their time frame. For the worst-case scenario, the following computations are considered:

- Storing sensory payload data
- Saving secondary payload data
- Perform formation flying computations
- Handle commands from ground station
- Send stored data to the transceiver

11.5.3 Software tests

The software of the OBC can be tested on a normal PC using emulators. Bugs in the software can be detected by utilising this method. The advantage of using emulators is that corrections can be made quickly. Because emulators can deviate from the physical devices the validation of the software system must be performed on the hardware of the satellite. Robustness is also an important aspect of the DH system. The software must be able to recover from sudden shut-downs and bit-flips.

11.5.4 Validation

If all individual hardware and software components have been tested, a final test can be performed on the DH system, testing both hardware and software of all different components and their interactions.

Chapter 12

Electrical Power System

In order to provide all subsystems with power, another subsystem is available: the Electrical Power System (EPS). This system is of high importance because it is connected to all other subsystems. If this system fails, all other subsystems do not receive power (or insufficient power), disabling them from performing their tasks. Furthermore, deployable solar arrays can be used to perform formation flying by incurring differential drag. More information about electrical power systems can be found in [44].

12.1 Power Budget

In order to design the EPS, a power budget needs to be made. In this power budget, the power needed by all loads during eclipse and sunlight period for every subsystem must be included, along with the corresponding duty cycles. The power budget can be found in Table 12.1.1. The requirements for the EPS flow down from this budget. They can be found in Appendix A with identifiers *PHI-QB50-1.3.1-D.1*, *PHI-QB50-1.3.1-D.2* and *PHI-QB50-1.3.1-D.3*.

Table 12.1.1: Power budget

Subsystem	Sunlight Period		Eclipse Period	
	Power [W]	Duty Cycle [-]	Power [W]	Duty Cycle [-]
ADCS	2.10	1	2.08	1
COMMS	0.2	1	0.2	1
COMMS PEAK	1.5	0	1.5	0.145
OBC& DH	0.1	1	0.1	1
GNC (GPS receiver)	0.1	1	0.1	1
Propulsion	0.023	1	0.023	1
Propulsion PEAK	13.98	0.001	13.98	0
FIPEX	0.077	0.610	0.077	0.610
Thermistor	0.13	0.010	0.13	0.010
Thermal	0.25	0.333	0.25	0.333
EPS	0.524	1	0.406	1
Camera	0.335	300	0	0
Acoustic Sensor	0.057	4000	0.057	1980
Total	3.5 W		3.24	

It must be noted that the communications peak load only appears once during each orbit, meaning that it appears either during sunlight period or during eclipse period, and thus only needs to be taken into account once when sizing the solar array area (if the power is not used during sunlight, it is used to charge the battery and therefore it can be used during eclipse time during that orbit). However, it needs to be taken into account when sizing the battery. To design the battery, an energy budget needs to be made in terms of Watt-hours. This power budget can be found in Table 12.1.2.

Table 12.1.2: Power budget in Wh

Subsystem	Eclipse Period		
	Power [W]	Duration [s]	Wh
ADCS	2.10	1980	1.156
COMMS	0.2	1980	0.110
COMMS PEAK	1.5	577	0.240
OBC& DH	0.1	1980	0.055
GNC (GPS receiver)	0.1	1980	0.055
Propulsion	0.023	1980	0.013
Propulsion PEAK	13.98	3	0.012
FIPEX	0.077	1207.8	0.026
Thermistor	0.13	19.5	0.001
Thermal	0.25	660	0.046
EPS	0.406	1980	0.223
Camera	0.335	0	0
Acoustic Sensor	0.057	1980	0.031
Total	2.3 Wh		

The spacecraft will detumble (second mode) by using the energy which is charged into the battery before launch as before the spacecraft is detumbled, the solar panels cannot be deployed. A third mode is the safe mode, which is activated when anomalies happen. During this mode only the necessary subsystems to recover from the anomaly are left on. The power needed to support the safe mode is not critical for the design of the EPS.

12.2 Theory

This section addresses the theory needed to understand the concepts of solar cells, batteries and peak power tracking respectively.

12.2.1 Solar cells

A solar cell is a device that converts solar energy (light) into electrical energy. It consists of PV-cells which are made of a semiconductor material such as Silicon or Gallium-Arsenide. To create a PV-cell, a junction is made of an N-type (negative) and a P-type (positive) material.

To create the N-type material, the semiconductor material is doped with another material, creating a prevalence of free electrons.

P-type material is created by doping the semiconductor with another material. After this, the P-type material has free openings which allow it to carry the positive charge.

When the P-type and N-type material are put together to form a junction, electrons are moving from the N-type to the P-type material and holes are moving from the P-type to the N-type material as presented in Figure 12.2.1. An equilibrium state arises, leaving an electric field in the junction (potential difference). If a photon hits the solar cell, an electron-hole pair is created. The electron moves towards the N-side and the hole towards the P-side under the influence of the electric field. When the external circuit is closed, the electron will flow towards the P-side, creating a current.

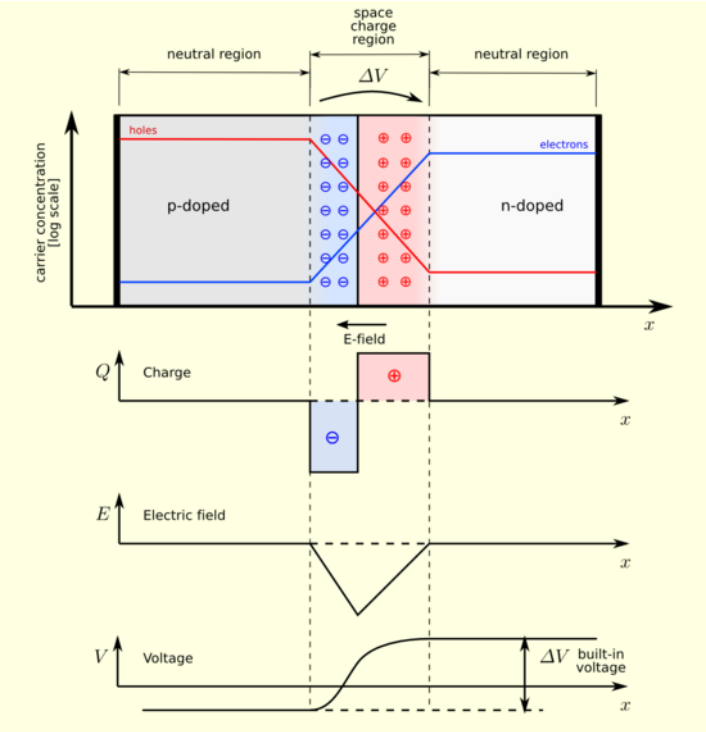

Figure 12.2.1: PN-junction [66]

12.2.2 Batteries

A battery is a device that converts chemical energy into electrical energy. It consists of two electrodes and an electrolyte. One of the electrodes is loaded with anions (negatively charged ions) and the other one is loaded with cations (positively charged ions). The two electrodes are connected in series through the electrolyte (see Figure 12.2.2).

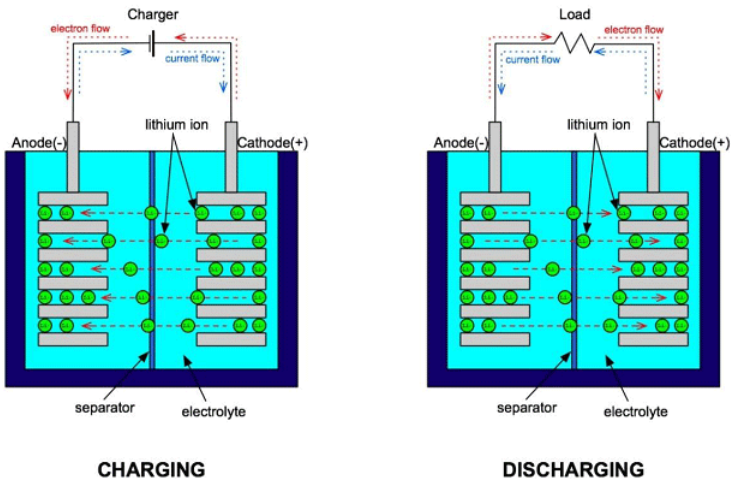

Figure 12.2.2: Lithium-ion battery [38]

To discharge the battery, the electrodes are submerged into the electrolyte, which induces an oxidation reaction at the anode. As a result of this reaction, electrons are released. At the cathode, a reduction reaction takes place (because positive ions have travelled from the anode to the cathode), making the cathode an acceptor for electrons. Due to this difference in potential, electrons are leaving the battery at the anode through a conducting wire, which leads to the load and entering the battery again through a wire from the load to the cathode.

To recharge the battery, the flow of electrons (and positive ions) needs to be reversed. This is done by applying a higher voltage over the battery. This forces the electrons to travel from the cathode to the anode. The movement of the electrons forces the positive ions to travel from the cathode to the anode as well.

12.2.3 Peak Power Tracking

The PV-curve of a solar array changes with changing temperature and solar insulation, and thus the maximum power point (MPP) also varies. To be able to get the maximum power out of the solar array during the entire orbit, a peak power tracking device can be used, which operates the array at the voltage for which the power output is the highest (and thus maximising the efficiency). A PV-curve is shown in Figure 12.2.3.

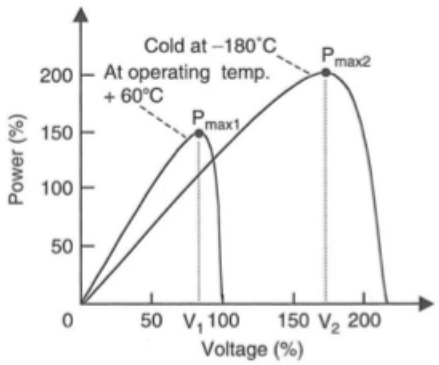

Figure 12.2.3: PV-curve

In this PV-curve it can be seen that with lower temperatures, the operating voltage gets higher as well as the output power. Suppose that one would operate the EPS at a temperature of 60° first at a voltage V_1, thus obtaining the maximum power from the solar array in that case. Without peak power tracking (PPT), the solar array would be operated at this voltage the entire time. This means that when the temperature drops to −180°, only 110 % power would be obtained, whilst with a PPT a power of 200 % would be obtained.

12.3 Solar Panel and Battery Sizing

Design decisions need to be made at every component level of the power system. Figure 12.3.1 gives an overview of all component levels and the choices that have to be made.

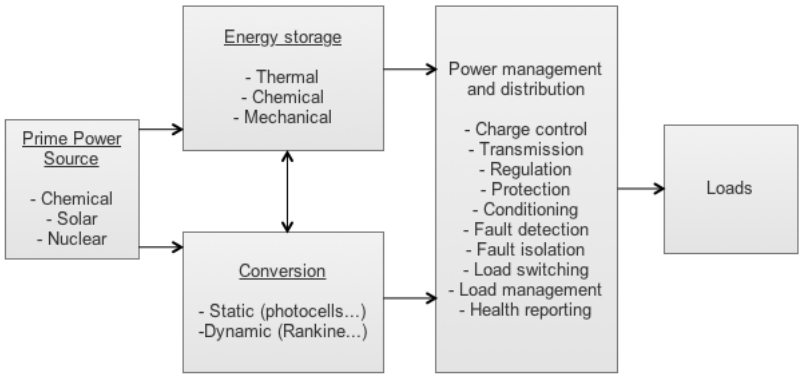

Figure 12.3.1: Functional breakdown of the EPS

Top level design decisions, which include choosing the primary energy source that is for the EPS, were described in the trade-offs in the Mid-Term Report [36]. Solar energy was chosen and elaborated upon. As a conversion method PV-cells are chosen, whilst batteries provide the energy storage, which is needed because of the need for operation during eclipse. A more detailed sizing of the solar arrays and the battery is performed in the following sections.

In order to design the EPS, design parameters need to be identified. Next, governing equations for the sizing of solar panels and batteries are discussed. Furthermore, the results are presented, followed by the choice of COTS components, along with the justification.

12.3.1 Design Parameters

First the design parameters for the solar panels are identified, followed by the parameters for the battery.

Solar Panel Design Parameters In order to be able to select the most suitable COTS component for the solar panels, important parameters are identified. These parameters are listed in Table 12.3.1. The main design drivers for the Phi-satellite are listed in bold-face.

Table 12.3.1: Solar panel selection parameters

Mass	**Voltage**	Thickness	**Specific Energy** $[Wh \cdot kg^{-1}]$
Volume	Efficiency	**Cost**	**Energy Density** $[Wh \cdot l^{-1}]$
Area	Maintenance	Availability	Environmental

The mass, volume, and cost need to stay within the constraints. The thickness of the solar arrays should comply with requirement *PHI-QB50-SYS-1.1.2* which states that the CubeSat in launch configuration has to fit entirely within the extended volume dimensions of 9 mm, including any protrusions.

Battery Design Parameters Selecting battery type and sizing of the battery depends on a large amount of factors, which are listed below in Table 12.3.2. The main design drivers for the Phi-satellite are listed in bold-face again.

Table 12.3.2: Battery selection factors [9]

Mass	**Voltage**	**Capacity**	**Specific Energy** $[Wh \cdot kg^{-1}]$
Volume	Rate Capability	**Cycle Life**	**Energy Density** $[Wh \cdot l^{-1}]$
Design	Maintenance	Availability	**Depth of Discharge**
Cost	Efficiency	Environmental	Temperature Range
Reliability	Storage	Voltage Profile	Voltage as f(Temp)

The amount of charging/discharging cycles (cycle life) is equivalent to the amount of orbits that the satellite will complete during its lifetime. From STK, the amount of 1341 cycles is obtained assuming no deviation from the velocity vector that yields the optimal lifetime (and thus the largest amount of cycles). When allowing a certain pointing error, the amount of cycles becomes lower, which means the above mentioned value can be used to size the batteries for worst case scenario. The depth of discharge is connected directly to the amount of cycles as for lower depth of discharges, the cycle life increases. The mass, cost and volume should stay as low as possible to comply with the constraints. Furthermore, the capacity is important to be able to deliver the peak loads. The most important value for the design is the peak load of 13.98 W which is needed by the propulsion system for ignition. Reliability is another important design parameter because if the batteries leak or explode, other subsystems or payloads can be damaged.

12.3.2 Calculations

The first step in sizing the battery and the solar panels is stating the assumptions. Next, the governing equations for both components are addressed, followed by appointing COTS components.

Assumptions

The following assumptions are made for the sizing of the EPS:

- The EPS is operated in two modes: detumbling mode and operating mode.
- The solar panels do not generate power beyond 80° (angle is defined between surface normal and incoming ray of sunlight) [45].
- The X_B-axis does not deviate from the velocity vector.
- The solar flux is independent of the season.

The solar array is designed for operating mode. Afterwards, a check will be performed upon detumbling mode in the sensitivity analysis.

Governing equations

Sizing of the solar panels is performed by using the book 'Spacecraft Systems Engineering, fourth edition '[44]. The following text and calculation method (including formulas) is based on this source unless stated otherwise.

First, the input parameters and their values need to be determined. They can be found in Table 12.3.3.

Table 12.3.3: Input parameters

Parameter	Remark	Value
Orbit Period [hours]	Worst Case	1.52
Sunlight Period [hours]	Worst Case	1.02
Eclipse Period [hours]	Orbit Period - Sunlight Period	0.50
Solar Flux $[W \cdot m^{-2}]$	Average from Calculations	428
Cosine of Influx Angle [-]	After Averaging Solar Flux	1
Packing Efficiency [-]		0.9
Cell Efficiency [-]		0.25
Battery Charge Efficiency [-]		0.9
Battery Discharge Efficiency [-]		0.9
Array Efficiency [-]		0.8
Degradation [-]	Over 3 months lifetime	0.005
Depth of Discharge [-]		0.30
Energy Density $[Wh \cdot kg^{-1}]$	ClydeSpace	150

Average incoming solar flux The Phi satellite is injected into a circular orbit. Assuming the orbit starts when the satellite is positioned normal to the Sun-Earth vector, this time instant is denoted as t_0. This is shown in Figure 12.3.2. In this figure, it can also be seen that regarding the sunlight incidence angles, the orbit is symmetric with respect to t_0, implying a symmetric solar flux variation pattern.

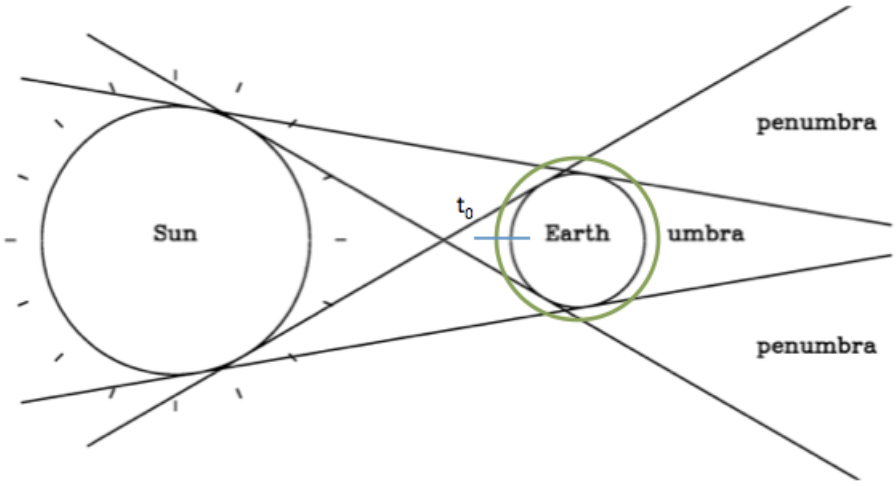

Figure 12.3.2: Denotion of time instant t_0

To make a more detailed estimation of the variation of the solar flux during the mission, a Matlab script was written. The incoming solar flux at time t [s] is modelled as a cosine function by Equation 12.3.1.

$$I = I_0 \cdot cos(n \cdot t) \tag{12.3.1}$$

in which I_0 $[W \cdot m^{-2}]$ is the standard solar flux and n is the mean motion $[rad \cdot m^{-1}]$.

The incoming solar flux depends on altitude through the mean motion. The mean motion can be calculated by the use of Equation 12.3.2.

$$n = \sqrt{\frac{\mu}{a^3}} \tag{12.3.2}$$

Figure 12.3.3 shows the variation of the incoming solar flux in function of the altitude and the time instant in the orbit.

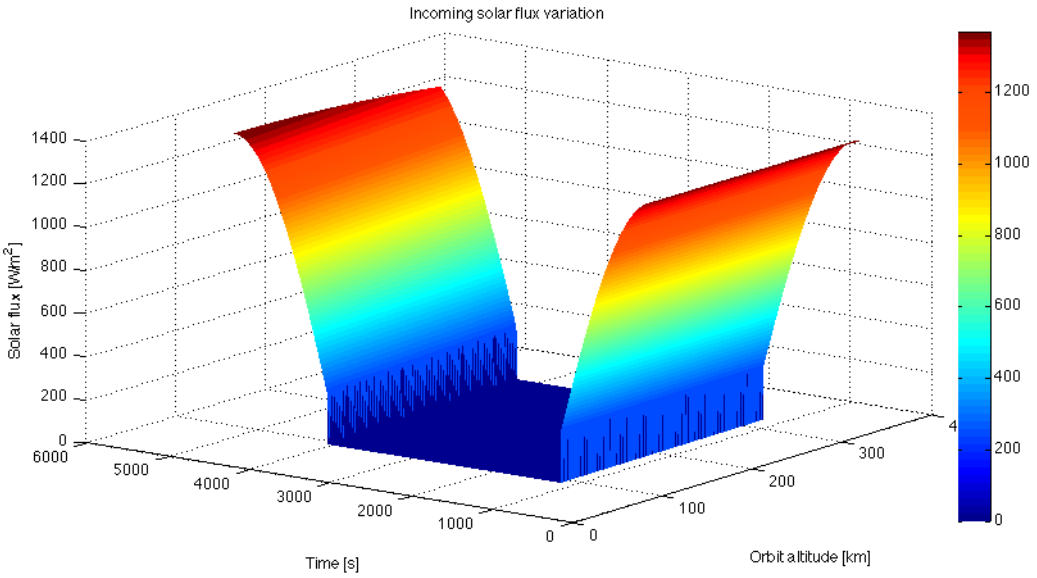

Figure 12.3.3: Variation of the incoming solar flux as a function of the altitude and time instant

The eclipse period starts at t = 1154 s and ends at t = 4252 s (the incoming solar flux is zero here), the graph is symmetric around the eclipse period, which fulfills expectations. The average incoming solar flux during one orbit can be calculated by Equation 12.3.3 and is found to be 428.44 $W \cdot m^{-2}$.

$$\text{Average solar flux} = \frac{\sum_{i=1}^{n} S_i}{n} \tag{12.3.3}$$

The eclipse time changes with altitude. This is shown in Figure 12.3.4.

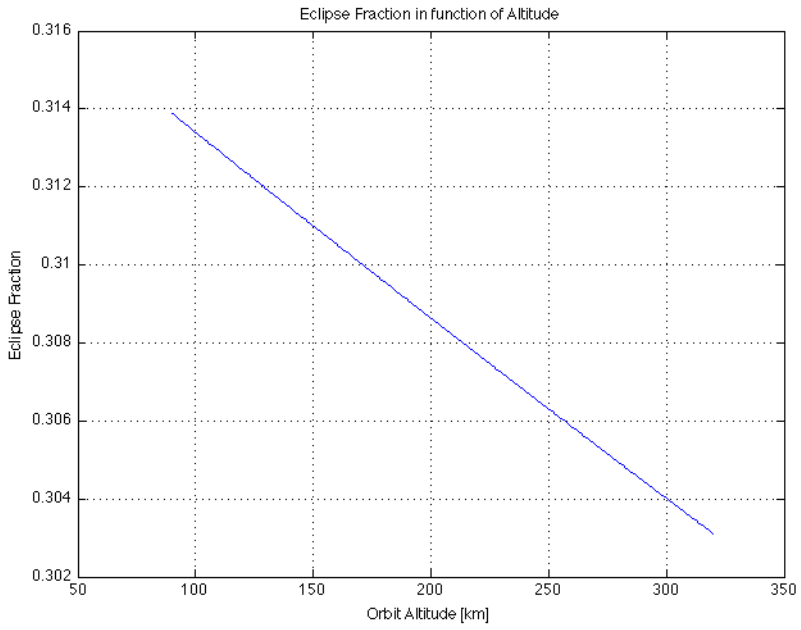

Figure 12.3.4: Variation of the eclipse fraction in function of the altitude

Solar Panel Sizing The power needed by the satellite during eclipse is supplied by the batteries. To calculate the amount of power needed to charge the batteries, Equation 12.3.4 can be used.

$$P_{charge} \cdot T_{sun} = \frac{1}{\eta} \cdot P_{eclipse} \cdot T_{eclipse} \tag{12.3.4}$$

in which P_{charge} is the amount of power needed to charge the batteries, T_{sun} is the sunlight period, $T_{eclipse}$ is the eclipse period, $P_{eclipse}$ is the power needed during eclipse to support the loads. The eclipse period and sunlight period

are calculated in Chapter 2. The power needed during eclipse follows from the power budget. η is the efficiency of the system, as given by Equation 12.3.5.

$$\eta = \eta_{BDR} \cdot \eta_{BCR} \cdot \eta_{AR} \tag{12.3.5}$$

η_{BDR} is the efficiency of the battery discharge regulator, η_{BCR} is the efficiency of the battery charge regulator and η_{AR} is the efficiency of the array.

The power that the array needs to deliver is now calculated by Equation 12.3.6 [70].

$$P_{array} = \frac{\frac{P_{sun} \cdot T_{sun}}{\eta} + \frac{P_{eclipse} \cdot T_{eclipse}}{\eta}}{T_{sun}} \tag{12.3.6}$$

P_{sun} is the power required during sunlit period and P_{array} is the amount of power that the array needs to produce.

The array size A_{array} is calculated by Equation 12.3.7.

$$A_{array} = \frac{P_{array}}{I_0 \cdot cos(\theta) \cdot \eta_{cell} \cdot \eta_{packing} \cdot (1 - D)} \tag{12.3.7}$$

I_0 is the solar flux, θ is the incidence angle of the sun with respect to the array normal, $\eta_{packing}$ is the packing efficiency, η_{cell} is the cell efficiency and D is the degradation factor over lifetime.

The results of these calculations are shown in Table 12.3.4.

Table 12.3.4: Output parameters

Parameter	Value
Power Required by Array [W]	7.84
Array Area [m^2]	0.082

The available area on the spacecraft for body-mounted solar panels is 0.054 m^2 (assuming only 90 % of the side area is occupied by solar cells). This means deployable solar panels are needed. For stability reasons, two deployables are used such that the necessary extra solar panel area of 0.028 m^2 can be divided over two panels. It needs to be taken into account that these panels need to be mounted to the body of the spacecraft, and thus can not be occupied with solar cells completely. Assuming an occupation factor (solar panel area over side panel area) of 80 %, these panels have dimensions 0.1 m x 0.18 m.

It needs to be noted that the deployable solar arrays have a different angle with respect to the Sun than the body-mounted solar panels. When the body-mounted solar panels have an incidence angle of 45 °, the deployables have an incidence angle of 90 ° which is more favourable. Another thing that needs to be noted is the fact that when the satellite has decayed to 200 km, a part of the body-mounted solar panel will be deployed. This panel will not be able to deliver power anymore as it will not be pointed towards the sun after deployment.

Knowing this, the MATLAB script used to calculate the variation of the solar flux can now be extended by use of Equation 12.3.4 in order to calculate the power output of the array. The array size was estimated to occupy 90 % of the illuminated body area to which the rectangular surface areas available on the wings are added (each 0.018 m^2) (note: the deployment of the part of the body-mounted solar panel at 200 km is not included in the MATLAB script).

The variation of the incoming power on the solar array is shown in Figure 12.3.5. It shows how the incoming power on the solar array varies with altitude and time instant.

The variation of the power output of the solar array is shown in Figure 12.3.6. It shows how the solar array output power varies with altitude and time instant. As the power output is defined by multiplying the incoming power with the efficiency, the graph has the same shape, but a different scale.

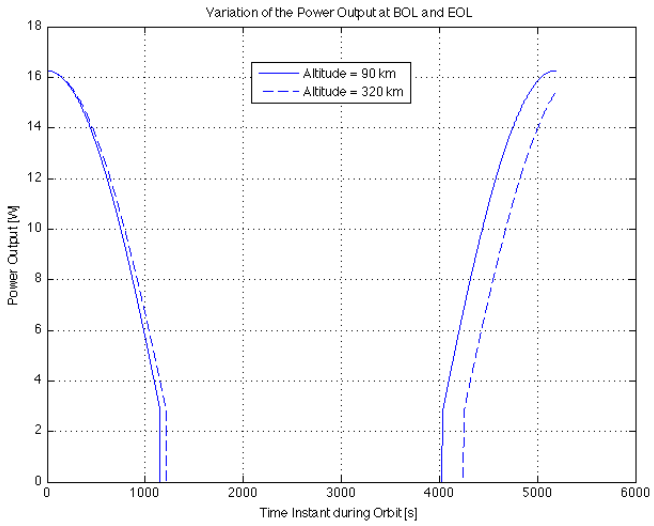

Figure 12.3.7: Variation of output power with time at altitude of 90 and 320 km

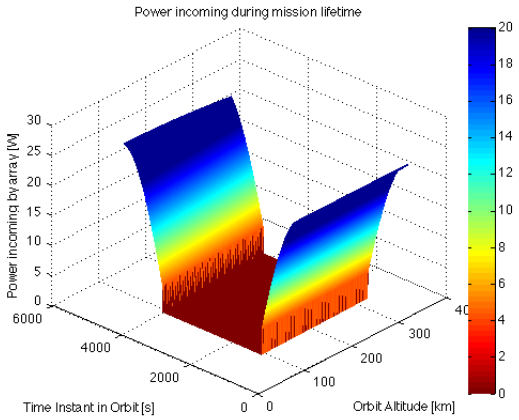

Figure 12.3.5: Variation of incoming power with orbit altitude and time

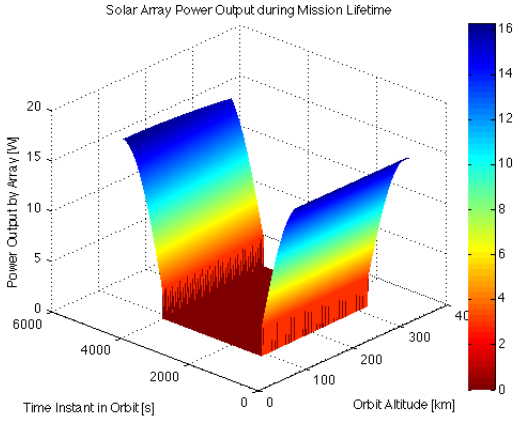

Figure 12.3.6: Variation of array output with orbit altitude and time

The variation of the ouput power at begin-of-life (BOL) and end of life (EOL) is shown in Figure 12.3.7.

A note needs to be made about the albedo. As the solar panels are illuminated at every time instant of the sunlit part of the orbit, they are never facing the Earth and thus the satellite does not benefit from albedo.

Battery The energy E_B [Wh] that the batteries need to store in order to be able to deliver the eclipse load $P_{eclipse}$ is given by Equation 12.3.8.

$$E_B = \frac{P_{eclipse} \cdot T_{eclipse}}{\eta_{charge} \cdot DOD} = \frac{Wh_{eclipse}}{\eta_{charge} \cdot DOD} \tag{12.3.8}$$

in which $T_{eclipse}$ is the period the satellite is in eclipse, η_{charge} is the charging efficiency, $Wh_{eclipse}$ is the amount of Wh needed during eclipse and DOD is the depth of discharge. The DOD can be chosen by the operator of the battery. In order to increase the cycle life of the battery, the DOD is set at 30 %. The orbit period and sunlight period are calculated in Chapter 2. The charging efficiency comes from the EPS-board and is set to be 90 %. This yields a stored energy in the battery of 6 Wh.

Architecture The next choice that needs to be made concerns the power system architecture. Two different architectures are available: Direct Energy Transfer (DET) or Peak Power Tracking (PPT). The advantages and disadvantages of both systems are listed in Table 12.3.5.

Table 12.3.5: DET vs PPT

System	Direct Energy Transfer	Peak Power Tracking
Advantages	Well regulated input voltage to all loads	No need for shunt regulator and battery charge regulator (in case of single battery bus)
	Simpler, lighter and more efficiency load converters	Makes maximum use of incident solar energy
Disadvantages	Need for more power converters	Lower efficiency at EOL than DET in many cases
	Series power loss between battery and load	More heat dissipation inside spacecraft body
	Loads requiring close regulation	

The peak power tracking architecture is chosen because the solar influx is changing a large amount of times during the lifetime of the satellite, which also gives a a large amount of changes in temperature of the solar panels.

Choice of COTS components

A large amount of CubeSat components, which are tested and have flight heritage, are available. Using COTS components also adds to the sustainability of the project. By using the results of the analysis above, the most suitable COTS components are selected. All COTS components will be bought from ClydeSpace, due to the large amount of flight heritage. "Over 40 % of all CubeSat missions fly ClydeSpace hardware; more than any other vendor" [59].

Solar Panels Two types of solar panels are chosen: two body-mounted solar panels and two deployable solar panels. The body-mounted solar panels are the 3U CubeSat Side Solar Panels from ClydeSpace. They operate at a voltage of 16.45 V (at maximum peak power) and a power of 7.29 W at the begin of life (BOL) at a temperature of 28°C. The deployed solar panels are the 1.5 U Front Solar Panels from ClydeSpace. They operate at a voltage of 4.70 V (at maximum peak power) and a power of 2.08 W at the BOL at a temperature of 28°C [59]. After 200 km, a part of one of the body-mounted solar panels need to be deployed because of aerodynamic reasons as was explained in Section 2.3. Therefore, a request needs to be handed in to ClydeSpace to make a customised version of one of the 3U CubeSat Side Solar Panels.

Battery The battery from ClydeSpace is a lithium-polymer battery with an energy density of 150 $Wh \cdot kg^{-1}$. Other versions are available for 10 Wh, 20 Wh and 30 Wh. Larger batteries have more volume and a higher cost. The requirement for the energy storage is 6 Wh, so the 10 Wh version has been chosen.

Printed Circuit Boards The board that will be used is the FleXible EPS 6 x 12W BCR (Battery Charge Regulator) board from ClydeSpace. This board has an integrated active solar array maximum power point tracking device, and six charging regulators with dedicated peak power tracking [cite website]. It features over-current protection and a true dead launch: ideal diode and separation switch. Voltage converters (12V, 5V and 3.3V) are included in the board.

The cost and mass budget of the COTS components chosen for the EPS is shown in Table 12.3.6.

Table 12.3.6: Cost and mass budget for the EPS

Component	Amount	Unit Mass [g]	Unit Cost [$]	Cost [€]
3U CubeSat Side Solar Panel (of which one needs to be customised)	2	135	5 550.00	4 206.14
1.5U Front Solar Panel	2	48	2 800.00	2 122.02
FleXible EPS 6 x 12W BC	1	139	9 650.00	7 313.38
CubeSat Standalone Battery	1	142	1 650.00	1 242.28
Total	6	647	28 000	21 211.98

Electrical Block Diagram The lay-out of the different EPS parts (electrical block diagram) is shown in Figure 12.3.8.

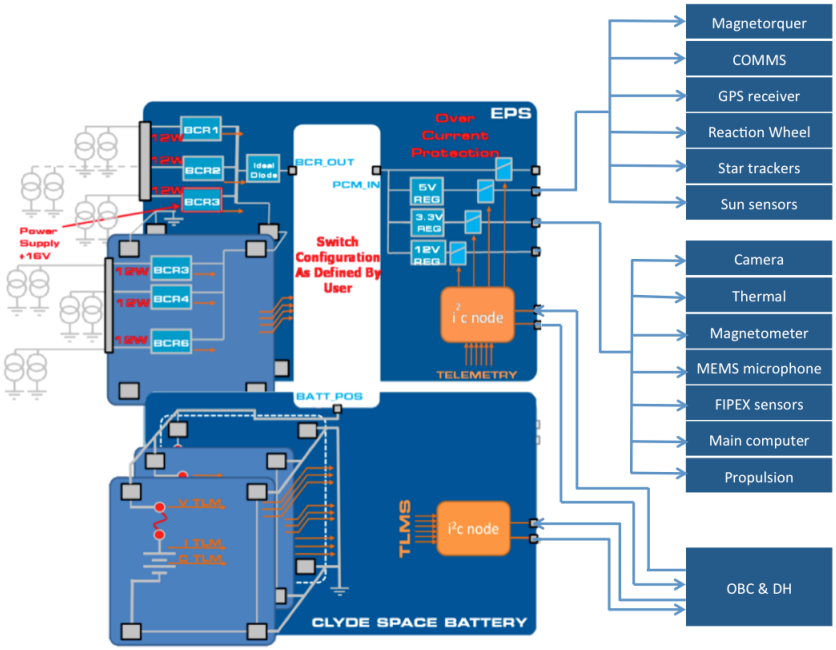

Figure 12.3.8: Lay-out/Electrical block diagram of the different EPS components

The switch configuration to be defined by the users has two options as mentioned in the user manual [61]: option 1 which consists of a separation switch and a pull pin whereas option 2 which consists of two separation switches. The separation switches provide isolation of the battery during launch, whilst the pull pin provides isolation of the battery on the ground (during shelf-life). For this mission, the first option is chosen as the satellite will need to be stored before launch.

12.4 Sensitivity Analysis

A sensitivity analysis is performed to predict how the change of launch date influences the design performance. If the launch date changes, there is a possibility that the satellite will need to operate in a different season.

"Due to 1.5 % eccentricity in Earth's orbit around the sun, the solar flux in LEO varies seasonally about ± 3 per cent with an annual average of 1358 ± 5 $W \cdot m^{-2}$, where 5 $W \cdot m^{-2}$ is an allowance for measurement errors. The flux is near the average value on both equinox days, maximum near winter solstice and minimum near summer solstice" [45]. The influence of a small variance in solar flux on the EPS needs to be investigated. Decreasing the average incoming solar flux by 3 % gives a new average incoming solar flux of 415 $W \cdot m^{-2}$, which results in a needed solar array area of 0.085 m^2.

The batteries have a self-discharging rate of 5 % per month. QB50 guarantees a maximum amount of on-ground storing without charging of 2 months, the batteries should be able to cope with a self-discharge of 10 %. As a 10 Wh battery is chosen, and only 6 Wh is needed, the design is not sensitive to shelf-life.

12.5 Failure Modes

The electrical power system can fail in several ways. The most important ones are discussed in this section. For the battery, the event with the worst adverse consequences is leakage of corrosive electrolyte, thereby affecting the structure and inducing failures of other systems, as well as battery explosion. The latter would put an end to the mission. For the power system, most probable failures are an open circuit or single short circuit failure, or a single-point failure. In case of the first two, the power system can be taken out completely. In case of the last one, only degradation of the power system takes place.

The design of the power system needs to take into account failure modes of other subsystems as well. For example, when the ADCS (attitude determination and control system) fails and the satellite is tumbling, the satellite should still be able to generate enough power to run all other subsystems.

12.6 Verification and Validation

Verification The solar panels need to be tested for efficiency and whether they comply to specifications. All interconnections (from solar panels to battery, battery to subsystems, solar panels to DC/DC converter, and connections

with regulators) need to be tested. The magnetic field that the complete configuration will impose needs to be measured and kept as low as possible in order to minimise the interaction with the Earth's magnetic field, in order to keep the resulting disturbance torques small.

As all components of the EPS are COTS components, that have been tested and certified for space environment. Proposals for integration testing (testing of the components after integration in the satellite) are available.

The EPS is fully tested and supplied with test reports. To verify the operation of the EPS, a user manual is included. Solar panels, batteries and the EPS board need to be connected in the correct manner as indicated in documents [61] and [40]. A test configuration for PCM testing, undervoltage protection, BCR testing, EoC (end of charge) operation and 5V USB charging is provided in the same documents.

Validation Validation can be performed by comparing the design of the electrical power system with the designs used in other CubeSats in similar orbits. Because the orbit imposed for this project is rather low (320 km), the CubeSats used as reference will be in orbits of 600 km. Thus when comparing them this fact needs to be taken into account. The lower the orbit, the more challenging the EPS design due to higher eclipse fractions and more charging-discharging cycles. Therefore, reference literature found for higher orbits will not lead to a conservative design. Delfi-C^3 is at an orbit of 600 km and has a power budget of 2.5 Watts. However, its ADCS system is not that power demanding, and the eclipse period is shorter. Delfi-N3xt was launched into an orbit at 700 km altitude and has a power budget of 4.24 Watts with a shorter eclipse period [13].

12.7 Recommendations

The design can be improved by integrating it and testing it as described in the verification section. The satellite will only be launched in over two years, so an improvement in solar cell efficiency can be expected. This would cause a decrease in required solar array area and make the design lighter and cheaper. However, it needs to be noted that the solar panels will be bought and integrated in advance, making it hard to change them afterwards. The battery of 10 Wh is now overdesigned as only 6 Wh are needed, and no smaller battery is available as COTS component in the ClydeSpace shop. A collaboration could be done with CubeSat companies such as ISIS and ClydeSpace to produce smaller batteries, as all QB50-satellites will cope with the same problem. The deployment of the part of the body-mounted solar panel needs to be investigated further as it will lead to a decrease in power.

Chapter 13
Thermal Control System

Space is a harsh environment with highly variable temperatures that can range from below $-100°C$ to over $120°C$. However, the spacecraft can only be guaranteed to function normally within their survival and operational temperature range. In addition, the thermal characteristics such as heat generation and temperature ranges of each component influence the internal layout of the satellite. Therefore, the thermal control system (TCS) is a necessary part of any spacecraft in order to prevent overheating or under-cooling and to ensure that all subsystems and payloads are kept within their survival and operational temperature ranges. This chapter presents the method of thermal analysis used for the Phi satellite's thermal design and the results obtained. The sensitivity analysis and procedure for verification and validation are then given.

13.1 Introduction

Since many Commercial Off-The-Shelf (COTS) products are used onboard the Phi satellite, it is desirable to have the thermal environment of the satellite at around room temperature so that the components can operate efficiently. For most missions, this can be achieved by passive control where thermal tapes and paint with special properties are applied on the surfaces of the satellite. The appropriate surface emissivity and absorptivity can then be calculated based on the desired temperature range and the surface paint/tape can consequently be selected.

There are 3 environmental heat sources present on the CubeSat:

- Solar radiation
- Earth albedo radiation
- Earth IR radiation

The only heat sink available to the satellite is heat radiation from the satellite into space. The heat sources and sink between the spacecraft and the environment are visualized in Figure 13.1.1. Within the spacecraft, another heat source is the heat dissipation of spacecraft components. Heat transfer between them is done through radiation and conduction. For a satellite in orbit, convection is ignored due to the high vacuum in space.

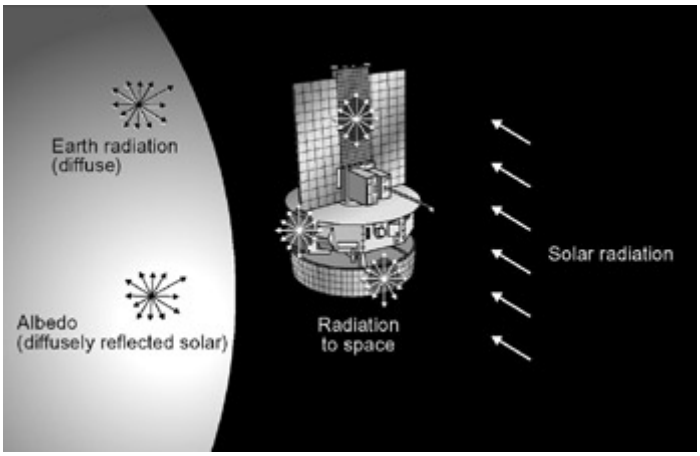

Figure 13.1.1: Heat sources and sink for a spacecraft [18]

13.2 Theory

Designing the TCS is dependent on requirements from QB50 [54] and heat sources from inside and outside of the satellite. The method outlined in the following subsections are derived from [44].

13.2.1 Requirements

PHI-QB501.61: The CubeSat shall maintain all its electronic components within its operating temperature range while in operation and within survival temperature range at all other times. [54]

13.2.2 Assumptions

Assumptions made in the thermal analysis method discussed here are as follows:

- Heat dissipation from components within the satellite are neglected for the surface temperature calculation
- The satellite is considered as consisting of discrete regions (isothermal nodes) within which temperature gradients are neglected
- The radius of the Earth's effective radiating surface R_{rad} is assumed to be the radius of the Earth $R_E = 6378km$
- Heat distribution via radiation from PCB's are assumed to be symmetric
- Conduction happens through the aluminium guide rails, while the conductivity of the PCB's are neglected

13.2.3 Equilibrium temperature calculation

If all goes well, the spacecraft should have similar temperatures as that of the Earth so that the radiated heat from the spacecraft will be in the infrared region of the spectrum. Since satellites are not black bodies, they absorb only a fraction α of the incident heat and emit a fraction ε of the radiation.

For equilibrium, the heat absorbed by the satellite must be equal to the heat radiated from the satellite. To calculate the surface temperature of the satellite, a heat balance equation is defined in Equation 13.2.1 where the internal heat dissipation is neglected.

$$(A_{solar} \cdot J_s + A_{albedo} \cdot J_a)\alpha + A_{planetary} \cdot J_p \cdot \varepsilon + Q = A_{surface} \cdot \sigma \cdot T^4 \cdot \varepsilon \tag{13.2.1}$$

Where A_{solar}, A_{albedo} and $A_{planetary}$ are the surface areas absorbing solar radiation, albedo, and planetary radiation, respectively. $A_{surface}$ is the area emitting heat from the satellite. α is the absorptivity and ε is the emissivity of the surface material. The solar intensity is calculated using Equation 13.2.2.

$$J_s = \frac{P_s}{4 \cdot \pi \cdot d^2} \tag{13.2.2}$$

Where P_s is the total emitted power output from the Sun, $3.856 \cdot 10^{26}$ W, and d is the distance [m] from the Sun to the planet nearest the satellite. For satellites in orbit around the Earth, the solar radiation is approximately 1371 Wm^{-2}.

The albedo radiation is given by Equation 13.2.3.

$$J_a = J_s \cdot a \cdot F \tag{13.2.3}$$

Where a is the planetary albedo, which for Earth is around 0.31-0.39, F is the visibility factor obtained from Figure 13.2.1.

The planetary infrared radiation is defined in Equation 13.2.4.

$$J_p = 237(\frac{R_{rad}}{R_{cm}})^2 \tag{13.2.4}$$

Where 237 Wm^{-2} is the assumed intensity of the Earth's IR radiation, R_{rad} is the radius of the Earth's effective radiating surface, which in this case is assumed to be the radius of the Earth, $R_E = 6378km$. $R_{cm} = 6378 + 200km$. As shown in Equation 13.2.4, J_p is inversely proportional to R_{cm}^2. The required operational range from QB50 is until 200 km. Therefore, TCS is designed for the worst case from 320 km to 200 km, which takes up 80% of the life time. For the orbit until 90 km, the analysis will be treated in the sensitivity analysis.

Finally, Equation 13.2.1 can be rearranged to find the equilibrium temperature on the surface of the CubeSat. This is given by Equation 13.2.5.

$$T^4 = \frac{A_{planetary} \cdot J_p}{A_{surface} \cdot \sigma} + \frac{Q}{A_{surface} \cdot \sigma \cdot \varepsilon} + \frac{(A_{solar} \cdot J_s + A_{albedo} \cdot J_a)}{A_{surface} \cdot \sigma} \cdot \left(\frac{\alpha}{\varepsilon}\right) \tag{13.2.5}$$

From this, the equilibrium temperature T of the satellite was found to be $33.3°C$ for the time the satellite spends in sunlight, and $10.3°C$ for the time the satellite spends in eclipse (approx. 30% of the orbital period at initial altitude,

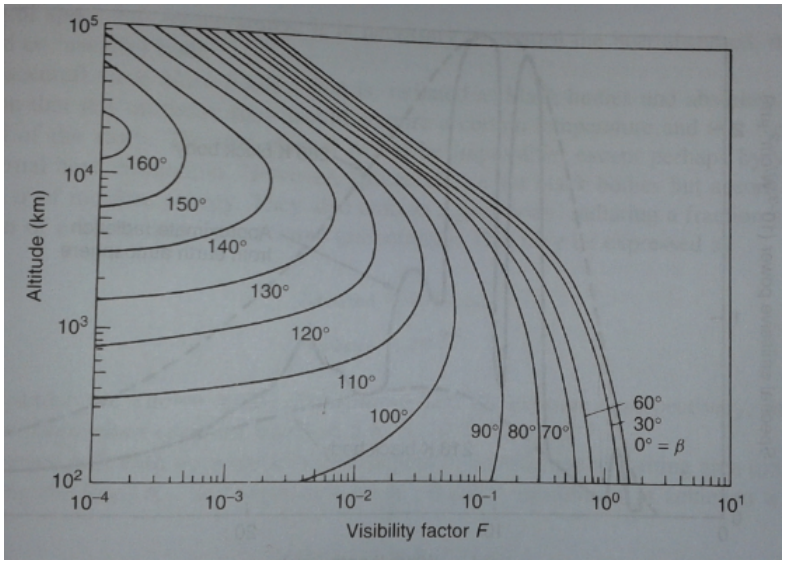

Figure 13.2.1: Spacecraft albedo irradiation. β is the angle between the local vertical and the Sun's rays [44]

for the worst-case where the Earth-Sun vector is lying in the orbital plane). This temperature range is suitable for the operational temperature ranges of the satellite components. To be able to achieve this, the chosen material was aluminized kapton tape, with kapton on the side facing the space environment. Its ratio of absorptivity to emissivity $\left(\frac{\alpha}{\varepsilon}\right)$ is 0.63.

13.2.4 Thermal mathematical model

Spacecraft have temperatures that vary continuously with orbital location and time. The use of a Thermal Mathematical Model (TMM) to calculate the temperatures at different places in the satellite requires visualizing discrete thermal nodes on the spacecraft where temperature gradients are neglected. The thermal nodes chosen are shown in Figure 13.2.2.

This internal layout of the satellite is subject to further changes since at the point of the thermal analysis the placement of subsystems have not yet been finalized (due to the fact that the center of gravity still needs to be calculated for requirement *PHI-QB50-SYS-1.1.3*). However, the thermal analysis results are anticipated to be quite similar for each subsystem, and thus the preliminary layout of the satellite given in Figure 13.2.2 should be representative of the analysis done on the thermal system.

In total, 22 nodes are defined on the Phi satellite. On each subsystem of the CubeSat, two nodes are depicted in corners opposite each other (represented by the red dots in Figure 13.2.2). Each node has temperature, thermal capacity, heat dissipation (if applicable) and radiative and conductive interfaces with other nodes. Nodes that are directly connected to space will have radiative interfaces with the external environment as well.

The temperature of the spacecraft is described by a set of n simultaneous non-linear differential equations, with i varying from 1 to n. The heat balance at node i is given by Equation 13.2.6.

$$m_i \cdot C_i \cdot \frac{T_i - T_{i,0}}{\delta t} = \frac{Q_{external,i,0} + Q_{external,i}}{2} + \frac{Q_{i,0} + Q_i}{2} - \sigma \cdot \varepsilon_i \cdot A_{space,i} \cdot \left(\frac{T_{i,0} + T_i}{2}\right)^4 - \sum_{j=1}^{n} h_{ij} \left(\frac{T_{i,0} - T_i}{2} - \frac{T_{j,0} - T_j}{2}\right) - \sigma \cdot \sum_{j=1}^{n} A_i \cdot F_{ij} \cdot \varepsilon_{ij} \cdot \left(\left(\frac{T_{i,0} - T_i}{2}\right)^4 - \left(\frac{T_{j,0} - Tj}{2}\right)^4\right) \quad (13.2.6)$$

Since this calculation is rather complicated, a programmed Excel sheet has been employed to analyze the thermal conditions within the satellite, using the same basic principles. The results obtained are presented in the next section.

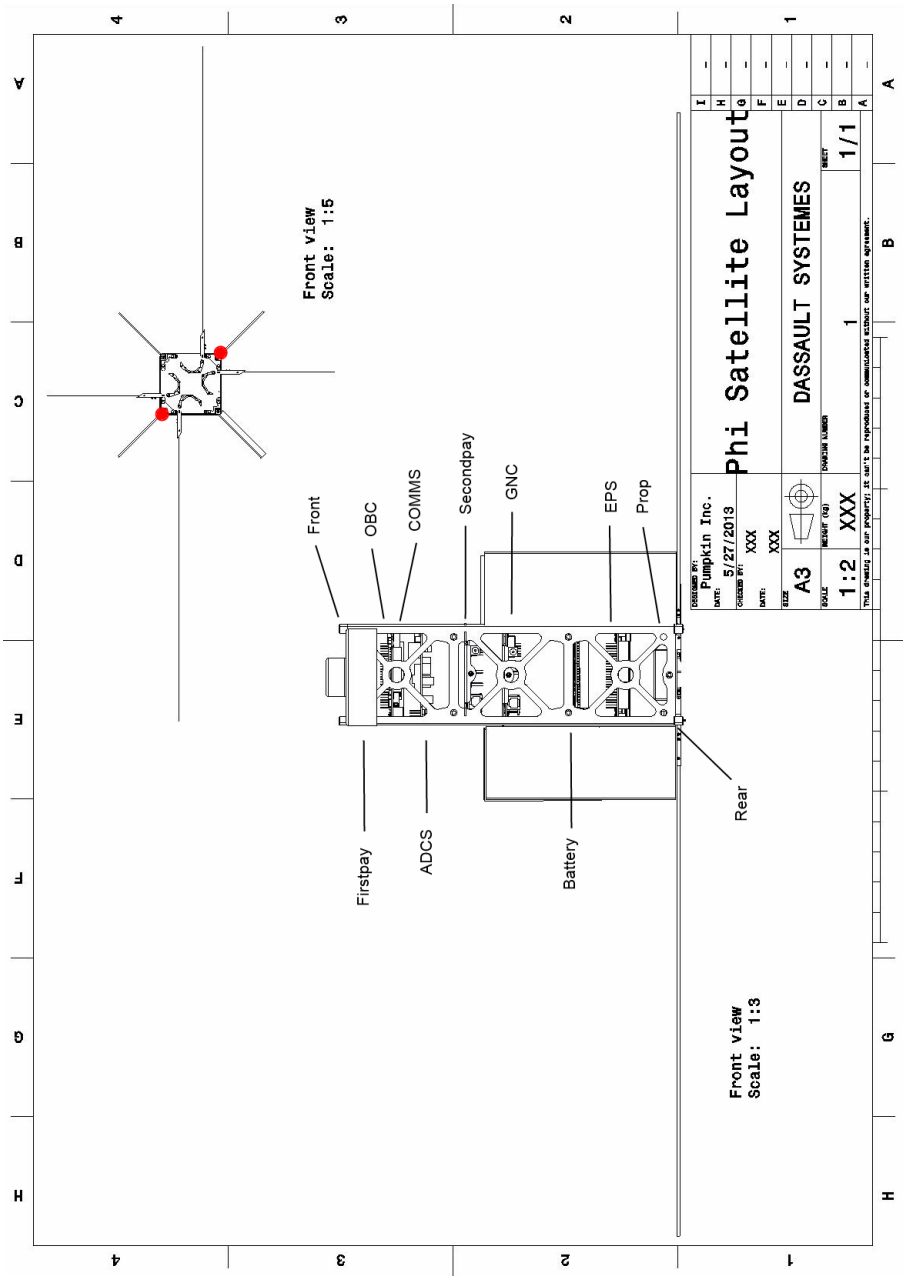

Figure 13.2.2: Definition of thermal nodes on the satellite

13.3 Results

Figure 13.3.1 shows the temperatures calculated using the Excel sheet *Analmeg* developed by Dutch Space, for the case of the satellite in sunlight. For the cold case of the satellite in eclipse, the results are given in Figure 13.3.2.

The calculations made are transient, taking into account the time taken for heat transfer to take place, which is approximated to be 5 minutes. As can be seen from the results, the temperatures in the satellite for each case do not vary significantly from each other. According to the thermal analysis done, the temperature range inside the satellite is around $23°C$ to $32°C$, which means that all components can function effectively within their operational temperature ranges. The operational temperature ranges of subsystems' components(as well as survival temperatures for the payloads) are shown in Figure 13.3.3.

Node		Temperature		Conductive heat flows			Radiative heat flows		
name	Node	°C	K	Coupling	in (W)	out (W)	Coupling	in (W)	out (W)
Rear1	1	31,92	305,07						
Rear2	2	31,93	305,08				0,91	0,05133	
Prop1	3	32,03	305,18	38,5	4,22532		0,91	0,64344	
Prop2	4	32,04	305,19				0,91	0,69806	
EPS1	5	31,97	305,12	19,25	1,06957		0,91	0,32567	
EPS2	6	31,98	305,13				0,91	0,38417	
Battery1	7	31,99	305,14	12,8	0,87602		0,91	0,40117	
Battery2	8	32,00	305,15				0,91	0,4645	
GNC1	9	31,96	305,11	9,625	0,3798		0,91	0,23127	
GNC2	10	31,97	305,12				0,91	0,30062	
Secondpay1	11	31,96	305,11	7,7	0,28267		0,91	0,21515	
Secondpay2	12	31,97	305,12				0,91	0,29241	
ADCS1	13	31,95	305,10	6,42	0,20837		0,91	0,19021	
ADCS2	14	31,97	305,12				0,91	0,27843	
COMMS1	15	31,95	305,10	5,5	0,15374		0,91	0,16382	
COMMS2	16	31,96	305,11				0,91	0,26847	
OBC1	17	31,94	305,09	4,8125	0,08998		0,91	0,10957	
OBC2	18	31,96	305,11				0,91	0,24304	
Firstpay1	19	31,93	305,08	4,28	0,03705		0,91	0,05073	
Firstpay2	20	31,96	305,11				0,91	0,25161	
Front1	21	31,81	304,96	3,85		0,42643	0,91		0,64868
Front2	22	32,01	305,16				0,91	0,51618	
Space	23	-270,15	3,00				0,093		45,6727

Figure 13.3.1: Satellite transient temperatures in sunlight

Node		Temperature		Conductive heat flows			Radiative heat flows		
name	Node	°C	K	Coupling	in (W)	out (W)	Coupling	in (W)	out (W)
Rear1	1	22,76	295,91						
Rear2	2	22,77	295,92				0,91	0,04878	
Prop1	3	22,79	295,94	38,5	0,85058		0,91	0,11816	
Prop2	4	22,80	295,95				0,91	0,16993	
EPS1	5	22,73	295,88	19,25		0,68125	0,91		0,18922
EPS2	6	22,74	295,89				0,91		0,13392
Battery1	7	22,82	295,97	12,8	0,66986		0,91	0,27994	
Battery2	8	22,83	295,98				0,91	0,33963	
GNC1	9	22,71	295,86	9,625		0,54325	0,91		0,30175
GNC2	10	22,72	295,87				0,91		0,23664
Secondpay1	11	22,70	295,85	7,7		0,50098	0,91		0,34783
Secondpay2	12	22,71	295,86				0,91		0,27559
ADCS1	13	22,69	295,84	6,42		0,46053	0,91		0,38348
ADCS2	14	22,71	295,86				0,91		0,30139
COMMS1	15	22,69	295,84	5,5		0,42345	0,91		0,41157
COMMS2	16	22,70	295,85				0,91		0,31479
OBC1	17	22,68	295,83	4,8125		0,41105	0,91		0,45658
OBC2	18	22,70	295,85				0,91		0,33421
Firstpay1	19	22,67	295,82	4,28		0,38775	0,91		0,48427
Firstpay2	20	22,71	295,86				0,91		0,30258
Front1	21	22,64	295,79	3,85		0,46748	0,91		0,64895
Front2	22	22,83	295,98				0,91	0,34561	
Space	23	-270,15	3,00				0,093		40,4322

Figure 13.3.2: Satellite transient temperatures during eclipse

		Operational temp		Survival temp	
Subsystem		min (˚C)	max (˚C)	min (˚C)	max(˚C)
Power					
	Batteries	0	40		
	Solar cells	-75	95		
	Peak power tracker				
	Charging regulator				
	Discharging regulator	-20	60		
	Battery charger				
1st payload	Sensors	-20	40	-30	65
Propulsion	T3µps	-40	75		
ADCS	Star tracker	-50	75		
	Magnetometer	-40	85		
	Reaction wheels				
	Magnetorquers	-40	70		
	Sun sensors	-25	50		
OBC & DH	Central microcontroller	-40	85		
GNC	GPS receiver	-10	50		
	GPS antennas	-30	70		
2nd payload	Cameras	0	50	-30	60
	Acoustic sensors	-30	70		
COMMS	VHF antennas	-30	70		
	VHF transceiver	-20	50		
Structure		-40	80		

Figure 13.3.3: Temperature ranges of satellite components

13.4 Final Thermal Design

Although according to the thermal analysis performed on the satellite, kapton thermal tape is sufficient for ensuring temperatures within the operational temperature ranges of components, verification done in the Satellite Tool Kit (STK) proves otherwise (see Section 13.6). Thus to be safe, since two walls of the satellite will be occupied with body-mounted solar panels, white paint is chosen for the final design of the TCS due to its low absorptivity and high emissivity. This is to be applied on the free walls of the satellite (excluding ones with FIPEX and body-mounted solar panels). On the inside of the satellite, all free walls will be covered with kapton tape.

Additionally, 5 thermistors will be placed inside the satellite to monitor the ambient temperature of the CubeSat. Thermistors are the more sensitive type of thermal sensors (compared to resistance temperature detectors (RTDs) and thermocouples) which can be calibrated to fit an individual component. Two negative temperature coefficient (NTC) epoxy contact chip thermistors will be taped (with epoxy tape for high temperature resistance) to two inside walls opposite each other. See Figure 13.4.1 for the placement of these sensors.

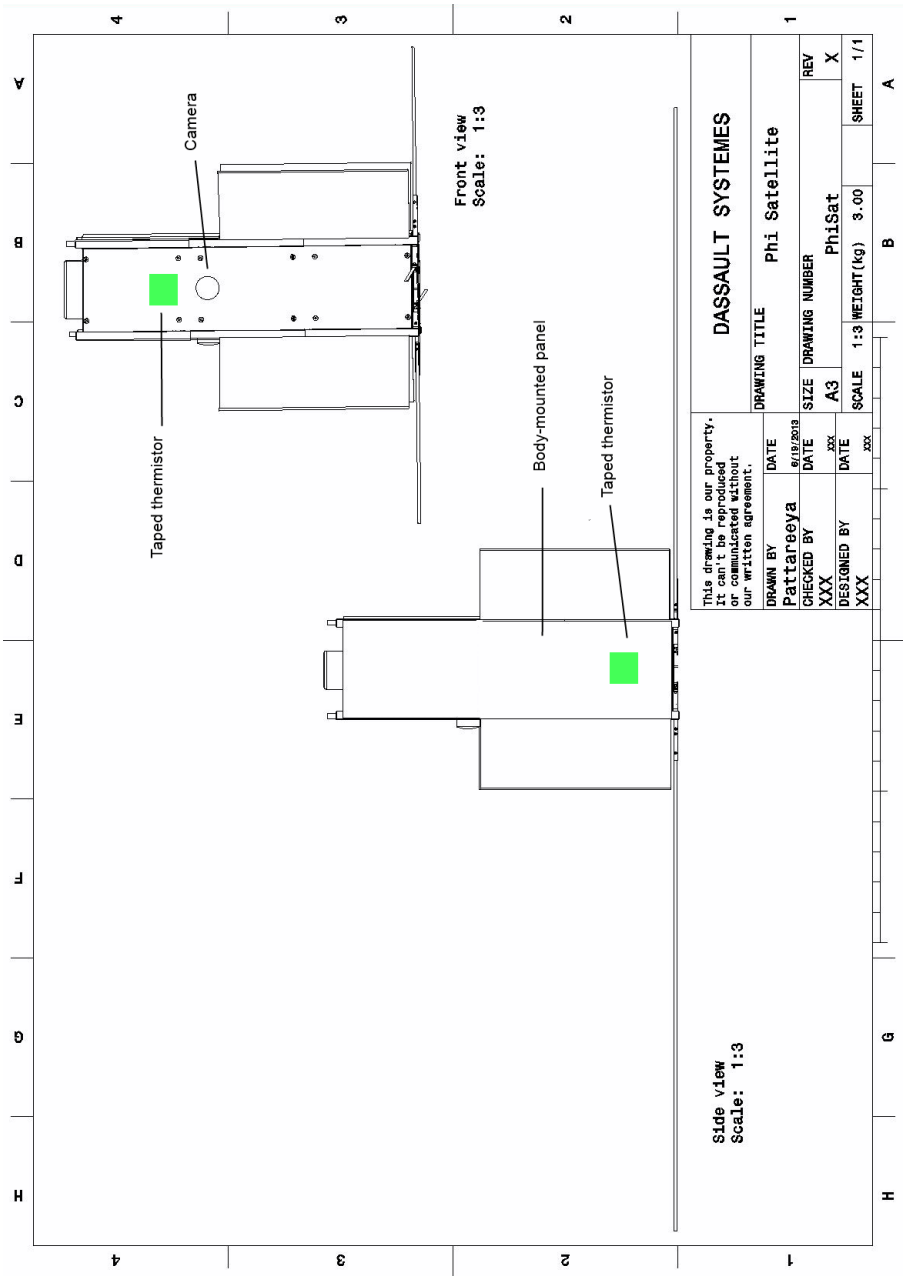

Figure 13.4.1: Placement of thermistors on inner satellite walls

One of the wall sensors will be near the camera payload on the upper half of the satellite, while the other on the opposite wall (with body-mounted panel) will be on the lower half. This is to obtain temperatures at the most varied positioning in the satellite.

Table 13.4.1: Thermal control system COTS components

Components	Unit	Retailer	Cost per unit [€]	Mass per unit [g]	Power required per unit [W]	Duty cycle
Thermistor	5	Tewa Sensors	0.99	3	0.01	On for 5 min every 15 min
Epoxy tape	1	3M	26.79	2	0	0
Kapton tape	1	Kapton Source	7.80	10	0	0
White silicate paint	1	EarthBorn	28.20	10	0	0
Total	8	-	67.74	37	0.05	-

Three other thermistors are surface mounted device (SMD), NTC thermistors. Each of these will be mounted on the PCBs of the secondary payload, ADCS, and GNC. The battery, which is a critical component due to its restrictive operational temperature range (charging has to be done at $0°C$ or above), has already been chosen with an integrated heat sensor and heater. The three PCBs chosen to place the thermistors are thus ones without integrated thermal sensors, whose ambient temperatures are of interest due to their varied positioning throughout the satellite. This more than satisfies the requirement given by the QB50, which states: "at least one thermal sensor will be used to monitor the temperature inside the CubeSat enclosure. This will be in addition to the thermistors in the Science Unit which are used for scientific measurement" [55]. The budgets of the chosen COTS components are given in Table 13.4.1.

13.5 Sensitivity Analysis

When the satellite lowers in altitude, the temperature increases due to the increased albedo and planetary IR radiation. For example, at the final altitude of 90 km, the satellite will experience an increased temperature of maximum 11%. This doesn't increase the temperature drastically and the satellite would still be within the operational temperature ranges of the components. Apart from this, if heat dissipation within the satellite increases, temperature will also be raised accordingly.

13.6 Verification and Validation

Results from the verification done on the thermal calculations will be presented in the next subsection, followed by a plan for validation of the thermal system.

13.6.1 Verification

Using STK, the solar radiation, albedo and planetary radiation can be simulated for the satellite in orbit. The resulting surface temperature is plotted as a variation of time within one day, as shown in Figure 13.6.1.

The temperatures modelled by STK are very varied compared to the results obtained from the Excel sheet, going from $13°C$ in eclipse to $41°C$ in sunlight. The hot case is rather dangerous for the FIPEX payload, whose operational temperature goes up to only $40°C$. This discrepancy in the hot case analysis may be explained by the fact that in STK a flat plate is used to model the satellite, receiving the most sunlight at worst-case when perpendicular to the Earth-Sun vector. Another discrepancy is that the Excel sheet gives rather constant temperatures compared to the varying temperatures modelled by STK. This can be explained by the fact that the calculations done in Excel are transient for the duration of 5 minutes, while STK looks at the surface temperature of the satellite throughout the whole orbits.

Apart from this, further verification can also be done by testing the material properties of the selected paint and thermal tape. The effective conductance of component placement can also be measured. As a recommendation, thermal inertia of the materials could also be looked into when sizing for the surface finishes. Thermal inertia is given by Equation 13.6.1.

$$I_{th} = \sqrt{\kappa \cdot \rho \cdot c} \tag{13.6.1}$$

Where κ is thermal conductivity $[Wm^{-1}K^{-1}]$, ρ is the density $[kgm^{-3}]$, and c is the heat capacity $[Jkg^{-1}K^{-1}]$

13.6.2 Validation

For validation, similar CubeSats such as Delfi-n3Xt and Delfi-C^3 are used as reference. Both of them maintain a comfortable temperature within the satellites through passive thermal control. Furthermore, the satellite could also

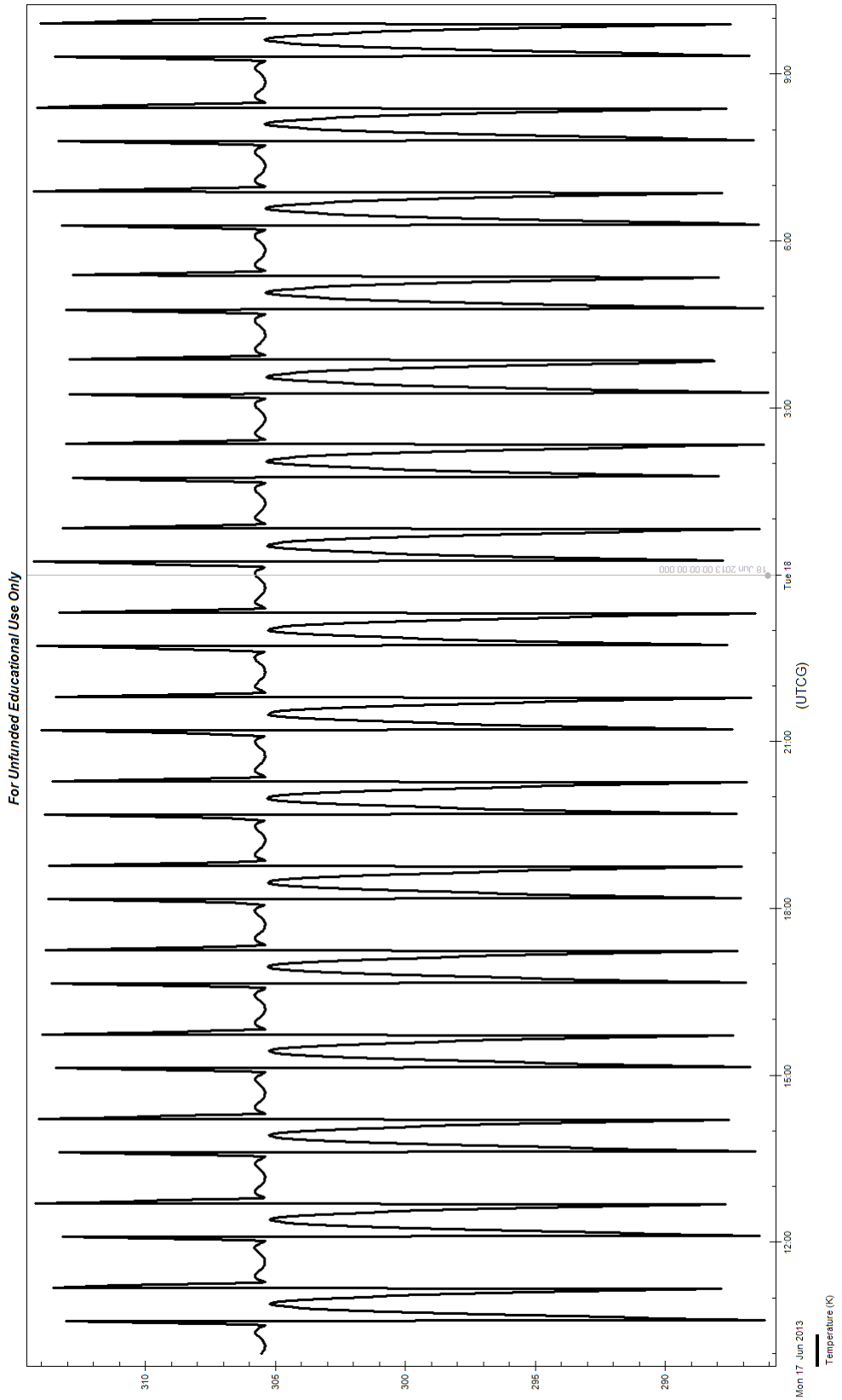

Figure 13.6.1: Thermal variation in orbit over 1 day

be tested to see if other components from different subsystems and payloads will function when in space. This is done by exposing qualification samples to conditions more severe than those found in space (for the worst case scenario). A thermal balance test can be done in a high vacuum conditions facility that involves simulated heat sinks and heat sources.

Chapter 14
Structures

The primary purpose of the structural subsystem is to provide support and protection to all the components contained within the satellite. The design of this subsystem centres primarily on making the structure robust enough to handle all the loads expected to be encountered throughout the spacecraft's lifetime, the most critical of which will occur during launch.

This section first outlines the choices executed throughout its design. A justification is then given for the internal configuration of the satellite, which refers to the placement of all its physical components within the primary structure. This is followed by a section outlining the structural analysis carried out on the final structure. Then, in conclusion, a verfication and validation plan is presented.

14.1 Structural Design

14.1.1 Requirements

The main constraints on the Phi project scope results from the limitations in volume and mass. The structural subsystem must primarily comply with the CubeSat standards. The satellite is a 3-Unit(3U) CubeSat, and must therefore have the standard 3U dimensions of 100x100x338 mm and a maximum mass of 3.6 kg. The latter specification follows from the QB50 requirement of 3 kg together with the concession of 600 g which the Von Karman institute allowed TU Delft. It is also important that the final design is compatible with the StackPack, which is the container that the CubeSat will be stored in during launch. The CubeSat will be mounted on to the StackPack on rails having an 8.5x8.5 mm cross-section, which must be incorporated in the design. The 10x10 cm surface on which the FIPEX payload is mounted will face the StackPack door, while the other face is in contact with a spring. During deployment into orbit, the CubeSats will be pushed out by the spring when the door, which is restraining the satellite from moving due to the spring force, is opened.

The complete list of physical requirements, for this satellite, is reproduced below:

- PHI-QB50-SYS-1.1.1 The CubeSat dimensions shall be as shown in Table 14.1.1
- PHI-QB50-SYS-1.1.2 In launch configuraton, a 3U CubeSat shall fit entirely within the extended volume dimensions shown in Figure 14.1.1 including any protrusions.
- PHI-QB50-SYS-1.1.3 The CubeSat centre of gravity shall be located within a sphere of 20 mm diameter, centered on the CubeSat geometric centre.
- PHI-QB50-SYS-1.1.4 The 3U CubeSat mass shall be no greater than 3 kg.
- PHI-QB50-SYS-1.1.5 Total Mass Loss(TML) shall be less than 1.0% and Collected Volatile Condesable Material (CVCM) shall be less than 0.1%
- PHI-QB50-SYS-1.1.6 The CubeSat rails and standoff, which contact the deployer railer, pusher plate and/or adjacent CubeSat standoffs, shall be constructed of a material that cannot coldweld.

Table 14.1.1: Cube Sat Dimensions [53]

CubeSat Dimensions	
Footprint	$100 \times 100 \pm 0.1$mm
Height	340 ± 0.1mm
Feet	$8.5 \times 8.5 \pm 0.1$mm
Rails	External edges shall be rounded $R \times 1$mm or chamfered $45° \times 1$mm

Aside from meeting the physical requirements, the structure must also be strong enough to withstand the anticipated loads. Presented first are the requirements regarding structural integrity that will be investigated in this chapter. QB50 does list more requirements regarding the structure's response to sine vibration, random vibration and shock loads. However, due to time constraints, these responses were not considered for structural analysis. Nevertheless, following the list is a brief description of all five of loads.

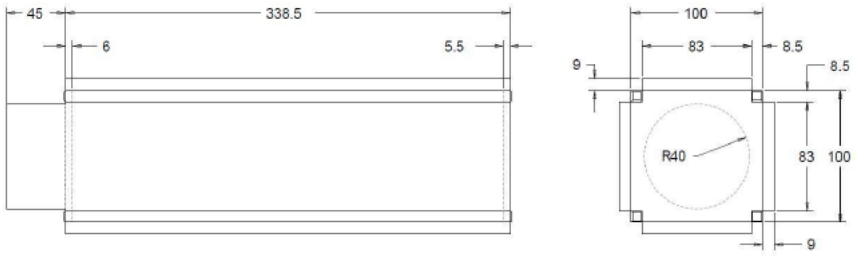

Figure 14.1.1: Extended volume dimensions /citeQB50

- PHI-QB50-SYS-3.1.1 The CubeSat shall withstand accelerations of up to 8.3 g in all three axes.

- PHI-QB50-SYS-3.2.1 The CubeSat shall pass a resonance survey and the lowest natural frequency of the CubeSat shall be >90 Hz

Quasi-Static and g-loads Quasi-static load testing and g-load testing are used to demonstrate that the spacecraft is able to tolerate the application of constant steady loads without incurring failure.

Resonant frequency A system's resonant frequencies are the frequencies at which amplitude magnification occurs. If the satellites natural frequencies match the natural frequency of the launcher, they will begin to oscillate at uncontrollable amplitudes, threatening the entire mission.

Sinusoidal vibration In sinusoidal vibration testing, the system is exposed to a single vibration that has discrete values of amplitude and frequency and are in a distinct phase at any moment. The frequency is adjusted across a range throughout this testing procedure. This test is again used to determine whether resonance occurs at any of the frequencies being tested. This test is carried out due to the possibility that such an excitation may derive from a motor in the launching vehicle.

Random vibration Unlike sinusoidal vibration testing where only one frequency is tested at any time, random vibration testing occurs at all frequencies simultaneously. This is a much more realistic representation of the environment in the launching vehicle. The peak values normally occur during the first stage of launch.

Shock loads As its name suggests, shock load testing involves observing the system's reaction to sudden, high impact loads. Such loads occur during launch stage separations and deployment from the launching vehicle.

14.1.2 Component Selection

- **Primary Structure** The design team has the option of either manufacturing the structure independently or purchasing a prefabricated structure from a CubeSat component retailer. The latter option was chosen because the COTS components available have already undergone vigorous validation tests, with many models possessing a sizable flight heritage. Using COTS components also eliminates the expense of resources on design, developments and testing. The component chosen for the final design is produced by ISIS CubeSatShop. Their 3 Unit CubeSat Structure (see Figure 14.1.2) consists of a frame and panels composed of aluminium, as well as support structures for mounting the PCBs. The combined mass of the primary and supporting structure is 580 g.

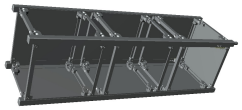

Figure 14.1.2: ISIS 3U CubeSat structure /citeISIS

- **Hinges** Hinges were required for supporting the deployable solar panels. It is important that the hinges are rigid enough to maintain the desired solar panel configuration. The CubeSat Kit hinge from Pumpkin were chosen because they have flight heritage from previous CubeSat missions

14.1.3 Configuration/Layout

The configuration of the satellite refers to the placement of the satellite components within the primary structure. Its design is strongly driven by QB50-SYS-1.1.3, which stipulates that the CubeSat center of mass (c.o.m) shall be located within a sphere of 20 mm diameter, centered on the CubeSat Geometric center. Throughout this section, the reference frame displayed in Figure 14.1.3 will be used to describe position within the satellite. The origin is located at its geometric center. Furthermore, all dimensions in this section are given in millimeters, unless otherwise specified.

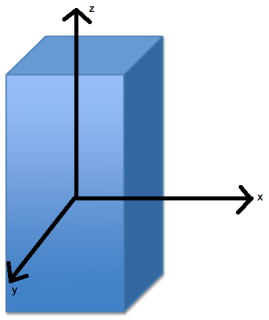

Figure 14.1.3: Reference frame

The development of the configuration began with identifying the components that are required to be mounted at a particular location. These fixed components are listed below:

- FIPEX payload : The QB50 CID states that the sensory payload must be partially deployed on one of the 10×10 cm faces
- Propulsion: The propulsion system must also be mounted on a 10x10 cm face.
- Retractable balloon: The retractable balloon must be situated next to the propulsion system.
- Deployables (including hinges): The solar panel configuration design places the deployables mostly on the -z surfaces of the satellite. Approximatley 12% of the +z axis is also covered by these deployables.

Next, the effect of the solar panel configuration on the structure's c.o.m was calculated. Because the configuration is aysmmetric across all three planes, all three c.o.m coordinates will be effected. The solar panels can be categorized into two categories- body mounted and deployable. The body mounted panels run across the length of the 10×30 cm sides and have a mass of 139 g. The deployables have a length equal to 56% of the CubeSat length and have a mass of 79 g. One side will contain both a body-mounted and a deployable panel. The side adjacent to this will contain one body mounted panel. The side across will carry only one deployable. It can be assumed that the solar panels have even mass distribution throughout, and can therefore be plotted as point masses along their geometric center. The contribution of the solar panels to the c.o.m. coordinates is first calculated for the $x-y$ plane using Figure 14.1.4 and then along the z axis in Figure 14.1.5.

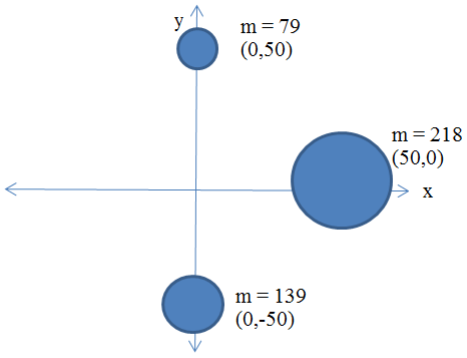

Figure 14.1.4: Solar panel mass distribution in the $x-y$ Plane

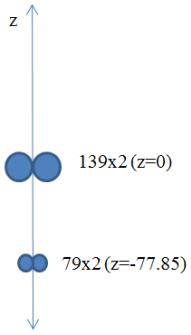

Figure 14.1.5: Solar panel mass distribution in the z Axis

For c.o.m calculations, the standard equation was used:

$$x_{cm} = \frac{\sum m_i x_i}{\sum m_i} = \frac{79 \times 0 + 139 \times 0 + 218 \times 50}{79 + 139 + 218} = 25$$

$$y_{cm} = \frac{\sum m_i y_i}{\sum m_i} = \frac{79 \times 50 + 139 \times -50 + 218 \times 0}{79 + 139 + 218} = -6.68$$

$$z_{cm} = \frac{\sum m_i z_i}{\sum m_i} = \frac{2(139 \times 0) + 2(79 \times -7.785)}{2(139) + 2(79)} = -28.21$$

Then, all remaining components possessing a mass greater than 50 g were isolated. All of these components are either PCBs or components mounted on a board. The mass distribution across these boards is assumed to be homogenous. If these boards were to be stacked horizontally along the length of the CubeSat, the x and y center of gravity coordinates will not vary significantly. The z coordinate, however, is heavily effected by the order of these boards. In the center of mass (c.o.m) calculation necessary for establishing an acceptable order, the boards were considered as point masses situated along the z-axis. The c.o.m would then be calculated by using the following equation, where m_i is the mass of the ith component and z_i is its position along the z-axis.

It is assumed that the the 12 thermocouples and 15 acoustic emission sensors, which have a combined mass of 396 g, are evenly distributed along the spacecraft. The magnetometer, which must be situated at a sufficient distance away from the magnetorquer to avoid interference, is mounted between the ADCS and the COMM PCBs. The two sun sensors, weighing 5 grams each, must be mounted towards the sun-pointing direction on the aluminum panels. The shifts in x_{cm} and y_{cm} created by the solar panels can be rectified by situating the components mounted on boards not through the center, but rather towards a particular side. The three reaction wheels, which have a combined mass of 270 g, can be located at the coordinates $x = 34.81$ and $y = -10.78$ to bring the x_{cm} and y_{cm} to 0.

After several iterations, a configuration that complied with the c.o.m requirement was achieved, shown in Table 14.1.2. The z_{cg} of this configuration is 0.7 mm, which meets the requirements.

Table 14.1.2: Internal configuration

Component	Mass	z_{cg}
FIPEX	400	169.25
COMM	85	141.87
GNC	30	113.5
Secondary Payload PCB	57	85.125
Magnetorquers+Sun Sensors	180	56.75
Reaction Wheels	270	28.375
ADCS	83	0
Computer	65	-28.375
EPS	142	-56.75
Battery	139	-85.152
Propulsion	428	-113.5
Balloon	50	-141.88
Antenna	85	-169.25
Deployable Panels+Solar Panels	436	-28.21

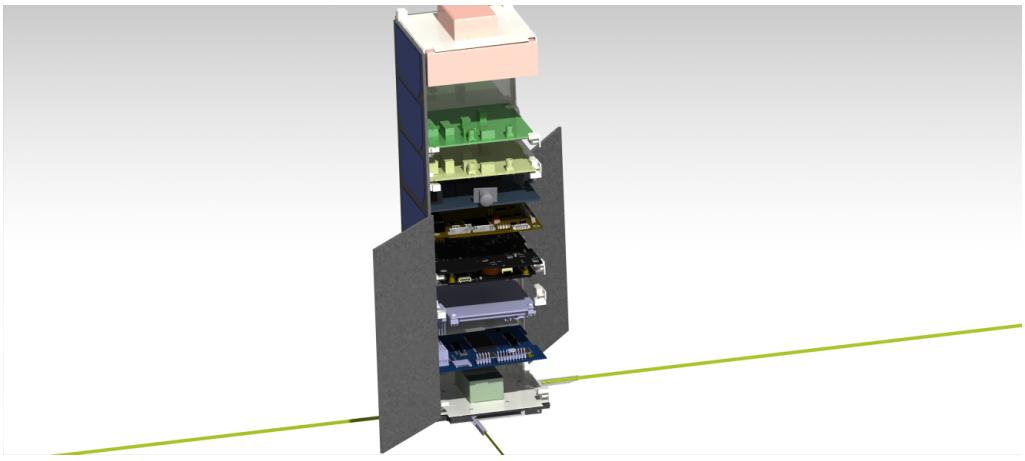

Figure 14.1.6: Internal configuration

14.2 Structural Analysis

14.2.1 Static Loading

According to requirement QB50-SYS-3.1.1, the structure must withstand an acceleration of 8.3g. The behavior of the structure in response to this load depends on the orientation of the StackPack with respect to the acceleration of the launching vehicle. If the StackPack is oriented perpendicular to the rocket's acceleration, the load will be distributed across the 328 mm faces of the rails, as illustrated in Figure 14.2.1. The second case occurs when the StackPack is oriented parallel to the launch direction because the load will be distributed across the 8.5x8.5 mm cross sections of the 4 rails, as seen in Figure 14.2.2. The rails are assumed to carry the direct loads, while the panels carry the shear loads.

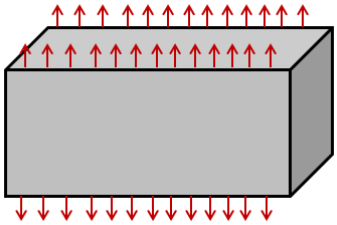

Figure 14.2.1: Case 1: Acceleration perpendicular to StackPack configuration

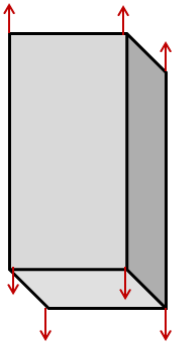

Figure 14.2.2: Case 2: Acceleration parallel to StackPack configuration

Tensile Failure

Tensile failure will occur first in case 2, where the loads are concentrated on the cross sections of the 4 rails. The CubeSat structure from the CubeSatShop used for the final design has rails composed of black anodized aluminium 7075, which has an ultimate tensile stress of 572 MPa. Assuming the final mass of the satellite reaches the upper limit value of 3.6 kg, the total force acting on the rails during 8.3 g acceleration would be $8.3 \cdot 9.81 \cdot 3.6 = 293.12$ N (the downward acceleration due to gravity is neglected in this calculation). The force is distribute across four rails, so the force on each rail is $293.12/4 = 73.28$ N. The stress is calculated by dividing the force on each railing by its cross sectional area: $73.28/(0.0085 \cdot 0.0085) = 1.01(10^6)$ Pa $= 1.01$MPa. Because the margin between the static stress and the material's ultimate tensile stress is consideraly high, it can be safely concluded that provided the structure is void of any major defects, the structure will not fail when under an acceleration of 8.3 g.

Buckling

While being transported in the launch vehicle, the structure will undergo compression loads. Therefore, it must be verified that the cross sectional areas of the rails is sufficient to avoid buckling at the 8.3 g load.

The critical load for buckling of a column clamped on one end and simply supported on the other is shown below:

$$P_{cr} = \frac{\pi^2 EI}{4L^2}$$

The length L is taken as 338.5 mm. The moment of inertia I of the cross sections is $5.11(10^{-8})$ m^3. With these values, the critical load for column buckling is 673.01 N. This is again significantly higher than the 73 N force that each rail is expected to undergo.

Shear Strength

It was stated earlier that the panels will carry the shear loads. Aluminum 7075 has an ultimate shear strength of 331 MPa. Assuming that the direction of shear load transfer is parallel to the cross section of the panels, the shear stress subjected to each panel can be calculated using the equation

$$\tau = \frac{\frac{P}{4}}{A}$$

The cross sectional area A differs for 10×30 panels and 10×10 panel. The worst case scenario involves the 10×10 panels, so only this is taken into account. The thickness of the panels is taken to be 1 mm. Therefore, $A = 0.001 \times 0.010$. The shear stress is calculated to be $7.3(10^6)$ N/m^2 or 7.3 MPa. It can therefore be concluded that the panels will not fail due to shear.

14.2.2 Modal Analysis

Analytical solution

An analytical solution for the natural frequencies of the CubeSat can be established by idealizing it as a beam. For this solution, the beam is assumed to have the same cross sectional properties as the assembly of the four longer panels and the rail frame. The cross section and its dimensions are shown in Figure 14.2.3. The next step in calculating the natural frequencies of the satellite is determining the boundary conditions imposed by the StackPack, where the vibrational behavior of the CubeSat carries the most importance. The CubeSat-StackPack interface, as illustrated by the developers of the StackPack themselves, is shown in Figure 14.2.4.

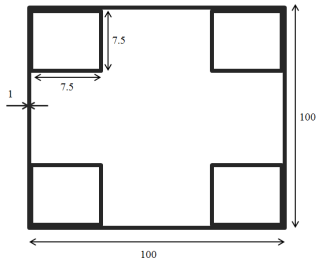

Figure 14.2.3: Representative Beam Cross Section

Figure 14.2.4: StackPack-CubeSat Interface [11]

From Figure 14.2.4, it can be deduced that the rails keep the CubeSat from translating in the x and y direction (see Figure 14.2.5). The rails also restrain any rotational movement. The spring and the door exert equal and opposite forces on the CubeSat, with the spring pushing the CubeSat out and the door retaining it in. Because natural frequency equations are not readily available for these boundary conditions, the system can be simplified. In the following analysis, it is assumed that the CubeSat has negligible translation motion along the z axis. Under this assumption, the beam can be assumed to be simply supported at both ends. The beam is not considered to be clamped since the front and the rear ends of the StackPack do not prevent rotation of the beam, but rather the rails.

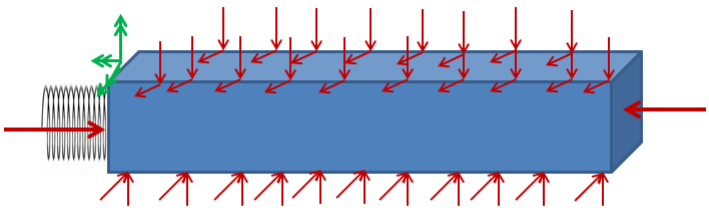

Figure 14.2.5: Constraint forces acting on CubeSat in StackPack

The calculation of the fundamental frequency f_1 of the beam simply supported on both ends is shown below [63]:

$$f_n = \frac{\omega_n}{2\pi} = \frac{\sqrt{\beta_n^4 \frac{EI}{m/L}}}{2\pi} \tag{14.2.1}$$

Where: E is the Young's modulus of the material; for aluminium 7075, this is $71.9(10^9)$ GPa
I is the beam's moment of inertia; using $I = \frac{1}{12}bh^3$, this was calculated to be $2.44(10^{-7})$ m^4
L is the length of the beam; the length of the beam is taken to be 0.3385 m

n defines the mode; for this analysis, only the fundamental freqeuncy (the first natural frequency) is of interest, so $n = 1$

β_n is a factor dependent on the boundary conditions; for simple-simple supports, $\beta_1 = \frac{\pi}{L}$

m is the distributed mass of the entire system; including both the structural and non-structural masses in the analysis, $m = 3.6$ kg

ω is the system's angular natural frequency

After substituting all the figures in the equation, a natural frequency of 557.2 Hz is calculated.

This calculation does not take into account the effect of the axial load applied by the door and the spring. This can be rectified by using the following equation [63]:

$$\omega^2 = \omega_0^2[1 - \frac{P}{P_c}]$$

Where:

ω_0 is the system's natural frequency without the axial loads

P is the axial load; this value is a function of time

P_c is the beam's critical load; for a simply supported beam $P_c = \pi^2 \frac{EI}{L^2}$

ω is the natural frequency corrected for the axial load

This equation only applies when $P < P_c$, or in other words, before the beam has buckled due to compression. It can nevertheless be deduced that the axial load will effectively lower the natural frequency of the structure.

The solution presented does not take into account the inertial effect of the components stored within the satellite. It can be logically assumed, however, that these components will decrease the natural frequencies of the system by imposing an increase in mass disproportional to the increase in stiffness.

Finite element analysis

Finite Element Analysis (FEM) was carried out on the Generative Structural Workbench Analysis in CATIA to determine more accurate values for the natural frequencies of the structure. In developing the finite element model, the following assumptions were made:

- The parts which compose the spacecraft's primary structure- the rails and the aluminum panels- were "fastened" to one another. This means that the overall structure will act as one body.

- The internal components were modelled as point masses. Their contribution to the model was solely and increase in mass. They were assumed to not carry any inertial properties, thereby effectively reducing the structure's stiffness. In reality, components such as the PCBs will have a finite contribution to the spacecraft's moment of inertia, which together with Young's Modulus, defines a structure's thickness.

- Details of the primary structure, such as the perforations seen in Figure /reffig:Isis are not incorporated into the model as they have a negligible effect on the structure's mass and stiffness, and therefore on the final outcome as well.

- The assumption that the CubeSat cannot translate in the axial direction is not applied in the FEM model. The rails are assumed to restrict the other two translational motions and rotations about all three axes. An axial constraint is applied on the CubeSat face adjacent to the door, but the other end is kept free. This defines the model's boundary conditions.

After these assumptions were implemented into the model, the natural frequencies for the first five modes were computed:

Table 14.2.1: Natural Frequencies

Mode Number	Frequency(Hz)
1	543.20
2	657.13
3	668.71
4	1202.32
5	1783.98

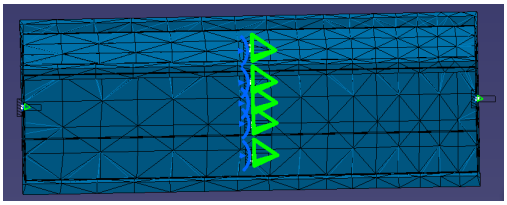

Figure 14.2.6: 1st mode shape

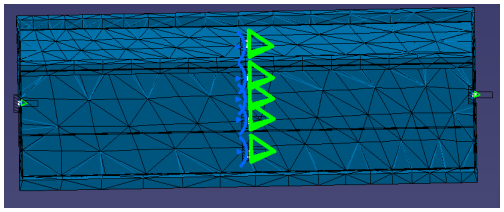

Figure 14.2.7: 2nd mode shape

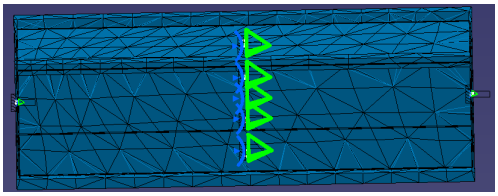

Figure 14.2.8: 3rd mode shape

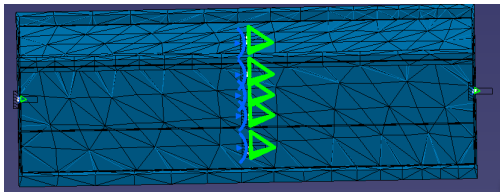

Figure 14.2.9: 4th mode shape

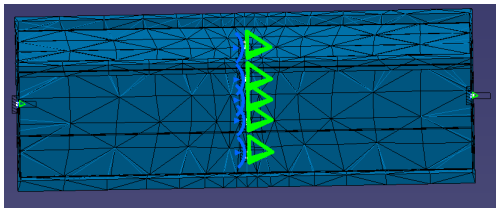

Figure 14.2.10: 5th mode shape

To evaluate the accuracy of the model, the results were compared to the natural frequencies of existing CubeSats. The first five modes computed for SwissCube ([50]), OutFI-1 ([46], ICE-Cube([29]), GeneSat-1 ([27]), ITU[17]) and an arbitrary CubeSat for an independent study([47]), were considered.

Table 14.2.2: Natural frequencies of other CubeSats

	Natural Frequencies(Hz)				
Mode:	1	2	3	4	5
Swiss Cube	153	158	175	189	537
OUTFI-1	522.6	591	604.3	643.2	709.5
ICE-Cube	158.18	160.84	166.12	166.68	383.71
Study	764.06	873.69	877.79	878.64	903.51
ITU	749.88	873.69	877.79	878.64	903.51
GeneSat-1	1117.5	-	-	-	-

Unfortunatley, the majority of these satellites are 1U CubeSats, with the exception of GeneSat-1 which is a 3U satellite. Nevertheless, it can be concluded by comparing the different satellites that the natural frequencies of these satellites vary, even if they are similar in size and mass distribution. The developers of these CubeSats did not mention the need for further design iterations because the natural frequency requirements were met, so the threat of non-compliance in case the results from the FEA were not accurate is marginal. All in all, it is recommended that the in later design stages, more FEA iterations are carried out using finer meshes so more modes can be calculated and higher accuracies can be achieved.

14.3 Failure Modes

- **Buckling** : Compression, which is the predominant steady state stress during launch /citeprinceton, can cause the rails to buckle; a critical load calculation for this failure mode is carried out in the Structural Analysis section.
- **Fatigue** : The structure may fail due to fatigue when cracks begin to form and propagate due to repetitive loading. One cause of fatigue are direct stresses above a certain amplitude applied on the structure for an excessive period of time. Though aluminium 7075 does not have a fatigue limit, the number of load cycles must exceed 10^6 for stress amplitudes of less than 200 MPa [1]. The direct stresses applied by the launching vehicle on the satellite structure is anticipated at 0.01 MPa, which indicates that it is unlikely that this type of failure mode

will occur. Conversely, acoustic fatigue, resulting from the high acoustic loads emitted by the launch vehicle, is a considerable threat to structural integrity. The aluminium panels are especially vulnerable to these loads and must therefore be tested to verify that they don't produce high responses when subjected to these loads.

- **Dynamic Coupling** : The natural frequency requirements not only pertains to the external structure with respect to the launch environments, but also the internal components. For instance, if the natural frequencies of the PCBs are close to that of their enclosing structure, the force that excited these frequencies will amplify, causing electronic failure. Because these PCBs form the backbone of this mission, this will result in mission failure [62].
- **Hinge Failure** : If the hinges lack sufficient rigidity and are unable to support the deployable solar panels as required, the entire solar panel configuration will not be at its optimum, resulting in reduced power. Furthermore, the structure's moment of inertia will also change. This will require modifications in the ADCS commands delivered to the spacecraft's actuators.

14.4 Sensitivity Analysis

The vibrational behaviour of the spacecraft structure is influenced by the mass and the placement of the components. Components add mass but do not have an inertial contribution comparable to that of the primary structure. Therefore, additional non-structural mass will decrease the stiffness and consequently its natural frequencies as well. Because vibrational loads drive the structural requirements more than quasi-static loading, a reduction in stiffness resulting from the addition of more components may necessitate thicker plates, which will not only result in an inrease in stiffness, but also a further increase in mass. Because the final design is less than a 100 g below the upper mass limit, such adjustments in the detailed design phase must be done with care.

14.5 Verification and Validation

Before the satellite is launched, it must be demonstrated that the system as a whole and its individual components comply with the requirements. The structural analysis performed in the previous section is just a preliminary step taken to verify the design. The steps that follow include testing and inspection. The final assembly must first be subjected to the loads anticipated to occur throughout the mission. The entire assembly must then be checked for any defects that may have formed due to the loads. In engineering projects, verification testing consists of several levels. The first two levels are qualification testing and acceptance testing. The former is primarily carried out to show that the system and subsystems meet mechanical specifications such as possessing an appropriate resonant frequency range. Acceptance testing, which follows successful qualification tests, is performed on the flight model to show that the entire system functions as planned in the expected environment.

Chapter 15
Spacecraft Systems Characteristics

An overview of all the important characteristics of the satellite is given in Table 15.0.1.

Table 15.0.1: Spacecraft systems characteristics

System characteristic	Value	Unit
Mission lifetime	3	Months
Altitude	90 - 350	Km
Eccentricity	≈ 0	-
Inclination	98	degrees
Launch date	april 2015	-
Total mass	3.6	Kg
Average bus power	3.49	W
Average bus power during eclipse	3.24	W
Solar panel area	820	cm^2
Battery capacity	10	Wh
ΔV	15	m/s
Propellant mass	88	g
Specific impulse	69	s
Thrust force	6	mN
Surface temperature range	10.3 - 33.3	C
Internal temperature range	23 - 32	C
Uplink data rate	1200	b/s
Downlink data rate	9600	b/s
Number of overpasses	3-6	/day
Overpass time	443-230	s
Memory	4	GB
Processor frequency	48	GHz
Processor word lenth	32	bit
Pointing accuracy (pitch & yaw)	2	degrees
Pointing accuracy roll	5	degrees
Along track seperation	1000	Km
Control window	100	Km
Control accuracy	10	Km
Navigation accuracy	1	Km

Chapter 16
Conclusion

The design of the Phi satellite has been presented in this report. This includes the design of the subsystems, which have been finalized through a process that flows down from literature study and requirements to trade-off, sizing and final selection. The primary and secondary mission objectives have also been discussed and sized for.

For mission design, an extensive treatment which included detailed computational models for the aerodynamic analysis was carried out. From this, the lifetime of the satellite has been estimated to be 50 days. This is much lower than the lifetime predicted by QB50 of 3 months, since the calculations took into account more realistic considerations. In this aspect, QB50 gave conflicting requirements concerning the initial altitude and lifetime.

Furthermore, the configuration of the CubeSat has also been discussed. Altogether there will be four deployable panels. The first two are solar panels which are deployed at initial altitude for power as well as stabilisation. At 200 km, the other two panels will be deployed, only one of which is a solar panel. Two sides of the CubeSat that are facing the Sun will be covered with body-mounted solar panels, while the other two sides will have cameras mounted on for the secondary mission objective.

For formation flying, it has been concluded that formation flying will be demonstrated in four modes of increasing complexity that will be performed after each other. A detailed analysis of the behavior of the formation has been performed, and it has been found that large uncertainties arise due to the fact that no data is available on the thrust accuracy of the selected cold-gas thruster. It is therefore recommended to perform tests to verify that the requirement PHI-MO-FF-4.1 can be met. Depending on the outcome, the formation might behave differently from what is expected and it should be verified that proposed nominal mission scenario is still feasible within the given ΔV budget.

In terms of the budget breakdown, the total mass of the satellite amounts to 3.55 kg. The cost comes up to 1.25 million Euro. Thus the budgets are kept within the constraints. The low cost of the satellite is due to the use of COTS components and student labour (both in design & development and ground operation).

For the payloads onboard the satellite, Phi has been allocated the FIPEX sensor developed by TU Dresden as its primary payload, as well as the thermocouples. Next to this two cameras for recording the deployment of solar panels and antennas, and acoustic sensors for analysing the satellite's vibrations, have been selected as secondary payloads.

Individual subsystems in the CubeSat have been treated in separate chapters. A summary of the CubeSat's system characteristics includes important parameters from the satellite's subsystems, and is given in Chapter 15.

For the sustainability aspect, the low initial altitude of the Phi mission has a milder radiation environment, which allows for the use of low-cost Commercial Off-The-Shelf products. Care is taken in ensuring that the chosen COTS products are environmentally friendly, such that waste is reduced in the production process and no toxic materials are used. Furthermore, the low initial altitude translates into a short mission life, at the end of which the satellite will de-orbit itself and be disposed of during re-entry, leaving no contribution to the space debris problem.

After this design phase, a number of things remain to be done. These are purchasing of the COTS components, assembly of the satellite, and various tests on the subsystems and satellite as a whole (qualification and acceptance tests). In particular the thrusters should be tested, as well as the cameras for structural vibrations. Further recommendations were also given in the report, such as MEMS gyroscope investigation for the ADCS and the use of smaller batteries for the EPS. All in all, the Phi satellite holds various potentials for scientific investigations and incorporates original elements that will contribute to educational purposes.

Appendix A
Compliance Matrix

Requirement	Met by design	Design value	Comment
PHI-QB50-1.1.1: The CubeSat shall dimensions shall not exceed 100x100x340.5 mm.	yes	-	
PHI-QB50-1.1.2-D.1: (Deployable) solar panels shall fit within the extended volume.	yes	-	
PHI-QB50-1.1.3: The CubeSat mass shall be no greater than 3.6 kg. Note: This requirement deviates from the QB50 CID. The reason for this is that TU Delft has requested and received approval for launching a CubeSat that exceeds the value stated in the CID by 0.6 kg.	yes	-	
PHI-QB50-1.1.4: The CubeSat centre of gravity shall be located within a sphere of 20 mm diameter, centered on the CubeSat geometric center.	yes	-	
PHI-QB50-1.2.1: The satellite shall be able to recover from tip-off rates of up to 10 degrees/second within 2 days.	yes	-	
PHI-QB50-1.2.2: The satellites carrying the science sensors shall have an attitude control with pointing accuracy of ± 10 deg and pointing knowledge of ± 2 deg from its initial launch altitude at 350 km down to at least 200 km.	yes	-	
PHI-QB50-1.3.1-D.1: The total average power to be provided by the EPS is 3.5 W.	yes	-	
PHI-QB50-1.3.1-D.2: The peak power to be provided by the EPS is 13.92 W.	yes	-	
PHI-QB50-1.3.1-D.3: The EPS shall be able to get rid of excess power.	yes	-	
PHI-QB50-1.3.1.-D.4: The average power that the EPS will provide to the loads during eclipse is 3.24 W.	yes	-	
PHI-QB50-1.3.1.-D.5: The ADCS shall be able to point the solar panels towards the Sun with an accuracy of 5°.	yes	-	
PHI-QB50-1.3.1.-D.6: The battery shall be able to store 6 Wh.	yes	-	
PHI-QB50-1.3.2: The CubeSat shall be able to be commissioned in orbit following the last powered-down state without battery charging, inspection or functional testing for a period of up to 4 months.	yes	-	
PHI-QB50-1.4.1: The CubeSat shall have 2 independent memory storage units of at least 2 GB to store all the science, telemetry and housekeeping data.	yes	-	

Requirement	Met by design	Design value	Comment
PHI-QB50-1.5.2: Each CubeSat carrying a set of standard QB50 science sensors shall communicate a volume of at least 2 Megabits of science data per day to the ground station that is operated by the university providing the CubeSat.	yes	-	
PHI-QB50-1.5.8-D.1: The receiver shall be operated continuously.	yes	-	
PHI-QB50-1.5.10: The CubeSat shall determine its position to within 1 km accuracy.	yes		GPS
PHI-QB50-1.5.11: Every science packet shall be tagged with the position of the CubeSat at the time that the RDY line goes high (indicating that that packet is ready in the science instrument), accurate to within 1 km. Position error estimates shall be provided for each position tag.	yes	-	
PHI-QB50-1.5.12: Every science packet shall be tagged with the real time that the RDY line goes high (indicating that that packet is ready in the science instrument), accurate to within 1 seconds. Time error estimates shall be provided for each time tag.	yes	-	
PHI-QB50-1.6.1: The CubeSat shall maintain all its electronic components within its operating temperature range while in operation and within survival temperature range at all other times.	yes	-	
PHI-QB50-1.7.1: The CubeSat shall be designed to have an in-orbit lifetime of at least 3 months.	no	-	
PHI-QB50-1.7.1-D.1: The solar panel configuration shall be such that the satellite stays above 90 km for a period of three months at a F10.7 index of 140 and a geomagnetic index of 30.	no	-	
PHI-QB50-1.7.1-D.2: Manoeuvres shall be spaced by differences in argument of latitude of 180 deg.	yes		
PHI-QB50-2.1.1: The payload shall withstand a maximum pressure drop rate of 3.92 kPa/sec (TBC before CDR).	yes	-	
PHI-QB50-3.1.1: CubeSat shall withstand accelerations of up to 8.3 g in all three axes.	yes	-	
PHI-QB50-3.2.1: The CubeSat shall pass a resonance survey and the lowest natural frequency of the CubeSat shall be $> 90Hz$.	yes		
PHI-QB50-3.3.1: The CubeSat shall pass the sinusoidal vibration tests as in the table.	Not yet performed		
PHI-QB50-3.4.1: The CubeSat shall pass the random vibration tests as in the table.	Not yet performed		
PHI-QB50-3.5.1: The CubeSat shall pass the shock tests as in the table taking into account the shock loads damping during propagation within the spacecraft structure.	Not yet performed		

Requirement	Met by design	Design value	Comment
PHI-MO-FF: The satellite shall demonstrate formation flying with the Delta satellite.	yes	-	
PHI-MO-FF-1: The torques due to thruster misalignment shall be smaller than $2.4 \cdot 10^{-5} Nm$.	yes	-	
PHI-MO-FF-2: The nominal distance between the satellites shall be 1000 km.	yes	-	
PHI-MO-FF-2.1: The inter-satellite link shall have a signal to noise ratio at the receiver of $> 10dB$.	yes	15.5 dB	
PHI-MO-FF-3: Control window shall be a cube with a side-length of 100 km.	yes	-	
PHI-MO-FF-3.1: The propulsion system shall be able to thrust at a frequency of 40 min.	yes	-	
PHI-MO-FF-3.2: Knowledge of the relative positions shall be provided every 12 hours.	yes	-	
PHI-MO-FF-4: The control accuracy shall be 10 km.	yes	-	
PHI-MO-FF-4.1: The delivered impulse shall have an accuracy of $3.6Ns$.	unknown	-	
PHI-MO-FF-4.3: The pointing accuracy for the thruster is 2 degrees.	yes	-	
PHI-MO-FF-4.4: Thruster misalignment shall be less than 2.5 mm.	yes	-	
PHI-MO-FF-5.1.1: The clock drift rates shall be less than $1.29 \cdot 10^{-4} s$.	yes	-	
PHI-MO-FF-5.2: The GPS antenna shall be pointed towards zenith with a pointing accuracy of 30 deg.	yes	-	
PHI-MO-FF-6: The duration of the formation flight shall be 7 days.	yes	-	
PHI-MO-FF-7: Formation flying shall be demonstrated even in the case of failure of one satellite.	yes	-	
PHI-MO-FF-7.1: Both satellites shall have a Δv budget of 13 m/s for formation maintenance.	yes	-	
PHI-MO-FF-8: Formation acquisition shall be performed regardless of the injection sequence determined by QB50.	yes	-	
PHI-MO-FF-8.1: Both satellite shall have a Δv budget of 1 m/s for formation acquisition.	yes	-	
PHI-MO-FF-9: Formation flying shall be performed directly after LEOP (9 days after injection).	yes	-	
PHI-MO-PP: The satellite shall be able to operate the QB50 primary payload.	yes	-	
PHI-MO-PP-1.1: FIPEX shall be operated with a duty cycle of TBD.	yes	-	
PHI-MO-PP-1.2: FIPEX shall be kept within its operational temperature range of -20 to +40 degrees celsius.	yes	-	
PHI-MO-PP-1.3: No component shall project in front if FIPEX.	yes	-	
PHI-MO-PP-2.1: The placement of the thermocouples shall be such that their measurement is not corrupted by heat generation of other components in the spacecraft.	yes	-	

Requirement	Met by design	Design value	Comment
PHI-MO-PP-2.2: The thermocouples shall be kept within their operational temperature range.	yes	-	
PHI-MO-PP-2.3: The thermocouples shall be provided with a power of 2-40mW.	yes	-	
PHI-MO-PP-2.4: Data from the thermocouples shall be read out every 0.1s.	yes	-	
PHI-MO-DD-1: The nominal along track separation shall be 1000 km.	yes	-	
PHI-MO-DD-2: The maximum deviation from the nominal along-track direction shall be 50 km.	yes	-	
PHI-MO-DD-3: The maximum difference in semi-major axis shall be 50 km.	yes	-	
PHI-MO-DD-4: The total loss in altitude shall be less than 2 days.	yes	-	
PHI-MO-DD-5: The control accuracy shall be 10 km.	yes	-	
PHI-MO-DD-5.1: The navigation accuracy shall be 1 km.	yes	-	
PHI-GQR-1: No toxic materials shall be used.	yes	-	
PHI-GQR-2: No pressurized containers shall be used.	yes	-	
PHI-GQR-3: The frequencies used for uplink and downlink shall be in the amateur radio band.	yes	-	
PHI-GQR-4: Pyrotechnics shall not be permitted.	yes	-	
PHI-GQR-5: No pressure vessels over 1.2 standard atmosphere shall be permitted.	yes	-	
PHI-GQR-6: Total stored chemical energy shall not exceed 100 Watt-hours (=369kJ).	yes	-	
PHI-TU-1: The cost shall be less than 2 million Euros.	yes	-	
PHI-TU-2: The development and testing of the satellite shall be completed by October 2014.	yes	-	
PHI-ENV-1: The EPS shall provide sufficient power until 90 km altitude.	yes	-	
PHI-ENV-2: Residual magnetic dipole shall be kept low enough for the ADCS to be able to handle the torques due to the interaction with the magnetic field.	yes	-	
PHI-ENV-3.1: All components shall be able to withstand a total radiation dose of TBD.	yes	-	
PHI-ENV-3.2: The OBC shall be able to recover from single event upsets.	yes	-	
PHI-ENV-4: The EPS shall be designed for a worst case RAAN and shall be able to dissipate any excess energy in any other case.	yes	-	
PHI-ENV-5: The volume of the data for downlink that is not telemetry or data form the primary QB50 payload shall be less than 4 Mb/day.	yes	5	Minimum during the mission. Link time dependent on altitude
PHI-ENV-6: The ADCS shall prove reduced attitude control of TBD when the satellite is in safe mode.	yes	-	

Requirement	Met by design	Design value	Comment
PHI-MO-CAM-1 The camera shall be able to monitor the deployment process.	yes	-	
PHI-MO-CAM-1.1 The frame rate shall be at least 48 fps.	yes	-	
PHI-MO-CAM-1.2 The resolution shall be at least 720 x 480 pixels.	yes	-	

Appendix B

Project Gantt Chart

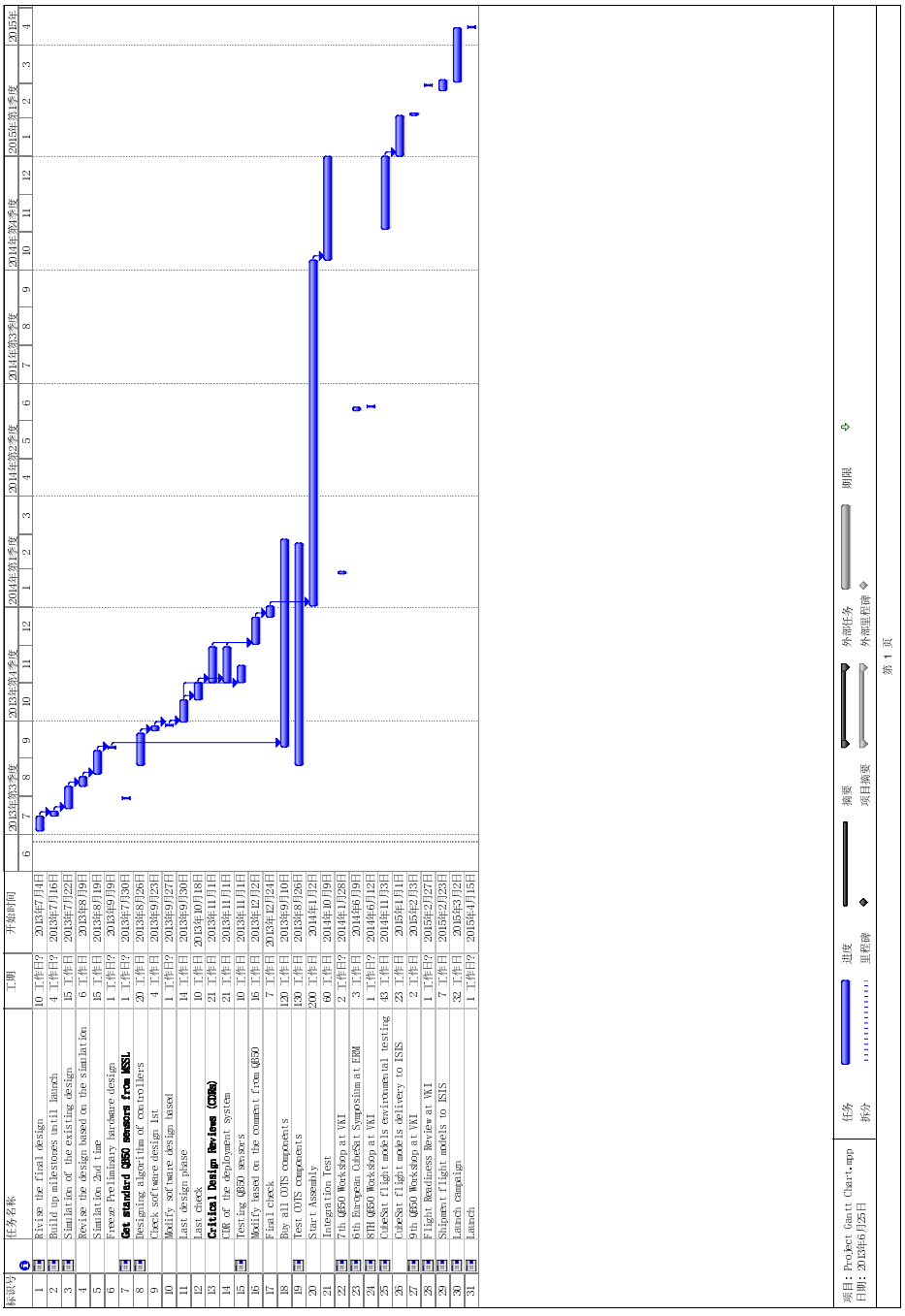

Figure B.0.1: DSE project Gantt Chart

Task Division

Work Package	Responsible
List of Symbols	Pattareeya
List of Abbreviations	Pattareeya
Acknowledgements	Chabely
Abstract	Freddy
1 Introduction	Chabely and Sneha
2.1 Mission Description	Sneha and Pattareeya
2.2 Mission Objectives	Freddy, Sneha and Pattareeya
2.3 Lifetime	Freddy
2.4 Environment	Margaret and Freddy
2.5 Configuration	Margaret
3.1 Operations and Logistics	Pattareeya
3.2 Functional Flow Diagram	Ronald
3.3 Functional Breakdown Structure	Chabely
3.4 Marget Analysis	Margaret
3.5 Manufacturing, Integration and Assembly Plant	Sneha
3.6 Project Design and Development Logic	Maryam
3.7 Cost Breakdown	Sneha
3.8 Risk Assessment	Chabely and Margaret
3.9 Sustainable Development Strategy	Maryam
4 Budget Breakdown	Sneha
5.1 Primary Payloads	Sneha
5.2 Secondary Mission Objectives	Chabely, Margaret, Pattareeya and Sneha
6 Guidance, Navigation and Control	Freddy and Maryam
7 Propulsion System	Maryam
8 Attitude Determination and Control Subsystem	Margaret
9 Communication System	Ronald
10 On-board Computer and Data Handling	Ronald
11 Electrical Power System	Chabely
12 Thermal Control System	Pattareeya
13 Structures	Sneha
14 Spacecraft Systems Characteristics	Ronald
15 Conclusion	Pattareeya

Table B.0.1: Task distribution of report deliverables

Work Package	Responsible
Technical content editing	Margaret and Freddy
Language and format editing	Pattareeya and Sneha
Latex and layout editing	Ronald and Chabely
Executive and jury summaries	Sneha
Catia model	Pattareeya
Poster	Freddy and Chabely
Presentation slides (main)	Margaret

Table B.0.2: Other tasks

Bibliography

[1] Aluminum 7075 specifications.

[2] Acoustic emission sensors specification, 2012.

[3] 1 gram camera, jun 2013.

[4] How many frames per second is best?, jun 2013.

[5] Solar panel deployment test, jun 2013.

[6] Wide angle lens for nano camera, jun 2013.

[7] European Space Agency. Gloab experts agree action needed on space debris, april 2013.

[8] European Space Agency. N^o 9–2013: Call for media: Conference on space debris risks and mitigation, jun 2013.

[9] R.L. Wiley et al. A.K. Hyder. *Spacecraft Power Technologies*. Imperial College Press, London, 2000.

[10] A. Anis. Cold gas propulsion - an ideal choice for remote sensing small satellites, may 2011.

[11] C.A. Bernal and M. van Bolhuis. Releasing the cloud: A deployment system design for the qb50 cubesat mission, 2012.

[12] J. Bouwmeester. Resistor photo, 2013. Old components CubeSats.

[13] Jasper Bouwmeester, 2013. Personal communication.

[14] etc B.T.C. Zandbergen, A. Migliaccio. Vacuum testing of a micropropulsion system based on solid propellant cool gas generators, 2010.

[15] A. Cervone. Application of an advanced micro-propulsion system to the delffi formation flying demonstration withing the qb50 mission. Master's thesis, University of Technology Delft, Delft, 2012.

[16] A. Cervone, 2013. Space Systems Engineering teacher.

[17] Melahat Cihan. A methodology for the structural analysis of cubesat, January 2008.

[18] J.F. Clawson and David G. Gilmore. *Spacecraft Thermal Control Handbook*. American Institute of Aeronautics and Astronautics, California, USA, 2002.

[19] Bruce Crouse. Introduction to acoustic emission testing.

[20] Dr. E. Doornbos. *Empirical Modelling of the Thermosphere*. Springer Berlin Heidelberg, Berlin, 2012.

[21] Eelco Doornbos, 2012. Variations in ballistic coefficients, Contribution to QB50 orbital dynamics working group report.

[22] Alex Ellery, Joerg Kreisel, and Bernd Sommer. The case for robotic on-orbit servicing of spacecraft: Spacecraft reliability is a myth, 2008.

[23] S. Engelen. Flap mechanism photo, 2013. Old components CubeSats.

[24] Steven Engelen, 2013. Educated guess.

[25] Jeff Foust. Emerging opportunities for low-cost small satellites in civil and commercial space. 2010.

[26] D. Gregory. Space debris elimination (spade), february 2013.

[27] Sam Harrison. Nanosatellite fabrication and analysis, June 2012.

[28] A.T. Hogedoorn etc H.M. Sanders, J.M. Boscher. System analysis and development of a cool gas generator based micropropulsion, 2007.

[29] Chia-Hsun Hsieh. Modal analysis of a satellite, April 2013.

[30] ASM Aerospace Specification Metals Inc. Characteristics of aluminum, 2013.

[31] ISIS. Small satellite ground station factsheet, jun 2013.

[32] ISIS. Trxuv factsheet, jun 2013.

[33] Jack A. Jones. Inflatable robotics for planetary applications. Master's thesis, California Institute of Technology, USA, 2000.

[34] Fedorov etc. K. Felix, A. Powell. Use of satellite and in-situ data to improve sustainability, june 2012.

[35] Wiley J. Larson and James R. Wertz. *Space Mission Analysis And Design.* Microcosm Press, El Segundo, California, USA, 2000.

[36] Y. Liu et al. M. Koshear. Mid-term report, 2013.

[37] D.C. Maessen. idod development of a generic inflatable de-orbit device for cubesats. Master's thesis, University of Technology Delft, Netherlands, 2007.

[38] Green Manufacturer. Sage supplier, lowering costs of lithium ion batteries for ev power trains, oct 2013.

[39] M. Matus. New research finds climate change is disrupting satellites and space debris in the atmosphere, november 2012.

[40] Vicki McLaren. User manual: Standalone 30wh battery, 2010.

[41] NASA. Water vapor confirmed as major player in climate change, november 2008.

[42] Department of Defense. Risk management guide for dod acquisition, 6th ed., 2006.

[43] University of Toronto Institute for Aerospace Studies Space Flight Lab. The canx-2 system, 2011.

[44] G. Swinerd P. Fortescue and J. Stark. *Spacecraft Systems Engineering.* Wiley, United Kingdom, 2011.

[45] M.R. Patel. *Spacecraft Power Systems.* CRC Press, Florida, 2005.

[46] Gathier Pierlot. Flight system configuration and structural analysis. Master's thesis, University of Liege, Liege, Belgium, 2009.

[47] C. Quiroz-Garfias. Finite element analysis and design of a cubesat class picosatellite structure. *Electrical and Electronics Engineering*, 2007.

[48] NASA Procedural Requirements. Agency risk management procedural requirements, 2008.

[49] A. Rivest. Earth, night glow, aurora and atmosphere., may 2012.

[50] Guillaume Roethlisberger. Swisscube structural design and flight system configuration. Master's thesis, Space Center, Switzerland, 2007.

[51] Michael J. Rycroft and Norma Crosby. *Smaller Satellites: Bigger Business?: Concepts, Applications and Markets for Micro/nanosatellites in a New Information World.* Microcosm Press & Springe, 1002.

[52] J. M. Forbes S. L. Bruinsma. Medium- to large-scale density variability as observed by champ. *Space Weather*, 6.

[53] Fiona Singarayar.

[54] Fiona Singarayar. Qb50 system requirements and recommendations, February 2013.

[55] Fiona Singarayar. System requirements and recommendations, 2013.

[56] Alan Smith. Qb50 sensor selection working group report, March 2012.

[57] Clyde Space. Clyde space, university of glasgow develop speed brake for cubesats, november 2012.

[58] Clyde Space. Clyde space, university of glasgow develop speed brake for cubesats, november 2012.

[59] Clyde Space. Cubesat, 2013.

[60] Clyde Space. Cubesat solar panel datasheet, 2013.

[61] Andrew Strain. User manual: Deployed electronic power system for cs-xueps2-60, 2010.

[62] Ephraim Suhir. *Structural Dynamics of Electronic and Photonic Systems.* John Wiley & Sons, Hoboken, New Jersey, 2011.

[63] Chelliah Sundararajan. Compendium of formulas for the structural vibration frequency analysis of beams, 2009.

[64] Phi team. Photo, 2013. Made by Phi team.

[65] A.Aruliah T.Scholt, C.O. Asma. Recommended set of models and input parameters for the simulations of orbital dynamics of te qb50 cubesats, 2012.

[66] Wikipedia. P-n junction, may 2013.

[67] Inc. C. Brown Wren Software. *Elements of spacecraft design.* AIAA Education Series, 1st edition, 2003.

[68] B.T.C. Zandbergen. Micropropulsion systems for cubesats. Master's thesis, University of Technology Delft, Delft, 2007.

[69] B.T.C. Zandbergen. About propulsion system failures, may 2011.

[70] B.T.C. Zandbergen. *Aerospace Vehicle Electrical Power Systems.* TU Delft, Delft, Netherlands, 2011.

[71] B.T.C. Zandbergen. Micropropulsion systems for cubesats, (year unknown).